Phase-Equilibrium-Mediated Assembly of Colloidal Nanoparticles

By

Seok Joon Kwon

Master of Science in Chemical Engineering
Seoul National University, Seoul, Republic of Korea, 2004
Bachelor of Science in Chemical Engineering
Seoul National University, Seoul, Republic of Korea, 2002

SUBMITTED TO THE DEPARTMENT OF CHEMICAL ENGINEERING
IN PARTIAL FULFILLMENT OF THE REQUIREMENT FOR THE DEGREE OF

DOCTOR OF PHILOSOPHY IN CHEMICAL ENGINEERING

AT THE
MASSACHUSETTS INSTITUTE OF TECHNOLOGY

JUNE 2013
[SEPTEMBER 2013]

Signature of Author

Department of Chemical Engineering
June 20, 2013

Certified by

T. Alan Hatton
Ralph Landau Professor of Chemical Engineering Practice
Thesis Supervisor

Accepted by

Patrick S. Doyle
Singapore Reseach Professor of Chemical Engineering
Chairman, Committee for Graduate Student

Phase-Equilibrium-Mediated Assembly of Colloidal Nanoparticles

By

Seok Joon Kwon

Submitted to the Department of Chemical Engineering
On June 6, 2013 in partial fulfillment of the requirements for the degree of
Doctor of Philosophy in Chemical Engineering
At the Massachusetts Institute of Technology

Abstract

Colloidal dispersion of nanoparticles (CNPs) has interesting properties both in terms of fundamental studies and industrials applications. Particular focus on the phase equilibrium and separation dynamics of CNPs has been necessary for understanding how exactly and fast CNPs are assembled and for controlling the assembly structure and dynamic properties. For understanding and controlling assembly structure and dynamics of CNPs, theoretical analysis in conjunction with computational approaches supported by experimental validation is necessary. In this thesis, studies on the phase-equilibrium-mediated assembly of CNPs are performed by using various computational tools accompanied by theoretical modeling to cover wide range of spatio and temporal dimensions of the desired system containing CNPs. To address the phase separation of CNPs, we studied on two main mechanisms; (1) cluster formation and (2) spinodal decomposition. In each mechanism, we developed novel, effective, and efficient computational algorithms to elucidate phase-equilibrium assembly structure and formation dynamics of CNPs: (1) a kinetic Monte Carlo (KMC) algorithm for cluster formation in microscopic dimensions and spinodal decomposition of homogeneous mixture of CNPs in mesoscopic scale, (2) a self-consistent mean-field (SCMF) model for surface-directed separation of a binary mixture of CNPs in mesoscopic-macroscopic scale, and (3) the spectral method for spinodal decomposition of a binary or ternary mixture of CNPs in macroscopic scale. All the algorithms and results from the simulations were verified by either mathematical proofs or comparisons to other computational methods. In particular, proof-of-concept experimental results of the fabrication of a functional thin film in which a binary mixture of CNPs form the controlled gradient concentrations profile across the thickness direction were presented. On the basis of the experimental demonstration, we showed the validity of the computational model and possible future applications of the fabricated thin film as an optically-functional material. The computational algorithms and numerical tools developed in this thesis supported by theoretical analysis and experimental demonstration can be applicable to various dynamic problems regarding CNPs, especially, for the complicated cases including multi-component, multi-phase systems. We expect that the work performed in this thesis can provide a substantial advantage for future research, such as controlled cluster formation of CNPs by polymer gel mesh, cluster formation of Janus CNPs, and physically controlled spinodal decomposition of CNPs in thin films, as well as progressive application to preparation of novel devices.

Thesis Supervisor: T. Alan Hatton, Ralph Landau Professor of Chemical Engineering Practice

Dedicated to my family,

Kayoung Lee my lovely wife,

Timothy Taewook Kwon my precious new-born son,

Haw Ja Park & Hak Hee Kwon my parents,

Kun Jin Lee & Hyunhee Jung my parents-in-law,

Seok Beom Kwon my younger brother,

& Soyoung Lee my sister-in-law.

Acknowledgements

First and foremost, I would like express my sincere thanks to my Lord, Jesus Christ. I could do the research during past 5 years with his insight and help whenever I met obstacles.

And I should be grateful for my family: my lovely wife Kayoung Lee and my adorable new-born son Timothy Taewook Kwon. Ever since we met in 2002 winter, Kayoung's support has made the driving force for me to push my life forward positive way. She makes me happy so as for me to feel that I'm a good man. And she has been always a good friend of mine. Additionally, my son's being active in the last semester keeps me awake anytime and anywhere. He is the most important variable in my life equation. With the love and cheers from my parents and my younger brother Seokbeom Kwon should also be acknowledged. And my parents-in-law prayed for me and showed heartful supports during past years. Thank you for your prayer, Soyoung, my sister-in-law, too.

I'm also in a debt to my thesis advisor Prof. Hatton. I have been continuously impressed by his ever-flowing ideas and non-stopping curiosities, while supervising a bunch of research projects spending much of his time up in the air. I should say that he is one of my role models if I have a job position in academia. I'm also grateful for my thesis committee members, Prof. D. Blankschtein, Prof. M. Bazant, and Prof. A. Chakraborty for their precious time and invaluable advices.

I would like to give my thanks to Dr. Tae-Sup Lee graduate fellowship for the first academic year 2008-2009 at MIT and Cabot Corporation for the research project with financial support since summer 2010. In particular, the Cabot people provided me good sense of practical applications of the research and enlightened me that I'm also an engineer who should consider application aspects of the research.

My lab mate Vinay Raman has been a resourceful partner with whom I can discuss various subjects even Indian music and Volloiwood movies as well as computating. Other people in the group including Dr. Sukyoung Suh, Dr. Emily Chang, Dr. Harada Takuya, and Dr. Lev Bromberg also helped me to initiate the proof-of-concept experiments and analyze the observations. My Korean Church friend Dr. Jongmin Lim and my friend Dr. Kiwan Bong also have been great helpers for me to obtain part of experimental results.

I was very lucky to cowork and live with brilliant people around MIT and Cambridge area involving my class mates at SNU, Dr. Seungwoo Lee, Dr. Tekhyung Lee, Dr. Youjin Lee, Dr. Eunjee Lee, Dr. Youngsub Lim, and Dr. Jungwoo Han. I feel warm heart thinking about my life friends Dr. Hyochol Koo, Dr. Hyunwook Kwak, Dohyun Kyung, Hyekyung Noh, and Changdae Kim (prestigious members of the DJ Club). And I am also feeling gratefulness in having precious time with my seniors at SNU, Dr. Changhoon Lim, Dr. Sungcap Im, Dr. Yongku Cho, Dr. Nakwon Choi, Dr. Jonghun Choi, Dr. Sunyoung Lee, M.D., Dr. Daeyoun Lee, Dr. Taeseok Moon, Dr. Changyoung Lee, and Dr. Jongnam Park. Korean friends in the department, Dr. Jinyoung Baek, Hyomin Lee, Siwon Choi, Juhyun Song, Wonjoon Cho, and Youngwoo Son also should be mentioned. Other people in DMSE involving Dr. Jinyoung Kim and Jaebyum Jang also intrigued much research interests for me in 2D NPSCs.

I have been supported by two main non-academic groups: (1) First Korean Church in Cambridge (FKCC) and (2) Boston 3040 tennis club. I was able to maintain my life balance by joining the choir activity at FKCC twice a week with a prominent music director Keeyoung Kim and by playing tennis on every Saturday in the tennis club.

Finally, I feel heart-breaking sorrow to leave my dear school MIT. Thank you MIT. I've learned much from you. All the people I've met during last 5 years at MIT were teachers to me. I should mention that the undergraduate students I met in Fall 2010 term 10.10 course when I was a TA because they inspired me on the teaching and learning. And I learned much from TLL (teaching & learning lab) at MIT in 2009-2010. I have been really happy to meet the new world of novel knowledge and perspectives.

Thank you again for all the help and support for the thesis. If I forgot mentioning credits of others, please forgive me for that. I wish I can help people in future both in academic and non-academic areas.

Table of Contents

(This page is intentionally left blank.)

List of Tables

List of Figures

Chapter 1

Introduction

1.1. Colloidal Dispersions of Nanoparticles

Inorganic nano-scale particles (NPs) and their dispersions as a colloidal phase (CNPs) are important as a foundation for both scientific and industrial applications. When NPs with magnetic properties form a stable and homogeneous colloidal phase, they have a wide range of industrial applications, such as magnetic refrigerator [1,2], sealing materials such as an O-ring for a shaft in a rotary pump, and high performance audio speakers [1]. This stable colloidal phase is called as a 'ferrofluid' [1,3,4], and these fluids are distinguished from magnetorheological (MR) fluids in that the particles in MR fluids are typically larger than 1 μm, whereas the size is typically less than 20 nm for CNPs [1]. Considering that many inorganic NPs containing ferromagnetic and ferroelectric materials show a wide range of refractive indices, it can be expected CNPs are useful for optical applications. In terms of conventional colloid science, CNPs can be considered as a sol in which the dispersed phase is solid and the dispersion medium is a liquid [5]. Studies of colloidal phases involving micrometer-scale particles (either inorganic or polymeric), still focus mostly on their phase equilibrium and stability, in addition to their applications as colloidal crystals (i.e., photonic crystal or glasses) [6-7]. Determining the applicability of CNP hinges mainly on understanding the detailed phase equilibrium and their dynamic characteristics. This understanding provides a basis on which the assembly properties of CNPs under variuous types of external confinement can be controlled. Additional reversible phase transitions involving order-to-disorder or order-to-order transitions of CNPs can be understood on the same basis. Further, these studies are essential to research on device applicability according to the posssible controllability of the physical properties.

The basic thermodynamic properties of phase equilibrium in CNPs are determined mainly by the temperature, NP size, strength if the interactions between the NPs- and the dispersion medium relative to that of NP-NP interactions, and NP concentration. Under specific conditions that produce a stable colloidal phase, CNPs behave as a homogeneous medium, whereas the unstable phase is separated into two phases (i.e., NPs-rich and NPs-dilute hases). Duriung the separation, unstable CNPs loss homogeneity by which NPs form assembled morphology. Considering the volume exclusion effects due to NPs and the different wetting properties that result from coating materials on the NPs' surfaces, approaches based on statistical thermodynamics are useful for analyzing the phase equilibrium. The phase equilibrium also depends on the dimensionality. In three dimensions (3D), the assembly of NPs driven by phase separation yields hexagonal close packed (HCP) structure, whereas this is not always the case for two dimensional (2D) assembly [8-15]. One can also understand the dynamic characteristics of phase transition of CNP phase transitions using the theoretical framework of nucleation followed by growth (i.e., binodal decomposition) and spinodal decomposition, which is a continuous phase separation mechanism [16,17]. Additionally, this understanding should be accompanied by a detailed understanding of how to control the phase equilibrium and separation dynamics using appropriate methods involving external stimulation such as a magnetic or electric field or temperature quenching. These detailed fundamental studies provide a basis on which to achieve controlled phase equilibrium-mediated assembly of CNPs. To develop CNPs control, the characteristics of spontaneous or induced assembly should be considered. An understanding of the assembly behavior under various external confinement involving geometric or dimensional confinements and an external field expands the realm of CNP control. This control corresponds directly to the manipulation of physical properties such as the magnetic, electrical, and optical properties. Further, manipulating the physical properties enables the fabrication of novel devices using the physical properties on a desirable time scale and with satisfactory process parameters. These types of fundamental and applicative studies accompanied by the search for device applications of CNP are attractive research subjects for both academia and industry. A brief history about CNP is given in Table 1.1.

In recent decades, numerous theoretical, experimental, and computational studies of various types of CNPs have revealed unknown phenomena and helped explain their novel properties [8-15,18-21]. Relatively few works, however, have described theoretical and computational studies of the phase equilibrium and separation dynamics of CNPs. The phase-equilibrium-mediated and external-stimuli-induced assembly behaviors of CNPs are also outside the range of intensive research. In particular, there have been no theoretical or computational studies on ternary mixtures of NP dispersions (either homogeneous CNPs in a binary mixture of solvents or binary mixture of CNPs in a homogeneous

solvent). In addition, studies focusing on the thermodynamic properties of CNPs have not considered more complicated but practically meaningful cases in which NPs are coated with structurally stabilizing organic shells such as low molecular weight polymers (i.e., oligomer ligands) and fatty. To expand the realm of knowledge on the fundamental physical properties of CNPs, these areas should be the subject of intensive theoretical and computational work accompanied by experimental studies. With this expansion, one can also expect more effective manipulation of the physical properties of different types of CNPs and good possibilities for demonstrating and fabricating novel devices that control these properties.

Table 1.1. A brief history of CNPs [8]

Year	Main Events
< mid 19c	Pigments for paintings and stained glass
1857	Synthesis of Au NPs (Faraday)
1864	Synthesis of carbon-black for ink
1982	Synthesis of colloidal nanocrystals (Bell Lab)
1989	Synthesis of colloidal nanocrystals with organic ligands (Bell Lab)
1995	Synthesis of core-shell colloidal NPs
1996	Preparation QD aqueous solution
1998-present	Beginning commercialization

1.2. Phase Equilibrium and Assembly of CNPs

The application of NPs largely depends greatly on the stable dispersion of materials in various types of solutions at desirable temperatures [23]. To stabilize the stabilize the dispersions, electrostatic method, such as the introduction of surface charge or an ionic solution [23], and steric methods, such as the use of an organic layer involving polymeric ligands [24-31], are widely applied. Colloidal science recently expanded its focus to the theoretical study of dispersions of various types of NPs such as magnetic and surface-modified inorganic particles in different types of solvents, including polar [32,33] and organic solvents [34]. In particular, the solubility of NPs in different solvents is an important issues that has been studied both experimentally and theoretically [34-38]. Although numerous studies still focus on the mechanism of CNP phase stabilization [32,33], only a few theoretical studies have intensively examined the thermodynamic aspect, such as the phase equilibrium and separation dynamics [36,37].

Thermodynamic analysis of CNPs is directly related to the solubility of the NPs and phase equilibrium, and it should be accompanied by comparable experimental approaches. An understanding of the nature of NP-solvent, NP-NP and solvent-solvent interactions enables quantitative analysis of the effect of enthalpy. This corresponds to the calculation of the total thermodynamic free energy of the dispersion for which the entropic effects obtained by mixing two materials of different sizes (i.e., NPs and solvent molecules) complete the form of the free energy. This basic approach has been widely employed to analyze various heterogeneous systems, such as metal alloys [16,39], polymer solutions [16,39], and the NRTL or UNIQUAC model of fluidic phase mixtures [16,39,40], and their behavior, as well as the static equilibrium of ferromagnetic colloidal systems under an external magnetic field [41,42]. In contrast to traditional models involving the regular solution theory [39,40,43], hydrodynamics [16], and quasi chemical approximation of the thermodynamic properties of solvent-solvent mixtures [39,40], a theoretical model of CNPs might need to pay more attention to the wetting properties of NPs when they are dispersed in a solvent in order to obtain a detailed understating of the thermodynamic properties [31]. This is mainly because of the size difference between the NPs (i.e., typically few~several tens of nanometers) and solvent molecules (i.e., typically several angstroms) [38] and the relatively high surface tension of inorganic NPs [44]. Another reason to consider the different wetting properties of NPs lies in experimental demonstrations of CNPs, which maintains their homogeneous phase stability when they are coated with organic surfactants [15,31]. When this organic surfactant layer between the inorganic NPs and the solvent is introduced, the interfacial properties vary greatly. In addition, long-range interaction among the NPs would be considered when it is comparable to or sufficiently greater than the short-range interaction among NPs [35].

NP assembly has also been a continuous focus of active research owing to the relationship of CNPs to fundamental condensed matter science as a model crystal and their applicability as functional materials for advanced devices [45,46]. In particular, mono-dispersity in both the size and shape and the stability of the assembled structure is important for the formation of well-ordered 2D or 3D assemblies composed of inorganic NPs [8-14,47-49]. Several studies have shown that photonic crystals and glasses can be fabricated by effectively controlling the size of the NPs [6,7]. For nearly mono-disperse NPs, the lack of order at either the short- or the long-range is due mainly to the formation clusters of NPs by isotropic (i.e., van der Waals interaction) or anisotropic (i.e., dielectric or dipolar magnetic interaction) attractive potentials corresponding to particle-particle, particle-cluster (or flocculate), and cluster-cluster interactions. An important method of producing nn ordered assembly of CNPs, such as a self-assembled monolayer (SAM) accompanied by both short- and long-range order, is to coat NPs with different materials that can yield a repulsive potential comparable to the attractive interactions [8-15] to stabilize

the aggregate phase. The repulsive potential originates in both the steric characteristics arising from the elastic deformation energy of the soft-sphere-like organic layer (i.e., capping ligand) and the entropic features arising from the loss of entropy due to overlapping of the capping ligand [50]. Organic materials consisting of surfactants, such as fatty acids and their amine and polymeric materials, can be employed as capping ligands for the NPs [8], and experimental and theoretical research on this strategy is one of the most meaningful paths to progress for both 2D SAMs [8-10,14,15] and 3D superlattices composed of NPs [8,9,11-14,18,19]. In a 3D ordered assembly composed of surface-functional-group-coated NPs, the formation of various types of symmetric structures was reported [8-13], and an empirical relationship was suggested that predicts different symmetries [20,21].

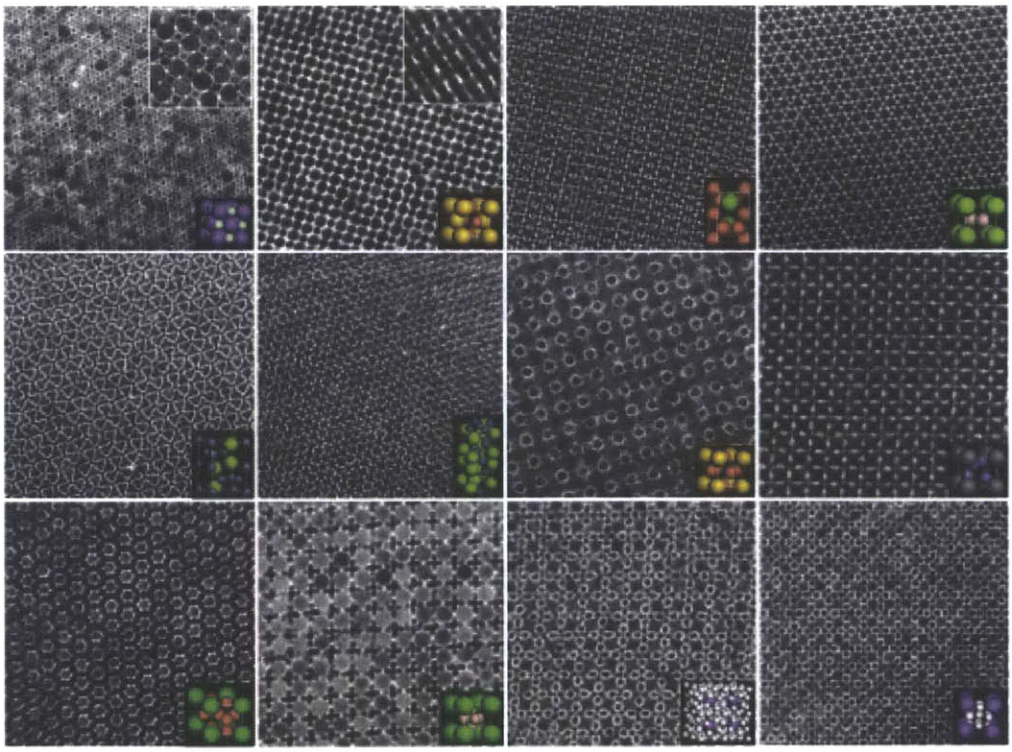

Figure 1.1. TEM images of various 3D self-assembled structures of inorganic NPs. Original images were taken from the literature [11,12,48].

Figure 1.1 shows a representative experimental realizations of the ordered structure of an NP-assembly [11,12,48]. According to the empirical model, the geometric factor given by the size ratio of the NPs and the thickness of the layer of the surface-functional group would be the prominent variable determining the

governing symmetry phase. In most cases, the dominant symmetry has been observed to have face-centered cubic (FCC), body-centered cubic (BCC), and HCP phases [8,9,11-14,18,19]. A theoretical analysis based on the hard-sphere-like potential [18,19] showed that the FCC phase is more stable than the HCP or BCC phase for a 3D superlattice, although their energy differences per unit particle are considerably small compared with the thermal energy at room temperature, which indicates the possible coexistence of heterogeneous phases. Using a free energy analysis focusing on dipolar interaction of the NPs, a recent study explained the origin of new phases such as the non-close packed simple hexagonal phase observed in several different 3D inorganic NP superlattices [49].

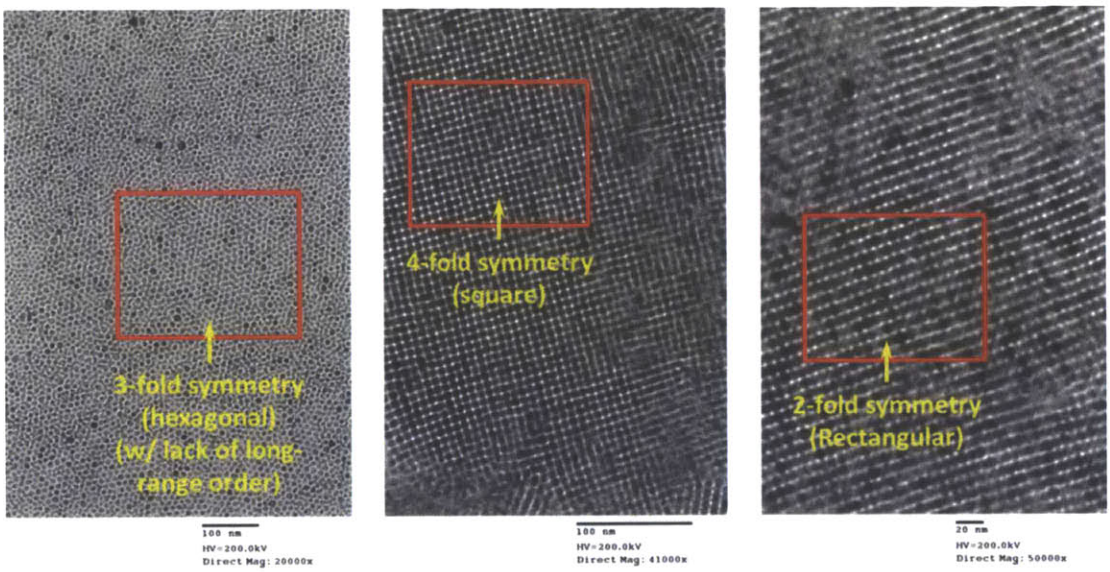

Figure 1.2. TEM images of 2D assembly structures of Fe_3O_4 NPs showing 3- (left), 4- (middle), and 2-fold (right) symmetries [66]

.

In a 2D SAM composed of core/shell structured ligand/inorganic NPs, numerous experimental studies have reported the existence of highly ordered and well-defined superlattice-type phases [8-10,14,15]. In contrast to the 3D case, interestingly, other types of 2D symmetry such as 2- (i.e., rectangular-shaped unit cell) and 4-fold symmetry (i.e., square-shaped unit cell) can be the dominant symmetric phases, as well as 3-fold (i.e., hexagonal-shaped unit cell) symmetry for a 2D SAM when the NPs are coated with a surfactant. Figure 1.2 shows the experimental results for a 2D assembly of Fe_3O_4 NPs [66]. The detailed experimental procedure for preparing the assembly is given elsewhere [10,15,66]. The 3-fold symmetry corresponds to an HCP array in a 3D superlattice, whereas 2- or 4-fold symmetries

correspond to the FCC or BCC phase [9], and it is also observed that their existence can be extended over a relatively large (micrometer scale) area [15]. For a 2D ordered array of ligand-coated NPs, however, no meaningful theoretical studies explaining the different symmetries have been reported. Moreover, the confinement effects for the order-to-order phase transition in a 2D assembly of CNPs given by external geometric confinement, e.g., by a micro-patterned elastomeric mold, are not under intensive investigation.

An assembled phase of CNPs shows more interesting properties when its degree of freedom is limited by external confinements such as geometric or dimensional confinements. For fluidic phase materials, soft-lithography techniques have served as an inexpensive and easy way of patterning thin films [51]. By applying these patterning techniques, 2D and 3D assembled structures of CNPs can be confined in a desirable geometry such as a confined area and shape [51,52], the number of particles in the assembly can be limited. Further, one can predict that these confinement effects can give rise to additional parameters that affect phase transitions such as order-to-order and order-to-disorder transitions in the assembled CNP structure. Interaction with an external field can reveal interesting properties of the assembled phase when it has permanent magnetic or electric properties [3,4,41,42,53]. Incontrast to MR fluids, which use large magnetic particles (≥ 1 μm) [1], a stable colloidal phase of ferromagnetic NPs 20 nm or smaller is used in a ferrofluid [1]. de Gennes and Pincus analyzed the equation of state for static equilibrium of CNPs with an electric or magnetic dipole (i.e., ferromagnetic) on the basis of pair-correlation to show that a ferromagnetic colloid could be aligned by controlling the electric or magnetic field [41]. Experimentally, Butter *et al.* reported a chain-like assembled structure of iron particles covered with a polymeric layer in organic solvents and its transition mechanism under an external field [4]. Singh *et al.* reported experimental observations of the nanowires-like morphology of an assembled structure of core-shell magnetic beads (i.e., poly-styrene beads coated with maghemite (γ-Fe_2O_3) NPs) using a magnetic field and a soft-lithographic patterning technique [53]. These assembled structures of CNPs have more potential as functional materials because the assembly can be easily manipulated by controlling the thermal energy, composition, and field direction and intensity.

A comprehensive study of the understanding and control of CNPs assembly would start by understanding the basics of the phase equilibrium and separation dynamics. The thermodynamic principle suggests the use of a thermodynamic state function, e.g., the free energy as a function of the intensive variables such as temperature and pressure, to describe phase equilibrium. For example, a functional profile of the grand potential G for an unstable ideal binary mixture governed by the designed order parameter ϕ can be found, as shown in Figure 1.3 [87].

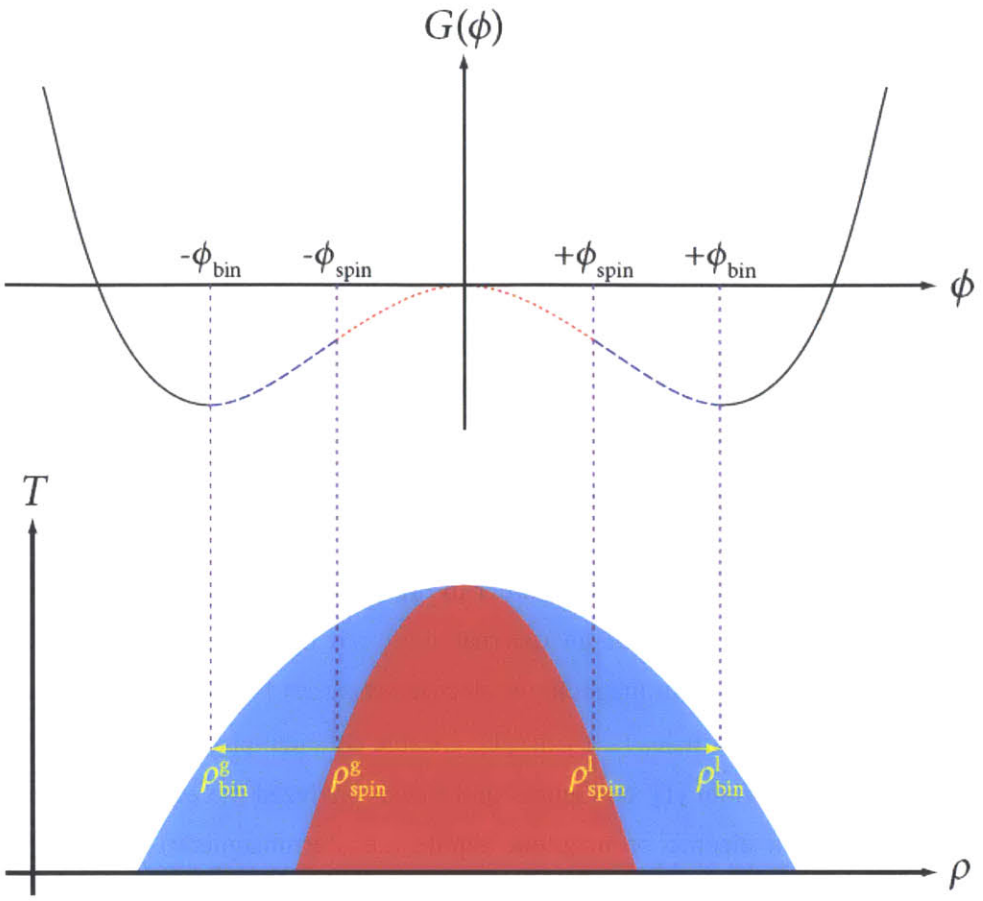

Figure 1.3. A functional profile of the grand potential, G, of an ideal binary mixture (top) as a function of the designated order parameter ϕ and the corresponding temperature (T)-density (ρ) phase diagram (bottom). For the diagram, blue-colored region denote the metastable phase while red regions is for the unstable phase. Yellow horizontal arrow denotes the phase boundaries given by profile of G at constant temperature. The original image was adapted from Lu's doctoral thesis [87].

The number of independent order parameters is equal to the number of independent densities of different components. For example, in an A-B binary mixture, there is only one independent order parameter, $\phi \equiv \phi_A - \phi_B$, where ϕ_i is the density of the ith component. Given the profile of $G(\phi)$, the stable, metastable, and unstable phases can be detemined by calculating the double derivative of $G(\phi)$ with respect to ϕ; $\left.\frac{\partial^2 G(\phi)}{\partial \phi^2}\right|_T < 0$ for the unstable phase. In this phase, the mixture tends to spontaneously

separate into two phases with different values of ϕ [39]. Further, for the unstable phase, the phase separation dynamics is normally governed by a continuous process such as spinodal decomposition, in which a small concentration fluctuation in the initial stage triggers phase separation with a continuous concentration profile over the spatial domain. Even in the phase with $\left.\frac{\partial^2 G(\phi)}{\partial \phi^2}\right|_T \geq 0$, it is still possible for the homogeneous phase to separate into two phases provided that the initial value of ϕ is between the spinodal and bimodal boundaries (see Figure 1.3). This is mainly because the summation of the free energies of the separated phases is smaller than the free energy of the homogeneous phase in this range. The difference between the unstable phase and the phase in this range is that the latter must overcome a certain energy barrier called the nucleation energy. This is why it is called the metastable phase. The phase separation dynamics of the metastable phase is bimodal decomposition, in which the nucleation of small and randomly formed nuclei proceeds with time. The concentration profile observed during bimodal decomposition is discontinuous around the boundary between the nuclei and other phases. When the homogeneous phase satisfies the condition $\left.\frac{\partial^2 G(\phi)}{\partial \phi^2}\right|_T \geq 0$ and the initial value of ϕ is outside of the bimodal boundaries, the phase maintains morphological and phase stability for a long time unless further stimuli are given. Therefore, it is natural to extend the concept of conttrol of the phase equilibrium and separation dynamics by introducing additives such as a phase stabilizer and surfactant, by controlling the temperature and/or pressure, or by manipulating the interface energy between the materials in the system. It is also possible to control the phase equilibrium by controlling the interaction range among certain components; this is done by introducing screening effects from other components. In CNPs, these methods can be applied progressively to obtain reliable controllability of the phase equilibrium and separation dynamics in order to guide the assembly and its dynamics.

Given a detailed understanding of the mechanism of the dynanmics of phase equilibrium/separation followed by CNPs assembly, more feasible and facile applications to the fabrication of functional materials can be expected. The electronics and photonics industries are intensively researching and commercializing phase-change memory (PCM) and storage devices based on a crystalline-amorphous reversible phase transition driven by rapid control of the temperature in the range of the glass transition temperature and melting point of chacogenide glasses such as germanium-antimony-tellurium (Ge-Sb-Te, GST) alloys [54]. In PCM, a temperature gradient in the GST layer is generated and manipulated with programmable Joule heating by an electrical pulse [54] to control the electrical properties of the materials.

This concept of the phase transition and control of the physical properties based on it can be implanted to develop phase change optical media such as the gradient (refractive) index (GRIN) lens. A conventional GRIN lens works because a desirable gradient of the refractive index is realized in a flat transparent medium in which light is bent. The bending of light is achieved not by geometricaly designed lens materials (i.e., conventional curved lens) but by guided refraction [22,55]. There are two types of GRIN lenses; the radial type (i.e., R-GRIN lens shown in Figure 1.4) and the axial type.

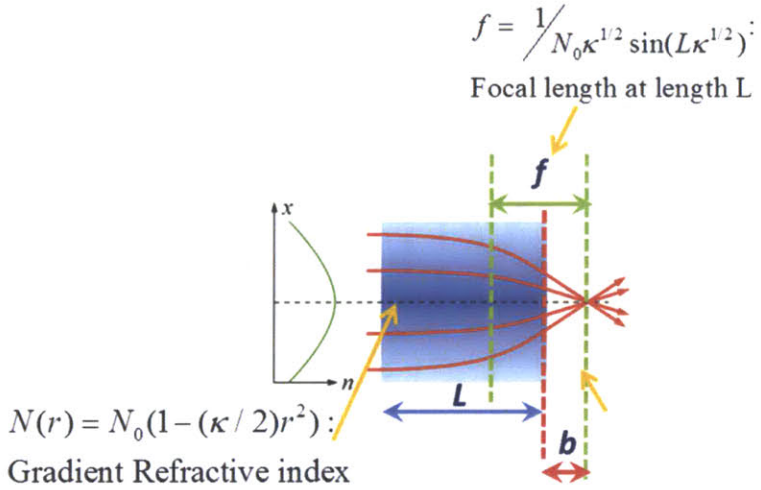

Figure 1.4. A schematic diagram for the radial-type GRIN lens. Profile of the refractive index along the radial direction, $N(r)$, and the relationship between the focal length (f) and the gradient coefficient (κ) are also given [55].

The fabrication of conventional GRIN lenses relies on an ion exchange method in a glass; for example, Sodium ions are immersed into and partially exchanged with Lilthium ions in a liquid melt, depending on the position in the sample (i.e., larger amount of exchange at the edge). Thus, the sample obtains a gradient material structure that realizes a refractive index gradient [55]. As a more inexpensive way of fabricating GRIN lenses, copolymerization of different monomers such as methyl methacrylate (MMA)-acrylonitrile (AN)-vinyl benzoate (VB) can be employed with controlled diffusion techniques [56]. However, the gradient properties of conventional GRIN lenses cannot be controlled after the lens is formed from the composite materials. Recently, Mao *et al.* demonstrated a micro-fluidic-system-based GRIN lens (also called the liquid GRIN lens) by controlling fluidic mixtures in a micro-channel; this result represents a significant advance toward *in situ* control of light [22]. They used the diffusion of a

$CaCl_2$ solute into co-injected laminar flows aligned in parallel and showed that light propagation could be controlled by manipulating the diffusion mechanism in the planar liquid GRIN lens. Considering that phase-equilibrium-mediated assembly of CNPs requires neither complicated processes nor devices such as PCM and the liquid GRIN lens nor an ion-exchange mechanism and relatively high temperature in a solid medium, it has potential as a material for novel optical devices such as GRIN lenses with *in situ* tunable optical properties. Additionally, one can expect more promising features because the control parameters for tunable optical properties based on phase-equilibrium-mediated assembly of CNPs can be derived from the control of process conditions such as temperature quenching, application of an external magnetic field, and composition variation.

1.3. Comparison of Computational Methodologies

We employ computational approaches, one of the most powerful tools tfor verifying and analyzing the physical properties of the assembly structures and dynamics of CNPs. Computational approaches achieve importance and usefulness when they can explain known physico-chemical phenomena, elucidate complicated experimental observations, and predict the physical properties of a desirable materials system that have been either unknown or considered to be difficult to prove experimentally. In the same spirit, we employ various computational methodologies to address the problems we encountered in our studies of the assembly of CNPs by different phase separation mechanisms in systems of different spatio-temporal dimensions. Depending on the feature size of the NPs and the characteristic length scale of the assembly, which are either comparable to the system dimension or not, one needs to consider the relevant computational tools for studying and analyzing the equilibrium and non-equilibrium properties of the CNP assembly structure.

1.3.1. Molecular Dynamics

The first computational tools we consider is molecular dynamics (MD) [67]. For fundamental studies, it is one of the most powerful and suitable methods in computational condensed matter science owing to its theoretical robustness, numerical convenience, wide applicability with different conditions, ability to incorporate complicated inter-molecular potentials, and other characteristics. The MD approach is then divided into two categories. (1) classical MD, in which the thermodynamic properties of a system are calculated by considering only the weak forces (i.e., non-bonding forces) and (2) quantum MD, in which

the chemical transformations of materials are calculated considering the strong forces that participate in chemical reactions, electron transfer, enzyme catalysis, and other processes. Quantum MD is usually accompanied by other quantum chemistry and mechanics-based methods such as density functional theory (DFT). Classical MD would be a more appropriate approach for the phase equilibrium and assembly of CNPs. The basic fueature of classical MD is a deterministic framework in which the outcomes of system dynamics can be calculated and predicted by a finite number of system updates using Newton's equations of motion. For example, consider a simple case of N NPs dispersed in a non-reacting non-polar liquid medium in which the effective molecular interaction potential between the ith and j th NPs separated by $r_{ij} \equiv \left|\mathbf{r_i} - \mathbf{r_j}\right|$. Then, the potential for the interaction between the two neighboring particles $V\left(r_{ij}\right)$ is assumed to be the Lennard-Jones potential,

$$V\left(r_{ij}\right) = 4\varepsilon\left[\left(\frac{\sigma}{r_{ij}}\right)^{12} - \left(\frac{\sigma}{r_{ij}}\right)^{6}\right], \tag{1.1}$$

where σ denotes the size of the NP, and ε represents the interaction energy density among the NPs. This potential assumes that the NPs interact with each other only via short-range two-body interaction. For the ith NP, the effective force driving the motion, $\mathbf{F_i}$, is written as

$$\mathbf{F_i} = -\sum_{j \neq i} \nabla V\left(r_{ij}\right). \tag{1.2}$$

The finite differential form of the equation of motion of the ith NP is then written using the Verlet algorithm [67] as

$$\begin{aligned}
\mathbf{r_i}\left(t+\delta t\right) &= \mathbf{r_i}\left(t\right) + \mathbf{v_i}\left(t\right)\delta t + \frac{\mathbf{F_i}\left(t\right)\delta t^2}{2m_i} + \frac{\partial \mathbf{F_i}\left(t\right)}{\partial t}\frac{\delta t^3}{6m_i} + \mathrm{O}\left(\delta t^4\right), \\
\mathbf{r_i}\left(t-\delta t\right) &= \mathbf{r_i}\left(t\right) - \mathbf{v_i}\left(t\right)\delta t + \frac{\mathbf{F_i}\left(t\right)\delta t^2}{2m_i} - \frac{\partial \mathbf{F_i}\left(t\right)}{\partial t}\frac{\delta t^3}{6m_i} + \mathrm{O}\left(\delta t^4\right),
\end{aligned} \tag{1.3}$$

where $\mathbf{v_i}\left(t\right)$ and m_i are for the velocity and mass, respectively, at time t. Then $\mathbf{v_i}\left(t\right)$ is given by

$$\mathbf{v_i}\left(t\right) = \frac{\mathbf{r_i}\left(t+\delta t\right) - \mathbf{r_i}\left(t-\delta t\right)}{2\delta t} + \mathrm{O}\left(\delta t^2\right). \tag{1.4}$$

Using eqs.(1.3) and (1.4) with the velocity Verlet algorithm [67], the master equation for the dynamics of the system can be written as

$$\mathbf{r}_i(t+\delta t) \approx \mathbf{r}_i(t) + \mathbf{v}_i(t)\delta t + \frac{\mathbf{F}_i(t)\delta t^2}{2m_i},\ \mathbf{F}_i(t) = -\sum_{j\neq i} \nabla V_i\left(\left|\mathbf{r}_i(t) - \mathbf{r}_j(t)\right|\right)$$
$$\mathbf{v}_i(t+\delta t) \approx \mathbf{v}_i(t) + \frac{\left(\mathbf{F}_i(t+\delta t) + \mathbf{F}_i(t)\right)\delta t}{2m_i}. \quad (1.5)$$

In the initial stage, the thermal energy associated with the kinetic energy affects the NPs' momentum distribution according to the Maxwell-Boltzmann distribution. Further, eq.(1.5) is numerically solved as a function of time. One of the advantages of using classical MD is that it preserves the total free energy of the system (i.e., sum of the potential and kinetic energies), which guarantees the physical exactness of the description of the system dynamics. However, the problem with using classical MD to describe the phase equilibrium and separation dynamics of CNPs is that it is computationally limited, although many have tried to use classical MD for this problem [67,71,73]. For example, for a system with a spatial domain of a few tens of micrometers in the planar direction and a few hundreds of nanometers in the thickness direction with a 0.1% initial volumetric fraction of 10-nm NPs, it is necessary to describe and update two independent information sets on the positions and momenta of $\sim 10^8$ NPs. Additionally, to investigate the most interesting dynamics phenomena, observers must examine the dynamic processes for at least a few micro seconds and up to a few hours. For a typical classical MD simulation, the characteristic time, $\tau = \left(m\sigma^2/\varepsilon\right)^{1/2}$, is normally $\tau \sim 10^{-9} \sim 10^{-8}$ s for NPs a few tens of nanometers in diameter. With the typical characteristic-time-based differential time for system updates, $\delta t \sim 10^{-11} \sim 10^{-10}$ s; therefore, it would be necessary to describe the system using $10^4 \sim 10^{14}$ iterations. This is a highly cost-ineffective approach. Although the number of independent information sets for the positions and momenta can be reduced by considering the nearest neighbors within a certain cut-off distance, it is still well beyond the computationally achievable realm. In addition, when the dispersion medium is a polar solvent or ionic liquid, the computational cost increase polynomially (i.e., $\sim N^2$), because the number of independent information sets for the positions and momenta rapidly increases.

1.3.2. Brownian Dynamics

Instead of classical MD, a computationally effective description such as Brownian dynamics (MD) would be a candidates for studying the phase equilibrium and separation dynamics. BD is based on the Langevin equation [67-71], which ignores the inertial effects of the particle. Instead, two additional forces are employed: (1) the frictional force from the dispersion media and (2) the stochastic force from random

collisions of NPs with solvent molecules. In particular, the stochastic effect is based on the implicit solvent model, which assumes that the solvent forms a background field represented by the screening constant, which is a function of the dielectric constant. The ignorable inertial effects should be checked considering that the mass of a single individual NP becomes negligibly small compared to the Stokes' drag coefficient $\zeta = 3\pi\eta\sigma$, where η is the viscosity of the liquid medium, when σ is sufficiently small. The stochastic force acts to make the diffusional motion of NPs a random walk such that

$$\frac{\mathbf{r}_i(t+\delta t)-\mathbf{r}_i(t)}{\delta t} \propto \left(\frac{2D}{\delta t}\right)^{1/2} \boldsymbol{\theta}_i(t),\ \boldsymbol{\theta}_i(t)=[\theta_{iX}(t)\ \theta_{iY}(t)\ \theta_{iZ}(t)],$$
$$P(\theta_{iK}(t)) = \frac{1}{\sqrt{2\pi}}\exp\left(-\frac{\theta_{iK}(t)^2}{2}\right), \tag{1.6}$$

where D is the diffusion coefficient of the NP which can be deduced from Einstein's relation as $D = k_B T \zeta^{-1}$, and θ_{iK} is a random variable for the motion of the ith particle in the Kth-dimension. The probability distribution $P(\theta_{iK})$ is assumed to satisfy the normal distribution with a mean of zero. In particular, the temporal correlation of the stochastic force should satisfy the equilibrium ensemble average relationships (denoted by brackets) such that

$$\langle \boldsymbol{\theta}_i(t) \rangle = 0,$$
$$\langle \boldsymbol{\theta}_i(t)\boldsymbol{\theta}_j(t') \rangle = \boldsymbol{\delta}(t-t')\boldsymbol{\delta}_{ij},$$

where is $\boldsymbol{\delta}(x)$ the Dirac delta function. This is from the dissipation-fluctuation theorem of the Langevin equation, in which the temperature is affected by the adjustment of ζ. The drag force reduces the velocity of the particle:

$$\delta\mathbf{v}_i(t) = -\frac{\nabla V(\mathbf{R}(t))|_{\mathbf{r}_i(t)}}{\zeta},\ V(\mathbf{R}(t)) = V_{LJ}(\mathbf{R}(t)) = \sum_{i\neq n}^{N} 4\varepsilon\left(\left(\frac{\sigma}{|\mathbf{r}_j(t)-\mathbf{r}_i(t)|}\right)^{12} - \left(\frac{\sigma}{|\mathbf{r}_j(t)-\mathbf{r}_i(t)|}\right)^{6}\right),$$
$$\mathbf{R}(t) = [\mathbf{r}_1(t),\cdots,\mathbf{r}_N(t)]. \tag{1.7}$$

Using the second-order stochastic Runge-Kutta (SRK) BD algorithm, the equation of motion of the NPs described in eqs.(1.6) and (1.7) can be expressed with the finite differential form of the system dynamics as [69]

$$\mathbf{r}_i(t+\delta t) = \mathbf{r}_i(t) - \frac{\delta t}{2\zeta}\left(\nabla V\left(\mathbf{R}(t)\right)\Big|_{\mathbf{r}_i(t)} + \nabla V\left(\mathbf{R}(t)\right)\Big|_{\mathbf{r}_i(t)+\delta\mathbf{r}_i(t)}\right) + \left(2D\delta t\right)^{1/2}\boldsymbol{\theta}_i(t). \quad (1.8)$$

Owing to the stochastic factor in the master equation, the system dynamics would not be reproducible; however, important ensemble-based statistical information such as the structure factor, radial distribution function $g(r)$, and correlation time and length can be obtained.

Using eq.(1.8), we examined a representative scenario for the phase separation of A- and B-NPs dispersed in a non-reacting non-polar Newtonian liquid medium. For the simulation, we used $\delta t \sim 5\times10^{-7}$ s on the basis of the characteristic time of the system dynamics, $\tau \sim 10^{-5}$ s (i.e., from the Brownian relaxation time $\tau \sim m/\zeta$) when A- and B-NPs are spontaneously demixed at room temperature; $\varepsilon_{AA} = \varepsilon_{BB} = 4\varepsilon_{AB}/3 = 2k_BT$, $\sigma = \sigma_A = \sigma_B = 2\sigma_{AB}/3 = 20$ nm [72], $D = D_A = D_B = 10^{-11}$ m^{2}s^{-1} , and $\phi_A = \phi_B = 8.5\times10^{-2}$ (i.e., 510 particles for each) in a 3D box of $0.2\times0.2\times1.2$ μm^3 . To study how fast the confining wall-effects emerge when the phase separation morphology is controlled, we also added wall effects represented by $V\left(\mathbf{R}(t)\right)\Big|_{\mathbf{r}_i(t)} = V_{LJ}\left(\mathbf{R}(t)\right)\Big|_{\mathbf{r}_i(t)} - \frac{A_W}{r_{i,z}(t)^3}$, where A_W is the wall-NP interaction parameter (i.e., $A_{WA} = 0$, $A_{WB} = 10\varepsilon\sigma^3$ for a B-attractive wall), and $r_{i,z}(t)$ is the vertical position of the NP relative to the bottom wall. As Figure 1.5 clearly shows, the BD simulation would describe the controlled concentration distribution of selectively attracted NPs (i.e., B-NPs) near the bottom wall.

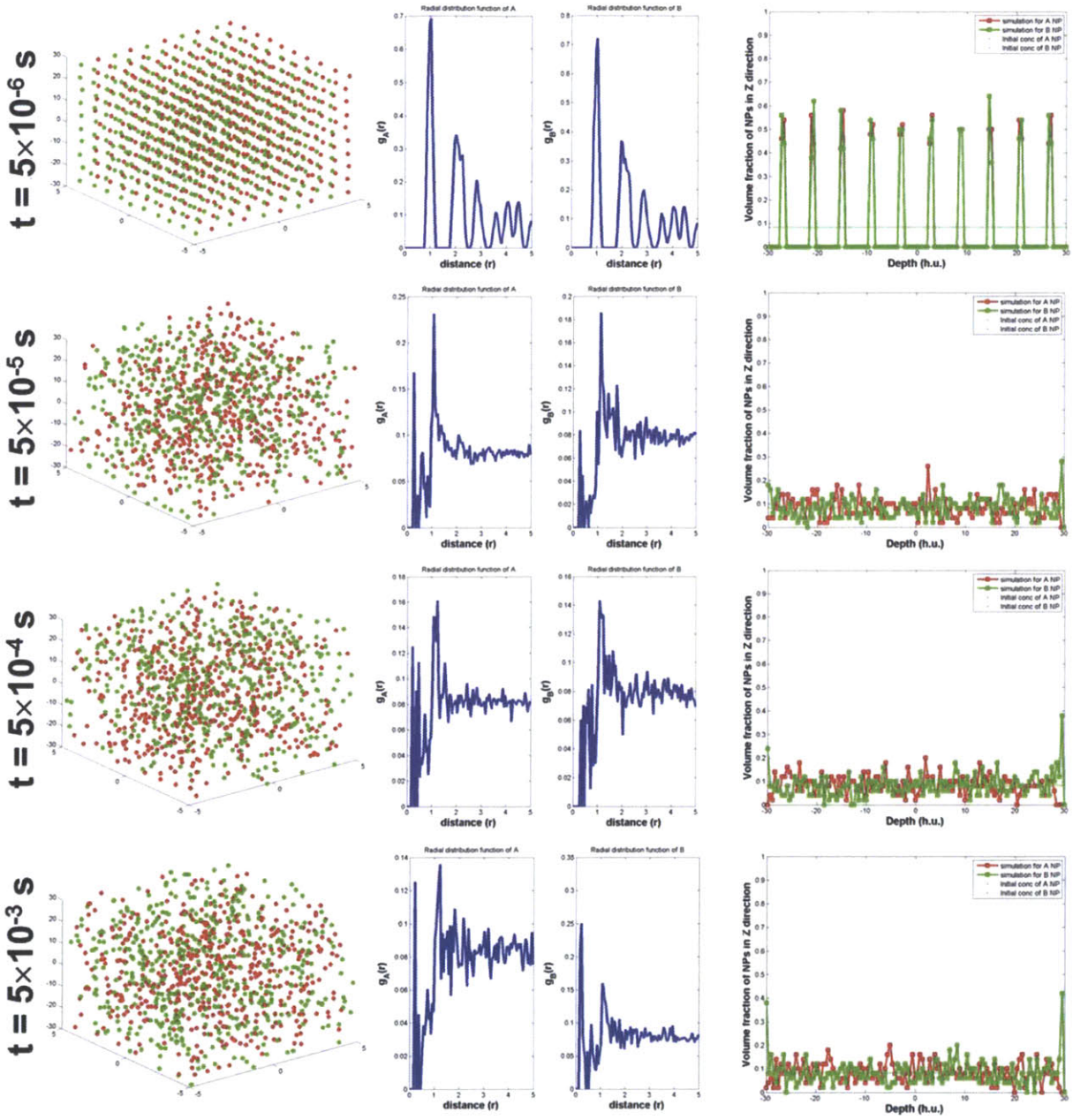

Figure 1.5. Brownian dynamics simulation of the temporal evolution of controlled separation of 20 nm-A- and B-CNPs in 3D box of $0.2\times0.2\times1.2\ \mu m^3$ with a B-selective attractive bottom confining wall. Distribution of A- and B-NPs (green dots for B- and red dots for A-NPs in the 1st column), radial distribution function for A- and B-NPs (left for A- and right for B-NPs in the 2nd column), and the concentration profile along the direction normal to the bottom wall (green for B- and red for A-NPs in the 3rd column). See the section 1.3.2 for the detailed simulation condition.

From the results we can also observe that the confining wall effects emerge rapidly after 10^{-4} s. Although it is not discussed in detail in this chapter, the computational efficiency was enhanced by considering only the nearest neighbors within the cut-off distance $r_C = 2.5\sigma$ and the minimal image convention [67,71,73].

Although BD simulations can be used for short-term processes during phase separation and imposes less computational cost than MD with advanced numerical schemes, it is still restricted to larger spatial domains and longer temporal dimensions. Another disadvantage is that it is difficult to incorporate either the short-time correlation, which is affected by the inertial effects, or realistic hydrodynamic interactions between NPs and solvent molecules. In addition, it is still computationally expensive to employ a polar solvent and ionic liquids as the dispersion medium; this also applies to MD simulations.

1.3.3. Monte Carlo Simulation

Simulation of an entire system composed of billions of particles is practically impossible. Instead, it is well known that sampling and averaging would represent the collective and average behaviors of the system. Statistically, the error introduced by sampling and averaging, $\Delta\delta$, is related to the sample size M as $\Delta\delta \propto M^{1/2}$ [67,71]. This implies that the distribution of a certain quantity is sharpened by introducing a larger sample size. For example, it would be critical to select an appropriate system configuration to realize the distribution of the system free energy around the average. However, it is difficult and ineffective to set the configuration in an *a prior* manner. In 1953, Metropolis *et al.* [67,71,73,74] introduced the importance sampling scheme considering a Markov chain, which tends to arrive at the equilibrium state considering that the Markov chain has 1) ergodicity, which suggests that the ensemble average should reach the average over time after a finite number of trials, 2) normalization, which sets the confining condition for the set of transition probabilities, and 3) reversibility, which guarantees arrival at the equilibrium state in a finite number of trials.

Let us assume a system composed of multiple configurations among which the transition probability, $T_r(A \to B)$, where A and B represent the configurations, is known. The master equation for the temporal evolution of the probability of the system being at configuration X at t, $P(X,t)$, can be written as

$$\frac{\partial P(X,t)}{\partial t} = \sum_{Y}\left[\left(P(Y,t)\cdot Q(Y,X)\right) - \left(P(X,t)\cdot Q(X,Y)\right)\right],\ Q(X,Y) \equiv T_r(X \to Y)\cdot A_c(X \to Y),\ (1.9)$$

where $A_c(A \to B)$ denotes the acceptance probability for the transition between configurations A and B. On the basis of the properties of the discrete Markov chain, we can find that $\sum_{Y} Q(X,Y) = 1$ and $\sum_{Y} P^{(eq)}(Y)Q(Y,X) = P^{(eq)}(X)$, where the superscript (eq) denotes the equilibrium state. At equilibrium, $\frac{\partial P(X,t)}{\partial t} = 0$; therefore, $\sum_{Y} P^{(eq)}(Y)\cdot Q(Y,X) = \sum_{Y} P^{(eq)}(X)\cdot Q(X,Y)$. Next, we find that $P^{(eq)}(Y)\cdot Q(Y,X) = P^{(eq)}(X)\cdot Q(X,Y)$, considering that the Markov chain configurations are independent of each other from eq.(1.9). The last relationship is called the detailed balance. When the energy of the specific configuration, $E(X)$, is known, we can apply the Boltzmann distribution at temperature T for $P^{(eq)}(X)$, $P^{(eq)}(X) = \exp\left(-E(X)/k_B T\right)/Z$, where k_B is the Boltzmann constant, and $Z = \sum_{Y} \exp\left(-E(Y)/k_B T\right)$, which denotes the partition function. The original concept of Metropolis *et al.* is to write [74]

$$A_c(X \to Y) = \min\left(1,\ \frac{P^{(eq)}(Y)}{P^{(eq)}(X)}\right),$$

which can be read through the Boltzmann distribution as $A_c(X \to Y) = \min\left(1,\ \exp\left(-\frac{\Delta E}{k_B T}\right)\right)$, where $\Delta E = E(Y) - E(X)$. This scheme to drive the system to equilibrium is called the Metropolis Monte Carlo (MMC) algorithm [67,71,73,74]. Although this scheme appears simple, it has been widely used and is well known to provide an exact description of a system at equilibrium. On the basis of the ergodicity property of the Markov chain, it can be conjectured that a system can reach the equilibrium state within a finite number of trials of the transitions among the configurations provided that the system can be described as a Markov chain. Most thermodynamic phenomena can be considered as Markov processes in which the next state function is considered to be only a function of the predecing state function; therefore, phase equilibrium can be successfully described and analyzed by the MMC algorithm. There can be additional forms for $A_c(X \to Y)$ that can satisfy the detailed balance; well-known examples include the Glauber dynamics and Kawasaki dynamics [67,71].

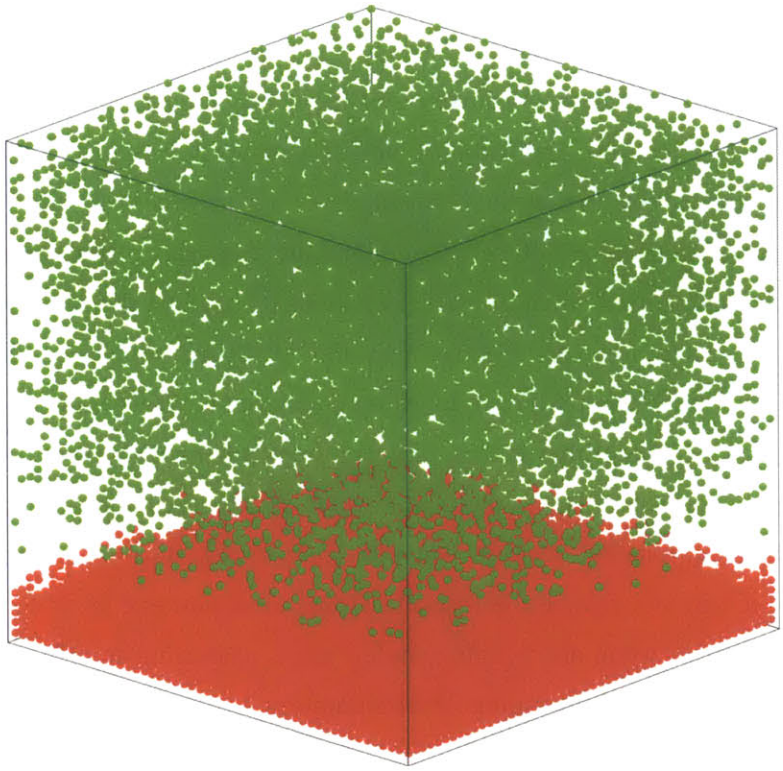

Figure 1.6. A simulation result based on the 3D Metropolis Monte Carlo (MMC) algorithm for the calculation of distribution of A- (red dots) and B- CNPs (green dots) in a thin film after 11,570 iterations. For the simulations, each of the NPs was assumed to interact via the Lennard-Jones potential and move on the square lattice in a 3D box with the dimensions of $L_X = L_Y = L_Z = 50\sigma$. For the confinements, the bottom surface was assumed to be attractive to A-NPs while repulsive to B-NPs.

It is advantageous to employ MC algorithms to study the equilibrium properties of the system; simultaneously, this is the most important shortcoming because it is difficult to describe the dynamic properties of the system without the aid of an additional dynamic framework, such as adaptive matching between the MC iteration step and the physical flow of time. It is also known that the MC algorithm can be parallelized to enhance the computational efficiency, particularly the particles move on a lattice [67,71].

Figure 1.6 shows a representative scenario of the phase separation of A- and B-NPs in a thin film simulated by the MMC algorithm. The simulation were similar to those of the BD simulation used to generate the results shown in Figure 1.5, except that $\phi_A = \phi_B = 0.1$ (i.e., $12,500$ particles per each NP-

type), $A_{WA} = 10\varepsilon\sigma^3$, and $A_{WB} = -10\varepsilon\sigma^3$. A periodic boundary condition was applied in the planar direction, whereas a non-flux condition (Neumann condition) was used for the direction normal to the confining walls (i.e., the z-direction). The bottom wall was assumed to be selectively attractive to A-NPs, whereas B-NPs were repelled by the wall. Although it is not shown in Figure 1.6, the calculated distribution of the concentrations of each type of NP along the z-direction shows good agreement with the results from other computational methods such as a method based on the self-consistent mean field (SCMF) (see Chapters 4 and 5). This implies that the MMC algorithm can be employed as a computational tool to describe the properties of the phase equilibrium and separation of CNPs. One of the disadvantages of using the MC algorithm is that it becomes computationally expensive for larger spatial and temporal dimensions, although this was also found when other computational methods were applied. Additionally, it takes an unreasonably long time when the simulation is stuck on the local minimum of the free energy, and thus, it may not realize the real and global minimum energy states at equilibrium. In particular, it is more expensive when one tries to simulate the system using an off-lattice method. This is because of the computational cost of generating random numbers.

1.3.4. Kinetic Monte Carlo Simulation

The conventional MC simulation can be used in combination with a powerful dynamic tool such as a stochastic algorithm to describe the system dynamics. One method of incorporating the dynamic calculation is to employ the relationship between the MC step and a realistic time scale. This is called dynamic MC (DMC) [67,71,75]. The problem with this method is that it cannot help introducing a certain numerical artifact when connecting the stochastic iteration step and real-world dynamic characteristic time. As an alternative and fundamental method, Gillespie [76] introduced a kinetic Monte Carlo (KMC) algorithm based on the reaction kinetics, which can be modeled as an independent discrete Markov process. In the reaction kinetics, the average waiting time of each reaction is compared to that of each of the others and the fastest reaction is fired, which affects the overall dynamic properties of system equilibrium. Gillespie's stochastic algorithm, also called the first reaction algorithm or direct algorithm [76], is exact and efficient for a small system; however, it is computationally limited for larger systems mainly because of a problem with sorting the waiting time for numerous reaction (or diffusion) propensities. To incorporate the sorting problem, Gibson and Bruck [77] introduced a binary tree data structure based on the heapsort scheme [73,77] to efficiently sort the waiting times with several specific data structures such as a dependence matrix. This algorithm is called the next reaction method (NRM) algorithm because it updated the system dynamics by considering only the affected reaction/diffusion

propensities. The NRM algorithm also exhibits dramatically enhanced computational efficiency because it can re-use the random numbers used for updating the system dynamics [77]. The most distinctive advantage of the KMC is that it is physically exact for a system under stochastic effects. It generates random numbers to update the dynamics as BD does; however, the update scheme is more robust because it considers a designed distribution of the waiting time before generating the stochastic effects. It is also advantageous for system dynamics simulations in large spatial- and temporal domains owing to the computational efficiency of the NRM algorithm. It is also flexible for incorporating a variety of dynamics processes. For example, we show that the KMC can be progressively applied under various conditions in Chapters 2 and 3. It is also promising to extend KMC algorithms over parallel computing environments by transforming the computable data structure over a set of computing cores. Note, however, that it is still limited to a few hours for larger domains covering a few hundreds of micrometers. Detailed information on the KMC algorithm is available in Chapter 3 and Appendix A.

1.3.5. Numerical Simulation based on Continuum Framework

If we can assume that the system is a coarse-grained entity or is in a continuum framework, the concentration of CNPs can be set as the continuous field variables. Using these variables, we can construct a macroscopic mass transport model to solve the problems of the phase equilibrium and separation dynamics of CNPs. For example, one may solve the partial differential equations (PDEs) for the phase separation governed by spinodal decomposition on the basis of the phase field model (PFM), which assumes that the concentration field is continuous around the interface. The PDEs can be solved in a reasonable amount of computation time by employing several advanced numerical methods, such as the finite difference method, with numerically effective and reliable integration schemes, such as the explicit Runge-Kutta algorithm [73,79], the second-order Adams-Bashforth algorithm [73,78-80], and spectral transform [81].

Since its recent introduction, the lattice Boltzmann method (LBM) has been increasingly used to solve phase separation problems [82-86]. It is beyond the scope ot this thesis to introduce detailed theoretical models based on the LBM to solve the problems of phase separation by spinodal decomposition. However, an increasing number of researchers found wide applicability of the LBM for complicated boundary conditions and multi-component and multi-phase system. A disadvantage of using the LBM is that it is still controversial whether numerical models for the LBM, such as the D2Q9 scheme, guarantee the conservation of energy and momentum [85,86]. Another open question regarding the use of the LBM is that there is no congruent viewpoint on the description of the boundary conditions [82-86].

Detailed discussions of the PFM and spinodal decomposition are provided in Chapters 3 and 6. The most distinctive advantage of using numerical methods to solve the PDEs is that they are fast and accurate for large spatial domains.

Another perspective on using the continuum framework is the SCMF model. A wide range of thermodynamic problems on equilibria based on statistical mechanics principles can be approached using the Boltzmann theorem. Given a specific ensemble for the system, such as a canonical or micro canonical ensemble, one can calculate the average probability of the distribution of specific thermodynamic variables such as the order parameter in either the spatial or temporal dimension. However, the distribution itself is a function of the distribution of other variables that affect the thermodynamic free energy. Therefore, it can be easily conjectured that the master equation, such as the system equation, has an implicit form; therefore, it is not possible to solve the problem using an analytic method. To solve the implicit problem, numerical methods can be applied; however, it is more effective and efficient to use a designed algorithm based on the SCMF method in particular cases, such as minimization of the morphology of a relaxed protein chain. In an equilibrium distribution of a mixture of CNPs in a system with the desired dimensions, we may also apply the SCMF method instead of conventional MC simulations to obtain computational efficiency. The disadvantage of using the SCMF method is that we cannot obtain dynamic information on the system from a simulation or on-the-fly calculation. Therefore, it would be difficult to analyze the phase separation dynamics of CNPs by using the SCMF algorithm.

1.3.6. User-Informative Diagram for Choosing Computational Methods

In the previous sections, we described the features and representative application results of a variety of computational methods of analyzing and describing the equilibrium and non-equilibrium dynamic properties of CNPs. It would be instructive to provide a summary illustrating the spatio-temporal domains and the corresponding effective and efficient computational tools. As shown in Figure 1.7, each of the methods exhibits strength and effectiveness in certain ranges of the spatial and temporal domains. Further, the applicable ranges usually overlap. Irrespective of the computational methods, a trade-off relationship always exists among the computational accuracy, scalable computable domains, and computational cost. All of the factors depend strongly on the computational power, e.g., the CPU speed and available memory. Ever increasing computational capacity allows users to combine different methods for more and wider applications.

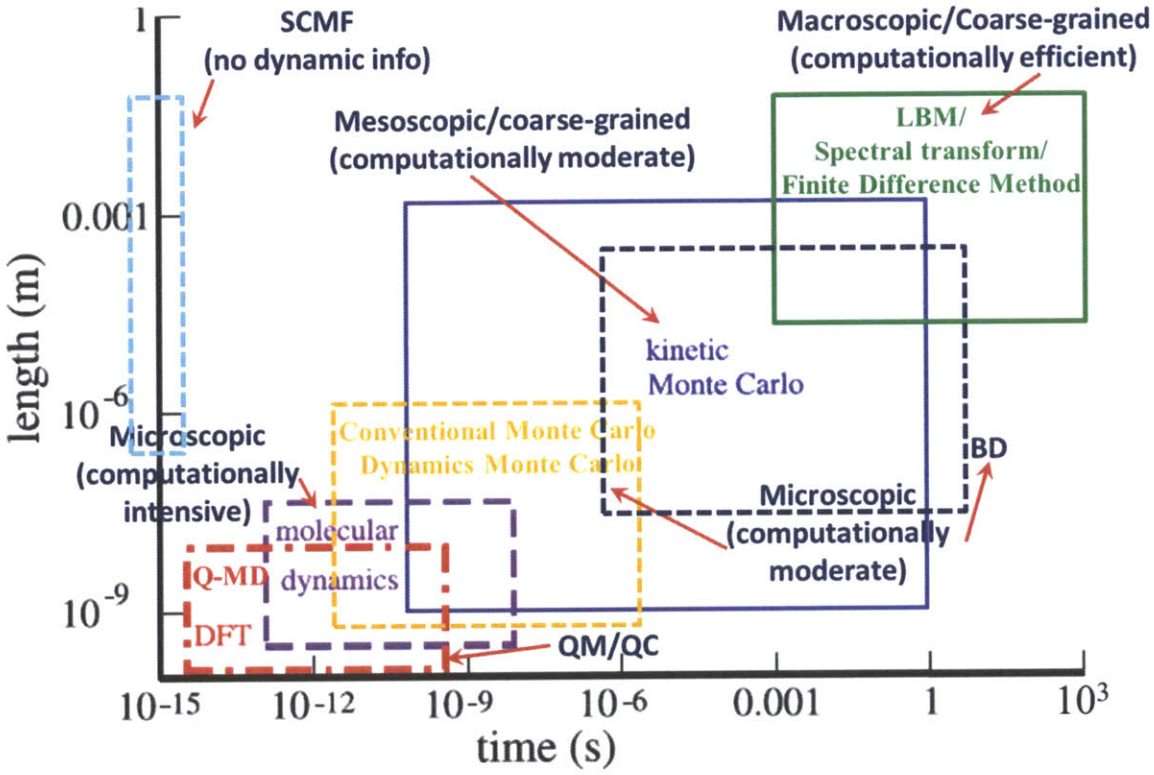

Figure 1.7. Comparison of a variety of computational methods both in computing-effective spatial and temporal ranges. The molecular dynamics (MD) area colored with violet denotes the classical MD. The SCMF algorithm concerns only spatial domain due to its limitation in calculation of the non-equilibrium dynamic properties. Note for the abbreviations: LBM = Lattice Boltzmann Method, SCMF = Self-Consistent Mean Field, QM/QC = Quantum Mechanics/Quantum Chemistry, DFT = Density Functional Theory, BD = Brownian Dynamics, Q-MD = Quantum Molecular Dynamics.

Recent progress in parallel computing algorithms using a general-use graphic process unit (GUGPU), for example, the Compute Unified Device Architecture (CUDA™) algorithm by NVIDIA® [88] would improve the computing performance by extending the computable domain while retaining reliable computational accuracy.

1.4. Structure of the Thesis

In this doctoral thesis, I performed the following research; 1) studies of the fundamentals of the phase equilibrium and separation dynamics of CNPs, 2) theoretical and computational studies of the assembly

behaviors driven by phase separation accompanied by external confinement, and 3) experimental realization of the possible application of CNPs as functional materials. For each of these items, I tried to develop novel computationally efficient and mathematically effective algorithms to solve the problems of the assembly structure and dynamics of CNPs. For the computational studies, I also developed several useful and convenient supplementary numerical algorithms. To verify the computational results and confirm the consistency of the theoretical model, comparative studies of the different computational and theoretical approaches were performed to solve the problems under consideration. Further, I suggested that theoretical and computational studies could be useful resources for preparing functional materials with seleected distributions of NP concentrations through proof-of-concept experiments. Figure 1.8 is a schematic diagram that summarizes the structure of this thesis. Note that some parts of the research are not included in this thesis for consistency and because of conflicts of interest concerning collaborative work with others.

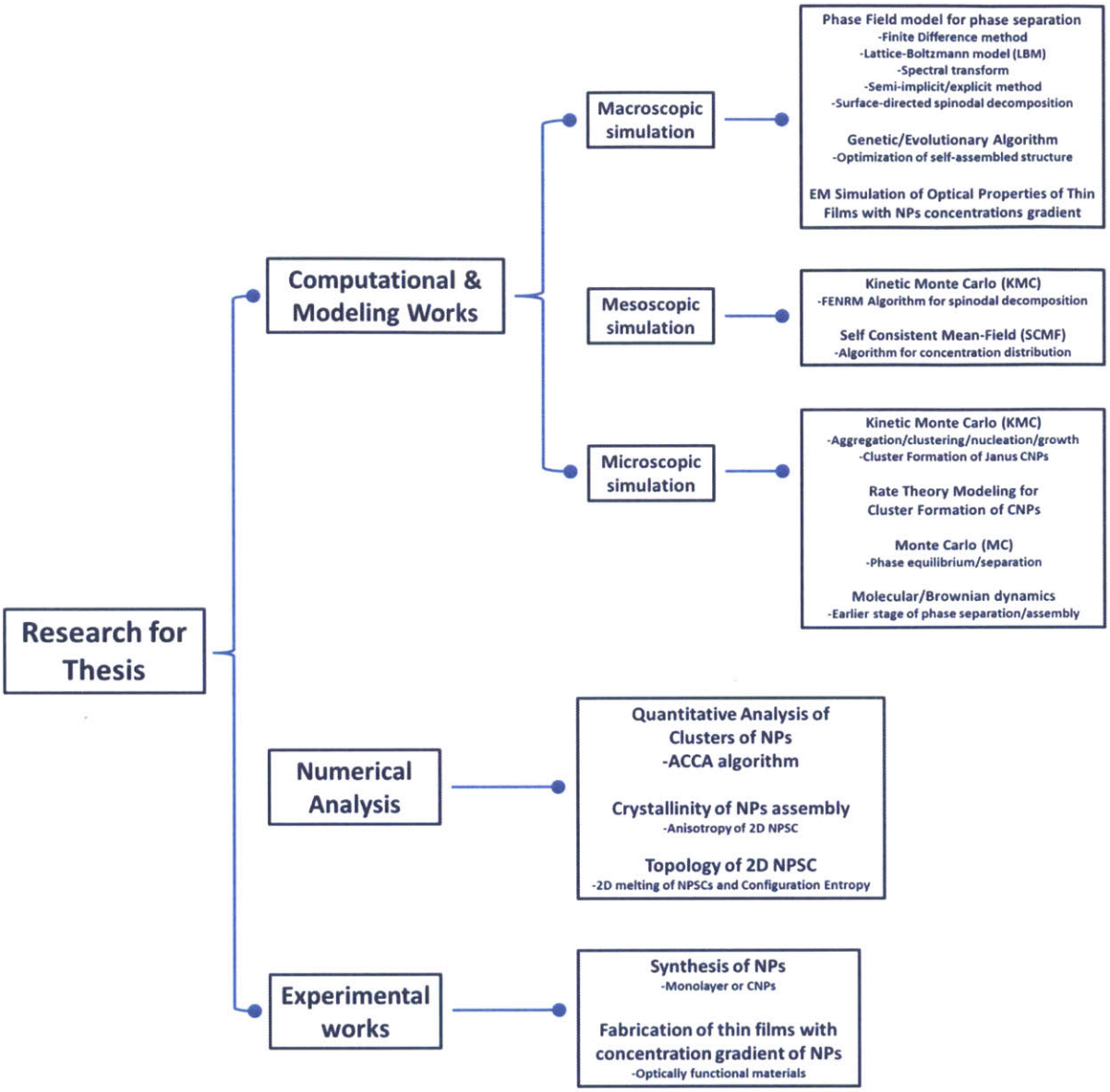

Figure 1.8. A schematic structure of the research I have done for the present thesis (Note: some parts of the works were not involved in this thesis)

1.5. Referebnces

[1]. R.E. Rosensweig, *'Ferrohydrodynamics'*, (Cambridge Univ. Press, New York, 1985).

[2]. K.A. Gschneidner Jr., V.K. Pecharsky, and A.O. Tsokol, *Rep. Prog. Phys.*, **68**, 1479 (2005).

[3]. S.A. Safran, *Nat. Mater.*, **2**, 71 (2003).

[4]. K. Butter, P.H. Boman, P.M. Fredrik, G.J. Vroege, and A.P. Philipse, *Nat. Mater.*, **2**, 88 (2003).

[5]. C. J. Brinker, G.W. Scherer, '*Sol-Gel Science: The Physics and Chemistry of Sol-Gel Processing*', (Academic Press, New York, 1990).

[6]. A. Rogach, A. Susha, F. Caruso, G. Sukhorukov, A. Kornowski, S. Kershaw, H. Möhwald, A. Eychmüller, and H. Weller, *Adv. Mater. (Weinheim)*, **12**, 333 (2000); V.L.Colvin, *MRS Bulletin*, August, 637 (2001).

[7]. P.D. Garcia, R. Sapienza, and C. Lopez, *Adv. Mater. (Weinheim)*, **21**, 1, (2009).

[8]. B.L. Cushing, V.L. Kolesnichenko, and C.J. O'Connor, *Chem. Rev.*, **104**, 3893 (2001).

[9]. S. Yamamuro, D.F. Farrel, and S.A. Majetich, *Phys. Rev. B*, **65**, 224431 (2002).

[10]. S. Sun and H. Zeng, *J. Am. Chem. Soc.* **124**, 8204 (2002); S. Sun *et al.*, *Ibid,* **126**, 273 (2004).

[11]. E.V. Shevchenko *et al.*, *Nature (London)*, **439**, 55 (2006).

[12]. E.V. Shevchenko *et al.*, *Adv. Mater. (Weinheim)*, **19**, 4183 (2007).

[13]. A. Ahniyaz, Y. Sakamoto, and Lennart Bergstrom, *Proc. Natl. Acad. Sci. USA*, **104**, 17570 (2007).

[14]. A.H. Lu, E.L. Salabas, and F.Schuth, *Angew. Chem. Int. Ed. (Weinheim),* **46**, 1222 (2007).

[15]. T. Harada and T.A. Hatton, *Langmuir*, **25**, 6407 (2009).

[16]. P.M. Chaikin and T.C. Lubensky, '*Principles of Condensed Matter Physics*', (Cambridge Univ. Press, New York, 2000).

[17]. A. Onuki, '*Phase Transition Dynamics*', (Cambridge Univ. Press, New York, 2002).

[18]. P.G. Blohuis, *Nature (London)*, **388**, 235 (1997).

[19]. R.E. Rudd, *Phys. Rev. B*, **58**, 5893 (1998).

[20]. B.A. Korgel and D. Fitzmaurice, *Phys. Rev. B,* **14**, 191 (1999).

[21]. R.L. Whetten *et al.*, *Acc. Chem. Res.* **32**, 397 (1999).

[22]. X. Mao, S.C. S. Lin, M.L. Lapsely, J. Shi, B.K. Juluri, T.J. Huang, *Lab. Chip.*, **9**, 2050 (2009).

[23]. R.H. Ottewill, *Langmuir*, **5**, 4 (1989).

[24]. S.M. Ilett, A. Orrock, W.C.K. Poon, and P.N. Pusey, *Phys. Rev. E*, **51**, 1344 (1995).

[25]. B. Vincent, J. Edwards, S. Emmett, and R. Croot, *Colloids Surface*, **31**, 167 (1986).

[26]. A.P. Gast, W.B. Russel, and C.K. Hall, *J. Colloid Interface Sci.*, **109**, 161 (1986).

[27]. M.H.G. Duits, R.P. May, A. Vrij, and C.G. de Kruif, *Langmuir*, **7**, 62 (1991).

[28]. H.N.W. Lekkerkerker, W.C.K. Poon, P.N. Pusey, A. Stroobants, and P.B. Warren,

Europhys. Lett., **20**, 559 (1992).

[29]. S.Y. Kang and K. Kim, *Langmuir*, **14**, 226 (1998).

[30]. A.M. Jackson, J.W. Myerson, and F. Stellacci, *Nat. Mater.*, **3**, 330 (2004).

[31]. A. Centrone, E. Penzo, M. Sharma, J.W. Myerson, A.M. Jackson, N. Marzari, and F. Stellacci, *Proc. Nat'l. Acad. Sci.,* **105**(29), 9886 (2007).

[32]. O.M. Bakr, B.H. Wunsch, and F. Stellacci, *Chem. Mater.*, **18**, 3297 (2006).

[33]. O. Uzun, *Chem. Comm.* **196-198**, 10.1039 (2008).

[34]. E. Dubois, V. Cabuil, F. Boue, and R. Perzynski, *J. Chem. Phys.* **111**(15), 7147, (1999).

[35]. C.F. Tejero, A. Daanoun, H.N.W. Lekkerkerker, and M. Baus, *Phys. Rev. Lett.*, **73**, 752 (1994).

[36]. W.M. Gellbart, R.P Sear, J.R. Heath, and S. Chaney, *Farad. Disc.*, **112**, 299 (1999).

[37]. G.M. Whitesides and B. Grzybowski, *Science*, **270**, 1335 (1995).

[38]. E. Rabani, D.R. Reichman, P.L. Geissler, and L.E. Brus, *Nature*, **426**, 271 (2003).

[39]. H.T. Davis, *'Statistical Mechanics of Phases, Interfaces, and Thin Films'*, (VCH Publishers Inc., New York, 1996).

[40]. J.W. Tester and J Modell, '*Thermodynamics and Its Applications*', *3rd ed.* (Prentice Hall PTR, New York, 1997).

[41]. P.G. de Gennes and P.A. Pincus, *Phys. Kondes. Materie.*, **11**, 189 (1970).

[42]. P.J. Camp, J.C. Shelly, and G.N. Patey, *Phys. Rev. Lett.*, **84**, 115 (2000).

[43]. J.H. Hildebrand, J.M. Prausnitz, and R.L. Scott, *'Regular and Related Solutions'*, (Van Nostrand Reinhold Co., New York, 1970).

[44]. J.N. Israellachivili, '*Intermolecular and Surface Forces', 2nd ed.* (Academic Press, New York, 1992).

[45]. C.T. Black *et al.*, *Science*, **290**, 1131 (2000).

[46]. S. Hoeppener *et al.*, *Adv. Mater. (Weinheim)*, **14**, 1036 (2002).

[47]. P.C. Ohara, J.R. Heath, W.M. Gelbart, *Angew. Chem. Int. Ed. (Weinheim),* **36,** 1077 (1997).

[48]. J.J. Urban *et al.*, *Nat. Mater. (London)*, **6**, 115 (2007).

[49]. D.V. Talapin *et al.*, *Nano Lett.* **7**, 1213 (2007).

[50]. E.L. Mackor, *J. Colloid Sci.* **6**, 492 (1951).

[51]. N. Bowden *et al.*, *Nature*, **393**, 146 (1998); K.Y. Suh, Y.S. Kim, and H.H. Lee, *Adv. Mater. (Weinheim)*, **13**, 1386 (2001).

[52]. S.J. Kwon, J.H. Park, and J.G. Park, *Appl. Phys. Lett.*, **87**,133112 (2005).

[53]. H. Singh, P.E. Laibnis, and T.A. Hatton, *Nano Lett.*, **5**, 2149 (2005); H. Singh, P.E. Laibnis, and T.A. Hatton, *Langmuir*, **21**, 11500 (2005).

[54]. S. Raoux, M. Wuttig (*Ed.*), '*Phase Change Materials; Science and Applications*', (Springer, New York, 2009).

[55]. E.W. Marchand, '*Gradient Index Optics*', (Academic Press, New York, 1978).

[56]. Y. Koike, H. Hidaka, and Y. Ohtsuka, *Appl. Opt.*, **24**, 4321 (1985).

[57]. J.W. Cahn and J.E. Hilliard, *J. Chem. Phys.*, **28**, 258 (1958).

[58]. T. Isojima and T.A. Hatton, *unpublished work* (2009).

[59]. J. Tang, G. Ge, and L.E. Brus, *J. Phys. Chem. B*, **106**, 5653 (2002).

[60]. H.C. Hamaker, *Physica*, **4**, 1058 (1937).

[61]. M.J. Vold, *J. Colloid Sci.* **16**, 1 (1961).

[62]. E.L. Mackor, *J. Colloid Sci.* **6**, 492 (1951).

[63]. L.D. Landau and E.M. Lifshitz, '*Theory of Elasticity*', *3rd ed.* (Elsevier, New York, 1986).

[64]. L. Bo and R.E. Waugh, *Biophys. J*, **55**, 509 (1989).

[65]. I. Langmuir, *J. Chem. Phys.* **1**, 756 (1933).

[66]. S.J. Kwon, T. Harada, and T.A. Hatton, *to be submitted* (2013).

[67]. D. Frenkel and B Smit, *'Understanding Molecular Simulation: From Algorithms to Applications'*, (Academic Press, New York, 2002).

[68]. D.J. Higham, *SIAM Rev.*, **43**, 525 (2001).

[69]. A.C. Branka and D.M. Heyes, *Phys. Rev. E*, **58**, 2611 (1998).

[70]. J. Dzubiella, G.P. Hoffmann, and H. Lowen, *Phys. Rev. E*, **65**, 021402 (2002).

[71]. M.P. Allen and D.J. Tildesley, *'Computer Simulation of Liquids'* (Clarendon Press, Oxford, 1989).

[72]. J.N. Canongia Lopes, *Phys. Chem. Chem. Phys.*, **4**, 949 (2002).

[73]. W.H. Press, S.A. Teukolsky, W.T. Vetterling, and B.P. Flannery, *'Numerical Recipes: The Art of Scientific Computing'*, *3rd ed.* (Cambridge University Press, Cambridge, 2007).

[74]. N. Metropolis, A.W. Rosenbluth, M.N. Rosenbluth, A.H. Teller, and D. Teller, *J. Chem. Phys.*, **21**, 1087 (1953).

[75]. S.A. Serebrinsky, *Phys. Rev. E*, **83**, 037701 (2011).

[76]. D.T. Gillespie, *J. Comp. Phys.*, **22**, 403 (1976).

[77]. M. Gibson and J. Bruck, *J. Phys. Chem. A*, **104**, 1876 (2000).

[78]. R. Mauri, R. Shinnar, and G. Triantafyllow, *Phys. Rev. E*, **53**, 2613 (1996).

[79]. D.J. Eyre, *Siam J. Appl. Math.*, **53**, 1686 (1993).

[80]. D. Cogswell, *Ph.D. Thesis, M.I.T.* (2010).

[81]. C. Canuto, M.Y. Hussaini, A. Qaurteroni, and T.A. Zang, *'Spectral Methods: Evolution to Complex Geometries and Applications to Fluid Dynamics'*, (Springer-Verlag, Berlin, 2007).

[82]. X. Shan and H. Chen, *Phys. Rev. E*, **49**, 2941 (1994).

[83]. J. Chin and P.V. Coveney, *Phys. Rev. E*, **66**, 016303 (2002);

[84]. P. Yuan and L. Schaefer, *Phys. Fluids*, **18**, 042101 (2006).

[85]. L.S. Luo, *Phys. Rev. Lett.*, **81**, 1618 (1998).

[86]. L.S. Luo and S.S. Girimaji, *Phys. Rev. E*, **66**, 035301(R) (2002);
L.S. Luo and S.S. Girimaji, *Ibid*, **67**, 036302 (2002).

[87]. P. Lu, *Ph.D. Thesis, Harvard University* (2009).

[88]. http://www.nvidia.com/object/cuda_home_new.html.

(This page is intentionally left blank.)

Chapter 2

Computational Study on Cluster Formation of Colloidal Nanoparticles: A Kinetic Monte Carlo Simulation and Rate Theory Modeling on Scaling Behaviors of Clusters*

Abstract

An understanding of the statistical and time-dependent features of cluster formation is essential for the application and control of the dispersion quality of colloidal nanoparticles (CNPs). We performed computational and theoretical studies on the formation of clusters in CNPs, focusing on the scaling behavior of the growth of the cluster size and size distribution, with analysis of the fractal dimension. For the study, we employed a kinetic Monte Carlo (KMC) algorithm in which NPs are moved by self-avoiding diffusive jumping with a random walk. To describe diffusion of the NPs in a colloidal environment, the diffusivity was modeled as a configuration-dependent function of the interacting potential of the clusters. To verify the computational analysis, a kinetic model based on rate theory (RT) was used to analyze the temporal evolution of the concentrations of the monomer and clusters. The KMC simulations agreed well with the predictions from RT in terms of the description of the scaling behaviors. In particular, we observed that the scaling exponents for the average cluster size and weight are smaller than the conventional predictions, although the fractal dimension of the cluster was comparable to that observed in the typical reaction-limited aggregation of particles. We provided a semi-empirical explanation of how the scaling exponent of the cluster size and weight should be reduced depending on the scaling behavior of the monomer concentration. We also provided a model to explain the dependence of the induction time for cluster formation on the initial monomer concentration; the model is supported by the KMC simulation and RT calculation. The results of this study can be used to design and control the colloidal quality of NP dispersions by understanding the cluster growth behavior and its dynamics.

Parts of Chapter 2 will be submitted to a peer-reviewed journal (Authored by S. Joon Kwon & T. Alan Hatton).

2.1. Introduction

Cluster formation has been a subject of intensive research interests in areas ranging from statistical physics to industrial applications [1]. Conventionally, theoretical and experimental studies have concentrated on cluster formation as a model for the aggregation of particles, agglomeration of soft matter, nucleation followed by growth in a continuum framework, and so on [1-5]. As the spatial scale of materials of which both the dimensions and shape can be controlled has decreased recently, the study of cluster formation has expanded to include nano-scale materials such as nanoparticles (NPs), nanocrystals, and nanowires as the cluster components [4-10]. At the atomic scale, for example, computational and experimental studies have already focused on the formation and growth of 2D islands of adatoms on the surface in the context of cluster formation [7,9,11]. On the selected surface, the statistical characteristics of cluster growth, such as the time-dependence of the average cluster size/weight, and the scaling behavior of the cluster size distribution, can be evaluated by assuming discrete movement of adatoms on the surface along the designed lattice directions with a hopping distance.

Conventionally, Brownian dynamics (BD) simulations as well as molecular dynamics (MD) has been intensively used to describe the dynamic properties of clustering or aggregation of colloidal particles. However it is computationally expensive toe simulate the dynamics for long times. In addition, the physical description from the BD simulation can be in accurate [18]. In addition, MD or BD simulations would be lacked with the consideration of the stochastic effects provided by the liquid dispersion medium when the colloidal particles are nanometer-scale. For the case where of solid adatoms form clusters on the 2D lattice surface in gaeous environment, statistical features of the clusters can be effectively evaluated using a kinetic Monte Carlo (KMC) simulation because the diffusional movement of adatoms is confined to a selected number of possible jumping directions (i.e., 4 on the square lattice) with a fixed jumping distance [8,9]. This feature of the KMC simulation provides enhanced computational efficiency compared to conventional simulations, particularly for longer time regimes [9]. Instead of the conventional MD or BD simulation, the KMC algorithm would be more suitable to simulate the long-time dynamics of the cluster formation of nanoparticles in a liquid medium. Ineed, the use of the KMC algorithm has attracted increasing interest for quantitative measurement of the cluster formation process under a variety of conditions that are difficult to set up and examine experimentally.

Unfortunately, little research has been done on theoretical and computational studies of systems that are more attractive to industry, such as NP dispersions in liquid media. In particular, a colloidal dispersion of nanoparticles (CNPs) required further study in terms of cluster formation. A CNP is a dispersion of NPs in a liquid medium that maintains phase stability by balancing the attractive and

repulsive forces among the NPs. Typically, NPs around ten nanometers in size interact with each other via van der Waals forces and electrostatic or dipolar interaction between surface-coating molecules such as oligomers [6,12]. With time, NPs tend to form cluster, because they lose the potential balance by with reductions in the surface functionality, temperature fluctuations, and so on. Once clusters consisting of NPs form, they can grow continuously in a manner similar to the Ostwald ripening. It is important to understand how cluster formation occurs and proceeds, mainly because the dispersion property of CNPs is affected by the growth of the hydrodynamic radius of clusters and its distribution. The quality of the dispersion of CNPs for a sufficiently long period depends on the temporal evolution of the clustering behavior of NPs.

In this chapter, we provided a computational and theoretical analysis of cluster formation in CNPs. To describe the colloidal dispersion, one can use a complicated potential model considering a variety of potential contributions arising from the relationship between NPs and the electrolyte used as the dispersion medium, and among NPs, the hydrodynamic interaction among NPs, the entropic effect yielded by the elastic properties of the surface-coating molecules, and so on. Although the complicated potential model can describe more realistic CNP environments, we employed the Lennard-Jones (LJ) potential, a simple potential model that can achieve potential balance. Without loss of generality, the simple potential model can allow us to more efficiently extract the critical features of the statistical and temporal evolution of cluster formation in CNPs. For the computational study, we employed a KMC simulation based on an efficient stochastic algorithm, the next reaction method (NRM) [13]. To verify the computational observation, we also analyzed the cluster formation based on rate theory (RT) assuming a continuum framework for the concentration of clusters and a single NP (i.e., monomer). The computational and theoretical analysis showed that the scaling of the average cluster size and weight as a function of time differs from the conventional expectation, although the fractal dimension of the clusters was similar to that observed in other studies such as those of reaction-limited aggregation (RLA). Interestingly, we found that the growth rate of a cluster consisting of CNPs is much slower than that observed in conventional cluster formation phenomena involving Ostwald ripening with a lower scaling exponent. We provid an explanation of how the scaling of the cluster size and weight are affected by the time-dependence of the monomer concentration. This work would provide a substantial advantage to those who want to understand, control, and modify clusters in CNPs.

2.2. Theoretical Framework

2.2.1. Configuration-Dependent Diffusivity

CNPs generally maintain their stability by balancing the repulsive and attractive forces among NPs. In particular, van der Waals interactions among NPs contributes greatly to the attractive potentials when the NP size is several tens of nanometers. Dipolar interactions between functional groups on the NP surfaces, mechanical stress caused by elastic deformation of the functional group, or the entropy cost, which increases with increasing distance r among the NPs, contribute to the repulsive force. Below the critical temperature, the entropy contribution to the free energy decreases; therefore, NPs try to aggregate to minimize the enthalpy contribution to the free energy. In this study, we employed the LJ potential model, one of the simplest models for the inter-particle potential, as follows:

$$F(r) = 4\varepsilon\left[\left(\frac{\sigma}{r}\right)^{12} - \left(\frac{\sigma}{r}\right)^{6}\right], \tag{2.1}$$

where ε and σ are the potential well depth and NP size, respectively. Although the LJ-potential model does not reflect the precise nature of the attractive and repulsive forces among NPs dispersed in a liquid medium, it is useful for obtaining critical features of the behavior of NPs when they move collectively, for example, in clusters. To realize the condition for cluster formation, we assume that the diffusion of monomers and clusters is discrete and depends on the configuration, as in KMC simulations of island growth on the lattice [6-8]. This assumption is in contrast to the continuous description of particle diffusion in Brownian dynamics (BD) or MD simulations [14,15]. To describe diffusion in our KMC simulations, we introduced the differential hopping distance of a monomer, h, by which the KMC simulation is physically equivalent to BD or MD simulations, as follows [14]:

$$h^2 = D_{m0}\delta t, \tag{2.2}$$

where D_{m0} is the diffusivity of a monomer, ignoring environments effects involving potentials from other monomers or clusters, and δt is the differential characteristic time employed in BD or MD simulations. In addition, the diffusivity of an individual particle that is not a monomer is assumed to depend on the configuration of the particle when it experiences environmental effects contributing to cluster formation. For the diffusivity of the ith particle, D_i, the Arrhenius-like dependence is employed as follows:

$$D_i = D_{m0}\exp\left(-\Delta E_i / k_B T\right), \tag{2.3}$$

where k_B is the Boltzmann constant, and T is a constant temperature. In eq.(2.3), the effect of the environment is reflected by the energy barrier ΔE_i, which can be calculated as:

$$\Delta E_i = -\int_{\sigma}^{r_C} 2\pi r g(r) \rho_0 F(r) dr, \tag{2.4}$$

where $g(r)$ and ρ_0 denote the 2D radial distribution function and the initial number density of the particles, respectively. In eq.(2.4), the cut-off distance among the particles, r_C, is conventionally set to $r_C = 2.5\sigma$.

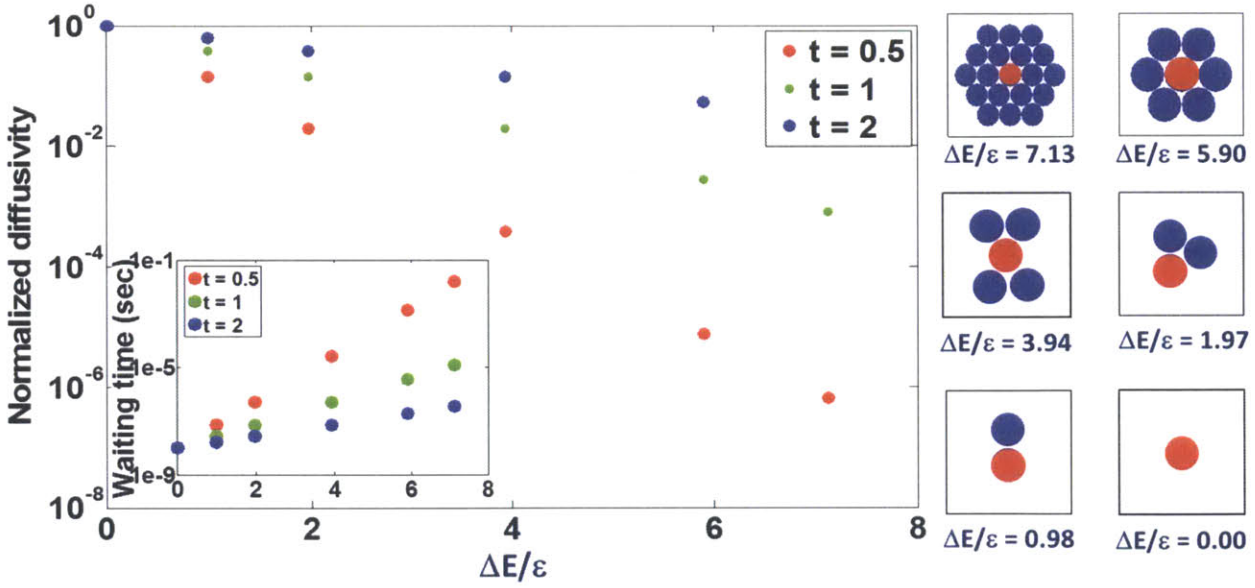

Figure 2.1. Behaviors of the normalized diffusivity, D_i / D_{m0}, of a single particle as a function of the configuration represented by the normalized energy barrier for the diffusion, $\Delta E / \varepsilon$, at different normalized temperatures ($t \equiv k_B T / \varepsilon$). Inset is for the relationship between the average waiting times for a single particle in the cluster to diffuse out of the cluster with different values of t. Right panels are for the illustrations for the diffusion energy barrier a single particle (depicted by red circle) feels for given configurations of particles (depicted by blue circles).

Eqs.(2.3) and (2.4) indicate that an individual particle in a cluster has a diffusivity much lower than that of the monomer because of its configuration in the cluster. This is illustrated in Figure 2.1, in which we see that as the number of neighbors surroundinga a single particle increases, the diffusivity becomes smaller, and waiting time for diffusion of the particle becomes longer. In the KMC simulation, the average waiting time for the next hopping event of the ith particle, τ_i, is inversely proportional to the particle's diffusivity, more precisely [16],

$$\tau_i = \frac{h^2}{D_i}\log\left(rand^{-1}\right),$$

where *rand* denotes a random number uniformly distributed between zero and unity. Therefore, the configuration-dependent diffusivity as well as the hard-sphere-like nature of a particle in the cluster kinetically interfere with detachment of the particle from the cluster. However, this does not necessarily define irreversible cluster formation in CNPs; rather, it is a reversible process, because a single particle at the edge of the cluster can become detached, although this occurs much more slowly than diffusion of monomers into the cluster. To estimate the configuration-dependent diffusivity of a particle at the perimeter of an (s)-mer cluster, namely, $D_1^{(s)}$, eq.(2.4) can be modified as follows:

$$D_1^{(s)} = D_{m0}\exp\left(\int_{\sigma}^{r_C}\int_{-\phi(r)}^{\phi(r)} rg(r)\rho_0\frac{F(r)}{k_BT}d\theta dr\right),\ \phi(r)=\arccos\left(\frac{r^2 - R_s\sigma + (\sigma/2)^2}{2r\left(R_s-(\sigma/2)\right)}\right), \tag{2.5}$$

where R_s is the characteristic size of an (s)-mer cluster. Considering that it is energetically favorable for a cluster to maintain its form and morphological stability by assembling particles in a hexagonal close packed (HCP) structure at the optimized interparticle-distance of the LJ-potential such that $r_e = 2^{1/6}\sigma$, eq.(2.5) can be further simplified as follows:

$$D_1^{(s)} = D_{m0}\exp\left(\sum_{k=1}^{4}\frac{\phi(r_k)L_k}{\pi k_BT}F(r_k)\right), \tag{2.6}$$

where the integer k represents the k th nearest shell of the particle at the edge, and L_k denotes the coordination number of the k th shell (i.e., $L_1 = 6$). Within the cut-off distance, the maximum number of shells interacting with the particle on the perimeter is four; therefore, $\left[L_1\ L_2\ L_3\ L_4\right] = \left[6\ 6\ 6\ 12\right]$ and $\left[r_1\ r_2\ r_3\ r_4\right] = \left[r_e\ 3^{1/2}r_e\ 2r_e\ 7^{1/2}r_e\right]$ for am HCP structure.

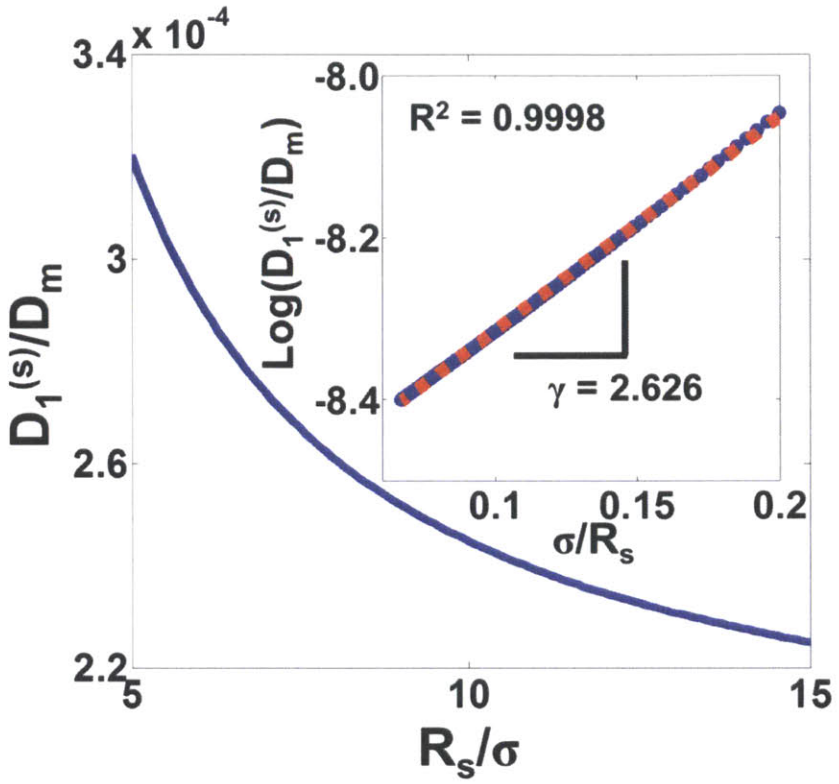

Figure 2.2. Dependence of the normalized diffusivity of a single particle out of an (s)-mer cluster, $D_1^{(s)} / D_{m0}$, on the normalized cluster size R_s / σ. Inset plot is for the linear fitting between σ / R_s and $\log\left(D_1^{(s)} / D_{m0}\right)$ with fitting line (red dot).

Eq.(2.6) can be further simplified as

$$D_1^{(s)} \approx D_{m0} \exp\left(\frac{\phi(r_1) L_1}{\pi k_B T} F(r_1)\right) \approx D_{m0} \beta \exp\left(\frac{\gamma}{R_s}\right),\ \beta \equiv \exp\left(-\frac{3\varepsilon}{\pi k_B T}\left(\pi + \frac{\sigma}{r_e}\right)\right),\ \gamma \equiv \frac{3\varepsilon r_e}{\pi k_B T}, \tag{2.7}$$

where we used the fact that the first term in the summation in eq.(2.6) governs the summation when R_s is not too close to σ (i.e., when $R_s \geq 5\sigma$) with the first order approximation of $\phi(r)$. Using this information with the condition that $\varepsilon = 2k_B T$ at room temperature [12], eqs.(2.6) and (2.7) yields the dependence of $D_1^{(s)}$ on R_s, as shown in Figure 2.2. As expected, Figure 2.2 shows that $D_1^{(s)}$ decreases with increasing R_s, which indicates that as a cluster becomes larger, it becomes more difficult to detach a

monomer. Additionally, the linear fitting of $\log D_1^{(s)}$ as a function of R_s^{-1}, shown in the inset, reveals that the simplified form of the dependence of $D_1^{(s)}$ on R_s works well. In particular, the linear relationship between $\log\left(D_1^{(s)} / D_{m0}\right)$ and σ / R_s, yields the fitting parameters $\gamma = 2.626$ and $\beta = 1.885 \times 10^{-4}$, which are close to the values predicted by eq.(2.7), $\gamma = 2.144$ and $\beta = 4.522 \times 10^{-4}$, respectively.

2.2.2. Characteristic Length Scale and Fractal Dimension of Clusters

From the analysis above and the results in Figure 2.1, we can conjecture that the average size of the clusters grow with increasing time, and small clusters merge into larger ones because the smaller ones lose monomers more quickly than larger ones do, as observed in Ostwald ripening [17]. The main difference between cluster formation in CNPs and the Ostwald ripening or island growth of adatoms on a lattice is that the former is a reversible process and does not depend on the lattice size or directionality. In particular, this KMC study also considers cluster formation in CNPs as the energetically preferable process by which cluster growth and monomer consumption are driven to minimize the total free energy of the system (or to make the energy difference before and after the diffusional jump, δE, negative) in the standard MC manner,

$$\delta E > 0: \text{ Acceptable if rand} \le 1/\left(1+\exp\left(\delta E / k_B T\right)\right)$$
$$\delta E \le 0: \text{ Always acceptable,}$$

where we used the Glauber acceptance scheme for the detailed balance in the Markov process [18]. This consideration reflects the prediction that clusters of hard-sphere-like particles interacting via the isotropic potential are more convex-shaped and compact instead of fractal-shaped, e.g., having the dendritic or snowflake-like shapes observed in typical diffusion-limited aggregation (DLA) [1,19] or RLA at longer times [1]. This prediction automatically corresponds to the prediction that the fractal dimension of the clusters, d_f, should approach two (however, smaller than two) in 2D simulations and three in 3D simulations with sufficient time. The existence of the fractal dimension also indicates that cluster formation is a scale-invariant process in which the growth of the cluster size and weight is governed by the power-law dependence between R_s and the number of particles in the cluster s:

$$R_s \approx \sigma\left(s / A_f\right)^{1/d_f} \sim \sigma\left(s / A_f\right)^{1/2}, \tag{2.8}$$

where A_f is the coefficient for the fractal relation. Computational and experimental studies of DLA and RLA found that the clusters formed by RLA are more compact and have a higher fractal dimension than those formed by DLA. The main reason for this difference is that the clusters formed by RLA require monomers to overcome the activation energy for the reaction; therefore, monomers try to maximize the number of neighboring particles in the cluster. Similarly, we can extend the discussion of these studies to predict the appearance of clusters in CNPs.

As a practical representation of the characteristic length scale of the clusters (R_s), the size of a cluster has been defined as the radius of gyration, R_g

$$R_g = \left(\sum_{\mathbf{r}} |\mathbf{r} - \mathbf{r_0}|^2 \right)^{1/2},$$

where $\mathbf{r_0}$ is the position of the particle that has the minimum total distance from the other particles at position $\mathbf{r}$ in the cluster. However, R_g tends to underestimate the real size of symmetrically shaped clusters, as shown in Figure 2.3(a). Determining the real size of clusters is particularly important in defining the capture length, R_{sC}, which affects the distance from the center of the (s)-mer cluster to the center of the monomers within which the monomers spontaneously approach the (s)-mer cluster to form a larger cluster. Additionally, R_g does not necessarily determine the effective hydrodynamic radius of clusters, which corresponds to the definition of the fractal dimension [2]. Instead of R_g, we can use another type of cluster size, R_M, which can be defined as:

$$R_M = \max\left(|\mathbf{r} - \mathbf{r_0}|\right).$$

We compared the measurement of the cluster size using R_g and R_M, assuming that the cluster is a 2D HCP structure composed of hard spheres. As Figure 2.3(a) shows, R_M describes the characteristic size of clusters in a geometrically more realistic manner than R_g does. In terms of defining R_{sC}, the cluster measured with R_g does not include particles outside the boundary of R_g; therefore, monomers might be allowed to occupy the same position as particles in the cluster.

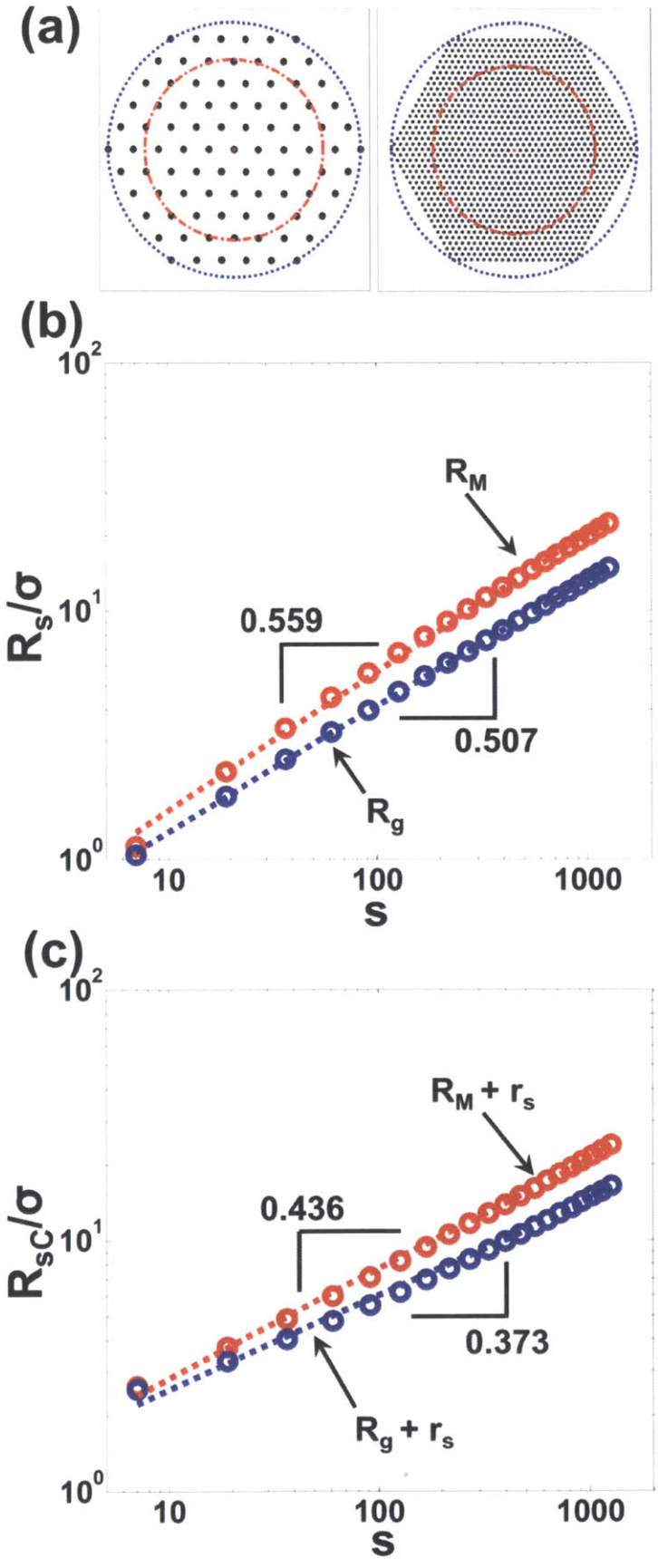
(a)
(b)
10^2
10^1
10^0
R_s/σ
R_M
0.559
0.507
R_g
10
100
1000
s
(c)
10^2
10^1
10^0
R_{sC}/σ
$R_M + r_s$
0.436
0.373
$R_g + r_s$
10
100
1000
s

Figure 2.3. (a) Measurement of cluster size for hexagonal-shaped clusters with R_M (left) and R_g (right). Blue and red lines denote the size measured by the maximum distance from the center of the cluster (R_M) and radius of gyration (R_g), respectively. (b) Dependence of R_s on s (R_M in red) and (R_g in blue) with slopes from the linear fitting. (c) Dependence of R_{sC} on s ($R_M + r_s$ in red) and ($R_g + r_s$ in blue) with slopes from the linear fitting.

This is unphysical, and therefore, this study does not use R_{sC}, which is based on R_g, to describe the detachment of monomers from clusters. From the double logarithmic relationship between R_s and s shown in Figure 2.3(b), R_g yields a larger value for d_f than R_M does (i.e., $d_f = 1.959$ vs. $d_f = 1.718$). In this study, we employ both R_M and R_g to quantitatively define R_s. To distinguish one cluster from another, we can also use R_{sC}. Energetically, R_{sC} can be defined as the range in which the free energy between the monomer and the cluster is negative, implies that $R_{sC} \approx R_s + r_C$. However, geometrically, it is more appropriate to define $R_{sC} \approx R_s + r_s$, where r_s denotes the distance from the center of a particle to the first nearest neighboring shells. Conventionally, r_s is calculated from the position at which the minimum between the first and second peaks in the 2D radial distribution function is located; $r_s = 1.58\sigma$. We also define a double logarithmic relationship between R_{sC} and s on the basis of both ($R_M + r_s$ in red) and ($R_g + r_s$ in blue) in Figure 2.3(c). Because of the addition of r_s, the cluster size measured using R_{sC} is observed to have a higher fractal dimension (i.e., 2.677 from $R_g + r_s$ and 2.292 from $R_M + r_s$, respectively); however, this does not necessarily mean that the real fractal dimension of the clusters can exceed two in a 2D system. This comparison also supports our choice of

$$R_{sC} \approx R_M + r_s,$$

Because the measured dimension is closer to two than that measured using $R_g + r_s$. As a convenient approximation, we use the power-law dependence of R_{sC} on s,

$$R_{sC} \approx 1.029\sigma s^{0.436}$$

for the calculations of the time-dependence of the average cluster size and size-distribution in RT.

2.2.3. Kinetic Model Based on the Rate Theory

Without chemical reactions, cluster formation is attributed entirely to mass transfer through reversible diffusion of monomers m and (s)-mer clusters s, as shown in eq.(2.9).

$$s + m \underset{d_-^{(s+1)}}{\overset{d_+^{(s)}}{\rightleftarrows}} s \cdot m, \tag{2.9}$$

where $d_+^{(s)}$ and $d_-^{(s+1)}$ are the kinetic rate constants for the attachment of a monomer to an (s)-mer cluster and the detachment of a monomer from an $(s+1)$-mer cluster, respectively. Noted that in eq.(2.9), neither aggregation (i.e., $s+q \xrightarrow{K(s,q)} s \cdot q$, where $K(s,q)$ denotes the reaction kernel between an (s)-mer and a (q)-mer clusters [20]) nor fragmentation of clusters (i.e., $s \xrightarrow{L(p,q)^{(s)}} p+q$, where $L(p,q)^{(s)}$ denotes the fragmentation rate constant of an (s)-mer cluster into a (p)-mer and a (q)-mer clusters) is allowed. This is one of the main differences between the conventional Smoluchowski coagulation model [20-22] and the cluster formation model in this study. CNPs cluster formation was reportedly controlled reversibly in an experimental study [10]. In eq.(2.9), an $(s+1)$-mer cluster forms when a monomer within R_{sC} diffuses toward the center of an (s)-mer cluster. Considering the flux of monomers at the perimeter of an (s)-mer cluster, it can be found that

$$d_+^{(s)} = 2\pi\left(D_s + D_{m0}\right),\ d_-^{(s+1)} = \frac{2\left(D_s + D_1^{(s+1)}\right)}{R_{sC}^{\ 2}}.$$

Notably, these quantities can be simplified such that $d_+^{(s)} \approx 2\pi D_{m0}$, whereas $d_-^{(s+1)} \approx 2D_1^{(s+1)} / R_{(s+1)C}^{\ 2}$ considering that the diffusivity of an (s)-mer cluster, D_s, is negligible compared to either D_{m0} or $D_1^{(s)}$ when s is sufficiently larger than unity [22]. The main reason is that clusters are rarely displaced by simultaneous diffusion of each of the particles in the cluster in the same direction; in addition, the cluster size generally exceeds the monomer size by one or more orders of magnitude. Thus, the master equation for the temporal evolution of clusters can be obtained using RT as follows [7,8,20]:

$$\frac{d\langle n_s\rangle}{dt} = 2\pi D_{m0}\langle n_1\rangle\left(\langle n_{s-1}\rangle - \langle n_s\rangle\right) + 2\left(\frac{D_1^{(s+1)}\langle n_{s+1}\rangle}{R_{(s+1)C}^{\ 2}} - \frac{D_1^{(s)}\langle n_s\rangle}{R_{sC}^{\ 2}}\right),\ s \geq 2,$$

$$\frac{d\langle n_1\rangle}{dt} = -2\pi D_{m0}\langle n_1\rangle\sum_{k\geq 2}\langle n_k\rangle - 4\pi D_{m0}\langle n_1\rangle^2 + \frac{4D_1^{(2)}\langle n_2\rangle}{R_{2C}^{\ 2}} + \sum_{k\geq 3}\frac{2D_1^{(k)}\langle n_k\rangle}{R_{kC}^{\ 2}}. \qquad (2.10)$$

To compare this to the conventional RT combined with the self-consistent mean field (SCMF) model [7,8], note that the factor for the capture number of a cluster employed in the SCMF model corresponds to 2π, whereas the escape rate of a monomer from an (s)-mer cluster is equal to $2D_1^{(s)} / R_{sC}^{\ 2}$ in eq.(2.10).

By assuming that n_1 is the continuum over the spatial dimension under the condition $\lim_{r\to\infty} n_1 = \langle n_1\rangle$, a diffusion-reaction-like equation regarding n_1 can be written as

$$\frac{\partial n_1}{\partial t} = J(t) + D_{m0}\nabla^2 n_1 - D_{m0}\xi(t)^{-2} n_1, \qquad (2.11)$$

where $J(t)$ and $\xi(t)$ denotes the monomer flux and the mean free distance for monomers to travel without engaging in cluster formation, respectively [7,8]. By comparing eq.(2.11) with the second term in eq.(2.10), we can extract J and ξ^{-2} as

$$J = \frac{4D_1^{(2)}\langle n_2\rangle}{R_{2C}^{\ 2}} + \sum_{k\geq 3}\frac{2D_1^{(k)}\langle n_k\rangle}{R_{kC}^{\ 2}}, \qquad (2.12)$$

and

$$\xi^{-2} = 2\pi\sum_{k\geq 2}\langle n_k\rangle + 4\pi\langle n_1\rangle, \qquad (2.13)$$

Respectively. By using eqs. (2.12) and (2.13), we can find the relationship [7,8]

$$\bar{\nabla}^2 n_1 - \left(n_1 - \langle n_1\rangle\right) \approx 0, \qquad (2.14)$$

where the spatial dimension is normalized (indicated by the over-bar) with respect to ξ ($\bar{\mathbf{r}} \equiv \mathbf{r} / \xi$), and the rate of fluctuation of n_1 around $\langle n_1\rangle$ is assumed to be negligible. Eq.(2.14) has a solution based on the zeroth-order modified Bessel function, $K_0(x)$, tailored for an (s)-mer cluster in which

$n_1(\bar{r}) = \langle n_1 \rangle - \lambda_s K_0(\bar{r})$, where λ_s is the constant determined by a boundary condition at the cluster radius.

2.2.4. Scaling Analysis

Assuming that a cluster is circular in shape, mass conservation based on a continuum approximation of the monomers flux for an (s)-mer cluster at its radius, J_{cont}, with eq.(2.14) gives rise to the relationship

$$\frac{\partial s}{\partial t} = -J_{cont} = 2\pi D_e^{(s)} R_s \left.\frac{\partial n_1}{\partial r}\right|_{R_s} = -2\pi D_e^{(s)} \frac{\lambda_s R_s}{\xi} K_1\left(\frac{R_s}{\xi}\right), \tag{2.15}$$

where $D_e^{(s)}$ denotes the effective diffusivity for the monomers flux at R_s. From the microscopic point of view, the flux attributed to detachment and attachment of monomers, J_{micro}, is written as [7,8]

$$J_{micro} = \frac{\langle n_{s+1} \rangle \omega_{s+1}}{\langle n_s \rangle} - 2\pi (R_s + r_s) \frac{D_{m0}}{h} n_1|_{R_s + r_s}, \tag{2.16}$$

where ω_s is the detachment rate of monomers from an (s)-mer cluster. For a microscopic mass balance, $J_{cont} = J_{micro}$; therefore, eq.(2.17) can be derived from eqs.(2.15) and (2.16) as

$$\left.\frac{\partial n_1}{\partial r}\right|_{R_s} = \chi_s \left(n_1|_{R_s} - n_1^{(eq)}|_{R_s} \right), \chi_s^{-1} \equiv \left(\frac{R_s D_e^{(s)} h}{(R_s + r_s) D_{m0}} - r_s \right), n_1^{(eq)}|_{R_s} \equiv \frac{h \langle n_{s+1} \rangle \omega_{s+1}}{2\pi (R_s + r_s) D_{m0} \langle n_s \rangle}, \tag{2.17}$$

where we used a continuum approximation for $n_1(r)$ in the first order, where $n_1|_{R_s + r_s} \approx n_1|_{R_s} + r_s \left.\frac{\partial n_1}{\partial r}\right|_{R_s}$.

From eq.(2.17), λ_s is calculated as

$$\lambda_s = \frac{\xi \left(n_1|_{R_s} - n_1^{(eq)}|_{R_s} \right)}{\xi K_0(R_s/\xi) + \chi_s^{-1} K_1(R_s/\xi)}. \tag{2.18}$$

To find $D_e^{(s)}$ as a function of D_{m0} and R_s, we can introduce another continuum approximation for the temporal evolution of $\langle n_s \rangle$ in eq.(2.11):

$$\frac{\partial \langle n_s \rangle}{\partial t} + \frac{1}{\partial s}\left[\left(2\pi D_{m0}\langle n_1 \rangle - \frac{2D_1^{(s)}}{R_{sC}^{\ 2}}\right)\langle n_s \rangle\right] = 0. \tag{2.19}$$

By comparing this to the continuity equation, we can express $\partial s / \partial t$ as

$$\frac{\partial s}{\partial t} = 2\pi D_{m0}\langle n_1 \rangle - \frac{2D_1^{(s)}}{R_{sC}^{\ 2}}. \tag{2.20}$$

According to eqs.(2.15), (2.18), and (2.20),

$$\frac{2\pi R_s D_e^{(s)}\left(n_1|_{R_s} - n_1^{(eq)}|_{R_s}\right)K_1(R_s/\xi)}{\xi K_0(R_s/\xi) + \chi_s^{-1}K_1(R_s/\xi)} = 2\pi R_s D_{m0}\, n_1|_{R_s} - \frac{2D_1^{(s)}}{R_{sC}^{\ 2}}. \tag{2.21}$$

When we use the convenient and conventional method of determining coefficients by term-by-term comparison, eq.(2.16) yields information on $D_e^{(s)}$ and ω_{s+1} as follows:

$$D_e^{(s)} = \frac{D_{m0}\left(\xi K_0(R_s/\xi) + \chi_s^{-1}K_1(R_s/\xi)\right)}{R_s K_1(R_s/\xi)}, \quad \frac{\langle n_{s+1}\rangle \omega_{s+1}}{\langle n_s \rangle} = \frac{D_{m0}}{(R_s + r_s)h}. \tag{2.22}$$

At longer times, $R_s \gg r_s$, so $D_e^{(s)}$ in eq.(2.22) can be further simplified to

$$D_e^{(s)} \approx \frac{2D_{m0}\xi^2}{R_s^{\ 2}}, \tag{2.23}$$

where we used the fact that $\xi \gg R_s$ and applied asymptotic forms of the modified Bessel function, $\lim_{x\to 0} K_n(x) = \frac{1}{n!}\left(\frac{x}{2}\right)^n$. From eqs.(2.8), (2.15), (2.17), (2.18), and (2.23), we can describe the temporal evolution of the cluster size as:

$$\frac{\partial R_s^{\ d_f}}{\partial t} \approx \frac{2\pi\sigma^{d_f} D_{m0}}{A_f}\left(n_1|_{R_s} - n_1^{(eq)}|_{R_s}\right), \tag{2.24}$$

where we used the fact that $R_s \gg h$. With the continuum approximation, the Gibbs-Thomson equation [17,19] can act as a boundary condition for a 2D circular cluster such that

$$n_1|_{R_s} = n_\infty \exp(\Gamma / R_s),$$

where n_∞ denotes the number density of monomers in equilibrium, and Γ represents the capillary length, which can be expressed as $\Gamma = \gamma_L \Lambda / k_B T$. For the capillary length defined in a 2D system, Λ indicates the area occupied by a monomer, and γ_L represents for the line tension of a circular cluster. At room temperature for typical inorganic materials [12], Γ is measured to be at the same order of magnitude as σ when σ is smaller than 10 nm. When the concentrations of clusters and monomers are sufficiently dilute, it can be found that

$$\langle n_\infty \rangle \approx \left\langle n_1^{(eq)} \right\rangle \Big|_{\langle R_s \rangle} \approx \langle n_1 \rangle.$$

Then, eq.(2.24) can be further simplified to

$$\frac{d_f}{d_f + 1} \frac{\partial \langle R_s \rangle^{d_f}}{\partial t} \approx \frac{2\pi\sigma^{d_f} D_{m0} \langle n_1 \rangle \Gamma}{A_f}. \tag{2.25}$$

When $\langle n_1 \rangle$ scales with time according to a scaling exponent μ satisfying $\langle n_1 \rangle \sim t^\mu$ at longer times, eq.(2.25) yields the following scaling behavior of $\langle R_s \rangle$:

$$\langle R_s \rangle \sim t^{\frac{\mu+1}{d_f+1}}. \tag{2.26}$$

In a 2D system, an ideal compact and isotropic cluster has a fractal dimension $d_f = 2$, and therefore, its scaling behavior is approximately $\langle R_s \rangle \sim t^{\frac{\mu+1}{3}}$ at longer times (c.f., for 3D clusters, it can be shown that $\langle R_s \rangle \sim t^{\frac{\mu+1}{d_f}}$, which will give rise to the same scaling behavior of $\langle R_s \rangle \sim t^{\frac{\mu+1}{3}}$ with an ideal fractal dimension $d_f = 3$). In addition, $\langle n_1 \rangle$ decreases with increasing time at longer times, whereby $\mu < 0$; thus, $\langle R_s \rangle$ grows less rapidly than predicted by a conventional dynamics such as Ostwald ripening. Interestingly, when $\mu = 0$, which implies that the monomer concentration is described by a continuum field and is sufficiently larger than the cluster concentrations throughout the cluster growth process, the scaling behavior of the cluster size converges into the conventional Lifshitz-Slylozov-Wagner (LSW) relationship for 2D circular droplet growth, such that $\langle R_s \rangle = \kappa t^{1/3}$ [23], where $\kappa = \left(3 D_{m0} n_\infty \Gamma \Lambda\right)^{1/3}$.

2.2.5. Scaling Behavior of the Cluster Weight Distribution

At longer times, it is also expected that the cluster weight will exhibit scaling behavior distributed around M_N when the distribution is self-similar (i.e., scale invariant). In other words, in the limit of a large cluster weight, M_N can act as the representative weight of the entire cluster. Among numerous forms, the following functional form has been conventionally defined as the cluster weight distribution [7,8]:

$$F(s) = s\frac{\langle n_s \rangle}{\langle n_0 \rangle}.$$

When the distribution functional form is invariant against scale, the homogeneity condition should be satisfied,

$$F(\omega s) = \omega^{-\vartheta} F(s),$$

where ω can be set to $\omega = M_N^{-1}$. By introducing the universal distribution function, $G(X)$, where $X \equiv sM_N^{-1}$, which acts throughout the cluster formation process at longer times, one can find the following:

$$G(X) = M_N^{\vartheta} F(s),$$

Further, because of the constraint given by particle number conservation in a closed system, $G(X)$ must satisfy

$$M_N^{\vartheta-1} = \int_0^\infty dX G(X),$$

from which the scaling exponent is found to be $\vartheta = 1$. Therefore, $G(X)$ can be written as [7,8]

$$G(X) = M_N^2 X\frac{\langle n_s \rangle}{\langle n_0 \rangle}. \tag{2.27}$$

The plot of $G(X)$ versus X reveals whether cluster formation is a self-similar process at longer times. In a simplified model based on the conventional Smoluchowski coagulation theory [20], $\langle n_s \rangle$ is known

to scale with time, with a scaling exponent of $-\theta$ at longer times and an exponential tail, which is a function of the cluster weight (s) such that [21]

$$\langle n_s \rangle \sim t^{-\theta} \exp\left(-\frac{\Psi s}{t^Z}\right)$$

where Ψ is a constant, and Z is the scaling exponent for the time-dependence of the tail function. With this form, it can be shown that $M_N \approx t^Z / \Psi$; therefore, the distribution function is given as $G(X) \sim X \exp(-X) t^{2Z-\theta}$. When the distribution function is universal, yielding time- and scale-invariant behavior, the condition of $2Z - \theta = 0$ is expected to be satisfied, and consequently, $G(X)$ peaks around $X = 1$, indicating that the distribution is effectively represented by M_N as the characteristic weight of the clusters. For irreversible DLA with more realistic cluster formation conditions, Marquesee and Ross provided a detailed calculation that describes $G(X)$ at equilibrium for cluster growth governed by Ostwald ripening [17,24]. In this study, however, we do not require the SCMF method of solving $G(X)$ because the capture number and detachment rate of monomers from the clusters can be derived in the RT-based model. Instead, we introduced a semi-empirical form of $\langle n_s \rangle$ to describe $G(X)$; it has a scaling dependence similar to that found in the Smoluchowski model by assuming that $\langle n_s \rangle \sim t^{-\theta} \exp\left(-\frac{\Psi s^y}{t^Z}\right)$, where y was introduced to address the possibility of an exponentially scaling tail with a nonlinear order of s at longer times (i.e., $y > 1$). With a continuum approximation, it can be shown that $M_N \approx \frac{\Phi(y)}{\Psi^{1/y}} t^{Z/y}$, where $\Phi(y) \equiv \Gamma(2/y)/\Gamma(1/y)$ and $\Gamma(x)$ denotes a gamma function. Then, unde the condition $2Z - y\theta = 0$, $G(X)$ is found to have the form

$$G(X) \sim X \exp\left(-\left(X\Phi(y)\right)^y\right). \tag{2.28}$$

Eq.(2.28) indicates that $G(X)$ peaks at $X_M = y^{-1/y} / \Phi(y)$. Note that $X_M = 1$ when $y = 1$, which corresponds to the expectation from the simplified form of $G(X)$ from the Smoluchowski model.

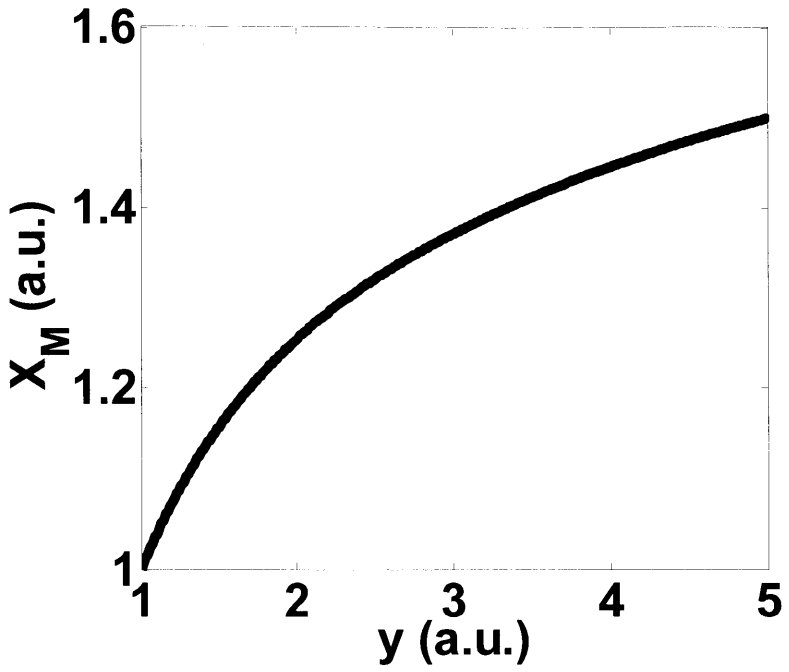

Figure 2.4. A relationship between the nonlinearity of the exponential tail function, y, of the universal distribution function of the cluster weight at longer times ($G(X)$) and the peak position X_M.

In Figure 2.4, we show the functional relationship between X_M and y, where the peak position in $G(X)$ shifts gradually from $X_M = 1$ as the nonlinearity of the exponential tail becomes stronger.

2.2.6. Induction Time for Cluster Formation

It is also important to understand how soon the clusters start to form as a function of the initial monomer concentration. We can expect that clusters form earlier at higher initial concentrations of monomers. The time for the first cluster formation can be defined as the induction time, t_{ind}. To determine t_{ind}, we can use a simplified form of the rate equations as follows:

$$\frac{\partial \langle n_1 \rangle}{\partial t} \approx -4\pi D_{m0} \langle n_1 \rangle^2 + \frac{4D_1^{(2)}}{R_{2C}^{\,2}} \langle n_2 \rangle,$$
$$\frac{\partial \langle n_2 \rangle}{\partial t} \approx 2\pi D_{m0} \langle n_1 \rangle^2 - \frac{2D_1^{(2)}}{R_{2C}^{\,2}} \langle n_2 \rangle, \qquad (2.29)$$

where we assumed that the concentration of clusters with $s \geq 3$ is negligible compared to $\langle n_1 \rangle$ and $\langle n_2 \rangle$ at $t \sim t_{ind}$. The temporal dependence of $\langle n_2 \rangle$ from the solutions of eq.(2.29) can be written as

$$\langle n_2 \rangle \approx \frac{2\pi D_{m0} \langle n_0 \rangle^2 t}{4\pi D_{m0} \langle n_0 \rangle t + 1}, \tag{2.30}$$

where we used the fact that $\langle n_2 \rangle \ll \langle n_0 \rangle$ with $D_1^{(2)} \sim 0.135 D_{m0}$ from eqs.(2.3) and (2.4). Defining t_{ind} as the time at which $\langle n_2 \rangle / \langle n_0 \rangle$ reaches a threshold ratio, υ ($0 < \upsilon \ll 1$), eq.(2.30) can be written as

$$t_{ind} \sim \frac{\upsilon}{2\pi D_{m0} \langle n_0 \rangle}. \tag{2.31}$$

This relationship holds for CNPs with a relatively dilute initial monomer concentration. For CNPs with a relatively rich initial monomer concentration, t_{ind} approaches zero when $\langle n_0 \rangle$ approaches $\langle n_0 \rangle = 2/\left(3^{1/2} r_s^2\right)$, which corresponds to the HCP structure of monomers in which entire monomers are aggregated in a single large cluster at $t = 0$. From eq.(2.31), we can find that t_{ind} is inversely proportional to $\langle n_0 \rangle$. Computationally and experimentally, t_{ind} can be measured from the time after which the growth of the average cluster size/weight scales with time.

2.3. Computational Method

For the simulation of cluster formation in CNPs in a 2D system, we used a KMC algorithm based on an efficient stochastic algorithm. One of the advantages of the KMC algorithm over other computational approaches for a dynamic system, such as MD or BD simulations, is that it is more appropriate for describing a system under stochastic effects involving thermal noise or noisy fluctuations in the external factors. Although it is not shown here, it is possible to incorporate noise effects during the simulations without adding a considerable computational load, whereas it is necessary to generate random numbers and calculate the noise effects at every iteration step in MD or BD simulations. Another advantage of the KMC algorithm is that it is much more efficient for describing dynamic processes, particularly at longer times. For example, at longer cluster formation times, most of the NPs are found in clusters, and their diffusivity $D_1^{(s)}$ is much smaller than D_{m0} (i.e., $D_1^{(s)} \sim 10^{-4\sim-6} D_{m0}$). This indicates that the average

waiting time for the next diffusional jump of an NP increases by four to size orders of magnitude at longer times. In MD or BD simulations, the time step at every iteration step is typically fixed unless an adaptive algorithm to update the differential time is incorporated; therefore, they require much more time to update the system dynamics at longer times, which prevents their use at longer times. In contrast, the KMC algorithm does not employ a fixed time step but updates the waiting time according to the order of all the particles' diffusional propensity at every iteration step to determine the next diffusional jump. Therefore, the system dynamics at longer times can be effectively and efficiently addressed.

For a chemical reaction with a rate propensity r_{rxn}, the probability that the reaction occurs in a sufficiently short time interval dt is $r_{rxn}dt$. Therefore the probability that the reaction occurs only after some time τ (i.e., definition of the waiting time) can be calculated as follows:

$$\begin{aligned} P(\tau) &= p(\text{no reaction for } 0 \le t < \tau) \times p(\text{reaction during } \tau \le t < \tau + d\tau) \\ &= p(\text{no reaction for } t < \tau - d\tau) \times p(\text{no reaction for } \tau - d\tau \le t < \tau) r_{rxn} d\tau \\ &= p(\text{no reaction for } t < \tau - d\tau) \times (1 - r_{rxn} d\tau) r_{rxn} d\tau. \end{aligned}$$

Then, defining $Q(\tau) \equiv p(\text{no rxn for } 0 \le t < \tau)$

$$\begin{aligned} & Q(\tau) = Q(\tau - d\tau)(1 - r_{rxn} d\tau) \\ & \rightarrow \ln Q(\tau) - \ln Q(\tau - d\tau) = \ln(1 - r_{rxn} d\tau) \approx -r_{rxn} d\tau, \\ & \rightarrow \frac{d \ln Q(\tau)}{d\tau} = -r_{rxn} \\ & \rightarrow Q(\tau) = A \exp(-r_{rxn}\tau) = \exp(-r_{rxn}\tau) \ (\because Q(0) = 1), \\ & \rightarrow \therefore P(\tau) d\tau = \exp(-r_{rxn}\tau) r_{rxn} d\tau \equiv \text{Probability density of the waiting time.} \end{aligned}$$

Therefore, the waiting time has an exponentially diminishing probability distribution.

For a simple Markov chain composed of two different possible transitions from state A to either state B or state C with transition rate r_B and r_C, respectively, the probability of any transition at time t, using the above relationship, is

$$p(t) dt = \exp(-r_B t) \exp(-r_C t)(r_B + r_C) dt.$$

Thus, the average lifetime of state A is

$$\langle t \rangle = \int_0^\infty tp(t)\,dt = \int_0^\infty t \exp\left(-(r_B + r_C)t\right)(r_B + r_C)\,dt = \frac{1}{r_B + r_C}.$$

For a random variable u between zero and unity, let us think about the other variable, θ, which has a 1-to-1 functional relationship (or mapping) with u, thus,

$$p(\theta) = p(u)\left|\frac{du}{d\theta}\right| = \left|\frac{du}{d\theta}\right|$$

$$\rightarrow If\ u = \exp\left(-r_{rxn}\theta\right)\ \left(\text{or equivalently } \theta = \frac{1}{r_{rxn}}\ln\left(\frac{1}{u}\right)\right),$$

$$\rightarrow p(\theta)d\theta = r_{rxn}\exp\left(-r_{rxn}\theta\right)d\theta.$$

This is exactly that same distribution as that of the reaction waiting time. Therefore, for m possible types of reaction with respective reaction rates of r_{rxni} $(i = 1, 2, \cdots, m)$, we can execute a numerical simulation for the stochastic process (i.e., Gillespie's first reaction method (FRM) algorithm [16]) according to a process as provided in Table 2.1.

Table 2.1. A summarized stochastic algorithm based on the Gillespie's first reaction method (FRM)

A Kinetic Monte Carlo (KMC) Algorithm on the basis of the FRM
Step 1. For each of the reactions, draw a random number, u_i, between zero and unity
Step 2. Generate the waiting time for each of the reactions using u_i based on the mapping such that $\theta_i = \frac{1}{r_{rxn}}\ln\left(\frac{1}{u_i}\right)$
Step 3. Choose a reaction which has the shortest waiting time
Step 4. Update the total reaction time and total system (number of species in the reaction network)
End of Algorithm

Conventionally, the original stochastic algorithms such as the first reaction method (FRM) and the direct method suggested by Gillespie [16] have been widely applied in KMC simulations to simulate chemical reactions. In a stochastic simulation of a spatio-temporal transition driven by a diffusion process, however, the original algorithms are often computationally inefficient. To solve multi-particle-based

diffusion problems, a more efficient KMC algorithm would be valuable, and the next reaction method (NRM) algorithm suggested by Gibson and Bruck [13] is an advanced algorithms used to address the problem. The NRM algorithm is based on a binary sorting method to determine the fastest transition at each iteration. Rapid calculation by the NRM requires the construction and maintenance of several hierarchical data structures such as a dependency graph, indexed priority queues, and an index structure for the individual transition processes. Although these data structures incur a computational cost, the NRM performs well when simulating a system with a larger number of transition, for example, in a multi-particle-based diffusion problem. In comparison, the computational cost of Gillespie's algorithms scales with the number of independent transition processes (N), whereas the NRM scales with $\log N$. In addition, the NRM reduces the computation time by re-using the random number at each of the iteration steps. With these advantages, the NRM algorithm provides a path to effective simulation of cluster formation in a system composed of thousands of NPs.

Table 2.2. A Kinetic Monte Carlo algorithm for the cluster formation of CNPs

A Kinetic Monte Carlo (KMC) Algorithm to Simulate Cluster Formation of CNPs
Step 1. Set initial positions (considering self-exclusion effects) of NPs
Step 2. Find a list of nearest neighbors (nns) for each of the NPs and calculate neighbors-dependent diffusivities
Step 3. Calculate exponentially distributed waiting time for each of the NPs
Step 4. Sort the waiting times using binary sorting algorithm, and fire the fastest diffusion
Step 5. Allow the fastest diffusion if the energy change is acceptable in Monte Carlo scheme (i.e. Glauber exchange scheme)
Step 6. Construct a list of new nns of the fastest NP
Step 7. Find affected diffusion processes by the fastest diffusion
Step 8. Update waiting times for the affected diffusion propensities
Step 9. Go back to the Step 4 during iteration
End of Algorithm

For the study described in this chapter, we used the KMC algorithm based on NRM with an iteration number of $10^8 \sim 2\times10^8$. In a 2D system, the desired number of self-avoiding particle, which model the NPs, were introduced with a periodic boundary condition. To avoid numerical artifacts that

might interfere with the measurement of the cluster size and weight, we employed a 2D simulation box with an edge length of $200\sigma \sim 300\sigma$. Each of the simulations was repeated 16-times to obtain statistically averaged results. To measure the cluster size and weight distributions, we used the Delaunay triangulation algorithm [25] to define the nearest particles, whether they exist in the cluster or as independent monomers with the cut-off distance of r_s, and to distinguish one cluster from another. Detailed algorithm is given in Table 2.1. More detailed fundamentals of the NRM algorithm are given in Appendix A.

For numerical integration of the equations in RT, we introduced the maximum weight of the cluster, N_0, which is the number of particles initially introduced to the 2D box in the KMC simulation. The differential equations given by RT were numerically integrated using the forward Euler method with a finite differential time that was evenly distributed over the log-scale time range.

2.4. Results and Discussion

By using RT and the KMC algorithm, we calculated and simulated the time-dependent properties of cluster formation in CNPs with five different initial concentrations of monomers, $\langle n_0 \rangle \sigma^2 = 3.872 \times 10^{-2}$, 6.255×10^{-2}, 9.771×10^{-2}, 1.123×10^{-1}, and 1.741×10^{-1}. For the calculation conditions, we used typical properties of inorganic NPs: $D_{m0} = 10^{-12}$ m^2/s, $\sigma = 10^{-9}$ m, and $\varepsilon = 2k_BT$ [12]. Figure 2.5 shows a representative KMC simulation result for cluster formation in CNPs as a function of time when $\langle n_0 \rangle \sigma^2 = 9.771 \times 10^{-2}$. As expected, the clusters grow with time in terms of both size and weight. In particular, we can also observe that the clusters maintain as compact a structure as possible, exhibiting a nearly close-packed structure, as the radial distribution function $g(r)$ of the particles in Figure 2.5 shows.

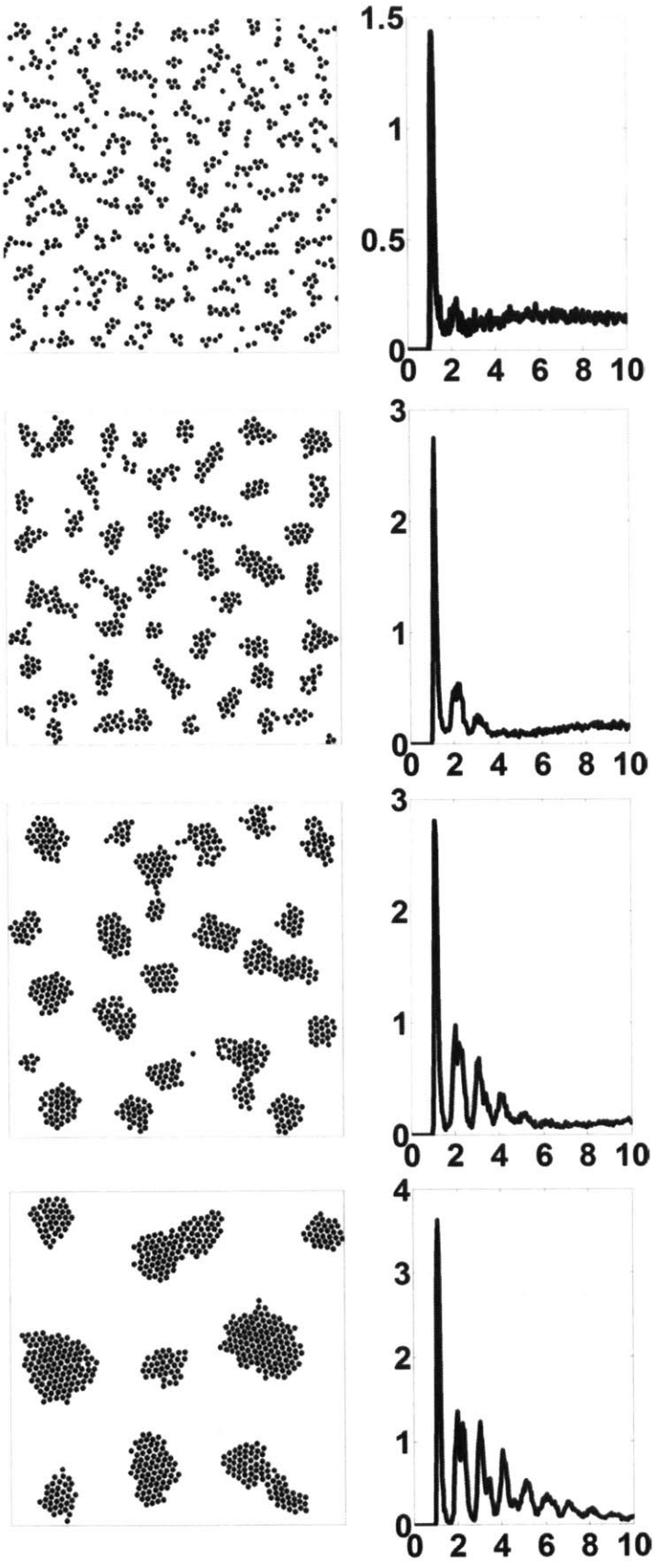
1.5
1
0.5
0
0 2 4 6 8 10
3
2
1
0
0 2 4 6 8 10
3
2
1
0
0 2 4 6 8 10
4
3
2
1
0
0 2 4 6 8 10

Figure 2.5. (Left column) Representative images of morphological evolution of the cluster consisting of NPs simulated by the kinetic Monte Carlo (KMC) algorithm with the initial monomer concentration of $\langle n_0 \rangle \sigma^2 = 6.255 \times 10^{-2}$ observed at $t = 4.571 \times 10^{-5}$s , $t = 2.722 \times 10^{-3}$s , $t = 2.101 \times 10^{-2}$s , and $t = 2.122 \times 10^{-1}$s , from the first to fourth row, respectively. Images correspond to the expanded region of a 2D simulation box with dimension of $100\sigma \times 100\sigma$. (Right column) Radial distribution function ($g(x)$) of the particles as a function of $x = r / \sigma$ observed at the same times.

We can calculate $g(r)$ using the equation [18]

$$g(r) = \frac{1}{N_0} \left\langle \sum_{j \neq k}^{N_0} \delta(\mathbf{r} - \mathbf{r_j} + \mathbf{r_k}) \right\rangle_{j,k} , \tag{2.32}$$

where $\mathbf{r}$ denotes the normalized position vectors, $\delta(x)$ represents the Dirac delta function, and the angular bracket denotes an ensemble average over every pair of NPs. Considering that the peaks in $g(r)$ determine the number of neighboring coordinate shells, it is evident that cluster growth proceeds while the NPs inside the cluster become close packed. In addition, we can also observe that the peaks become narrower and the intensity of the peaks at longer distances increase, indicating that the cluster shape becomes isotropic and circular. When the cluster shape is dendritic or chain-like, the peak height at longer distances are much smaller and thus cannot be observed.

To validate of the RT and KMC simulations for describing cluster formation, we compared the calculated and simulated temporal evolution of the normalized monomer and cluster number density, $\langle n_1 \rangle / \langle n_0 \rangle$ and $\langle N_S \rangle / \langle n_0 \rangle$, where $\langle N_S \rangle$ denotes the total number density of the clusters: $\langle N_S \rangle \equiv \sum_{s \geq 2} \langle n_s \rangle$. As Figure 2.6 shows, the KMC simulation results agree with the RT calculation with different $\langle n_0 \rangle$, although $\langle N_S \rangle$ from the KMC algorithm is commonly underestimated compared to that yielded by RT at shorter times (i.e., before the time at which $\langle N_S \rangle$ reaches the maximum). This discrepancy in $\langle N_S \rangle$ between the RT and KMC simulations might be explained by the following facts: (1) the governing clusters are dimers at shorter times, (2) the approximate form of the detachment rate constant of monomers from the cluster in eqs.(2.7) and (2.10) is inversely proportional to the size of the cluster, and (3) RT overestimates the cluster size of dimers.

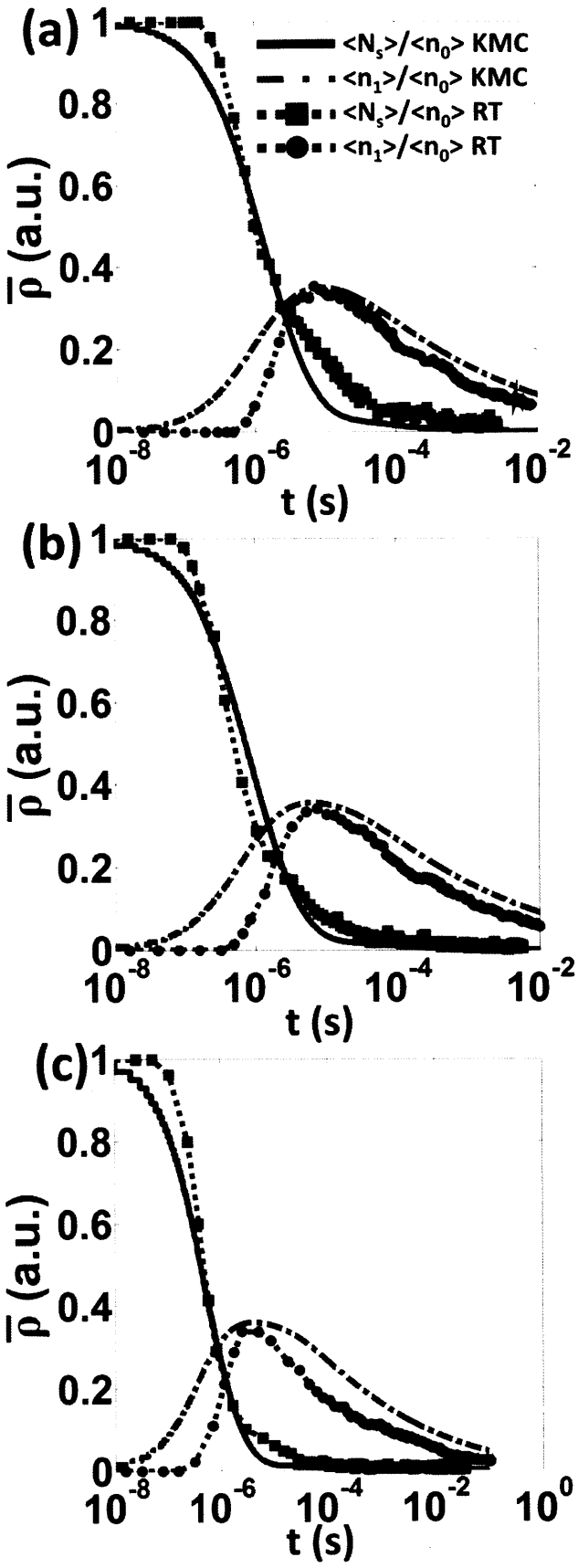
(a)
(b)
(c)
<N_s>/<n_0> KMC
<n_1>/<n_0> KMC
<N_s>/<n_0> RT
<n_1>/<n_0> RT
p̄ (a.u.)
t (s)
0
0.2
0.4
0.6
0.8
1
10^-8
10^-6
10^-4
10^-2
10^0

Figure 2.6. Comparison of calculation results from the rate theory (RT) and the KMC simulation on the temporal evolution of the normalized number densities ($\bar{\rho}$) of monomers ($\langle n_1 \rangle / \langle n_0 \rangle$) and clusters ($\langle N_s \rangle / \langle n_0 \rangle$) with different initial monomer densities ($\langle n_0 \rangle \sigma^2 = 6.255 \times 10^{-2}$, 9.771×10^{-2} , and 1.741×10^{-1} for (a), (b), and (c), respectively).

Therefore, at earlier times, RT underestimates the detachment rate of monomers from the clusters, which leads to overestimation of the number of clusters. Because of this property, it is also easily predicted that the number- (M_N) and weight-averaged cluster weights (M_W), which are defined as

$$M_N = \frac{\sum_{s \geq 2} s \langle n_s \rangle}{\langle N_S \rangle},$$

and

$$M_W = \frac{\sum_{s \geq 2} s^2 \langle n_s \rangle}{\sum_{s \geq 2} s \langle n_s \rangle},$$

respectively (c.f., where the 'weight' of the cluster does not physically mean the real molecular weight; rather it denotes the number of unit particles in the cluster), are overestimated in the RT calculation compared to the KMC simulation at earlier times. This prediction is verified later. After $\langle N_S \rangle$ reaches the maximum, simulation results of $\langle N_S \rangle$ from the KMC algorithm show good agreement with those of the RT calculations. Notably, there is still a discrepancy between the RT and KMC results when $\langle n_0 \rangle$ is relatively high (i.e., $\langle n_0 \rangle \sigma^2 = 1.741 \times 10^{-1}$ in Figure 2.6(c)). This may be explained by considering that the average distance between clusters decreases with increasing $\langle n_0 \rangle$, and at longer times, the number of clusters can be underestimated when the distance is within the cut-off distance for configuring the clusters. The overall deviation of the KMC simulations with respect to the RT calculation are reduced as the simulation box size and N_0 increase.

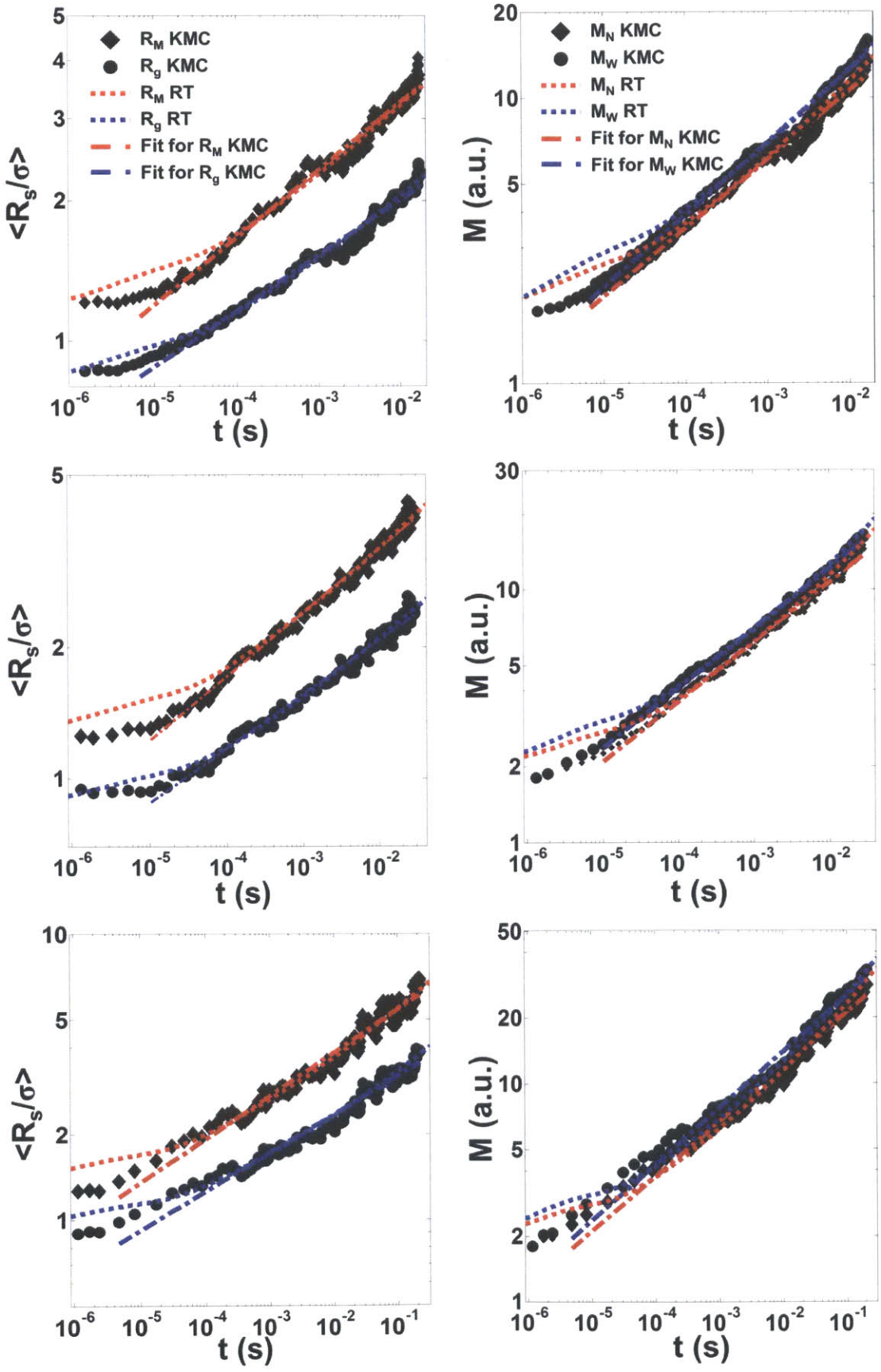
R_M KMC
R_g KMC
R_M RT
R_g RT
Fit for R_M KMC
Fit for R_g KMC
$<R_s/\sigma>$
t (s)
M_N KMC
M_W KMC
M_N RT
M_W RT
Fit for M_N KMC
Fit for M_W KMC
M (a.u.)

Figure 2.7. Comparison of calculation results from the RT and the KMC simulation on the scaling behavior of the average cluster size ($\langle R_s / \sigma \rangle$ in the first column) and weight (M in the second column) with different initial monomer densities ($\langle n_0 \rangle \sigma^2 = 6.255\times10^{-2}$, 9.771×10^{-2}, and 1.741×10^{-1} for the first to third row, respectively). Linear fitting for the scaling behaviors of $\langle R_s / \sigma \rangle$ measured from the KMC simulations are represented by red (for $\langle R_M / \sigma \rangle$) and blue (for $\langle R_g / \sigma \rangle$) dash-dot lines, respectively. For the linear fitting of the scaling behaviors of M observed in the KMC simulation, red and blue dash dot lines denote the number averaged (M_N) and weight-averaged cluster weight (M_W), respectively.

Table 2.3. Comparison of scaling exponents for the average cluster size and weight obtained from the linear fitting of the kinetic Monte Carlo (KMC) simulations and the rate theory (RT) predictions at long times. The fractal dimensions of the clusters, d_f, are calculated based on the scaling exponents.

	$\langle n_0 \rangle \sigma^2$	$\langle R_M \rangle$	$\langle R_g \rangle$	M_N	M_W	d_{fNM}	d_{fWM}	d_{fNg}	d_{fWg}
KMC	3.872×10^{-2}	0.140	0.131	0.249	0.251	1.78	1.79	1.91	1.93
	6.255×10^{-2}	0.141	0.130	0.250	0.252	1.77	1.78	1.92	1.93
	9.771×10^{-2}	0.141	0.130	0.247	0.250	1.76	1.77	1.90	1.93
	1.123×10^{-1}	0.142	0.121	0.251	0.251	1.77	1.77	1.91	1.92
	1.741×10^{-1}	0.143	0.132	0.254	0.256	1.77	1.79	1.92	1.94
RT	3.872×10^{-2}	0.140	0.131	0.249	0.251	1.77	1.79	1.90	1.92
	6.255×10^{-2}	0.142	0.131	0.250	0.251	1.76	1.78	1.90	1.92
	9.771×10^{-2}	0.141	0.129	0.247	0.250	1.75	1.77	1.91	1.93
	1.123×10^{-1}	0.141	0.131	0.252	0.250	1.79	1.78	1.93	1.92
	1.741×10^{-1}	0.145	0.132	0.253	0.257	1.75	1.78	1.92	1.95

We also compared the RT calculations and KMC simulation results for the scaling behavior of the average cluster size $\langle R_s \rangle$ and weight M . For the comparison, we measured $\langle R_s \rangle$ using either R_g or R_M and measured M using either M_N or M_W . As shown in Figure 2.7, the RT and KMC results both show power-law dependences of $\langle R_s \rangle$ and M on the time at later stages of cluster formation. From the plots, notably, the RT and KMC results agree well in describing the power-law for both $\langle R_s \rangle$ and M at longer cluster formation times with different $\langle n_0 \rangle$. Interestingly, we found that the scaling exponents of $\langle R_s \rangle$ and M obtained by linear fitting do not vary considerably up to relatively high initial monomer concentrations (i.e., $\langle n_0 \rangle \sigma^2 = 1.123 \times 10^{-1}$). For example, as provided in Table 2.3, the KMC and RT calculations show scaling exponents of $\alpha_{R_M} = 0.145 \sim 0.148$ for $\langle R_M \rangle \sim t^{\alpha_{R_M}}$ and $\alpha_{R_g} = 0.123 \sim 0.125$ for $\langle R_g \rangle \sim t^{\alpha_{R_g}}$.

Table 2.4. Comparison of d_f observed from the KMC simulations and the RT (d_{fNM} and d_{fNg}) with the expected values, $d_{f,\exp}$, based on the scaling exponent of the monomer concentration predictions at long times.

	$\langle n_0 \rangle \sigma^2$	μ	d_{fNM}	$d_{fNM,\exp}$	d_{fNg}	$d_{fNg,\exp}$
KMC	3.872×10^{-2}	-0.610	1.78	1.78	1.91	1.99
	6.255×10^{-2}	-0.613	1.77	1.74	1.92	1.97
	9.771×10^{-2}	-0.615	1.76	1.74	1.90	1.97
	1.123×10^{-1}	-0.612	1.77	1.74	1.91	1.96
	1.741×10^{-1}	-0.616	1.77	1.68	1.92	1.91
RT	3.872×10^{-2}	-0.611	1.77	1.77	1.90	1.92
	6.255×10^{-2}	-0.612	1.76	1.74	1.90	1.92
	9.771×10^{-2}	-0.615	1.75	1.73	1.91	1.98
	1.123×10^{-1}	-0.611	1.79	1.77	1.93	1.98
	1.741×10^{-1}	-0.614	1.75	1.67	1.92	1.93

For M , they show scaling exponents of $\alpha_{M_N} = 0.237 \sim 0.240$ for $M_N \sim t^{\alpha_{M_N}}$ and $\alpha_{M_W} = 0.234 \sim 0.241$ for $M_W \sim t^{\alpha_{M_W}}$. When $\langle n_0 \rangle$ is considerably high (i.e., $\langle n_0 \rangle \sigma^2 = 1.741 \times 10^{-1}$), the exponents increases notably. This observation might be attributed to the fact that the distance among clusters is not sufficiently greater than the cluster size when the initial monomer concentration is high. This finding corresponds to the gelation point observed in studies of DLA [1,4]. In this study, we limit the scaling behavior observed in cluster formation to the case in which $\langle n_0 \rangle \sigma^2 \leq 1.741 \times 10^{-1}$. From the observed scaling exponents, we can calculate d_f, and it is possible to define four different d_f values with four combinations of scaling exponents from among $\left[\alpha_{R_M} \;\; \alpha_{R_g}\right]$ and $\left[\alpha_{M_N} \;\; \alpha_{M_W}\right]$.

In Table 2.3, we presented the calculated values of the four different d_f values, denoted by $d_{fNM} = \alpha_{M_N} / \alpha_{R_M}$, $d_{fWM} = \alpha_{M_W} / \alpha_{R_M}$, $d_{fNg} = \alpha_{M_N} / \alpha_{R_g}$, and $d_{fWg} = \alpha_{M_W} / \alpha_{R_g}$. Interestingly, the RT and KMC results both reveal that d_{fNM} and d_{fWM} range between 1.75 and 1.79, whereas d_{fNg} and d_{fWg} range between 1.90 and 1.95. The difference between the fractal dimensions measured using R_M and R_g is due mainly to the measurement method, as identified in the analysis of the characteristic cluster size shown above and in Figure 2.3. The fractal dimension measured by d_{fNM} and d_{fWM} is comparable to the observation from stochastic simulations of DLA assuming 2D irreversible on-lattice diffusion (i.e., $d \sim 1.7$) [3]. Additionally, we must note here that the fractal dimensions d_{fNM} and d_{fNg} are also comparable to d_f for the HCP structure in Figure 2.2 measured using R_g and R_M , $d_f = 1.72$ and $d_f = 1.96$, respectively. This finding also indicates that the cluster shape is nearly isotropic and compact, which is consistent with the finding from $g(r)$ in Figure 2.5. To verify the predicted scaling behavior of $\langle R_s \rangle$ as a function of the scaling behavior of the monomer concentration, $\langle R_s \rangle \sim t^{\frac{\mu+1}{d_f+1}}$ in eq.(2.25), we compared d_f and $d_{f,\exp}$, where

$$d_{f,\exp} = \frac{\mu+1}{\alpha} - 1$$

On the basis of the observation of μ , d_{fNM} , and d_{fNg} from the KMC and RT calculations. As Table 2.4 shows, $d_{fNM,\exp}$ agree well with d_{fNM} , although it is generally smaller than d_{fNM} . Interestingly, $d_{fNg,\exp}$

is generally greater than d_{fNg}, although it also shows good agreement with d_{fNg}. The overall agreement between the prediction and the simulation and calculations verifies that the model we used in this study is self-consistent. Unfortunately, the observed scaling exponents and fractal dimension do not show good agreement with the experimental observation of colloidal gold NPs by Wilcoxon *et al.* [4], who reported that the observed scaling of the cluster size is much slower than the conventional DLA behavior (i.e., $\langle R_s \rangle \sim t^{0.38}$ vs. $\langle R_s \rangle \sim t^{0.56}$ [4]). Considering our observation from the KMC simulation and RT calculation that $\langle R_s \rangle \sim t^{0.14}$, the clusters grow even more slowly than the rate observed experimentally for the Au CNPs. Note, however, that the dimensionality dependence, which determines the scaling of the cluster size employed in conventional diffusion-limited studies as well as in the experimental observation, is based on the theoretical model of the Brownian Smoluchowski process, in which the rate constant for the attachment of clusters plays an important role [4,20]. The present study excluded cluster-cluster interactions, assuming virtually immobile clusters compared to the fast movement of monomers. In addition, the experimental observation is of the expedited cluster formation rate obtained by the addition of pyridine in the earlier stages of cluster formation. In the present study, the addition of this phase destabilizer was addressed neither in the KMC simulation nor in the RT calculation. These differences would produce the observed difference in the scaling exponent for the cluster size.

Figure 2.8 compare the results of the RT calculation and KMC simulation regarding the scalability of the cluster weight distribution, $G(s/M_N)$, during cluster formation as a function of the normalized cluster weight s/M_N, observed at different times with different $\langle n_0 \rangle$ and different initial monomer concentrations. As the plots demonstrate, we can find neither the existence of a peak nor convergence of the distribution function in either KMC simulations or the RT calculations at earlier times. In contrast, the scale-invariant property of $G(s/M_N)$ emerges at longer cluster formation time (i.e., $t \geq 10^{-4}$ s). The converged form of $G(s/M_N)$ predicted from the RT calculation is comparable to the KMC observations. In particular, $G(s/M_N)$ at longer times shows a peak around $s/M_N \sim 1.1$.

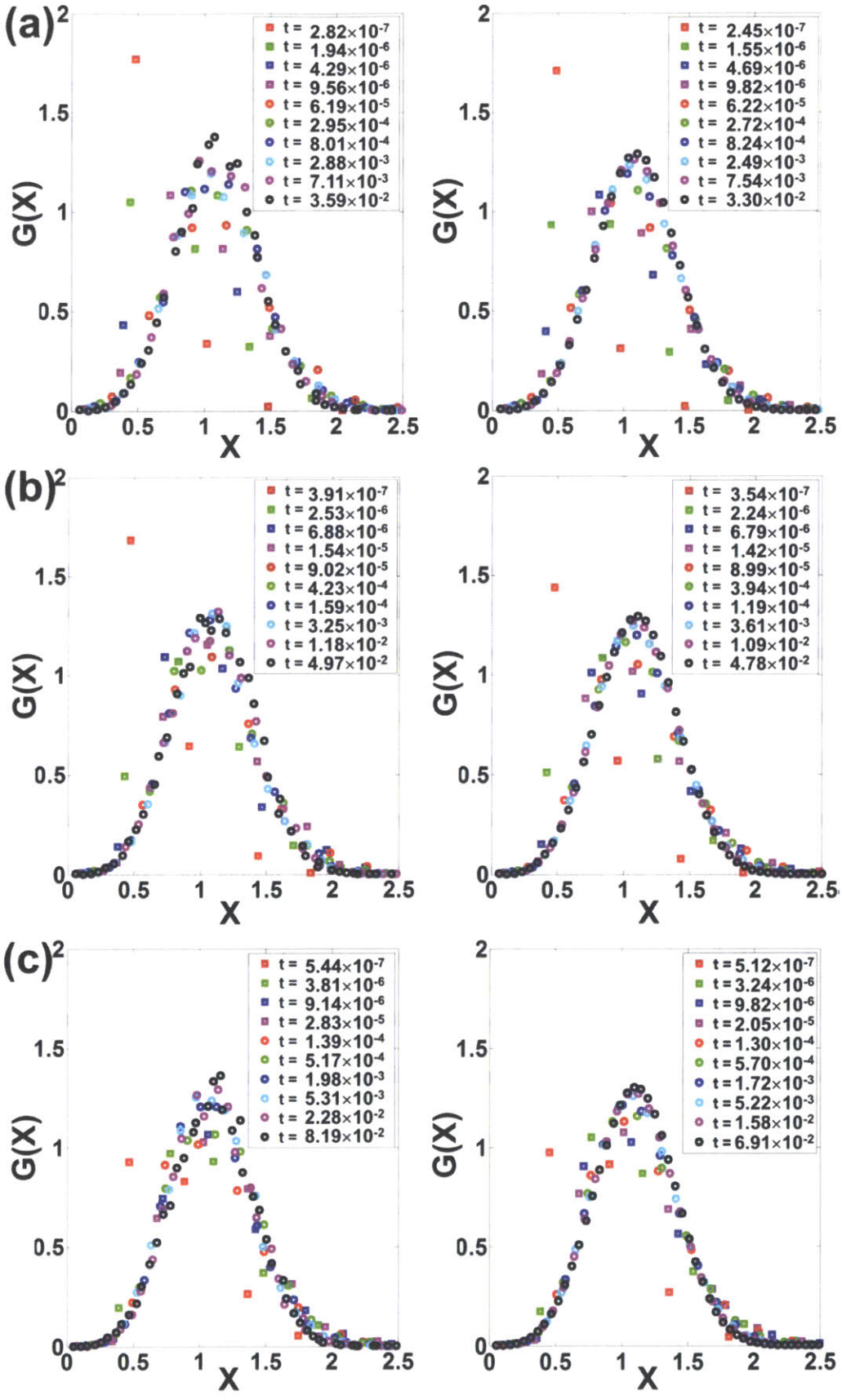
(a)
t = 2.82×10-7
t = 1.94×10-6
t = 4.29×10-6
t = 9.56×10-6
t = 6.19×10-5
t = 2.95×10-4
t = 8.01×10-4
t = 2.88×10-3
t = 7.11×10-3
t = 3.59×10-2
t = 2.45×10-7
t = 1.55×10-6
t = 4.69×10-6
t = 9.82×10-6
t = 6.22×10-5
t = 2.72×10-4
t = 8.24×10-4
t = 2.49×10-3
t = 7.54×10-3
t = 3.30×10-2
(b)
t = 3.91×10-7
t = 2.53×10-6
t = 6.88×10-6
t = 1.54×10-5
t = 9.02×10-5
t = 4.23×10-4
t = 1.59×10-4
t = 3.25×10-3
t = 1.18×10-2
t = 4.97×10-2
t = 3.54×10-7
t = 2.24×10-6
t = 6.79×10-6
t = 1.42×10-5
t = 8.99×10-5
t = 3.94×10-4
t = 1.19×10-4
t = 3.61×10-3
t = 1.09×10-2
t = 4.78×10-2
(c)
t = 5.44×10-7
t = 3.81×10-6
t = 9.14×10-6
t = 2.83×10-5
t = 1.39×10-4
t = 5.17×10-4
t = 1.98×10-3
t = 5.31×10-3
t = 2.28×10-2
t = 8.19×10-2
t = 5.12×10-7
t = 3.24×10-6
t = 9.82×10-6
t = 2.05×10-5
t = 1.30×10-4
t = 5.70×10-4
t = 1.72×10-3
t = 5.22×10-3
t = 1.58×10-2
t = 6.91×10-2
G(X)
X

Figure 2.8. Relationship between the cluster weight distribution function ($G(X)$) and X , where $X = s / M_N$, with different initial monomer densities ($\langle n_0 \rangle \sigma^2 = 6.255 \times 10^{-2}$, 9.771×10^{-2} , and 1.741×10^{-1} for (a), (b), and (c), respectively). Different symbols in the plots denote data taken at designated time (time scale: s). Left column is for the KMC simulation results and right column is for the results from the RT.

From the peak position and eq.(2.27), the nonlinearity factor is found to be $y = 1.30$. Although it is not shown here, however, the expected distribution form of $G(s / M_N)$ in eq.(2.28) with $y = 1.30$ does not match the KMC and RT data well. This deviation implies that an unknown correlation with cluster growth affects the equilibrium distribution of the cluster weight [7,8]. This peak position, interestingly, is comparable to that predicted when the initial monomer concentration is relatively high from the mean-field model of Marquesee and Ross for diffusion-limited coarsening [24]. The distribution function is well known to be peaked when the cluster formation is a diffusion-limited process; therefore, the observed behavior of $G(s / M_N)$ supports the idea that the modeled cluster formation process of CNPs is diffusion-limited even when the diffusion of monomers is a configuration-dependent reversible process.

Finally, we describe the relationship between t_{ind} and $\langle n_0 \rangle$. To quantitatively define t_{ind} , we calculate the time at which the fitting curve of the average cluster size for longer periods and the horizontal fitting line for earlier times of cluster formation meet. As shown in Figure 2.9, the observations from the KMC simulations and RT calculations both show a linear relationship between t_{ind} and $\langle n_0 \rangle^{-1}$, as expected from eq.(2.30), except for $\langle n_0 \rangle \sigma^2 = 1.741 \times 10^{-1}$. As expected, when the initial concentration of monomers is relatively rich, t_{ind} deviates from linearity and approaches zero. For a dilute initial concentration of monomers, the inverse proportional relationship of t_{ind} with respect to $\langle n_0 \rangle^{-1}$, accompanied by good agreement between the KMC simulation and RT calculation, also validates the model in this study to describe cluster formation in CNPs in a self-consistent manner.

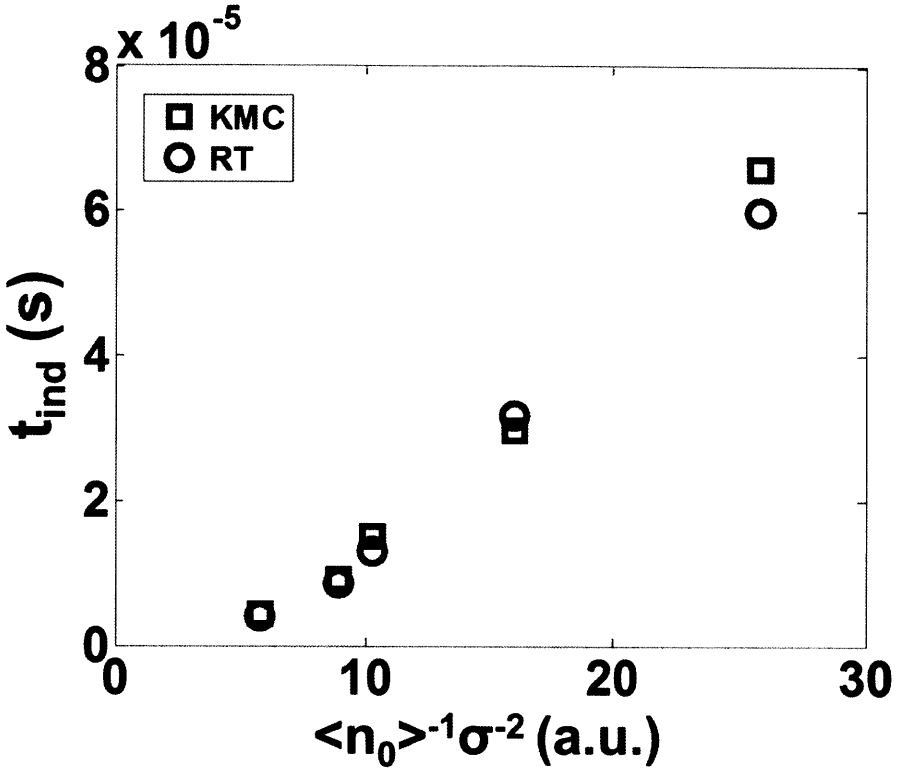

Figure 2.9. Relationship between the induction time for the cluster formation (t_{ind}) and the initial monomer densities ($\langle n_0 \rangle \sigma^2$).

2.5. Conclusion

In Chapter 2, we presented a study of cluster formation in colloidal nanoparticles (CNPs). To represent the CNPs, which maintain a balance between the attractive and repulsive potentials among NPs dispersed in a liquid medium, we employed the Lennard-Jones potential and the potential-dependent diffusivity of a single NP (configuration-dependent diffusivity of a monomer). To describe the stochastic movement of NPs in the liquid dispersion medium, we employed a kinetic Monte Carlo (KMC) algorithm based on an advanced stochastic diffusion model. The KMC simulation results were compared to the results of rate theory (RT) calculations focusing on the analysis of not only the temporal evolutions of the monomer and cluster concentrations but also the scaling behavior of the clusters. For the scaling analysis, we concentrated on the scaling of the average cluster size and weight as a function of time, which is represented by a power law at longer times. To measure the cluster size and weight, we also employed two different quantities. The observed scaling exponents for the cluster size and weight were smaller in

both the KMC simulations and the RT calculations than those in conventional cluster formation studies. The reduction in the scaling exponents was attributed to the reversible diffusion of a single NP from the cluster, although the detachment of a monomer is much slower than the attachment. In particular, the observed scaling exponent for the cluster size from the KMC simulation and RT calculation agreed well with the prediction from RT, in which the scaling behavior is a function of the time dependence of the monomer concentration for longer cluster formation times. We also observed scale-invariance of the cluster weight distribution at longer times irrespective of the initial monomer concentration when it is sufficiently small. Additionally, we also compared a theoretical prediction based on RT of the relationship between the induction time for the initial cluster formation and the monomer concentration with the corresponding results of the KMC simulation and RT calculation. The comparison verified the predicted inversely proportional relationship of the induction time and the initial monomer concentration. This study is expected to provide useful information for those who want to understand and control the morphological stability of a colloidal phase consisting of NPs. In addition, this study can be applied to CNPs with higher dimensions and multiple-components.

2.6. References

[1]. M.Y. Lin, H.M. Lindsay, D.A. Weitz, R.C. Ball, R. Klein, and P. Meakin, *Nature (London)*, **339**, 360 (1989).

[2]. J. Feder, T. Jossang, E. Rosenqvist, *Phys. Rev. Lett.*, **53**, 1403 (1984).

[3]. M. Thorn and M. Seesselberg, *Phys. Rev. Lett.*, **72**, 3622 (1994).

[4]. J.P. Wilcoxon, J.E. Martin, and D.W. Schaefer, *Phys. Rev. A*, **39**, 2675 (1989).

[5]. R. Pastor-Satorras and J.M. Rubi, *Progr. Colloid Polym. Sci.*, **110**, 29 (1998).

[6]. G. Schmid (*Ed.*), *'Nanoparticles: From Theory to Application', 2nd ed.* (John Wiley & Sons, New York, 2004).

[7]. G. Bales and D.C. Chzran, *Phys. Rev. B*, **50**, 6057 (1994); G. Bales and A. Zangwill, *Ibid*, **55**, R1973 (1997).

[8]. D.O. Yi, M.H. Jhon, I.D. Sharp, Q. Xu, C.W. uan, C.Y. Liao, J.W. Ager III, E.E. Haller, and D.C. Chrzan, *Phys. Rev. B*, **78**, 245415 (2008).

[9]. F. Shi, Y. Shim, and J.G. Amar, *Phys. Rev. E*, **76**, 031607 (2007).

[10]. X. Yuan, K. Fischer, and W. Scharl, *Adv. Funct. Mater. (Weinheim)*, **14**, 457 (2004).

[11]. S.F. Hopp and A. Heuer, *J. Chem. Phys.*, **133**, 204101 (2010).

[12]. J.N. Israellachivili, *'Intermolecular and Surface Forces', 2nd ed.* (Academic Press, New York, 1992).

[13]. M. Gibson and J. Bruck, *J. Phys. Chem. A*, **104**, 1876 (2000).

[14]. E. Sanz and D. Marenduzzo, *J. Chem. Phys.*, **132**, 194102 (2010).

[15]. H. Chen and E. Ruckenstein, *J. Chem. Phys.*, **131**, 244904 (2009).

[16]. D.T. Gillespie, *J. Comp. Phys.*, **22**, 403 (1976).

[17]. J.H. Yao, K.R. Elder, H. Guo, and M. Grant, *Phys. Rev. B*, **47**, 14110 (1993).

[18]. D. Frenkel and B Smit, *'Understanding Molecular Simulation: From Algorithms to Applications'*, (Academic Press, New York, 2002).

[19]. T.A. Witten, Jr., and L.M. Sander, *Phys. Rev. B*, **27**, 5686 (1983).

[20]. M.v. Smoluchowski, *Phys. Z.*, **17**, 557, 585 (1916).

[21]. P.G.J. van Dongen and M.H. Ernst, *Phys. Rev. Lett.*, **54**, 1396 (1985).

[22]. F. Leyvraz and S. Redner, *Phys. Rev. Lett.*, **88**, 068301 (2002).

[23]. I.M. Lifshitz and V.V. Slylosov, *J. Phys. Chem. Solids*, **19**, 35 (1961); C. Wagner, *Z. Elektrochem.*, **65**, 581 (1961).

[24]. J.A. Marqusee and J. Ross, *J. Chem. Phys.*, **80**, 536 (1984).

[25]. D.J. Bray, S.G. Gilmour, F.J. Guild, and A.C. Taylor, *Appl. Statist.*, **61**, 253 (2012).

Chapter 3

A Kinetic Monte Carlo Algorithm for Spinodal Decomposition of Colloidal Nanoparticles*

Abstract

An algorithm based on the kinetic Monte Carlo (KMC) method for spinodal decomposition of a colloidal dispersion of nanoparticles (CNPs) as a binary mixtureis presented. For the algorithm, we considered the free energy barrier calculated from the phase field model (PFM). We also considered the diffusive jump of particles among discrete compartments to be constrained by the free energy barrier. These considerations were combined to develop an efficient KMC algorithm namely free energy-limited next reaction method (FENRM). By constructing the diffusive master equation for the discretized system, we also demonstrate that the biased diffusive jump governed by the Boltzmann distribution is mathematically in accordance with the governing spatio-temporal differential equation known as the Cahn-Hilliard equation for the spinodal decomposition of a binary mixture. Computer simulations with different initial conditions based on the FENRM exhibited the typical temporal evolution of microstructures in the course of phase separation governed by spinodal decomposition except for the existence of an intermediate stage before the late stage. The physical validity of the proposed algorithm is also examined by comparson with different numerical calculations. The proposed KMC algorithm demonstrated its ability to describe the dynamics of unstable systems by capturing most of the critical characteristics of the microstructural evolution and its dynamic properties. We expect that this stochastic algorithm can be extended and applied to simulate more complicated dynamic systems involving unstable multi-phase multi-component mixtures and reaction-diffusion systems with phase separation.

*Parts of Chapter 3 will be submitted to a peer-reviewed journal (Authored by S. Joon Kwon & T. Alan Hatton).

3.1. Introduction

The Kinetic Monte-Carlo (KMC) method, a meso-scale computational method, is noted for its power and success in describing both equilibrium and non-equilibrium processes in dynamic systems [1]. Owing to its ability to track the state-by-state transition kinetics, it can effectively and accurately simulate the temporal evolution of a dynamic system in an unstable state. This feature of the KMC algorithm has made it an important tool for the stochastic simulation of a network of biochemical reactions [1,2]. In addition to chemical reactions, the KMC algorithm can be extended to describe the spatio-temporal evolution of unstable systems on the basis of diffusion processes [3,4]. In particular, the KMC algorithm is adequate for application to a dynamic system under stochastic effects, such as randomized intrinsic noise, that drive the system through the stochastic states. An interesting spatio-temporal dynamic of unstable systems, spinodal decomposition, has been intensively analyzed experimentally and theoretically as a mechanism of the phase separation of a mixture [5-13]. Most of the theoretical approaches to spinodal decomposition have been done in the continuum regime by solving the deterministic governing differential equation [6-9,13], although there are several different approaches such as the Monte-Carlo (MC) method [10,12] and molecular dynamics (MD) [11]. It is well known that in principle, the continuum approach has many computational difficulties owing to the highly nonlinear properties of the governing equation, such as the concentration-dependent mobility and the fourth-order partial derivative in the spatial domain [14,15]. Because of this nonlinearity, the continuum-based method is prone to accumulate computational uncertainty and error, especially in later stages of the dynamics. Other approaches also face difficulties in describing the decomposition process. For example, a solid physical relationship is required when using an MC simulation to connect the MC step and the real time scale [16]. Otherwise, it is necessary to employ empirical or phenomenological parameters for matching the probabilistic jumping to the movement of particles such that the conventional MC method describes the real-time process of diffusive motion. The introduction of these parameters leads to unexpected errors in describing the time-dependence of the separation process. In addition, most MC methods can analyze only a limited spatial domain in a reasonable computation time. These limitations make MC methods an inefficient way of simulating the evolution of the microstructures of a dynamic system. MD methods provide the most accurate description by tracing the time-dependent configuration of particle-by-particle movements in the system; however, they are computationally limited in not only the spatial domain but also the time domain, because the duration of the computable course is often less than 10^{-3} s. Considering that the typical time scale for many real-world meso-scale dynamic phenomena involving spinodal decomposition is greater than 1 s, this time-limitation reduces the effectiveness and efficiency of the MD method for simulating microstructural evolution.

In Chapter 3, we suggest a simple, efficient KMC algorithm for spinodal decomposition of CNPs. The KMC method employed in this study is based on a discrete system with compartments in which designated numbers of different particles are traced throughout their temporal evolution. When the size of the compartment is appropriate for the diffusive process, the compartment-based simulation work as the coarse-grained simulation method that can allow the expansion of the computationally approachable number of dimensions in the spatial domain. This feature makes a significant advance in the statistically more appropriate approach for molecular simulation without much computational cost, which has been a main obstacle for MD or Brownian dynamics (BD) simulations. Therefore, it is highly probable that the KMC algorithm can effectively describe microstructural evolution in longer times and in larger spatial dimensions compared to the conventional MD or BD simulations. By enumerating and determining the fastest diffusion process, the KMC algorithm also guarantees that both real-time progress is maintinaed and the stochastic nature of time-dependent processes is considered. For computational efficiency, we started with an advanced KMC algorithm called the next reaction method (NRM), a powerful tool for the computation of a dynamic network consisting of a thousand or more processes [2].

The most distinctive aspect of the proposed algorithm is the introduction of a biased diffusion process. In contrast to conventional idea on diffusion, the jumping of a single particle from one compartment to anoother is not completely random in that it is a probabilistic process governed by the free energy difference. In particular, the free energy is not homogeneous but is non-uniform over the spatial domain when the system is an unstable multi-component mixture. To consider the free energy as a functional of the non-uniform concentration, we employed the phase field model (PFM) [5]. This model includes additional free energy from the interface energy, which is a function of the spatial variation in the concentration. By mathematically matching the probabilistic diffusion master equation with the PFM, we consider the discretized interface energy to determine the time dependence of the diffusion process. And the derived numerical scheme and computational algorithm guarantee more physically accurate description of spinodal decomposition because it consider the appropriate form of the concentration-dependent mobility for the separation dynamics. The results of a computer simulation based on a method combining the PFM with the KMC algorithm demonstrate that the stochasticity, in conjunction with the biased-diffusion model, can describe the temporal evolution of microstructure found in spinodal decomposition. Although we simulated CNP assuming it as an A-B binary mixture with identical diffusivity as the simplest model, the proposed computational algorithm can be easily extended to more complicated non-equilibrium transitions affected by the free energy, such as the nucleation and spinodal decomposition of multi-phase and multi-component mixtures with different-sized molecules and different diffusivities.

3.2. Theoretical Framework

3.2.1 Free Energy Model for Mixtures

As the free energy model, a regular solution model was employed for a homogeneous A-B mixture. Without loss of generality, let A denotes the NPs, whereas B represents the solvent. A normalized form of the total Helmholtz free energy ($F_0 / k_B T$) as the volume fraction of A particles (ϕ) is given as

$$\frac{F_0}{k_B T} = \chi\phi(1-\phi) + \left((1-\phi)\ln(1-\phi) + \phi\ln\phi\right),\ \chi \equiv \frac{\kappa}{k_B T},\ \kappa \equiv \frac{Z\left(\varepsilon_{AA} + \varepsilon_{BB} - 2\varepsilon_{AB}\right)}{2}, \tag{3.1}$$

where ε_{AA}, ε_{BB}, and ε_{AB} represent the interaction energy among the nearest A-A, B-B, and A-B pairs, respectively; k_B is the Boltzmann constant; T is the temperature; and Z is the coordination number (i.e., $Z = 6$ for 3D system). By applying thermodynamic stability criteria, the boundaries for the phase stability, such as the spinodal (T_S) and binodal curves (T_M), are expressed as [17]:

$$\begin{aligned} k_B T_S &= 2\kappa\phi(1-\phi), \\ k_B T_M &= \frac{\kappa(2\phi-1)}{\ln\left(\frac{\phi}{1-\phi}\right)}, \end{aligned} \tag{3.2}$$

A metastable condition is satisfied when $T_S \le T \le T_M$, which leads to binodal decomposition of a homogeneous mixture via nucleation followed by growth due to the threshold homogeneous or heterogeneous nucleation energies [17]. An unstable condition such that $T \le T_S$ results in spontaneous dynamics instability followed by phase separation via spinodal decomposition [5,17]. In this study, we focus on spontaneous phase separation of a mixture when it is quickly quenched below T_S by spinodal decomposition.

3.2.2. Spinodal Decomposition

In the spirit of the original idea of the PFM suggested by Cahn and Hilliard, the driving force for phase separation is the difference of the chemical potential of two coexisting phases and the interface energy [5]. When a homogeneous mixture is unstable under fluctuations in an order parameter such as the

concentration, the free energy can be expressed as a functional form of the order parameter, which is a function of the spatial coordinates. Accordingly, the normalized Helmholtz free energy, $F_N / k_B T$, is expanded to include the free energy contributed by the interface as follows:

$$\frac{F_N}{k_B T} = \frac{F_0}{k_B T} - Cl^2 \phi \nabla^2 \phi, \; C = \frac{\chi}{2}. \tag{3.3}$$

In eq.(3.3), C is the normalized gradient energy coefficient, which describes the free energy of the diffuse-interface between phases, and l is the phenomenological interaction distance between two distinctive phases [5]. The gradient energy coefficient was obtained from an expansion of the homogeneous energy such that $F_N\left[\phi(\mathbf{r})\right] = F_N\left(\phi, \nabla\phi\right)$ based on a lattice model. The flux of A-particles relative to B-particles in a closed system conserving the total volume $\mathbf{J}$ is defined as:

$$\mathbf{J} = (1-\phi)\mathbf{j_A} - \phi \mathbf{j_B} = -M(\phi)\nabla(\mu_A - \mu_B), \; \mu_A - \mu_B = \left.\frac{\partial F_N}{\partial \phi}\right|_T, \; M(\phi) = \frac{\phi(1-\phi)L_A}{\upsilon},$$

$$\mathbf{j}_i = -c_i L_i \nabla \mu_i, \; L_i = \left(\frac{L_{ii}}{c_i} - \frac{L_{ji}}{c_j}\right), \text{ where } i, j = A, B, \tag{3.4}$$

where υ is the molecular volume of an individual A- or B-particle, c_i is the concentration of i-particles (i.e., $c_i \upsilon = \phi_i$), and L_{ii} and L_{ji} are the Onsager coefficients for the diffusion of materials in a binary mixture [18]. In eq.(3.4), we used the Gibbs-Duhem relationship incorporated with a condition of mass conservation such $\phi L_A \nabla \mu_A + (1-\phi) L_B \nabla \mu_B = 0$. We can ignore the cross Onsager coefficients for isotropic transport process [19], L_{ij} ; therefore, simply the composition-dependent mobility, $M(\phi)$, considering the Nernst-Einstein equation, $L_{AA} = \frac{\phi D^*}{\upsilon k_B T}$, where D^* is the intrinsic diffusivity of B-particles. The flux $\mathbf{J}$ in eq.(3.4) can be simplified as

$$J = -\frac{\phi(1-\phi)D^*}{\upsilon k_B T} \frac{\partial}{\partial x}\left[\frac{\partial F_N}{\partial \phi}\right]$$

by assuming an isotropic diffusion flux. By substituting J into the continuity equation, we can obtain the Cahn-Hilliard (CH) equation:

$$\frac{\partial \phi}{\partial t} = \upsilon \left[M \left(\frac{\partial^2 F_0}{\partial \phi^2} \left(\frac{\partial^2 \phi}{\partial x^2} \right) - 2Cl^2 k_B T \left(\frac{\partial^4 \phi}{\partial x^4} \right) \right) + \left(\frac{\partial \phi}{\partial x} \right)^2 \frac{\partial}{\partial \phi} \left(M \frac{\partial^2 F_0}{\partial \phi^2} \right) - 2Cl^2 k_B T \left(\frac{\partial M}{\partial \phi} \right) \left(\frac{\partial \phi}{\partial x} \right) \left(\frac{\partial^3 \phi}{\partial x^3} \right) \right]. \quad (3.5)$$

This equation can be further simplified as shown in eq.(3.6) by assuming that the Fourier component governing the compositional fluctuation in the earlier stage of spinodal decomposition is sufficiently small to neglect the second-order terms in eq.(3.5).

$$\frac{\partial \phi}{\partial t} \approx \phi(1-\phi) D^* \left(\frac{\partial^2 (F_0 / k_B T)}{\partial \phi^2} \left(\frac{\partial^2 \phi}{\partial x^2} \right) - 2Cl^2 \left(\frac{\partial^4 \phi}{\partial x^4} \right) \right), \quad (3.6)$$

To calculate the governing spatial fluctuation of ϕ, it is convenient to Fourier transform $\phi(x,t)$ in the spatial domain into $\hat{\phi}(q,t)$ in the wave vector (q) domain. The application of linear stability analysis to the earlier stage of spinodal decomposition allows one to transforme eq.(3.6):

$$\frac{\partial \hat{\phi}}{\partial t} \approx -\phi_0(1-\phi_0) D^* \hat{\phi} g(q), \; g(q) = q^2 \left(\left. \frac{\partial^2 (F_0 / k_B T)}{\partial \phi^2} \right|_{\phi_0} + 2q^2 Cl^2 \right). \quad (3.7)$$

In eq.(3.7), ϕ and $\partial^2 F_0 / \partial \phi^2$ were expanded and approximated up to the first derivative terms near the initial condition, ϕ_0. The critical wave vector q_C describes the exponential decay or growth of the compositional fluctuation (i.e., $g(q_C) = 0$ from eq.(3.7)). In the earlier stage of phase separation, the fastest-growing fluctuation mode, q_m, is expressed as $q_m{}^2 = q_C{}^2 / 2$ from the condition that $\left. \frac{\partial g}{\partial q} \right|_{q=q_m} = 0$, which yields

$$q_m = \left(\frac{1}{4Cl^2} \left. \frac{\partial^2 (-F_0 / k_B T)}{\partial \phi^2} \right|_{\phi_0} \right)^{1/2} = \frac{1}{l} \left(1 - \frac{1}{2\chi \phi_0 (1-\phi_0)} \right)^{1/2}. \quad (3.8)$$

Conventionally, computer simulations of spinodal decomposition of a mixture have employed the CH equation in various forms, as shown in eqs.(3.5)-(3.7) in conjunction with deterministic calculation such as numerical integrations [8], the cell-dynamical system approach [7], spectral transforms [13], and the lattice Boltzmann model [9]. The characteristic length scale in the earlier stage of spinodal decomposition, $\lambda_m = 2\pi / q_m$, acts as a standard to determine the appropriate compartment size employed in the algorithm we suggest in this study.

3.2.3. Kinetic Monte Carlo Algorithm for Spinodal Decomposition

The KMC algorithm for a system undergoing temporal transitions calculates and updates the stochastic distribution of the waiting times of different independent temporal processes. In particular, it is well known that the probability density for the waiting times in a time-independent Markov process is governed by an exponential distribution [1,2]. The exponential distribution of the waiting times, τ is mathematically equivalent to the uniform distribution of random variables between 0 and 1, θ,

$$\tau = \frac{1}{r}\ln\left(\frac{1}{\theta}\right), \tag{3.9}$$

where r is the propensity, which is equal to the transition rate constant multiplied by the number density c. In diffusional processes, the system is spatially discretized with a finite number of compartments, and the diffusion processes between any two nearest neighbor compartments with size h are considered to be independent of each other and governed by a Markov process. This is supported by the assumption that a single particle comes into local thermodynamic equilibrium between hop from one compartment to another. The diffusional propensity is expressed as $r = dc$, similar to that of a first-order chemical reaction, where d is the normalized diffusion coefficient (or diffusion rate constant) with respect to the compartment size (i.e., $d = D/h^2$). Although transition problems involving diffusion processes are described deterministically in a continuum framework, the KMC method has advantages for simulating the stochastic nature of diffusional processes. Conventionally, Gillespie's algorithms, such as the first reaction method (FRM) and direct method, have been widely applied to KMC simulations of chemical reaction networks. In particular, it is well known that the algorithms are effective for stochastic descriptions of the temporal evolution of biochemical reaction networks in which reactions affect each other relatively frequently (i.e., relatively high connectivity among reactions). For stochastic simulations of spatio-temporal transitions in a system evolving via diffusion processes, however, those algorithms are computationally expensive. The chief reason is that the connectivity among different diffusion processes is relatively low. Gibson and Bruck recently suggested a mathematically equivalent but more computationally efficient KMC algorithm called the next reaction method (NRM) [2]. The NRM is based on an advanced updating algorithm such as a binary sorting method for determining the fastest transition at each iteration. It hinges on the construction and maintenance of several data structures, such as a dependency graph, indexed priority queues, and an index structure, during the computation. Although maintainting these data structures incurs a computational cost, the NRM is suitable for simulating systems with more transitions. In comparison, the computational cost of Gillespie's algorithms scales with the

number of independent transition processes (N), whereas the NRM scales with $\log N$. In addition, the NRM reduces the computation time by re-using the random number at each iteration step. These advantages of the NRM algorithm provide a path to effective simulation of spinodal decomposition in which diffusion is affected by the free energy difference.

In the conventional KMC algorithm, the free energy difference is not conbsidered during the temporal process. Sauwerwine and Widom recently tried to incorporate the free energy difference into Gillespie's direct method in order to stochastically simulate the thermodynamic equilibrium structures of biological molecules [1]. However, their approach is limited to specific cases depending asymptotically on the Arrhenius model. In comparison, the classical Metropolis Monte-Carlo (MMC) algorithm can simulate a system considering a free-energy-directed diffusion process. Indeed, it is an efficient way to describe the equilibrium state of a mixture of interacting particles [10,12]. However, it is intrinsically limited because it required the use of empirical or experimentally obtained kinetic parameters for each diffusional jump [16]. This limitation causes artificial errors in the kinetic and dynamic properties of the system. It is our goal in this study, therefore, to develop a KMC algorithm that can describe real-time transitions in an unstable system via diffusion processes. This is done by modifying the NRM algorithm to appropriately incorporate a diffusion process limited by the free energy difference.

First, we need to determine an appropriate value for the compartment size, h . A fundamental assumption is that in each compartment, the mixture remains homogeneous as a phase. This assumption corresponds to the maximum limit of h . For example, h should be sufficiently smaller than the interface thickness l_I and the characteristic wavelength governing the earlier stage of spinodal decomposition λ_m. Considering that l_I and λ_m are comparable in size according to the diffuse interface model [5], it is sufficient to set λ_m as a guide to the maximum limit of h . For a 50:50 A-B binary mixture with $\chi = 3$, $\lambda_m = 2\pi\sqrt{3}l$ from eq.(3.8). This indicates that setting h as comparable to the interaction distance of the interface between neighboring phases l is appropriate because $h \ll \lambda_m$. For the minimum limit of h , the particle size l_p and the molecular interaction cut-off distance l_{cut} can be used. In particular, h should be sufficiently larger than l_{cut} to ensure that the fraction of pairs interacting in the short range confined in the inner compartment is larger than that of pairs interacting inter-compartmentally. Conventionally, l_{cut} is set to $l_{cut} \sim 2.5 l_p$ for pairs undergoing van der Waals interaction; therefore, setting $h >> l_{cut}$ is appropriate for the minimum limit. In this study, we set $h = l = 20 l_C \sim 8 l_{cut}$.

Second, the free energy of an inhomogeneous system with a finite number of compartments is written as follows from eq.(3.3):

$$F_N = \sum_{n=1}^{m} f_0(\phi_n) - \frac{Cl^2}{h^2} \sum_{n=1}^{m} \phi_n \left(\sum_{k=1}^{Z_n} \phi_{n,k} - Z_n \phi_n \right), \quad \frac{f_0(\phi_n)}{k_B T} = \chi \phi_n (1-\phi_n) + (1-\phi_n)\ln(1-\phi_n) + \phi_n \ln \phi_n, \quad (3.10)$$

where m denotes the number of compartments, ϕ_n is the local volume fraction of A-particles in the nth compartment, Z_n is the number of nearest interacting neighbor compartments of the nth compartment (i.e., $Z_n = 6$ for three-dimensional system with periodic boundary condition), and $\phi_{n,k}$ is the local volume fraction of the kth nearest neighbor compartment of the nth compartment. For the discretized form of the interface energy involving second order spatial derivative terms, we used the central finite difference scheme. The factor of two in the denominator of the interface energy term is added to avoid double-counting of the interface energy. At each iteration step, F_N is updated by

$$F_N(t_n + \Delta t_n) = F_N(t_n) + \Delta F_N(t_n),$$

where t_n is the absolute time after n iterations, and Δt_n is the waiting time of the fastest diffusion at the nth iteration, provided that randomly attempted diffusion of a single particle from one compartment to another is not energetically rejected. In an A-B binary mixture, diffusion from one compartment to another occurs by transport of either a single A or a single B particle. Accordingly, it is necessary to consider two possible but different values of $\Delta F_N(t_n)$, $\Delta F_N{}^A(t_n)$ and $\Delta F_N{}^B(t_n)$, for A- and B-particle diffusion, respectively. On the basis of the MMC algorithm [10,12], the NRM algorithm can be implemented with a free energy comparison reflected by the Boltzmann factor, $Q^A(t_n) = \exp(-\Delta F_N{}^A(t_n)/k_B T)$ and $Q^B(t_n) = \exp(-\Delta F_N{}^B(t_n)/k_B T)$ to construct the free energy-limited NRM (FENRM) algorithm. To elucidate the mathematical equivalence of the FENRM algorithm to the original CH equation, we can construct a master equation for a model diffusion system with a biased transition rate in a 1D chain-like space. For a 1D chain space with K compartments, the temporal evolution rate of the concentration of A-particles in the ith compartment at time t, $\phi_i(t)$, is written as follows:

$$\frac{\partial \phi_i(t)}{\partial t}$$
$$= \psi\left(1-\phi_i(t)\right)\times$$
$$\left[\left(\phi_{i-1}(t)\,p_{i-1,i}(t)+\phi_{i+1}(t)\,p_{i+1,i}(t)-\phi_i(t)\left(p_{i,i-1}(t)+p_{i,i+1}(t)\right)\right)-\left(\phi_{i+1}(t)+\phi_{i-1}(t)-2\phi_i(t)\right)\right], \qquad (3.11)$$

where ψ is the transition rate of the concentration of A-particles, and $p_{m,n}(t)$ is the probability that A-particles move from the mth compartment to nth compartment at time t. Note that eq.(3.11) considers the diffusion of A-particles relative to that of B-particles, which is realized by adding $-\psi\left(1-\phi_i(t)\right)\left(\phi_{i+1}(t)+\phi_{i-1}(t)-2\phi_i(t)\right)$. In eq.(3.11), the factor $1-\phi_i(t)$ is added to the transition rate to consider the convergence of the local mobility of A-particles relative to the motion of B-particles in a closed system with an NVT ensemble of the A-B binary mixture. Without this consideration, the extreme case in which $\phi_i(t)\to 1$ does not make physical sense because diffusion occurs with zero concentration gradient. This is also in accordance with the Nernst diffusion relationship [18]. Further, $p_{m,n}(t)$ is a function of the difference in the total free energy of the system derived by the m-to-n transition, ${F_N}^{m,n}(t)$, and can be expressed in Boltzmann form as follows:

$$p_{m,n}(t)=\exp\left(-\frac{{\Delta F_N}^{m,n}(t)}{k_BT}\right)\simeq 1-\frac{{\Delta F_N}^{m,n}(t)}{k_BT}, \qquad (3.12)$$

where the approximation is based on the simulation condition that the free energy does not change greatly per single diffusion event satisfying $\frac{{\Delta F_N}^{m,n}(t)}{k_BT}\ll 1$.

From eqs.(3.3), (3.11), and (3.12), the master equation for 1D biased diffusion is found by calculating the free energy change yielded by each of the possible transitions in the discretized 1D chain-like system:

$$
\begin{aligned}
&\frac{\partial \phi_i(t)}{\partial t} \\
&= \psi\left(1-\phi_i(t)\right)\times \\
&\left[\begin{array}{l}
-\phi_{i-1}(t)\left\{2C\delta\phi\left(\phi_{i-2}(t)-3\phi_{i-1}(t)+3\phi_i(t)-\phi_{i+1}(t)\right)+6C\delta\phi^2+\delta\phi\left(\dfrac{f_0\left(\phi_{i-1}(t)-\delta\phi\right)-f_0\left(\phi_{i-1}(t)\right)+f_0\left(\phi_i(t)+\delta\phi\right)-f_0\left(\phi_i(t)\right)}{k_BT}\right)\right\} \\
-\phi_{i+1}(t)\left\{2C\delta\phi\left(\phi_{i-1}(t)-3\phi_i(t)+3\phi_{i+1}(t)-\phi_i(t)\right)+6C\delta\phi^2+\delta\phi\left(\dfrac{f_0\left(\phi_{i+1}(t)-\delta\phi\right)-f_0\left(\phi_{i-1}(t)\right)+f_0\left(\phi_i(t)+\delta\phi\right)-f_0\left(\phi_i(t)\right)}{k_BT}\right)\right\} \\
+\phi_i(t)\left\{2C\delta\phi\left(-\phi_{i-2}(t)+3\phi_{i-1}(t)-3\phi_i(t)+\phi_{i+1}(t)\right)+6C\delta\phi^2+\delta\phi\left(\dfrac{f_0\left(\phi_i(t)-\delta\phi\right)-f_0\left(\phi_i(t)\right)+f_0\left(\phi_{i-1}(t)+\delta\phi\right)-f_0\left(\phi_{i-1}(t)\right)}{k_BT}\right)\right\} \\
+\phi_i(t)\left\{2C\delta\phi\left(\phi_{i-2}(t)-3\phi_{i-1}(t)+3\phi_i(t)-\phi_{i+1}(t)\right)+6C\delta\phi^2+\delta\phi\left(\dfrac{f_0\left(\phi_i(t)-\delta\phi\right)-f_0\left(\phi_i(t)\right)+f_0\left(\phi_{i+1}(t)+\delta\phi\right)-f_0\left(\phi_{i+1}(t)\right)}{k_BT}\right)\right\}
\end{array}\right], \qquad (3.13)
\end{aligned}
$$

where $\delta\phi$ denotes the differential increase in the concentration of A-particles bdue to the transition. Eq.(3.13) can be further simplified by a linear expansion

$$
\frac{\partial \phi_i(t)}{\partial t} \simeq \psi\delta\phi l^2\phi_i(t)\left(1-\phi_i(t)\right)\left[-2Cl^2\left.\frac{\partial^4\phi(t)}{\partial x^4}\right|_{\phi_i(t)}+\left.\frac{\partial^2\phi(t)}{\partial x^2}\right|_{\phi_i(t)}\left.\frac{\partial^2\left(f_0/k_BT\right)}{\partial\phi^2}\right|_{\phi_i(t)}\right], \qquad (3.14)
$$

where we ignored second-order terms such as $\delta\phi^2$, $\left(\frac{\partial\phi}{\partial x}\right)^2$, and $\left(\frac{\partial\phi}{\partial x}\right)\left(\frac{\partial^3\phi}{\partial x^3}\right)$. For detailed derivation of eq.(3.14), see Appendix for Chapter 3. By setting $D^* = \psi l^2\delta\phi$, we find that the approximated master equation, eq.(3.14), is mathematically equivalent to the original CH equation given in eq.(3.6). This finding also indicates that it is not necessary to make an additional approximation of the constant mobility, which has been widely used in theoretical analysis and computation based on a continuum framework [6-9,14]. In particular, the mobility for diffusion has been linearly approximated around the initial condition such that $D^*\phi\left(1-\phi\right) \approx D^*\phi_0\left(1-\phi_0\right)$ for simplicity [6-9,14]. The CH equation is well known to present some degree of difficulty in the numerical calculations owing to its non-linear terms in the differential equation. In particular, when the initial mixture is far from equilibrium, more complicated factors such as a composition-dependent diffusivity involving $D^*\phi\left(1-\phi\right)$ make the problem more difficult to solve. Therefore, the biased diffusion algorithm is more accurate for describing the kinetics, especially at later stages of spinodal decomposition, and this feature represents an additional advantage of the proposed KMC algorithm for simulating spinodal decomposition. On the basis of the mathematical justification from the master equation, the FENRM algorithm for biased diffusion-derived spinodal decomposition of A-B binary mixture in an NVT ensemble is given in Table 3.1.

Table 3.1. A summarized algorithm for a kinetic Monte Carlo calculation of spinodal decomposition

FENRM Algorithm

Step 1. Set initial configuration of A- and B-particles over finite number of compartments

Step 2. Construct a dependency graph for every possible diffusion processes

Step 3. Generate exponentially distributed waiting times of every possible diffusion processes

Step 4. Do a binary sort for the possible diffusion processes ascending order of waiting times and construct an indexed priority queue and an index structure for every diffusion processes

Step 5. Fire the first diffusion process in the priority queue (the one with the shortest waiting time)

Step 6. Calculate $Q^A(t_n)$ and $Q^B(t_n)$

Step 7. Determine whether the first diffusion process by transporting single A- or B-particle occurs or not

If $Q^A(t_n) \geq 1$ and $Q^B(t_n) \geq 1$

Calculate relative probability of A- or B-particle diffusion such that

$P^A(t_n) \equiv \dfrac{\phi(t_n)Q^A(t_n)}{\left(\phi(t_n)Q^A(t_n)\right)+\left(\left(1-\phi(t_n)\right)Q^B(t_n)\right)}$ and generate a random number R_n

If $P^A(t_n) \geq R_n$

Fire A-particle diffusion

Else

Fire B-particle diffusion

End if

Else If $Q^A(t_n) \geq 1$ and $Q^B(t_n) < 1$

Generate two random numbers, $R_{n,1}$ and $R_{n,2}$

If $Q^B(t_n) \leq R_{n,1}$

Set $Q^B(t_n) = 0$

End If

If $P^A(t_n) \geq R_{n,2}$

Fire A-particle diffusion

Else

Fire B-particle diffusion

End if

Else If $Q^B(t_n) \geq 1$ and $Q^A(t_n) < 1$

Generate two random numbers, $R_{n,1}$ and $R_{n,2}$

If $Q^A(t_n) \leq R_{n,1}$

Set $Q^A(t_n) = 0$

End If

If $P^B(t_n) \geq R_{n,2}$

Fire B-particle diffusion

Else

Fire A-particle diffusion

End if

Else If $Q^A(t_n) < 1$ and $Q^B(t_n) < 1$

Generate two random numbers, $R_{n,1}$ and $R_{n,2}$

If $\left[Q^A(t_n) + Q^B(t_n)\right] \geq R_{n,1}$

Calculate $P^A(t_n)$

If $P^A(t_n) \geq R_{n,2}$

Fire A-particle diffusion

Else

Fire B-particle diffusion

End if

Else

Fire neither A- nor B-particle diffusion

End if

End if

Step 8. Update free energy of the system, waiting times for next diffusion and the priority queue

Step 9. Iterate by going back to the Step 5

End of Algorithm

The algorithm uses an efficient diffusion process by simultaneously searching for opportunities for either A- or B-particle diffusion instead of separately calculating the A- and B-particle diffusion. Detailed description about updating schemes for the waiting times and the data structures at each iteration are given elsewhere [1,2] and explained in Appendix A.

3.3. Results and Discussion

By using the FENRM algorithm, we simulated A-B binary mixtures with 50:50 or 40:60 number ratios. A constant number-volume-temperature (NVT) ensemble was employed at $\chi = 3$. For the simulation system, we used 60×60 compartments that discretize a 2D plane with dimensions of $12 \times 12\ \mu m^2$, because of a 2D system can capture the critical properties of the dynamic process, although many real cases are more effectively represented by computations using a 3D system. The total number of A- and B-particles per compartment was assumed to be $N = 400$. For simplicity, the diffusivities of the two particles were both assumed to be $D = 10^{-12} m^2 / s$, which is a typical value for nanometer-scale particles. To avoid potential artificial effects of the simulation box size on the determination of the characteristic length scale of the microstructure, a periodic boundary condition was applied. The dynamic process was initiated by a random fluctuation in the number of A-particles in each compartment from the initial value. Each simulation was repeated with 160 trials to obtain statistical features of the simulated system's kinetics. Figure 3.1 shows the temporal evolution of a phase-separated symmetric A-B binary mixture undergoing spinodal decomposition. As is apparent from the 2D images, an interconnected morphology of the concentration distribution over the system emerges after a certain period of initial fluctuation. The dynamics of spinodal decomposition in the simulation also exhibits growth of the characteristic length scale λ of the separated morphology. This growth due mainly to the reduction in the free energycontributed by the interface energy. By merging and ripening, the growth of λ drives the system to have the minimum interface energy and reach thermodynamic equilibrium. To capture the critical aspects of the phase separation dynamics, the time-dependent variation in the histogram of the distribution of the A particle concentration over the system is also presented (see middle column in Figure 3.1). As expected from conventional thermodynamics, we can observe a bifurcation of the A particle concentration governed by a bimodal curve, which produces two peaks in the histogram at later times.

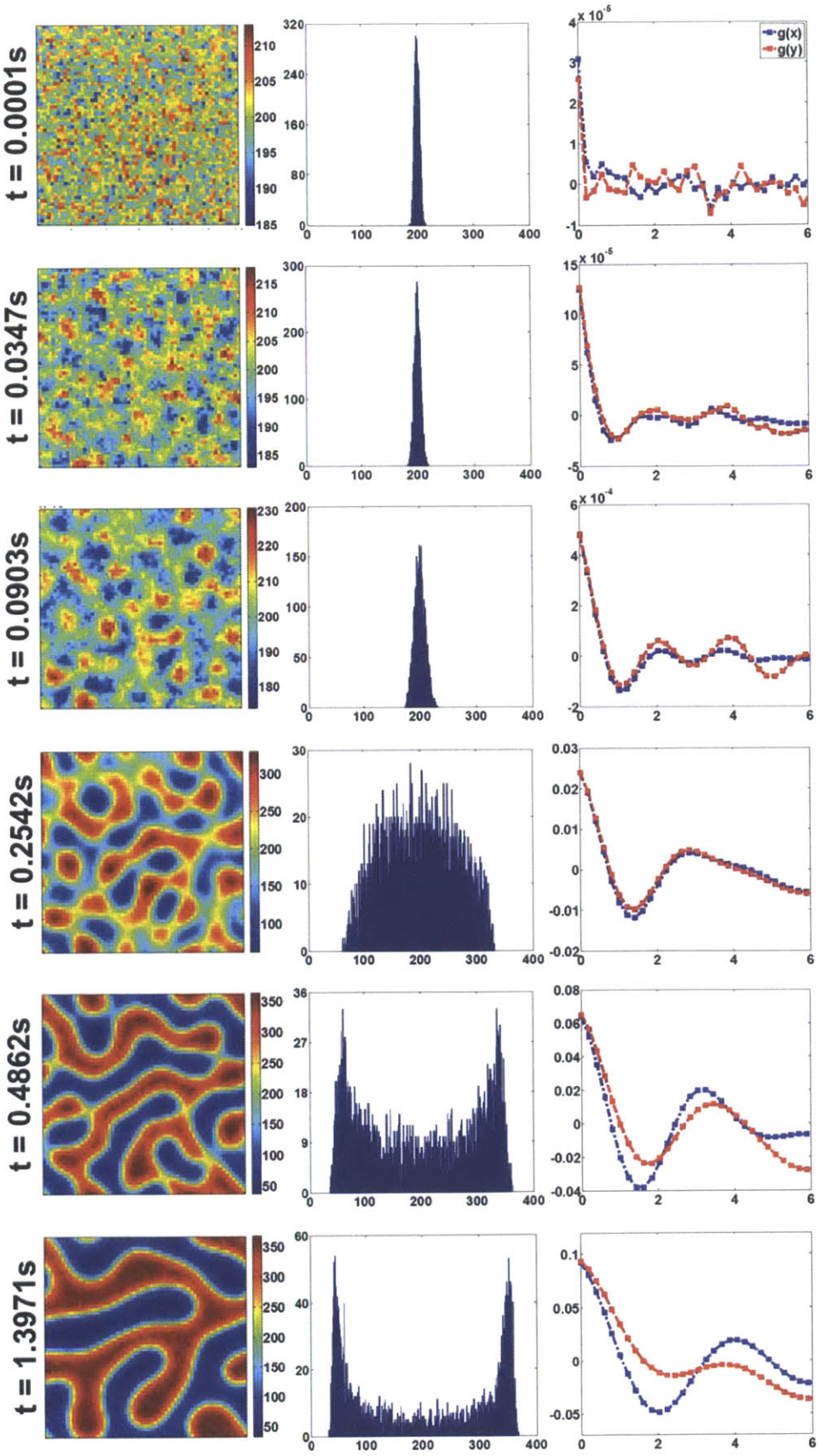
t = 0.0001s
t = 0.0347s
t = 0.0903s
t = 0.2542s
t = 0.4862s
t = 1.3971s
g(x)
g(y)
x 10^-5
x 10^-4

Figure 3.1. Computer simulation results of phase separation of a 50:50 A-B binary mixture based on the kinetic Monte-Carlo (KMC) algorithm. For the simulation, 60×60 compartments which discretize a 2D plane of 12×12 μm^2 dimensions with periodic boundary condition examined under 2×10^8 iterations were employed. Sizes of the A- and B-particles were assumed to be 10 nm. Diffusivities of the two particles were assumed to be identical as $D = 10^{-12}$ m^2/s. In the first column, temporal evolution of phase separation via spinodal decomposition at $\chi = 3$ is provided. Statistically analyzed data of the temporal evolution are shown in the second (histogram for the distribution of number of A-particles per compartment) and the third columns (Pair-correlation function, g(r), both in the x- and y-directions).

Another method of quantitatively analyzing the separation dynamics is the pair-correlation function $g(\mathbf{r},t)$, which captures the long-range order and kinetic properties of the system

$$g(\mathbf{r},t) = \frac{1}{N}\sum_{\mathbf{r}'}\langle\phi(\mathbf{r}+\mathbf{r}',t)\phi(\mathbf{r}',t)\rangle, \tag{3.15}$$

where the bracket denotes values averaged over the initial concentration condition, ϕ_0. The obtained quantitative measure is λ, which corresponds to the smallest value satisfying $g(\mathbf{r},t)\big|_{\lambda} = 0$. A dynamic system with infinite size maintaining isotropicity is expected to have identical functional behavior of $g(\mathbf{r},t)$ without respect to the orientation of $\mathbf{r}$. In the third column in Figure 3.1, we show the temporal evolution of $g(\mathbf{r},t)$ in both the x- and y-directions. The growth of λ is also identified from the increase in the axial intercepts in both the x- and y-directions. Although slight discrepancies appear between $g(\mathbf{r},t)$ in the x- and y-directions, they exhibit similar functional behavior. The discrepancies are due mainly to the finite size of the simulation system. Here, λ is obtained by calculating the radial intercept of $g(\mathbf{r},t)$ by taking the circular average (average over angles). Similarly, we also analyzed the spinodal decomposition dynamics of an A-B binary mixture with an asymmetric initial composition (i.e., 40:60 mixture). In the first column of Figure 3.2, we can observe an island-like morphology of the concentration distribution after the earlier stage of the separation. As the separation develops, features representative of spinodal decomposition, such as bifurcation of the concentration governed by a bimodal curve and the growth of λ, are also identified from the simulations (second and third columns).

According to a model of diffusion-limited coalescence [3,5-15], the dynamics of phase separation driven by ordinary spinodal decomposition with a system dimensionality larger than two is known to be governed by a power-law, $\lambda \sim t^{1/3}$.

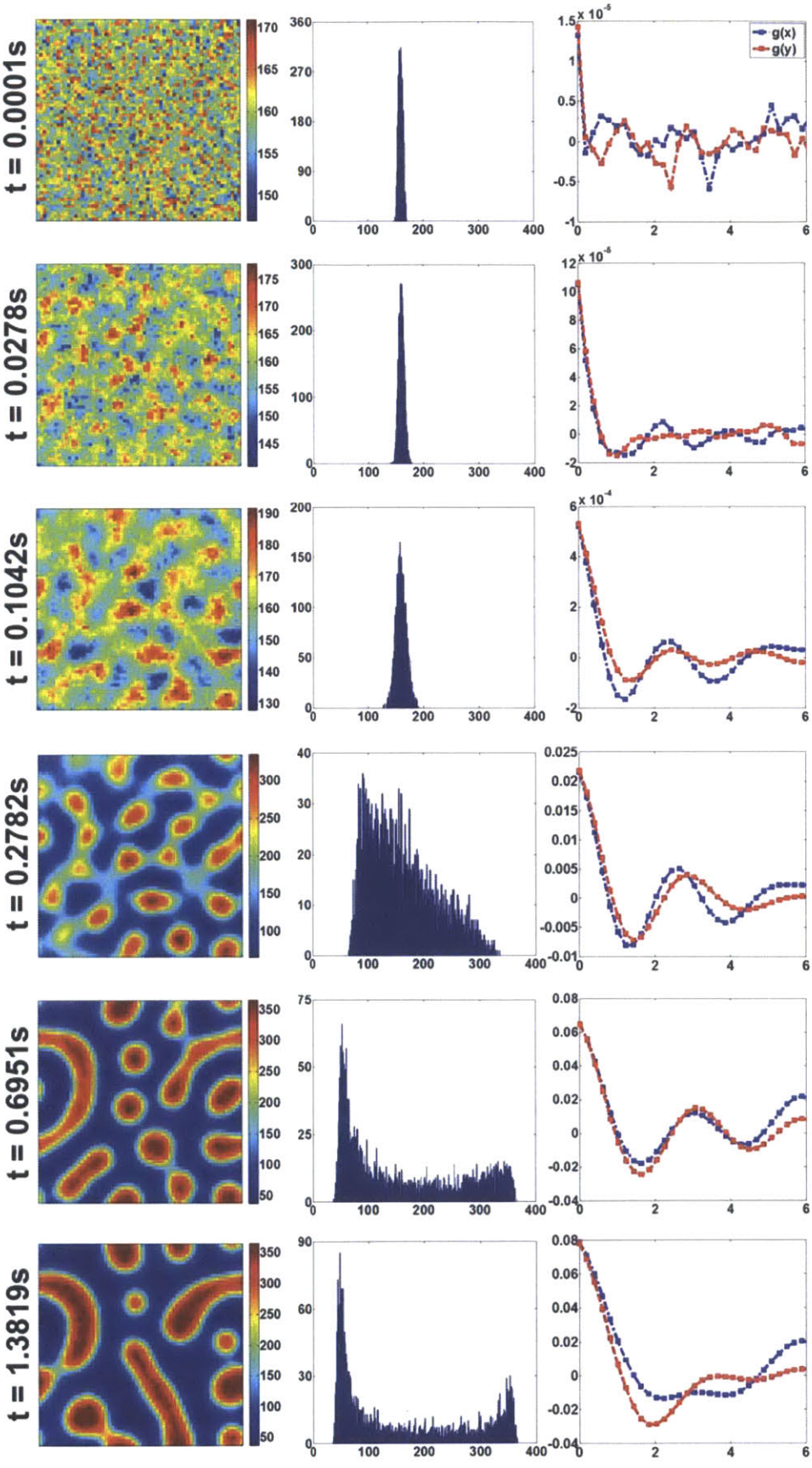
t = 0.0001s
t = 0.0278s
t = 0.1042s
t = 0.2782s
t = 0.6951s
t = 1.3819s
g(x)
g(y)
x 10^-5
x 10^-4

Figure 3.2. Computer simulation results of phase separation of a 40:60 A-B binary mixture based on the KMC algorithm. Simulations conditions were identical to those employed in Figure 3.1 except initial concentration of A-particles. In the first column, temporal evolution of phase separation via spinodal decomposition at $\chi = 3$ is provided. Statistically analyzed data of the temporal evolution are shown in the second (histogram for the distribution of number of A-particles per compartment) and the third columns (Pair-correlation function, g(r), both in the x- and y-directions).

Actually, this scaling law is modified slightly to consider incubation time t_C for the emergence of a diffuse interface between phases, $\lambda \sim (t - t_C)^{1/3}$. This scaling behavior of λ has been observed in both theoretical and experimental studies [3-14]. To examine the capability of the proposed algorithm to describe the scaling law, we analyzed the growth of λ during spinodal decomposition with both symmetric and asymmetric initial compositions. For a comprehensive analysis, the simulation was repeated with 160 trials. From Figure 3.3, we can identify scaling behavior in the growth dynamics of λ after t_C. Interestingly, it seems that there exists an intermediate stage in which λ grows but its growth dynamics is slower than that of the later stage. For the asymmetric binary mixture, we identified the seemingly intermediate stage by isolating the scaling behavior such that $\lambda \sim (t - t_C)^{0.127 \pm 0.011}$, where t_C is measured to be around 0.002 s (see Figure 3.3(a)). Further, the intermediate and later stages are observed to be separated at another critical time, t_I, which is around 0.278 s. After t_I, the growth of λ is accelerated with an increase in the exponent while maintaining the power-law dependence. In contrast to the conventional prediction, however, the observed value of the scaling exponent for the growth of λ in the later stage, 0.284 ± 0.013, differs from the expected value (i.e., $1/3$), for a discrepancy of about 11%. For the symmetric binary mixture, we also identified an intermediate stage with slower growth dynamics of λ, in which $\lambda \sim (t - 0.032\,\mathrm{s})^{0.126 \pm 0.017}$. It is notable that the scaling exponents for the intermediate stage are nearly the same for the asymmetric and symmetric cases, although t_C differs by one order of magnitude. The observed discrepancy in t_C would be explained by difference in the initial conditions at which the unstable states undergo phase separation. According to the thermodynamic principles and the CH equation [5,7,17,18], t_C increases with increasing the distance from the critical point. At constant temperature, the symmetric composition initial condition is farer from the critical point (i.e., spinodal boundary) than the asymmetric composition condition is.

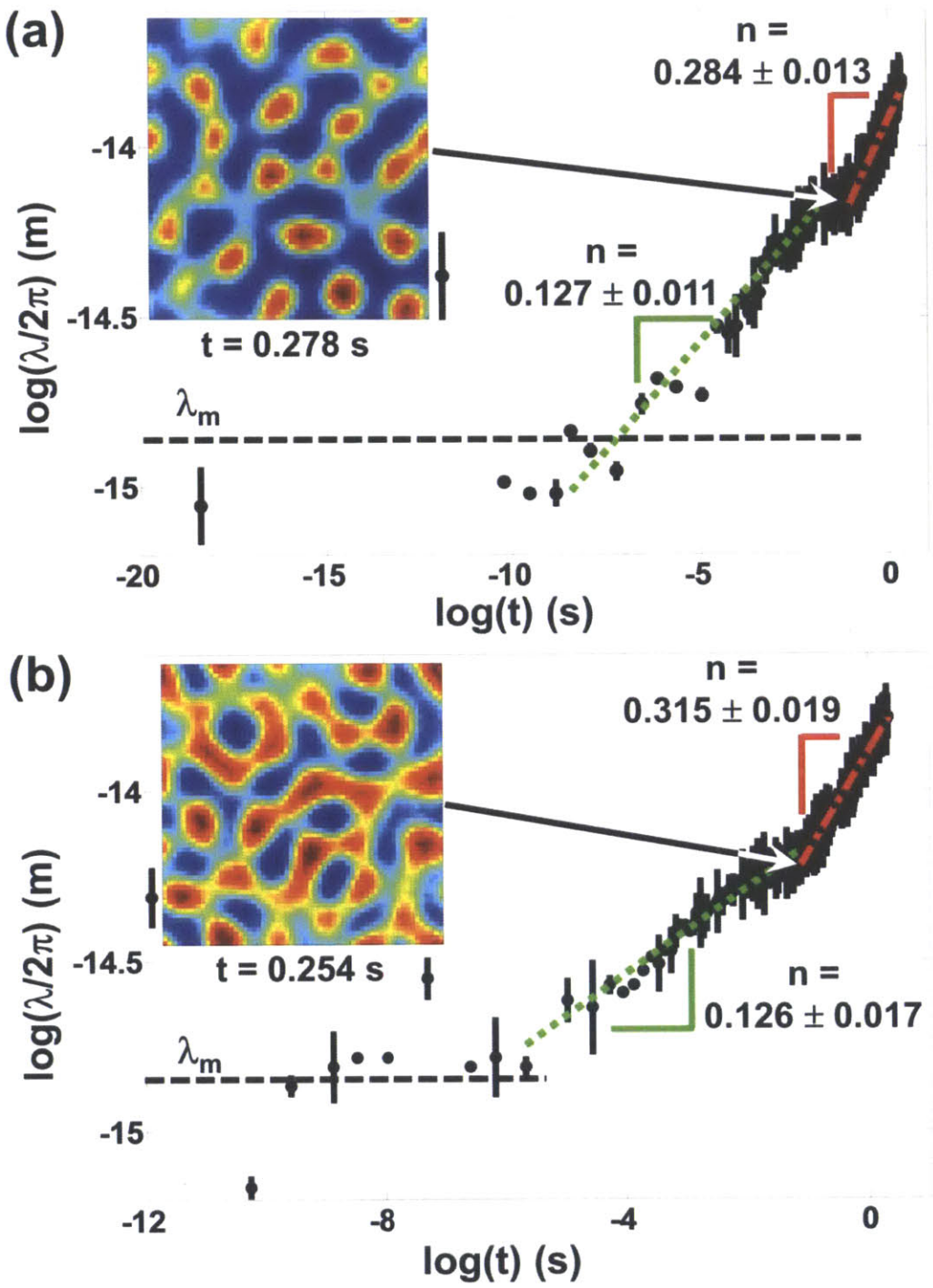

Figure 3.3.Time-dependent behavior of the characteristic length scale, λ, of the spinodal decomposition of 50:50 (a) and 40:60 (b) A-B binary mixtures at $\chi = 3$. Inset figures accompanied by arrows in each plot indicate the moment from which λ_m grows faster (fitted with red dash dot lines) than ever it does in the intermediate stage (fitted with green dot lines). Horizontal black dash lines denote the characteristic length scales in the earlier stage, λ_m, theoretically predicted from continuum model.

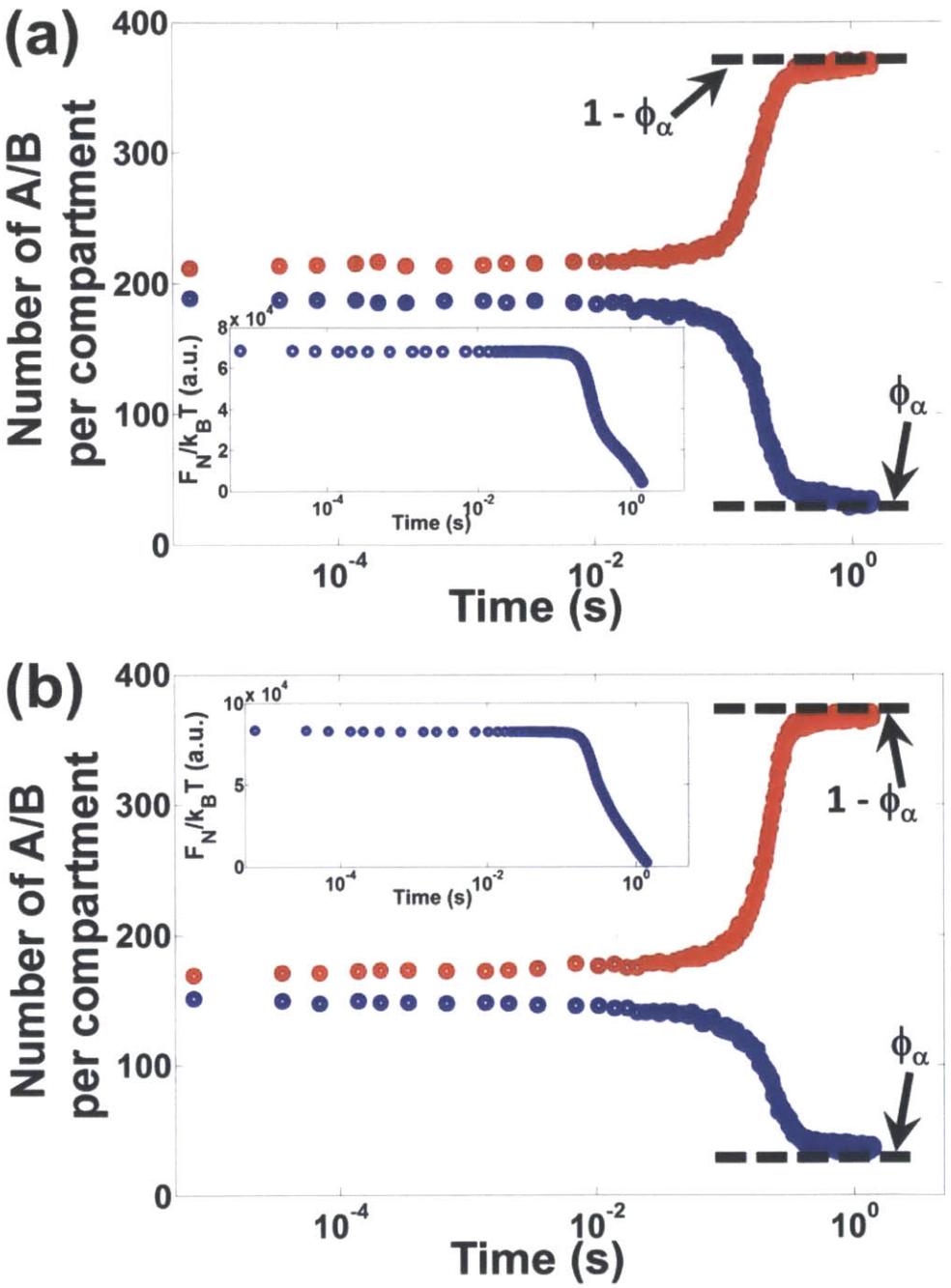

Figure 3.4. Time-dependent behavior of the maximum and minimum number of A- and B-particles per compartment during the spinodal decomposition of 50:50 (a) and 40:60 (b) A-B binary mixture at $\chi = 3$. Considering the simulation deals NVT ensemble (i.e., total number of A- and B-particles, N, is constant such as N = 400 per compartment), minimum number of A-particles corresponds to maximum number of B-particles per compartment. In each plot, thermodynamically predicted minimum and maximum numbers of the particles per compartment are provided. Insets in each plot denote time-dependency of the normalized total Helmholtz free energy (F_N/k_BT).

Therefore, it takes longer for the unstable mixture with the symmetric initial condition to initiate the separation process than the case with asymmetric condition. Interestingly, we observed the scaling behavior of λ in the later stage for the symmetric case to be $\lambda \sim (t - 0.254\text{s})^{0.315\pm0.019}$, where the scaling exponent 0.315 ± 0.019 is considerably similar to the predicted behavior. Another notable finding is that t_1 in the symmetric case ($t_1 = 0.254\text{s}$) is similar to that in the asymmetric case ($t_1 = 0.278\text{s}$) [20].

The observed deviation of the scaling exponents of the dynamic evolution of the characteristic length scales from the expected value, $1/3$, is strongly supported by several considerations. The conventional mass transport model predicts that transport in a closed system occurs solely by bulk diffusion, which results in $\lambda \sim t^{1/3}$ in the later stage of spinodal decomposition. As Zhu *et. al.* reported [13], however, the composition-dependent mobility can interfere with the dominance of bulk diffusion in mass transport by allowing an increase in the effect of interface-driven diffusion. This interference can lower the scaling exponent value to $1/4$. The exact value of the scaling exponent is therefore believed to depend on the mobility function and interface diffusion effects, whereby the exponent varies between $1/3$ and $1/4$ [8,13]. In numerical studies using an advanced finite difference scheme with a spectral method, Zhu *et al.* demonstrated that fully bulk or fully interface-driven diffusion gives rise to a scaling exponent of $1/3$ or $1/4$, respectively. In our simulation, therefore, we can conclude that the KMC algorithm incorporating composition-dependent mobility intrinsically describes a system under the diffusion effect partially governed by interface diffusion. Further quantitative analytical studies are necessary to determine how the partial portion of the interface-driven diffusion is represented by the KMC algorithm during spinodal decomposition and is linked to the scaling property of the characteristic length scale.

As another method of quantitative analysis, the time-dependence of the minimum and maximum number of A-particles per compartment was examined during spinodal decomposition. These values correspond directly to the bifurcated values of ϕ, ϕ_α (i.e., A-particles dilute) and $1-\phi_\alpha$ (i.e., A-particles rich), described in eq.(3.2). At $\chi = 3$, $\phi_\alpha = 0.071$, and the simulation data shown in Figures 3.4(a) (for the symmetric composition case) and (b) (for the asymmetric composition case) agree well with this value at later times. In contrast to the difference in dynamic behaviors observed in Figure 3.3, the dynamic behavior of the amplification of the composition (i.e., difference between maximum and minimum number of A-particles per compartment) during bifurcation is nearly identical irrespective of the initial conditions. In addition, the time-dependence of the total free energy shown in the insets of Figure 3.4 also exhibits nearly the same functional behavior.

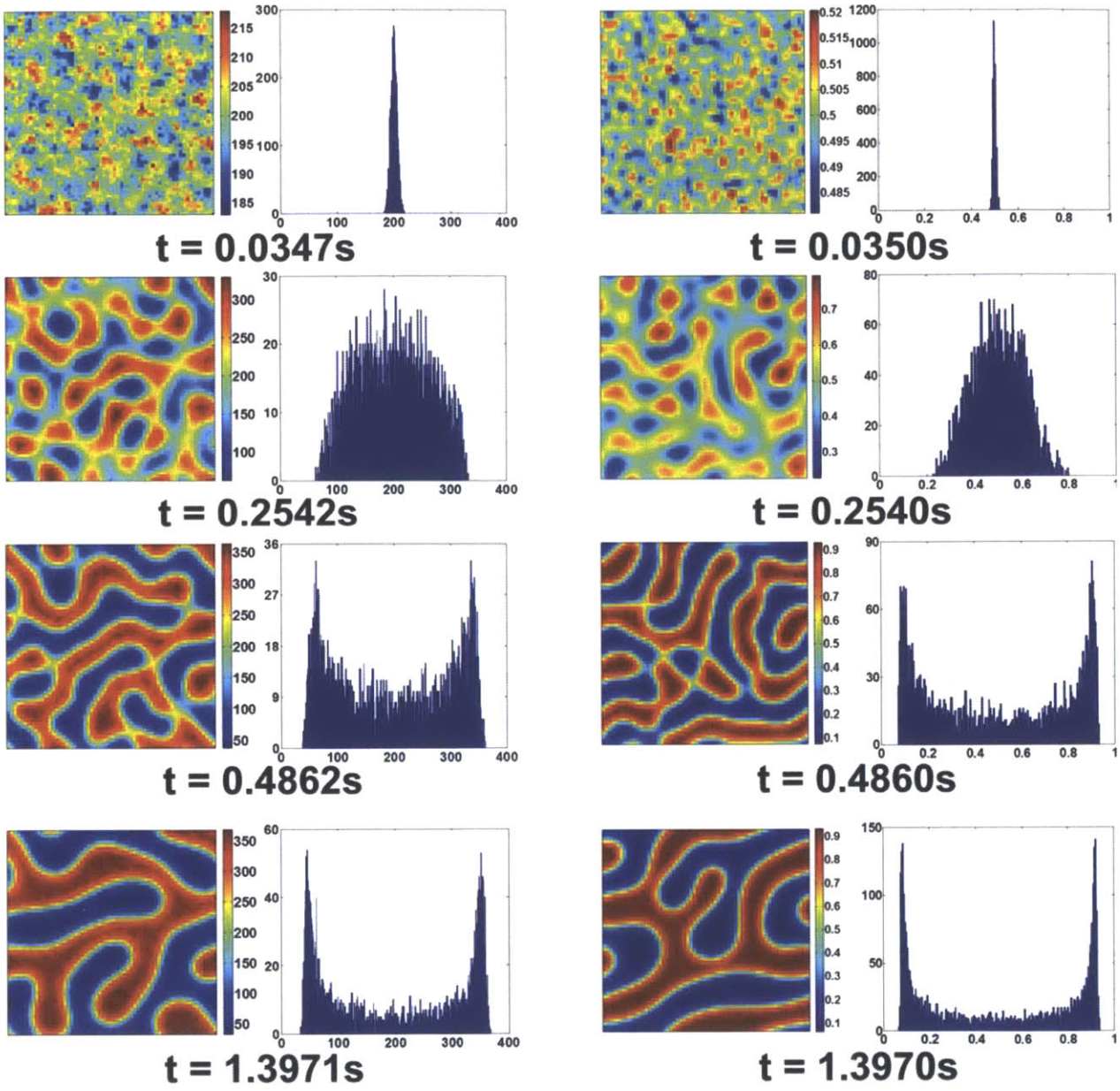

Figure 3.5. Comparison between computational results taken at different time points from the proposed KMC algorithm (left column) and from the conventional finite difference method solving the partial differential Cahn-Hilliard (CH) equation (right column). For more robust comparison, we considered composition-dependent mobility during solving the CH equation. Simulation conditions are the equivalent to those used in Figure 3.1.

These similar features of the separation dynamics (except for t_C) observed in different cases with different initial conditions indicate the universality of phase separation governed by ordinary spinodal decomposition. Further, these findings from the simulations allow us to conclude that the KMC algorithm presented in this chapter can capture most of the important aspects of spinodal decomposition.

To examine the physical validity of the proposed algorithm, we compared the calculated results based on FENRM with those obtained from numerical experiments using a different method. Among various types of numerical approaches, few methods can be applied to address the composition-dependent mobility in the calculation. A finite-difference scheme in both the time and space domains is one of the most effective and simplest methods of solving the partial differential CH equation that satisfies this condition. For the time domain, we employed the forward Euler scheme with $\Delta t = 10^{-6}$ s, which ensures the numerical stability of the computation. In particular, this differential time increase was carefully examined and chosen mainly for the consideration of the composition-dependent mobility [14,15] and mass conservation during a lengthy simulation. For the space domain, we used an semi-implicit and explicit (semi-IMEX) method [14,15]. The explicit scheme was applied to address the nonlinear stiff functions involving the composition-dependent mobility and free energy function, whereas the implicit scheme was selectively applied to address linear part of the free energy function and the fourth-order derivative term in the CH equation. The detailed numerical techniques, including the semi-IMEX approach to the finite difference method for solving a binary mixture's spinodal decomposition, can be found in the literature [14,15]. Figure 3.5 compare the results calculated by the proposed KMC algorithm and by the finite difference method. The model systems were 50:50 A-B binary mixtures under the same simulation conditions. As expected, the two approaches yield nearly identical temporal evolution of the concentration field. This comparison ensures that the dynamic properties of the spinodal decomposition described by the proposed KMC algorithm converge with those obtained by a deterministic analytical method. The characteristic length evolution was also compared (results were not shown); the scaling exponents for the symmetric and asymmetric cases were found to be 0.295 ± 0.011 and 0.317 ± 0.017, respectively. Although these values are slightly larger than those found in the KMC simulations, they are considerably similar and also range between $1/3$ and $1/4$. This comparison also supports the conclusion that the proposed KMC algorithm is valid for describing the later-stage behavior and representing the dynamic properties of spinodal decomposition.

3.4. Conclusion

In Chapter 3, we present an efficient, effective kinetic Monte-Carlo (KMC) algorithm for spinodal decomposition of an unstable binary mixture of CNPs. The algorithm considered a biased diffusion process affected by the free energy of the non-uniform dynamic system. For the free energy calculation, we employed the phase-field model (PFM) by calculating the interface energy. We also demonstrated mathematical equivalence between the deterministic model described by the Cahn-Hilliard (CH) equation and the probabilistic model framed by the diffusion master equation. On the basis of this demonstration and an efficient KMC algorithm called the next reaction method (NRM), we developed an algorithm namely the free energy biased NRM (FENRM). A computer simulation of the temporal evolution of CNPs as an unstable A-B binary mixture with different initial conditions using the FENRM showed that the proposed algorithm captured most of the spatio-temporal characteristics of spinodal decomposition, such as bifurcation of the dilute/rich concentration morphology and the emergence and growth of an isotropic characteristic length scale. These characteristics representing the temporal evolution of the microstructures were also in quantitative agreement with the results of a conventional theoretical analysis of spinodal decomposition. We also found that the growth of the characteristic length scale seems to have two stages late in the later times of the decomposition. The stages were distinguished by different scaling exponents, indicating the existence of an intermediate stage between the earlier and later stages of decomposition. From the simulation results, we also identified the universality of the temporal evolution of the microstructure, which indicates that the proposed KMC algorithm effectively describes spinodal decomposition. A comparison with numerical experiments based on a finite difference method that also considers the composition-dependent mobility adds additional support for the claim that the proposed KMC algorithm can effectively describe the dynamic properties of spinodal decomposition. We expect that the proposed algorithm can be applied to more complicated dynamic systems involving phase separation of a metastable system governed by a nucleation/growth mechanism and temporal evolution of the microstructures of a multi-phase, multi-component CNPs system. In particular, the proposed KMC algorithm can be actively extended to simulate a phase-separated system of multiple-components that also simultaneously and chemically react either in bulk or at the interface. The KMC algorithm's ability to address this complicated problem is attributed to its intrinsic characteristics, which enable it to addess the stochastic nature of the system. For example, deterministic approaches such as the finite difference method or spectral method are not positively expected to effectively describe a dynamically and stochastically unstable system undergoing phase separation in conjunction with chemical reactions, which would result in bistable steady states. In the future, we plan to present computer simulations of these complicated reaction-diffusion systems under phase separation using the KMC algorithm that we have developed.

3.5. References

[1]. D.T. Gillespie, *J. Comp. Phys.*, **22**, 403 (1976).

[2]. M. Gibson and J. Bruck, *J. Phys. Chem. A*, **104**, 1876 (2000).

[3]. F. Shi, Y. Shim, and J.G. Amar, *Phys. Rev. E*, **76**, 031607 (2007).

[4]. B. Sauerwine, M. Widom, *Phys. Rev. E*, **84**, 061912 (2011).

[5]. J.W. Cahn and J.E. Hilliard, *J. Chem. Phys.*, **28**, 258 (1958);
J.W. Cahn and J.E. Hilliard, *Ibid.* **31**, 688 (1959).

[6]. E.D. Siggia, *Phys. Rev. A*, **20**, 595 (1979).

[7]. Y. Oono and S. Suri, *Phys. Rev. Lett.*, **58**, 836 (1987).

[8]. A.M. Lacast, A.H.Machado, and J.M. Sancho, *Phys. Rev. B*, **45**, 5276 (1992).

[9]. X. Shan and H. Chen, *Phys. Rev. E*, **47**, 1815 (1993).

[10]. S.C. Glotzer, D. Stauffer, and N. Jan, *Phys. Rev. Lett.*, **72**, 4109 (1994).

[11]. S. Toxvaerd, *Phys. Rev. E*, **53**, 3710 (1996).

[12]. E. Sander and T. Wanner, *J. Stat. Phys.*, **95**, 925 (1999).

[13]. J. Zhu *et al.*, *Phys. Rev. E*, **60**, 3564 (1999).

[14]. D.J. Eyre, *Siam J. Appl. Math.*, **53**, 1686 (1993).

[15]. D. Cogswell, *Ph.D. Thesis, M.I.T.* (2010).

[16]. S.A. Serebrinsky, *Phys. Rev. E*, **83**, 037701 (2011).

[17]. H.T. Davis, *'Statistical Mechanics of Phases, Interfaces, and Thin Films'*,
(VCH Publishers Inc., New York, 1996).

[18]. R.W. Balluffi, S.M. Allen, and W.C. Carter, *'Kinetics of Materials'*,
(Wiley-Interscience, Cambridge, MA, 2005).

[19]. J.R. Manning, *Phys. Rev. B*, **4**, 1111 (1971).

[20]. One point that should be mentioned here is that we also observed a statistically acceptable fitting relationship $\lambda \sim (t - 0.4\,\mathrm{s})$ for the assymetric composition case. The statistical significance represented by a correlation coefficient is comparable to that from the power-law fitting. Although it is not shown in this chapter, this finding indicates that a simple linear proportional relation would determine the temporal evolution of separation morphology at later stage of spinodal decomposition when the unstable mixture is relatively close to the critical point. However, the statistical significane for the linear fitting for the symmetric composition case is not as good as the asymmetric composition case is. Further, the statistical significance for the simple linear fitting was not comparable to that from the power-law fitting. Therefore, for the consistency, we provided only power-dependence relationships for the growth of λ for both cases in discussion.

Appendix for Chapter 3. Derivation of Equation (3.14)

To derive eqn.(3.14) , eq.(3.13) can be further simplified by a linear expansion

$$
\begin{aligned}
&\frac{\partial \phi_i(t)}{\partial t} \\
&= \psi\left(1-\phi_i(t)\right)\times \\
&\left[\begin{array}{l}
-2Cl^2\delta\phi\left\{\left(\phi_i(t)+\phi_{i-1}(t)\right)\left.\frac{\partial^2\phi(t)}{\partial x^2}\right|_{\phi_{i-1}(t)}+\left(\phi_i(t)+\phi_{i+1}(t)\right)\left.\frac{\partial^2\phi(t)}{\partial x^2}\right|_{\phi_{i+1}(t)}-\left(\phi_{i-1}(t)+\phi_{i+1}(t)-2\phi_i(t)\right)\left.\frac{\partial^2\phi(t)}{\partial x^2}\right|_{\phi_i(t)}\right\} \\
-6C\delta\phi^2\left(\phi_{i-1}(t)+\phi_{i+1}(t)-2\phi_i(t)\right) \\
+\delta\phi\left\{\left(\phi_i(t)+\phi_{i+1}(t)\right)\left(\left.\frac{\partial\left(f_0/k_BT\right)}{\partial\phi}\right|_{\phi_{i+1}(t)}-\left.\frac{\partial\left(f_0/k_BT\right)}{\partial\phi}\right|_{\phi_i(t)}\right)-\left(\phi_i(t)+\phi_{i-1}(t)\right)\left(\left.\frac{\partial\left(f_0/k_BT\right)}{\partial\phi}\right|_{\phi_i(t)}-\left.\frac{\partial\left(f_0/k_BT\right)}{\partial\phi}\right|_{\phi_{i-1}(t)}\right)\right\}
\end{array}\right] \\
&\simeq \psi\left(1-\phi_i(t)\right)\times \\
&\left[\begin{array}{l}
-2Cl^4\delta\phi\left\{\phi_i(t)\left.\frac{\partial^4\phi(t)}{\partial x^4}\right|_{\phi_i(t)}-\left(\left.\frac{\partial\phi(t)}{\partial x}\right|_{\phi_i(t)}\left.\frac{\partial^3\phi(t)}{\partial x^3}\right|_{\phi_i(t)}\right)\right\}-6Cl^2\delta\phi^2\left.\frac{\partial^2\phi(t)}{\partial x^2}\right|_{\phi_i(t)} \\
+\delta\phi\left\{\left(\left(\phi_{i+1}(t)^2-\phi_i(t)^2\right)\left.\frac{\partial^2\left(f_0/k_BT\right)}{\partial\phi^2}\right|_{\phi_{i+1}(t)}\right)-\left(\left(\phi_i(t)^2-\phi_{i-1}(t)^2\right)\left.\frac{\partial^2\left(f_0/k_BT\right)}{\partial\phi^2}\right|_{\phi_i(t)}\right)\right\}
\end{array}\right] \\
&\simeq \psi\delta\phi l^2\phi_i(t)\left(1-\phi_i(t)\right)\left[-2Cl^2\left.\frac{\partial^4\phi(t)}{\partial x^4}\right|_{\phi_i(t)}+\left.\frac{\partial^2\phi(t)}{\partial x^2}\right|_{\phi_i(t)}\left.\frac{\partial^2\left(f_0/k_BT\right)}{\partial\phi^2}\right|_{\phi_i(t)}\right], \qquad (A3.1)
\end{aligned}
$$

where we ignored second-order terms such as $\delta\phi^2$, $\left(\frac{\partial\phi}{\partial x}\right)^2$, and $\left(\frac{\partial\phi}{\partial x}\right)\left(\frac{\partial^3\phi}{\partial x^3}\right)$. By setting $D^* = \psi l^2\delta\phi$, we find that the approximated master equation, eq.(3.14), is mathematically equivalent to the original CH equation given in eq.(3.6).

Chapter 4

A Self-Consistent Mean-Field Algorithm for Designing Concentration Distribution of Colloidal Suspension of Nanoparticles in Thin Films*

Abstract

Understanding and controlling colloidal dispersion of nanoparticles (CNPs) are essential for transforming them into functional materials. When they are dispersed in thin films, it is also necessary to consider the effects on external confinements by an external field or the chemical selectivity of the surface on the phase separation of CNPs. For studies of molecular interaction, molecular dynamics (MD) or Monte Carlo (MC) simulations can provide useful information about the equilibrium and non-equilibrium properties of the phase separation, which is represented by the spatial distribution of the NP concentration in the film. However, most of simulation approaches are limited, mainly because of the computational demands of describing the dynamics of NPs in a liquid medium in both the spatial and temporal dimensions. In this study, we provide a simple, efficient algorithm based on the self-consistent mean field (SCMF) model for predicting the spatial distribution of the NP concentration in a thin film at equilibrium. The algorithm employs discretized layers along the direction normal to the film and allows the calculation of a thermodynamically optimized distribution of the concentrations of chemically different types of NPs when the molecular interactions among the materials are known. To verify this algorithm, we examined several different cases of CNPs confined in thin films with different externally confining environments and compared the calculation results from the SCMF algorithm with those of 3D MC simulations. Additionally, the algorithm's self-consistency is also supported by a mathematical proof. The comparison revealed that the proposed algorithm provide predictions that showed considerable agreement with those of the MC simulations while enhancing the computational efficiency greatly. We applied the algorithm to

*Parts of Chapter 4 will be submitted to a peer-reviewed journal (Authored by S. Joon Kwon & T. Alan Hatton).

explore the effects of various combinations of parameters such as the film thickness, initial concentration of NPs, and chemical selectivity of the confining walls on the spatial distribution of the NP concentations inside a thin film. The results provided detailed information on the effects of these parameter combinations on the phase separation of CNPs in thin films, which allows one to design functional thin films composed of CNPs with desirable properties by controlling these parameter combinations. We also describe how the present algorithm can be employed to design functional thin films such as a gradient (refractive)-index (GRIN) lens. We expect that the present algorithm can be extended to describe the NP-concentration-dependent material properties in more complicated and diverse environments to efficiently design and control these properties.

4.1. Introduction

Colloidal dispersions of nanoparticles (NPs) have received increasing attention recently, with an emphasis on both fundamental studies and practical applications [1], because of their broad applicability and processability as functional materials in a wide range of disciplines. NP suspensions are tailored to ensure phase and morphological stability in order to develop and discover colloidal suspension of NPs (CNPs) having novel properties [2-17]. In particular, understanding the physical properties of CNPs is a critical step in the further development and application of functional materials. This understanding requires theoretical analysis combined with computational modeling such as molecular dynamics (MD), Brownian dynamics (BD), and Monte Carlo (MC) simulations. A basic theoretical approach to CNPs is thermodynamic analysis focusing on their phase stability, because it is important to control and regulate the stability of the suspension. A thermodynamic understanding allows one to modify and predict the physical properties of the colloidal suspension by controlling variables such as the temperature, concentration, additional stabilizing components such as surfactants, and surface/interface treatments [15,16].

A controllable and useful variable is the number of components in the system, such as the number of chemically different NPs with stabilizers. This variable not only yields multiple-functionalites in the composite materials themselves but also reveals potentially stable phases in which relatively particle-concentrated CNPs do not lose colloidal stability. At a constant temperature, the chemical affinity among the different NPs determines the phase stability of the colloidal suspension, and this affinity is affected by molecular interactions among the NPs. Another variable controlling the phase stability of CNPs is the external confinement, which gives rise to both geometrical and physical boundary conditions. In

particular, confinement by chemical selectivity and/or electric/magnetic fields affects the phase stability of CNPs. It can result in particle-depleted or -concentrated regions near the boundary or throughout the system, depending on the spatial range of the confining effects. For example, CNPs dispersed in a thin film can be selectively phase-separated near the confining substrate, yielding a high concentration gradient in a thin film [18]. Additionally, a colloidal dispersion of charged NPs under a controlled electric field enables the construction of a functional thin film with controllable optical properties [19]. To obtain a thermodynamic understanding of how these variables act to control the phase stability and separation of CNPs, a comprehensive study is required. At the molecular level, the study would need to focus on the many-body properties of the interacting materials in the suspension. In contrast to conventional studies of the phase separation of fluid mixtures in a continuum frame, the effect of the NPs' size and discreteness on their physical properties should be taken into account in the analysis. For instance, particles with sizes of a few tens of nanometers not only behave like hard-sphere particles but also exceed the feature size of liquid molecules by two to four orders of magnitude.

That being said, computational studies based on MD, BD, or MC simulations have been used extensively to understand the dynamics and equilibrium properties of CNPs [20-27]. Computer simulations dealing with CNPs can provide detailed and more robust information about non-equilibrium properties such as the phase separation dynamics [20-27]. These approaches excel when we have information about the molecular interaction among materials rather than bulk-scale thermodynamic information about the mixture. However, most computer simulations dealing with the dynamics of thousands to millions of particles over a relatively long period (up to few milliseconds) require considerable computational resources. For example, a simple 3D box simulating a 100-μm-thick film of CNPs 10 nm in diameter with 10% volumetric fractions requires the tracking of at least 10^6 particles in order to obtain appropriate statistical behaviors of the CNPs. In addition, when the molecular interactions among the particles are relatively long-range such as the dipolar interaction among ionic or magnetic particles, more intensive computational efforts are required. Therefore, it would be preferable to develop and use a more efficient but still effective algorithm when one confine the goal of the study is limited to the calculation of equilibrium properties such as the spatial distribution of the NP concentration in a thin film after a long time. Further, it is preferable that the algorithm can be easily extended to systems with more complicated environments, with variable sizes of NPs, and with larger scales.

In Chapter 4, we propose a simple, efficient algorithm based on the mean-field model to calculate the equilibrium spatial distribution of CNPs in a thin film. By "thin film", we mean that its thickness exceeds the size of the NPs by at least two orders of magnitude. The algorithm's computational scheme is based on the probabilistic distribution of the differential particle concentration at every iteration step over

the entire system along the primary axis (i.e., the direction normal to the film). The probability is determined using the Boltzmann statistics by calculating the free energy of the system. A useful and notable point of the proposed algorithm is that it considers the possibility that the system is saturated. The possibility of saturation suggests that the NPs can build up multiple-layers of close-packed structure such as face-centered cubic (FCC) or hexagonal close-packed (HCP) structures near the confining substrate. The claim that the algorithm is consistent with a self-consistent thermodynamic model is supported by both a mathematical proof and 3D MC simulations. By using the algorithm, we analyzed the phase separation behavior of CNPs in which NPs interact with each other via the Lennard-Jones potential and with the confining substrates via the van der Waals force. The calculation results revealed the effects of the chemical affinity between NPs of two different types and the chemical selectivity against the confining substrate on the spatial distribution of the NP concentration. Taking advantage of the algorithm's computational efficiency, we present detailed simulation results on the effects of different combinations of controllable parameters on the NP concentration profile a thin film. We expect that the proposed algorithm can be widely applied to analysis and understanding of the thermodynamic properties of various types of CNPs confined in thin films and their controllability.

4.2. Theoretical and Computational Framework

We assume a closed 3D system box with the primary axis (i.e., the z -direction) in the canonical ensemble, in which are dispersed N chemically different but geometrically identical (i.e., same size and shape) hard-sphere-like NPs. The primary axis is aligned in the direction of the external field(s) or normal to the geometric confinement surfaces. We employ a discretization scheme to calculate the NP concentration distribution. By using the mean-field approximation, we can estimate the free energy of an individual discrete $x-y$ plane over which the particles are randomly dispersed. For the n th discrete layer, in the absence of external fields, this free energy is physically equivalent to the summation of the potential energies for a single particle of the ith ($i=1,\ 2,\cdots,\ N$) component when it is placed in the layer, namely $U_i^{(n)}$. When particle placement is affected by external factors, the total free energy includes the potential energy from the external field(s) or confinement, which is a function of the position of the discrete layer, $G_i^{(ext)}(n, L_Z)$, where L_Z denotes the system size along the primary axis. The probability of a single particle being located in the n th discrete layer is determined thermodynamically through the Boltzmann distribution.

To calculate $U_i^{(n)}$, we need to consider the particle's interaction potential with other particles in the entire system. For the sake of computational efficiency, however, it is relevant to consider interactions only with other particles in layers that are within a cut-off distance r_C of the layer of interest. In a dimensionless framework, $U_i^{(n)}$ can be represented as

$$U_i^{(n)} = \sum_{j=1}^{N}\left[\int_1^{r_C} 2\pi r g_j^{(n)}(r)\rho_j^{(n)}F_{ij}(r)dr + \sum_{k=-l_C,\neq 0}^{l_C}\left(\int_0^{\left(r_C^2-k^2\right)^{1/2}} 2\pi r g_j^{(n+k)}(r)\rho_j^{(n+k)}F_{ij}(r)dr\right)\right], \qquad (4.1)$$

where $g_j^{(n)}(r)$ and $\rho_j^{(n)}$ denote the 2D (i.e., in the $x-y$ plane) radial distribution function and number density of the particles, respectively, of the j th component in the n th layer. The integer k in the second summation term indicates the k th nearest discrete layer. $F_{ij}(r)$ describes the contributions from inter-particle interactions between the ith and j th component particles to the total free energy. The quantity l_C is the distance to the farthest nearest discrete layers satisfying $l_C \le r_C$. In eq.(4.1), the spatial dimension is normalized with respect to the diameter of the NPs σ. The continuum framework shown in eq.(4.1) requires the functional form of $g_j^{(n)}(r)$ *a priori*; this requirement can be circumvented by using a lattice-based model. For simplicity, the size of the lattice cell can be set to the size of the particles. Discretization of the 2D layer in both the x - and y -directions transforms eq.(4.1) to the form

$$U_i^{(n)} \simeq \sum_{j=1}^{N}\left[\sum_{\xi\le p} M_\xi \rho_j^{(n)}F_{ij}(r_\xi) + \sum_{k=-l_C,\neq 0}^{l_C}\left(\sum_{\zeta\le q_k} M_\zeta \rho_j^{(n+k)}F_{ij}(r_\zeta)\right)\right],\ r_p \le r_C,\ \left(r_{q_k}^{\ 2}+k^2\right)^{1/2} \le r_C, \qquad (4.2)$$

where M_ξ and r_ξ denote the number of and distance to the ξ th-nearest-neighbor lattice cells, respectively, and p and q_k are the maximum values of the indices of neighboring lattice cells to which the distance is not larger than r_C. Specifically, the index q_k is for the lattice cell in the k th-nearest discrete layer. To calculate these indices, without loss of generality, we applied a 3D square lattice model to eq.(4.2), from which we can calculate the distribution probability over the L_Z discrete layers for each of the different particles at constant temperature T,

$$P_i^{(n)} = \exp\left(-\left(U_i^{(n)} + G_i^{(ext)}(n, L_Z)\right)/k_BT\right)/Z_i,\ Z_i = \sum_{k=1}^{L_Z}\exp\left(-\left(U_i^{(k)} + G_i^{(ext)}(k, L_Z)\right)/k_BT\right), \qquad (4.3)$$

where k_B is the Boltzmann constant. To solve the nonlinear equation sets of $U_i^{(n)}$ (or $P_i^{(n)}$) and $\rho_i^{(n)}$ provided in eqs.(4.2) and (4.3), one can try to employ the self-consistent mean field (SCMF) algorithm. However, it incurs a high computational cost to solve several thousand or several ten thousand unknown variables numerically. For example, it is necessary to solve a set of 4×10^3 nonlinear equations for an A-B binary particle mixture dispersed over a thin film composed of 10^3-layers (which corresponds to 10-μm-thick film for 10-nm-size NPs). Instead, we can use a more efficient solution method by introducing the differential particle densities distributed over the entire layer in a thermodynamically self-consistent manner. At every iteration step, the probability is determined on the basis of eq.(4.3). The updated probability directs the spatial distribution of the particle concentrations along the primary direction at the next iteration step, such that $\rho_i^{(n)}(t+1)-\rho_i^{(n)}(t)\propto P_i^{(n)}(t)$. At each iteration, differential increments in the particle concentrations, $\Delta\rho_i$, $i=1,2,\cdots,N$, are provided to the system simultaneously. Iteration stops when the total number density of the particles reaches the objective, $\rho_i^{(eq)}$, which is also equal to the initial number densities, $\rho_i^{(0)}$, $i=1,2,\cdots,N$. Note that the differential particle concentrations for each component should be set to be $\Delta\rho_i=\rho_i^{(eq)}/Iter$, where $Iter$ denotes the total number of iterations, to avoid computational artifacts such as asynchronous distribution of the concentrations of different types of NPs at equilibrium.

The concentration of NPs in each discrete layer is limited. For close-packed hard spheres, the maximum dimensionless number density is unity. When the updated number density of particles in the n th discrete layer exceeds this limit, the n th layer is excluded in the next iteration step because it is saturated. To justify the exclusion of the saturated discrete layers in the calculation algorithm, it is necesary to prove that the particle concentrations in the saturated discrete layers do not change until the unsaturated discrete layers reach equilibrium, i.e., when $\rho_i^{(n)}=\rho_i^{(n,eq)}$. In the appendix, this requirement is proven mathematically in one of the simplest cases, dispersion of a single type of NP in a thin film in which one of the confining walls in the primary direction is an attractive wall and the other is a free surface. On the basis of the model and scheme shown above, the algorithm described below can be used to compute the spatial distribution of the NP concentration in a system at equilibrium.

Table 4.1. A summarized procedure for the self-consistent mean-field (SCMF) algorithm

A Self-Consistent Mean-Field (SCMF) Algorithm for Calculation of the Concentration Distribution of Particles
Step 1. Discretize the system along the z-axis with L_z layers
Step 2. Set initial number densities of particles such that $\rho_i^{(n)} = 0$, $n = 1,2,\cdots,L_z$, $i = 1,2,\cdots,N$
Step 3. Calculate the probability of distribution of particles in the unsaturated discrete layers, $P_i^{(n)}$
Step 4. Distribute the differential concentration of particles, $\Delta\rho_i$, over the unsaturated discrete layers according to $P_i^{(n)}$
Step 5. Update particles concentration in each of the discrete layers such that $\rho_i^{(n)}(t+1) = \rho_i^{(n)}(t) + \Delta\rho_i P_i^{(n)}$.
Step 6. Update potentials for the unsaturated discrete layers $U_i^{(n)}(t+1)$ using $\rho_i^{(n)}(t+1)$
Step 7. Compare the total particles concentration in the layer, $\sum_{i=1}^{N}\rho_i^{(n)}(t+1)$, with the maximum limit of the number concentration of particles in a single discrete layer. If $\forall_n \sum_{i=1}^{N}\rho_i^{(n)}(t+1) \geq 1$, exclude indices of the layers which are saturated in next iteration step
Step 8. For the saturated discrete layers satisfying a condition of $\forall_n \sum_{i=1}^{N}\rho_i^{(n)}(t+1) \geq 1$, fix $\rho_i^{(n,eq)} = \rho_i^{(n)}(t+1)$.
Step 9. Update the number of unsaturated discrete layers in which particles are to be distributed such that $N(t+1) = N(t) - (\text{number of saturated discrete layers})$
Step 10. Iterate by going back to the Step 3 until the total concentration of particles of each type is reached.
Step 11. Obtain concentration distribution of particles in the system at equilibrium
End of Algorithm

In this study, we calculated the spatial distributions of chemically different NPs assuming a no-flux boundary condition in the z-direction (i.e., the system was confined along the primary axis), whereas periodic boundary conditions were applied in both the x- and y-directions. These latter

boundary conditions apply to an infinite thin film confined at the top and bottom by substrates or free surfaces.

4.3. Results and Discussion

4.3.1. Free Energy Model

One of the simplest and most physically relevant models is the Lennard-Jones potential between an individual particle of the ith component in the n th layer and a particle of the j th component in the $(n\pm k)$th layer, $F_{ij}(r_{ij})$, where $r_{ij} = |\mathbf{r_i} - \mathbf{r_j}|$. $F_{ij}(r_{ij})$ is given by

$$F_{ij}(r_{ij}) = 4\varepsilon_{ij}\left[\left(\frac{(\sigma_{ij}/\sigma)}{r_{ij}}\right)^{12} - \left(\frac{(\sigma_{ij}/\sigma)}{r_{ij}}\right)^{6}\right]. \tag{4.4}$$

In eq.(4.4), the effective potential parameters ε_{ij} and σ_{ij} can be expressed using the Lifshitz approximation of the non-retarded van der Waals interaction as follows [28]:

$$\varepsilon_{ij} = \delta_\varepsilon(\varepsilon_i\varepsilon_j)^{1/2},\ \sigma_{ij} = \frac{\delta_\sigma(\sigma_i+\sigma_j)}{2} = \delta_\sigma\sigma, \tag{4.5}$$

where δ_ε and δ_σ are the deviation factors from the ideal arithmetic and geometric averages for the potential well depth ε and particle size σ, respectively. These factors control the phase stability of a mixture of chemically different particles at a given temperature. For the confining walls, we also assumed that a particle of the ith component in the n th layer can interact via the van der Waals potential for a dispersive interaction between a hard sphere and an infinite plane, as follows [28]:

$$G_i^{(ext)}(n, L_Z) = \left(\frac{A_i^{(b)}}{(n-0.5)^3} + \frac{A_i^{(t)}}{(L_Z - n + 0.5)^3}\right), \tag{4.6}$$

where $A_i^{(b)}$ and $A_i^{(t)}$ are the interaction parameters for an individual particle of the ith component with the bottom and top walls, respectively. For the calculations, we assumed that the two particles have the same size but are not spontaneously mixed at room temperature. In particular, we used the following

combination of the molecular interaction parameters for the A and B NPs: $r_C = 3\sigma$, $\varepsilon_{AA} = 2k_BT$, $\varepsilon_{BB} = 2.4k_BT$, $\delta_\varepsilon = 0.75$, and $\delta_\sigma = 1.5$ at $T = 300K$ [29].

4.3.2. Comparison to 3D Monte-Carlo Calculations

In Figure 4.1, we compares the results of a 3D MC simulation and the results calculated using the SCMF algorithm. We examined four different confinement cases of A- and B-type NPs of dilute and relatively high concentrations such that $\left(\rho_{A0}\sigma^3, \rho_{B0}\sigma^3\right) = (0.02, 0.02)$ and $(0.10, 0.10)$, confined in a thin film in the z-direction with $\left[A_A^{(b)}, A_A^{(t)}, A_B^{(b)}, A_B^{(t)}\right]$ and; (1) $k_BT[-1, 0, 1, 0]$ for weak and (2) $10k_BT[-1, 0, 1, 0]$ for strong attractive/repulsive confinements. These values of A_A and A_B are in the range of typical values for inorganic substrates [29]. All the MC simulations were based on the Metropolis Monte Carlo (MMC) algorithm for the random movements of A- and B-NPs in a simulation box with dimensions of $L_X \times L_Y \times L_Z = 50 \times 50 \times 50\sigma^3$, assuming that 2.5×10^3 + 2.5×10^3 (for the case of $\rho_0\sigma^3 = 0.02$) or 1.25×10^4 + 1.25×10^4 (for the case of $\rho_0\sigma^3 = 0.10$) particles move on a 3D square lattice. The MC simulations for each case were ended after 9,500-13,400 iteration steps, when the total free energy of the system had settled to a plateau with small fluctuations (not shown).

A comparison of the calculated number density distributions in the z-direction indicates that the SCMF algorithm predicts the concentration distributions of the two different types of NPs for all four cases considerably well. In particular, the distributions of NPs that are attracted by the confining walls (i.e., A-NPs) show are nearly the same as those predicted by the MC simulations. The formation of build-up layers composed of A-NPs near the bottom surface has been also expected and observed from theory and experiments [30,31]. Cahn introduced the critical-wetting theory for the unstable binary mixture under the surface-direction effects [30]. According to his first-order surface transition theory, unstable phase will maintain its wetting property on the surface if the short-range surface interaction makes the system minimize free energy. And the transition in the wetting is interfered with temperature under the critical point when the composition is fixed. In our case, instead of the temperature, the composition is observed to control the surface-wetting behavior when temperature is fixed. For example, the formation of the build-up layer of A-NPs is observed to be affected by initial concentration (i.e., Figure 4.1(a) vs. (b), (c) vs. (d)).

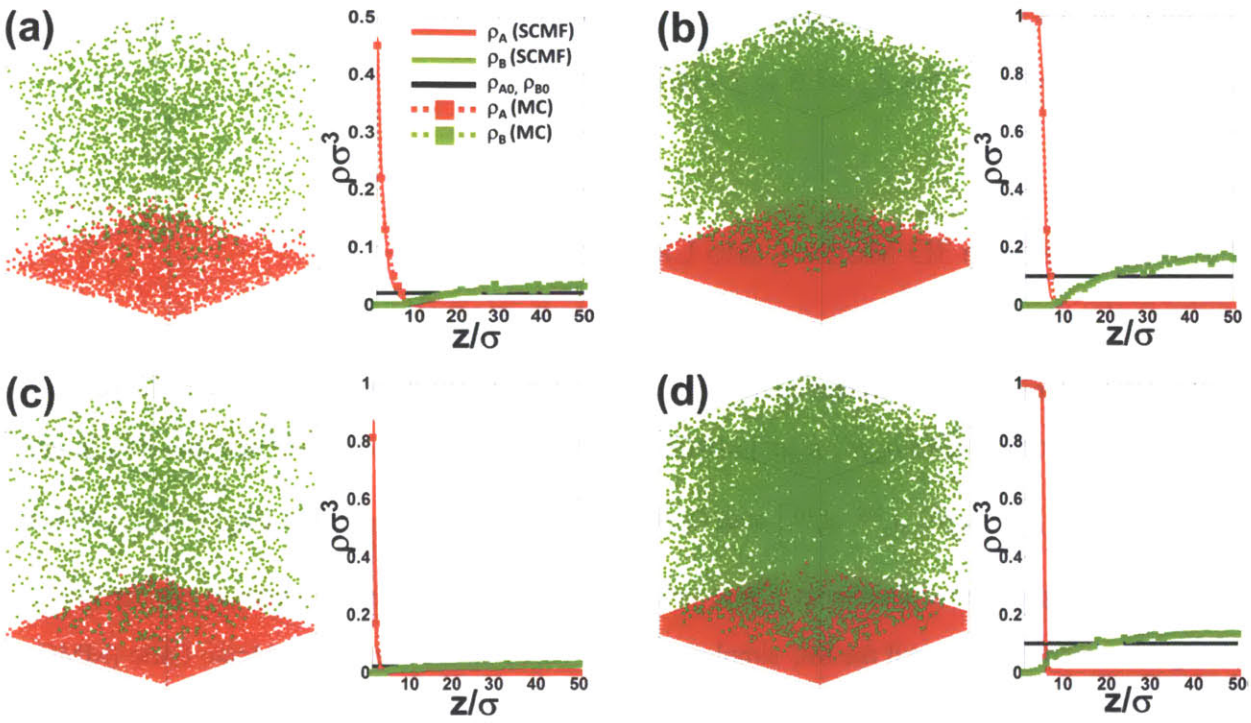

Figure 4.1. Comparison between the calculation results using the self-consistent mean-field (SCMF) algorithm and 3D Metropolis Monte Carlo (MC) simulations for the spatial distributions of A- (red solid for the SCMF and dot lines for the 3D MC) and B-type colloidal NPs (green solid for the SCMF and dot lines for the 3D MC) along the z -direction. Calculations are done with different conditions combined with different strengths of the chemical selectivity ($A^{(b)} = 1$ for the first and $A^{(b)} = 10$ for the second row, respectively.) and different initial densities ($\rho_0\sigma^3 = 0.02$ for the first and $\rho_0\sigma^3 = 0.10$ for the second column, respectively.). For the simulations, each of the NPs were assumed to interact via the Lennard-Jones potential and move on the square lattice in a 3D box with the normalized dimensions of $L_X = L_Y = L_Z = 50\sigma$. For the confinements, the bottom surface was assumed to be attractive to A-NPs while repulsive to B-NPs (i.e., $A_A^{(b)} = -A_B^{(b)}$).

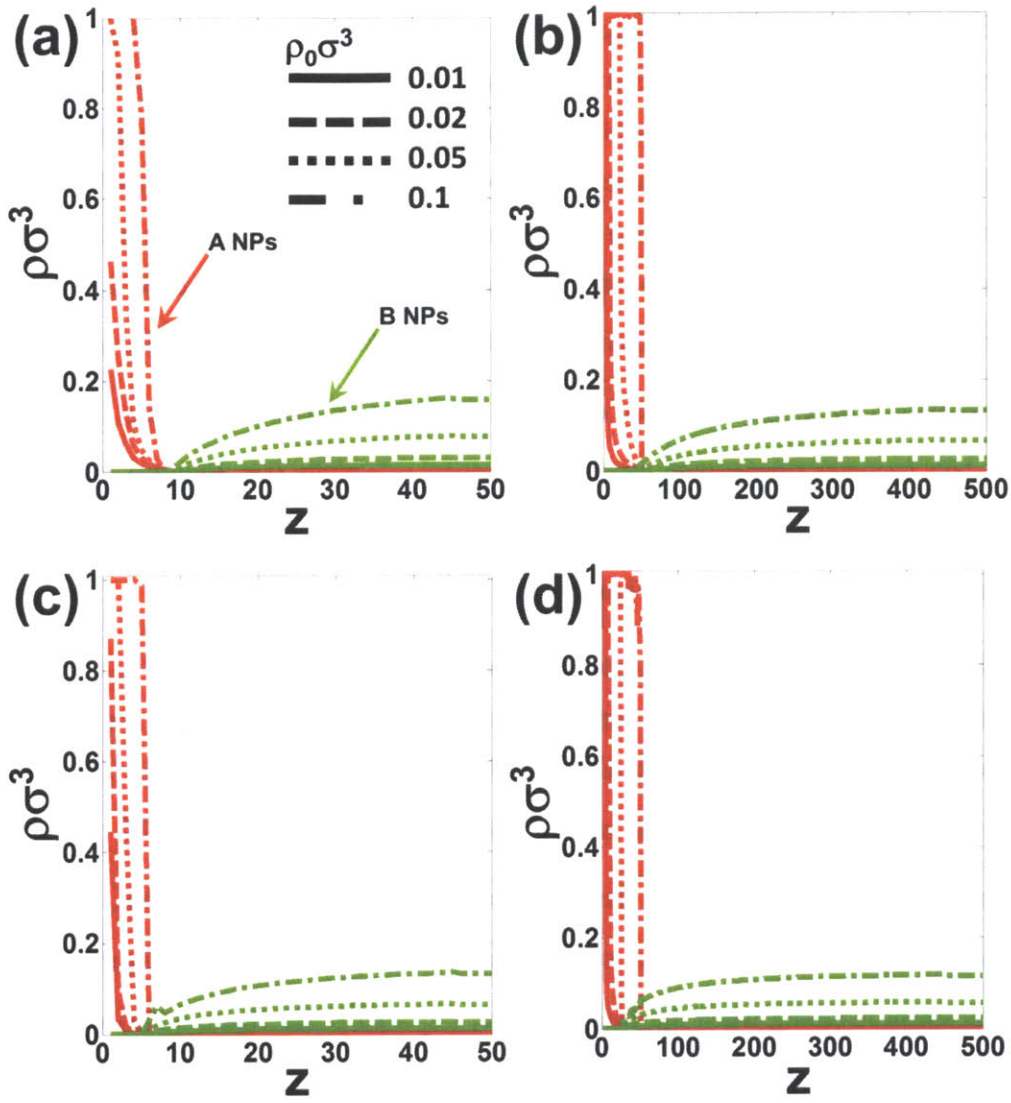

Figure 4.2. Results from the SCMF simulation for the concentration distributions with different ρ_0 and film thickness (L_Z). For the chemical selectivity of the bottom surface, $A^{(b)}=1$ for (a) and (b) and $A^{(b)}=10$ for (c) and (d).

For other type of particle, which feel a repulsive force from the confining walls (i.e., B-NPs), we also find that the SCMF algorithm still captures the critical behavior of the concentration distribution, although there are some discrepancies between the SCMF calculations and MC simulations. Those discrepancies are due mainly to the nature of the repulsive force considered in the MC simulations and the nature of the MC simulations. The particles feeling a repulsive force from the confining walls tend to move away from

the walls and are more or less loosely packed over a wide range of space, whereas particles feeling an attractive force tend to move toward the walls and are packed as closely as possible. An interesting finding from the figure is the formation of built-up layers of NPs attracted by the bottom surface. For instance, both the SCMF and 3D MC simulations show several built-up layers of A-NPs when the initial concentration is relatively high (i.e., Figure 4.1(b) and (d)). We also applied the SCMF algorithm to determine the effects of the initial concentration on the distributions of A- and B-NPs in thin films with different film thickness and surface selectivity combinations. As Figure 4.2 shows, an increase in ρ_0 induces the formation of a built-up layer of A-NPs when $\rho_{A0}\sigma^3 \geq 0.05$. Further, the concentration gradient of A-NPs becomes steeper with increasing chemical selectivity (i.e., Figure 4.2(a) verssus Figure 4.2(c)) as well as with increasing ρ_0. An increase in the film thickness flattens the slope of the concentration distribution of B-NPs (i.e., Figure 4.2(a) versus Figure 4.2(b)).

It would be more interesting to investigate the effects of the compatibility of A- and B-NPs on the NP concentrations distribution. Figure 4.3 compares two cases where A- and B-NPs are incompatible (see Figure 4.3(a) and (b)) and they are relative compatible (see Figure 4.3(c) and (d)). In particular, the compatibility among the A- and B-NPs is controlled mainly by δ_σ : $\delta_\sigma = 1.15$ for the relatively compatible case, whereas $\delta_\sigma = 1.5$ for the incompatible case. First, as expected, the incompatible mixture shows greatly enhanced separation of the NPs near the bottom wall (see Figure 4.3.(a) and (b)), and the enhancement is strong when the film is thicker ($L_z = 10^2\sigma$ for figure 4.3(a) versus $L_z = 10^3\sigma$ for figure 4.3(b)). This indicates that the gradient of concentration of NPs is more gradual for relatively thin film. In addition, the separation is more distinctive across the entire thickness with increasing ρ_0. In contrast, the compatible mixture shows relatively mild separation of the NPs; and the normalized concentration of A-NPs near the bottom wall is smaller than that from the imcompatible case by one or two orders of magnitude. Moreover, the effects of the film thickness is nearly negligible irrespective of ρ_0. From the observations shown in Figure 4.3, the thermodynamic properties of the constituent NPs in CNPs represented by δ_σ can be strategically used for the practical applications in designing functional thin film.

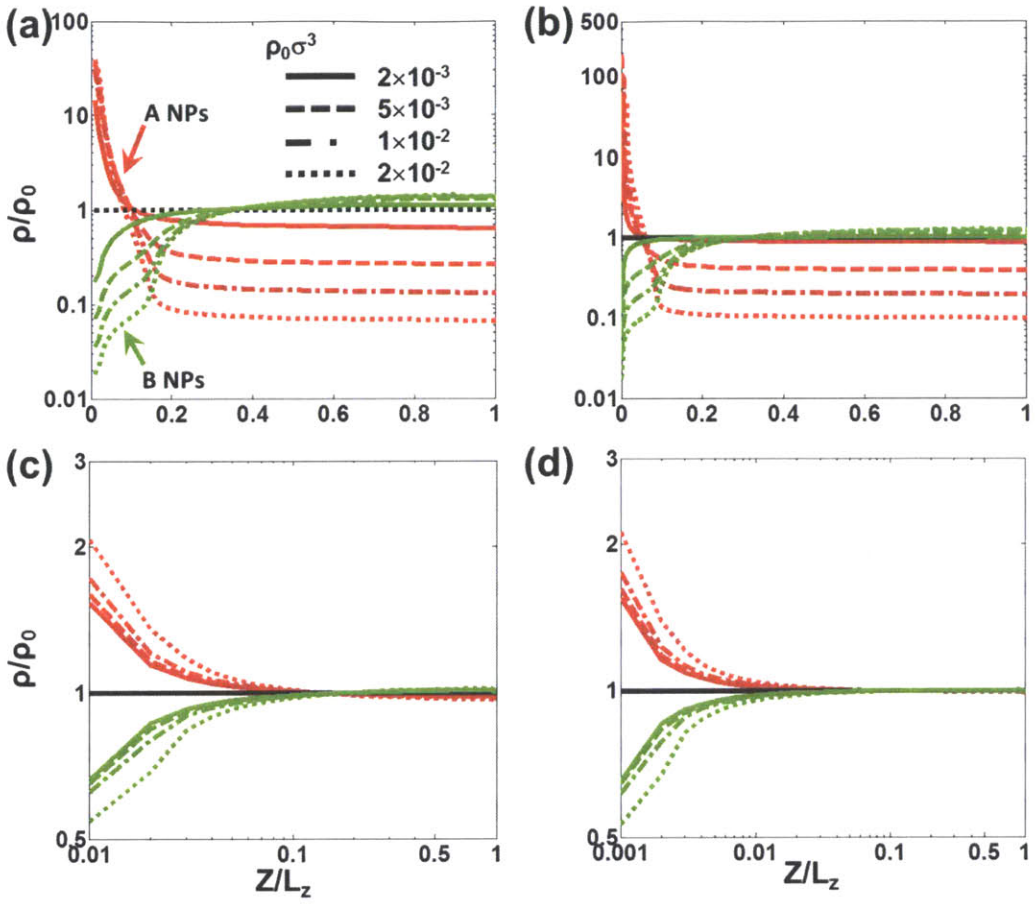

Figure 4.3. Results from the SCMF simulation for the normalized concentration (ρ / ρ_0) distributions as a function of normalized position (z / L_Z) in the film with different ρ_0 and film thicknesses (L_Z) when A- and B-NPs are either incompatible ((a) and (b)) or compatible ((c) and (d)) with the fixed selectivity for the bottom surface at $A^{(b)} = 0.1$. For (a) and (c), $L_z = 10^2 \sigma$, whereas $L_z = 10^3 \sigma$ for (b) and (d).

The computational efficiency is enhanced dramatically (by three to four orders of magnitude) by using the SCMF algorithm (i.e., takes 30-70 s per simulation run for ~$10^{5\text{-}6}$ iterations) rather than the computationally-intensive MC simulations (i.e., 2.5×10^5-4.2×10^5 s) when using a commercially available laptop (i.e., Intel® Core i7™-2820QM 2.30 GHz, 16 GB RAM). Moreover, it is possible to enhance the computational efficiency by optimizing the number of iteration steps for the SCMF simulations. For example, we employed an *Iter* of 5-10×10^5 for the simulations, but this number can be adjusted depending on the system size and initial NP concentrations. Although it is not shown here, we also found that to obtain reliable and stable simulation results, it is best to set *Iter* to be proportional to $L_Z \rho_0$. The

overall agreement between the spatial distributions of the NP concentrations using the two strategies, along with the great increase in computational efficiency, indicates that the proposed SCMF algorithm can be employed extensively in the design of functional materials composed of CNPs to examine a multitude of experimentally controllable parameters in order to modify the properties of the materials. In particular, when the dispersion media are curable materials, the mechanical or optoelectronic properties of a thin film can be adjusted because those properties depend directly upon the spatial distribution of NPs across the film. We provide examples later.

4.3.3. Applications to Controllable Parameters Exploration

One possible use of the proposed efficient algorithm, therefore, is the examination of a variety of conditions that can affect the NP distribution in thin films. For simplicity and to consider the most likely future applications, we can narrow down the experimentally controllable parameters into the following: ρ_0, L_Z, and intensity of the confining walls' chemical selectivity against specific NPs ($A^{(b)}$ and $A^{(t)}$). Instead of the chemical selectivity, the external field strength or another type of measurable external confinement can be used. To quantify the effects of these parameters on the distribution of CNPs in a thin film at equilibrium, we can introduce several useful measurable quantities such as the number density of NPs near the substrate and the free surface (i.e., $\rho_A(n=1)$), $\rho_A(n=L_Z)$, $\rho_B(n=L_Z)$, and $\rho_B(n=L_Z)$). These quantities are directly measurable using methods such as dynamic secondary ion mass spectroscopy, Auger electron spectroscopy, and ellipsometry. Figure 4.4 shows the dependences of these quantities on ρ_{A0}, ρ_{B0}, and L_Z simulated using the SCMF algorithm when the film is confined by an attractive/repulsive bottom wall with a chemical selectivity of $A_A{}^{(b)} = -A_B{}^{(b)} = -1$. As shown in Figure 4.4(a), $\rho_A(n=1)$ is proportional to both ρ_{A0} and ρ_{B0}, and reaches the maximum value of unity when $\rho_{A0}\sigma^3 \geq 0.04$ and $\rho_{B0}\sigma^3 \geq 0.04$ when the film is relatively thin (i.e., $L_Z = 50\sigma$). Interestingly, for a relatively thick film (i.e., $L_Z = 500\sigma$ in Figure 4.4(e)), it is nearly constant ($\rho_A\sigma^3(n=1)=1$) except when the initial concentration of B-NPs is very dilute (i.e., $\rho_{B0}\sigma^3 = 0.01$). In contrast to the results for $\rho_A(n=1)$, those for $\rho_A(n=L_Z)$ show different dependences on ρ_{A0} and ρ_{B0}; it is proportional to ρ_{A0} but inversely proportional to ρ_{B0} when $L_Z = 50\sigma$ (Figure 4.4(b)). When the film is thick, $\rho_A(n=L_Z)$ approaches zero when $\rho_{B0}\sigma^3 \geq 0.05$ (Figure 4.4(f)).

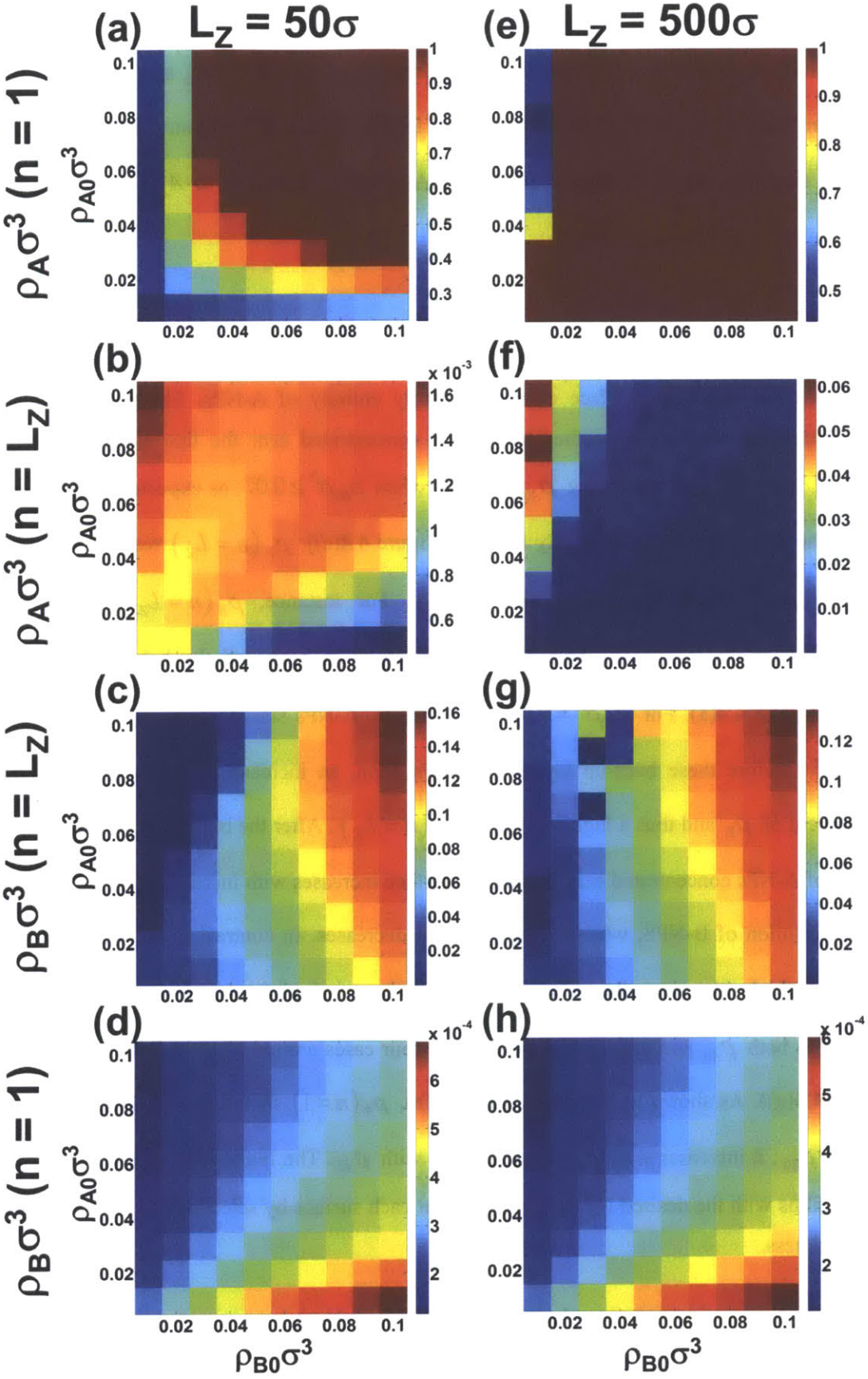
(a) $L_Z = 50\sigma$
(e) $L_Z = 500\sigma$
(b)
(f)
(c)
(g)
(d)
(h)
$\rho_A\sigma^3$ (n = 1)
$\rho_A\sigma^3$ (n = L_Z)
$\rho_B\sigma^3$ (n = L_Z)
$\rho_B\sigma^3$ (n = 1)
$\rho_{A0}\sigma^3$
$\rho_{B0}\sigma^3$
x 10^{-3}
x 10^{-4}
0.02 0.04 0.06 0.08 0.1

Figure 4.4. Simulation results of dependences of densities of A- and B-type colloidal NPs at the bottom and the top surfaces of the thin film on the initial densities of the NPs (ρ_{A0} and ρ_{B0}) with different values of film thickness ($L_Z = 50\sigma$ and $L_Z = 500\sigma$ for the 1st and 2nd columns, respectively). For the confinement, the selectivity of the bottom surface for A- and B-NPs was set to $A_A^{(b)} = -1$ and $A_B^{(b)} = 1$, respectively.

This is an interesting finding because we can control the film thickness to obtain a film with one surface lacking A-NPs and the other surface composed nearly entirely of A-NPs. The particles that feel a repulsive force from the bottom surface tend to be concentrated near the free surface. In particular, $\rho_B(n = L_Z)$ increases with increasing ρ_{A0} and ρ_{B0} when $\rho_{B0}\sigma^3 \geq 0.07$, as expected (see Figures 4.4(c) and (g)). If the film thickness is relatively thin (see Figure 4.4(c)), $\rho_B(n = L_Z)$ reaches the maximized values when $\rho_{B0}\sigma^3 \leq 0.06$ at certain value of ρ_{A0}. For instance, $\rho_B(n = L_Z)$ is maximized at $\rho_{A0}\sigma^3 \sim 0.05$ when $\rho_{B0}\sigma^3 = 0.04$. This can be understood in terms of the behavior of $\rho_A(n = 1)$ observed in Figure 4.4(a). For $\rho_{B0}\sigma^3 = 0.04$, for example, A-NPs start to form a built-up layer when $\rho_{A0}\sigma^3 \geq 0.05$. Before these built-up layers of A-NPs form, an increase in ρ_{A0} would give rise to a steeper gradient of ρ_B and thus a higher value of $\rho_B(n = L_Z)$. After the built-up layers of A-NPs form, the number of A-NPs concentrated near the bottom surface increases with increasing ρ_{A0}. This will cause a flatter distribution of B-NPS, whereby $\rho_B(n = L_Z)$ decreases. In contrast to the case of a relatively thin film, the thick film case shows a simpler dependence of $\rho_B(n = L_Z)$ on ρ_{A0} and ρ_{B0}: it is proportional to both ρ_{A0} and ρ_{B0} except for three or four cases around $\rho_{A0}\sigma^3 \sim 0.09$ and $\rho_{B0}\sigma^3 \sim 0.035$ (see Figure 4.4(g)). As shown in Figures 4.4(d) and (h), $\rho_B(n = 1)$ shows nearly identical dependences on ρ_{A0} and ρ_{B0}; it increases with ρ_{B0} but decreases with ρ_{A0}. The findings from Figure 4.4 help us to design thin films with the desired NP concentrations at each surface by selecting the inital concentrations and film thickness.

Figure 4.5 summarizes the dependence of $\rho_A(n=1)$, $\rho_A(n=L_Z)$, $\rho_B(n=L_Z)$, and $\rho_B(n=1)$ on different values of $A^{(b)}$ and L_Z when the initial concentrations of A- and B-NPs are identical ($\rho_{A0}=\rho_{B0}=\rho_0$). Figure 4.5(a) shows the effect of the chemical selectivity on the formation of the built-up layer of A-NPs when $L_Z=200\sigma$. Except when $\rho_0\sigma^3=0.01$, a built-up layer of A-NPs (i.e., $\rho_A\sigma^3(n=1)=1$) always exists regardless of the chemical selectivity. For $\rho_0\sigma^3=0.01$, additionally, increasing the chemical selectivity contributes to an increase in $\rho_A(n=1)$. When the chemical selectivity is fixed at $A^{(b)}=1$, the built-up layer of A-NPs forms more easily as the film thickness increases (see Figure 4.5(e)). For $\rho_A(n=L_Z)$, it is notable that the increase in the rate of $\rho_A(n=L_Z)$ as a function of ρ_0 grows with decreasing chemical selectivity when the film thickness is fixed (see Figure 4.5(b)), whereas the rate is nearly identical for different values of L_Z when $A^{(b)}$ is fixed (see Figure 4.5(f)). Interestingly, the growth rate and the value of $\rho_B(n=L_Z)$ as a function of ρ_0 reach maximum values at an intermediate chemical selectivity (i.e., $A^{(b)}=1$ in Figure 4.5(c)). This finding may imply the existence of a critical chemical selectivity beyond which the chemical selectivity would interfere with the concentration of B-NPs at the free surface. This can be explained by the fact that a too-weak selectivity of the confining substrates is less affected by the effects of particle crowding at higher concentrations. This will result in a proportional relationship between the chemical selectivity and $\rho_B(n=L_Z)$. However, beyond the critical chemical selectivity, an increasing number of A-NPs will join to form the built-up layer near the attractive bottom surface; therefore, the distribution profile of B-NPs will be flatter, decreasing the value of $\rho_B(n=L_Z)$. With increasing film thickness, $\rho_B(n=L_Z)$ decreases (see Figure 4.5(g)) indicating that B-NPs are driven less intensively to the free surface as the fiml thickness increases. Similar to the finding from the growth rate of $\rho_A(n=L_Z)$ as a function of ρ_0 for different values of the chemical selectivity, $\rho_B(n=1)$ is less varied for a stronger chemical selectivity and nearly zero when $A^{(b)}\geq 5$ (see Figure 4.5(d)). When we fix the chemical selectivity and vary the film thickness, $\rho_B(n=1)$ exhibits a nearly identical growth rate with respect to ρ_0 (see Figure 4.5(h)). Interestingly, $\rho_B(n=1)$ is reduced with increasing film thickness, whereas $\rho_A(n=L_Z)$ shows the opposite behavior with respect to the film thickness (see Figure 4.5(f)).

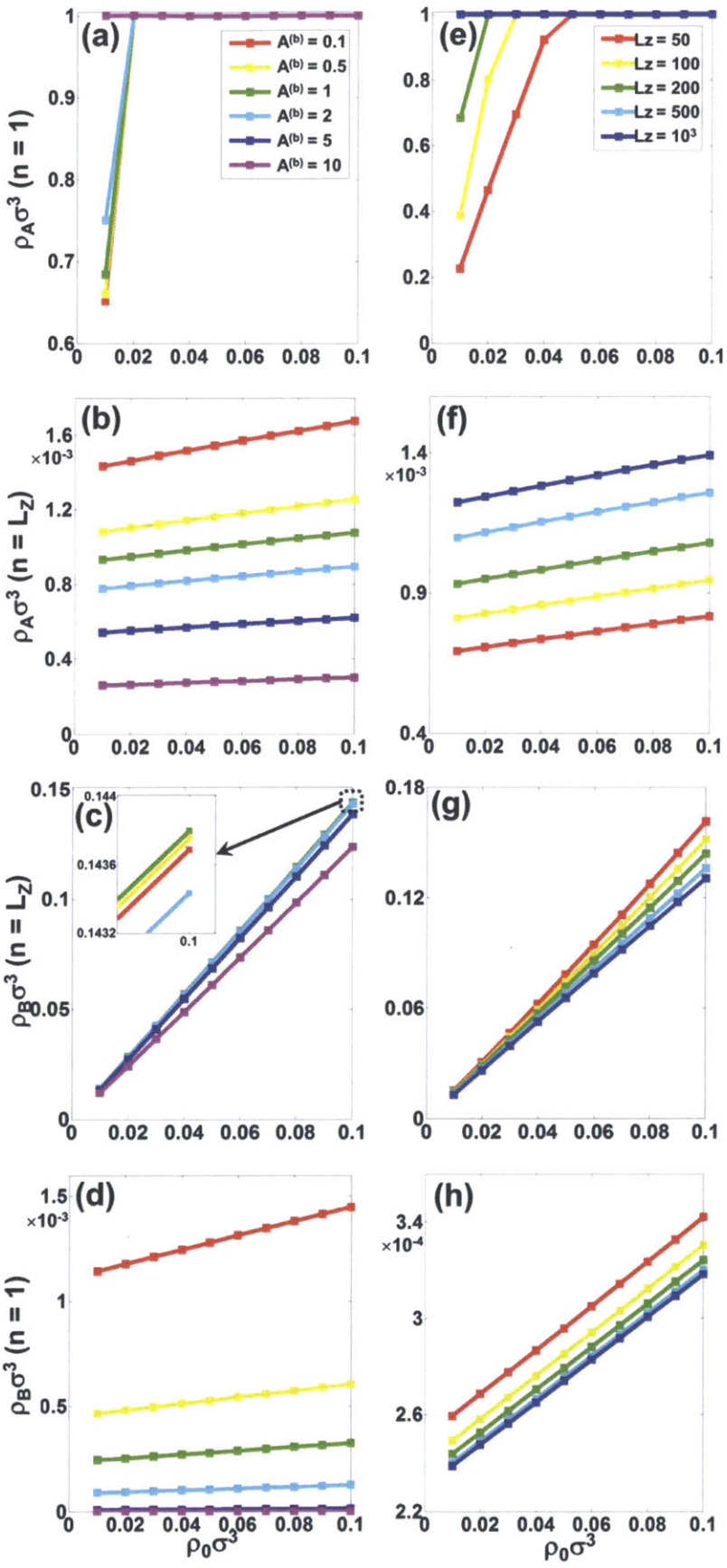
(a)
(b)
(c)
(d)
(e)
(f)
(g)
(h)
$A^{(b)} = 0.1$
$A^{(b)} = 0.5$
$A^{(b)} = 1$
$A^{(b)} = 2$
$A^{(b)} = 5$
$A^{(b)} = 10$
Lz = 50
Lz = 100
Lz = 200
Lz = 500
Lz = 10^3
$\rho_A\sigma^3$ (n = 1)
$\rho_A\sigma^3$ (n = L_Z)
$\rho_B\sigma^3$ (n = L_Z)
$\rho_B\sigma^3$ (n = 1)
$\rho_0\sigma^3$
$\rho_0\sigma^3$
×10⁻³
×10⁻³
×10⁻³
×10⁻⁴

Figure 4.5. Simulation results of dependences of densities of A- and B-type colloidal NPs at the bottom and the top surfaces of the thin film as a function of the initial density ($\rho_0 = \rho_{A0} = \rho_{B0}$). On the left column, effects of different $A^{(b)}$ are shown with fixed film thickness of $L_Z = 200\sigma$. On the right column, effect of different L_Z are shown with fixed chemical selectivity such that $A^{(b)} = 1$.

4.3.4. Applications to Designing Optically Functional Thin Films

From the exploration of the different parameters that can control spatial distribution of CNPs illustrated in Figures 4.4 and 4.5, we can obtain detailed information for designing a thin film composed of CNPs with a desired concentration profile within a reasonable computation time. In particular, considering that the proposede algorithm is based on information on the molecular interaction among NPs when they are dispersed in a liquid medium, a promising application is the control of the concentration profiles of a single type of NPs that have two or more different chemical groups on the surface. For example, it has been experimentally reported that the surfaces of many metallic or metal-oxide NPs can be modified by either hydrophobic, or hydrophilic, or amphiphilic organic compounds [2-17]. Detailed information on the interactions among those organic compounds on the surfaces of NPs can be obtained by experiments or computer simulations; therefore, it is possible to construct a thin film inside of which the concentration profile of a single type of NPs can be varied by surface treatments. In addition, the effects of the external field intensity on the variation in the concentration profile can be examined when one of the NPs is a dipolar interacting type such as ionic or magnetic NPs. Further, we can easily extend the proposed algorithm to efficient computational design of more complicated and advanced functional thin films with NPs of three or more different types. For instance, a representative result for the concentration distributions of A, B, and C-NPs in a ternary particle mixture dispersed in a liquid medium is shown in Figure 4.6(a), assuming that those particles are spontaneously demixed and the film confinement is symmetric (i.e., attractive for A-, repulsive for B-, and inert for C-NPs, respectively). As a practical example of this NP mixture, we can consider a colloidal dispersion of Au, TiO_2, and Ag NPs confined between two alkanethiol-coated surfaces.

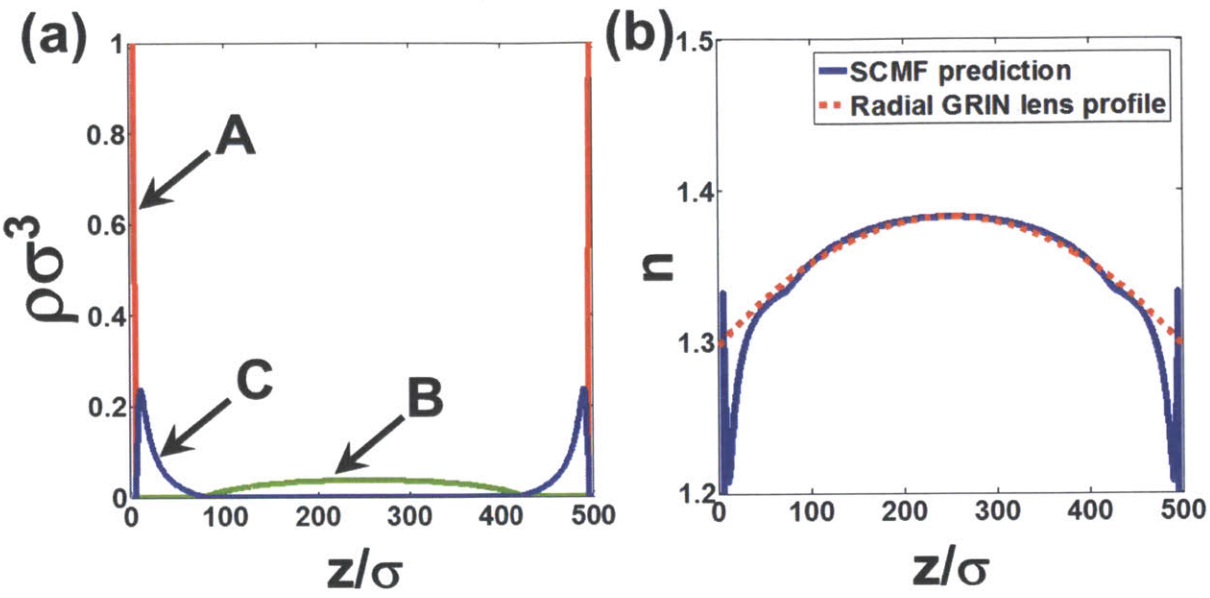

Figure 4.6. (a) Result obtained from the SCMF simulation for concentration distribution of A, B, and C-NPs with $\rho_{A0}\sigma^3 = \rho_{B0}\sigma^3 = \rho_{C0}\sigma^3 = 0.02$ in thin film of thickness $L_Z = 500\sigma$. For the selectivity, the ternary NPs mixture is assumed to be demixed and A feels an attractive ($A^{(b)} = A^{(t)} = -1$), B feels a repulsive force ($A^{(b)} = A^{(t)} = 1$) from the bottom surface, while C is inert. (b) Predicted profile of the refractive index distribution inside the thin film (blue solid line) based on the concentration calculation in (a) assuming that A is Au, B is TiO_2, and C is Ag NPs dispersed in aqueous solution. For the comparison, the distribution profile of the refractive index of the ideal radial type gradient refractive index (GRIN) lens calculated by least square fit (fitting range: $0.1L_Z \le z \le 0.9L_Z$) is provided (red dot line).

In this case, the formation of a concentrated layer of Au NPs is preferable to the formation of other NP layers near the confining surfaces. Ag NPs are attracted to the surfaces less than Au but more than TiO_2, which will produce a repulsion effect on the TiO_2 NPs due to crowing. For simplicity, we assumed that the A, B, and C NPs have identical initial sizes and densities (i.e., $\rho_A\sigma^3 = \rho_B\sigma^3 = \rho_C\sigma^3 = 0.02$) when dispersed in a thin film of $L_Z = 500\sigma$, which corresponds to several tens of micrometers when the NPs are several tens of nanometers in diameter. As the figure shows, the A-NPs form built-up layers near the confining surfaces; however, the B- and C-NPs show continuous concentration distribution profiles. More interestingly, we can apply the calculation of the concentration distributions of a ternary NP mixture to the calculation and design of the optical properties of thin films. The densities can be converted into the volume fraction, ϕ, and, the effective refractive index n_{eff} can be calculated as:

$$n_{eff}{}^2 = \sum_{k=A,B,C,S} \phi_k n_k{}^2, \tag{4.7}$$

where n_k denotes the refractive index of the k -NPs and the subscript S represents the dispersion medium. In practical applications, $n_A = 0.17$, $n_B = 2.57$, $n_C = 0.18$, and $n_S = 1.33$, for incident light with a wavelength of 540 nm when the dispersion medium is an aqueous solution. By using eq.(4.7), we can convert the concentration distribution information in Figure 4.6(a) into the refractive index distribution information, as shown in Figure 4.6(b). Interestingly, the concentration profile reaches the maximum value at the center of the film, suggesting that thin films with a concentration gradient might be employed as gradient (refractive) index (GRIN) lenses [30,31]. To construct a radial type GRIN (R-GRIN) lens, the desired refractive index distribution profile is described as [31]

$$n_{eff}(z) = \eta\left(z - \frac{L_Z}{2}\right)^2 + n_M, \tag{4.8}$$

where n_M is the maximumrefractive index, and η .is the gradient coefficient. As shown in Figure 4.6(b), the distribution profile of n_{eff} over 80% of the entire thin film (i.e., $50 \le z/\sigma \le 450$ out of $0 \le z/\sigma \le 500$) can be effectively fitted with the desired profile function in eq.(4.8) for $n_M = 1.38$ and $\eta = 1.38 \times 10^{-6}$ with the least-square fitting method. For an ideal R-GRIN lens, the lens performance is measured using the focal length of the lens, f_L, which is predicted to be [31]

$$f_L = \left(n_M \eta^{1/2} \sin\left(L_p \eta^{1/2}\right)\right)^{-1}, \tag{4.9}$$

where L_p denotes the distance of the incident light through the lens. In the present case of a ternary NP mixture, $f_L \sim 1.4 L_Z$, assuming $L_p \sim 10^2 L_Z$. This focal length ranges from a few to a few tens of micrometers depending on the size of the NP, and indicates that the incident light can be focused with micrometer-scale resolution. This also indicates the potential application of a thin film with a concentration gradient as an endoscope device, in which a R-GRIN lens without surface curvature can be easily implemented. Because of the mathematical validity of the proposed SCMF algorithm, confirmation by comparisons with 3D MC simulations, as well as its strongly enhanced computational efficiency and potential applications in functional thin films, it can be employed for wider applications in functional material design and combined with other types of numerical calculation or simulations to extract critical material properties.

4.4. Conclusions

In Chapter 4, we presented an efficient algorithm based on the self-consistent mean field (SCMF) model for calculating the spatial distribution of the NP concentration. The algorithm includes an iterative update of the NP concentrations in discrete layers along the thickness direction. It also considers the possibility of saturation of the discrete layers with NPs; the algorithm excludes the saturated discrete layers during the iterative updates. This exclusion is justified by a mathematical proof. For verification, we applied the algorithm to calculate the spatial distribution of concentrations of spontaneously non-mixing (phase-separating) A- and B-NPs dispersed in a thin liquid film confined in the thickness direction. The simulations employed the Lennard-Jones potential among the NPs and the van der Waals force between the NPs and the confining substrates. The calculated results were compared with those of 3D lattice-based Metropolis Monte Carlo (MMC) simulations with different types of thin film confinement. The comparison revealed that the results of the proposed algorithm agreed with those of the MMC simulations, and the computational efficiency was greatly enhanced. The effects of controllable parameters, such as the film thickness, initial NP concentration, and intensity of the chemical selectivity of the confining substrates, on the variation in the NP concentration profile in the thin film were intensively analyzed using the SCMF algorithm. The simulations demonstrated that NPs that feel an attractive force from the bottom substrate are concentrated near the substrate, whereas those that feel a repulsive force form a concentration gradient along the thickness direction. From the simulation results, we could conclude that the proposed SCMF algorithm can be extensively applied to the design of functional thin films composed of CNPs with desirable physical properties by computationally obtaining the relevant combination of controllable parameters. To provide a sense of the practical application of the algorithm, we expanded the study to the analysis of the concentration distributions of A, B, and C NPs in a ternary mixture dispersed in a liquid medium and illustrated their possible applicability as optical devices such as a GRIN lens with micrometer-scale focal length resolution for use in medical examinations. We expect that the proposed algorithm could easily be extended to more complicated suspensions containing multiple types of NPs of various sizes and to systems with different geometries as well as thin films.

4.5. Reference

[1]. G. Schmid (*Ed.*), *'Nanoparticles: From Theory to Application', 2nd Ed.* (John Wiley & Sons, New York, 2004).

[2]. R.H. Ottewill, *Langmuir*, **5**, 4 (1989).

[3]. S.M. Ilett, A. Orrock, W.C.K. Poon, and P.N. Pusey, *Phys. Rev. E*, **51**, 1344 (1995).

[4]. B. Vincent, J. Edwards, S. Emmett, and R. Croot, *Colloids Surface*, **31**, 167 (1986).

[5]. A.P. Gast, W.B. Russel, and C.K. Hall, *J. Colloid Interface Sci.*, **109**, 161 (1986).

[6]. M.H.G. Duits, R.P. May, A. Vrij, and C.G. de Kruif, *Langmuir*, **7**, 62 (1991).

[7]. H.N.W. Lekkerkerker, W.C.K. Poon, P.N. Pusey, A. Stroobants, and P.B. Warren, *Europhys. Lett.*, **20**, 559 (1992).

[8]. S.Y. Kang and K. Kim, *Langmuir*, **14**, 226 (1998).

[9]. A.M. Jackson, J.W. Myerson, and F. Stellacci, *Nat. Mater.*, **3**, 330 (2004).

[10]. A. Centrone, E. Penzo, M. Sharma, J.W. Myerson, A.M. Jackson, N. Marzari, and F. Stellacci, *Proc. Nat'l. Acad. Sci.,* **105**, 9886 (2007).

[11]. O.M. Bakr, B.H. Wunsch, and F. Stellacci, *Chem. Mater.*, **18**, 3297 (2006).

[12]. O. Uzun, *Chem. Comm.,* **196-198**, 10.1039 (2008).

[13]. E. Dubois, V. Cabuil, F. Boue, and R. Perzynski, *J. Chem. Phys.* **111**, 7147, (1999).

[14]. C.F. Tejero, A. Daanoun, H.N.W. Lekkerkerker, and M. Baus, *Phys. Rev. Lett.*, **73**, 752 (1994).

[15]. W.M. Gellbart, R.P Sear, J.R. Heath, and S. Chaney, *Farad. Disc.*, **112**, 299 (1999).

[16]. G.M. Whitesides and B. Grzybowski, *Science*, **270**, 1335 (1995).

[17]. E. Rabani, D.R. Reichman, P.L. Geissler, and L.E. Brus, *Nature*, **426**, 271 (2003).

[18]. J. Kim, H. Yang, and P.F. Green, *Langmuir*, **28**, 9735 (2012).

[19]. T.S. Shim *et al.*, *Adv. Mater. (Weinheim)*, **22**, 4494 (2010).

[20]. P. Tandon and D.E. Rosner, *J. Coll. & Inter. Sci.*, **213**, 273 (1999).

[21]. O. Iglesia and A. Labarta, *Phys. Rev. B*, **63**, 184416 (2001).

[22]. D. Mukherjee, C.G. Sonwane, and M.R. Zachariah, *J. Chem. Phys.*, *119*, 3391 (2003).

[23]. A.Y. Sinyaing A. Belov, Z. Tang, and N.A. Kotov, *J. Phys. Chem. B*, **110**, 7500 (2006).

[24]. Y. Qin and K.A. Fichthorn, *J. Chem. Phys.*, **119**, 9745 (2003).

[25]. S. Izvekov, A. Violo, and G.A. Voth, *J. Phys. Chem. B*, **109**, 17019 (2005).

[26]. H. Zhang and J.F. Banfield, *Nano Lett.*, **4**, 713 (2004).

[27]. M. Luo *et al.*, *Langmuir*, **22**, 6385 (2006).

[28]. J.N. Israellachivili, *'Intermolecular and Surface Forces', 2nd ed.* (Academic Press, New York, 1992).

[29]. J.N. Canongia Lopes, *Phys. Chem. Chem. Phys.*, **4**, 949 (2002).

[30]. J.W. Cahn, *J. Chem. Phys.*, **86**, 3667 (1977).

[31]. R.B. Heady and J.W. Cahn, *J. Chem. Phys.*, **58**, 896 (1973).

[31]. E. Hecht, '*Optics*', *4th ed.* (Addison-Wesley Longman Inc., New York, 2002).

[32]. E.W. Marchand, '*Gradient Index Optics*', (Academic Press, New York, 1978).

Appendix for Chapter 4. Mathematical proof for the exclusion of particles-saturated discrete layers in the iterative update of particles concentration

For simplicity, let us assume that the system is a dispersion of a single type of particles in a thin film that is confined by walls along the primary direction (i.e., the z -direction) of which the bottom one is attractive to the particles, whereas top one is a free surface. In this simple case, we can safely consider that the first discrete layer right next to the bottom substrate is the first one which is saturated with the particles. In other words, at time t, the first layer is a monolayer of close-packed particles satisfying $\rho^{(1)}(t)=1$. Then the total free energy of the system, $H_T(t)$, can be written as:

$$H_T(t)=\sum_{n=2}^{L_Z}\rho^{(n)}(t)\left(\frac{U^{(n)}(t)}{2}+G^{(ext)}(n)\right)+\left(\frac{U^{(1)}(t)}{2}+G^{(ext)}(1)\right). \tag{A4.1}$$

Let us define two different scenarios: (1) scenario A where there is no flux of particles out of the saturated discrete layer (the first layer) during differential time Δt, and (2) scenario B where the saturated discrete layer loses differential amount of particle concentrations, $\Delta\rho_C$, during Δt.

First, the total free energy of the system at time $t+\Delta t$ for scenario A, $H_T^{(A)}(t+\Delta t)$, is

$$H_T^{(A)}(t+\Delta t)=\sum_{n=2}^{L_Z}\left(\rho^{(n)}(t)+\Delta\overline{\rho^{(n)}}^{A}(t)\right)\left(\frac{U^{(n)}(t+\Delta t)}{2}+G^{(ext)}(n)\right)+\left(\frac{U^{(1)}(t)}{2}+G^{(ext)}(1)\right),$$

$$\Delta\overline{\rho^{(n)}}^{A}(t)\equiv\Delta\rho\Delta t P_A^{(n)}(t), P_A^{(n)}(t)=\exp\left(-\left(U^{(n)}(t)+G^{(ext)}(n)\right)/k_BT\right)/Z_A(t),\ Z_A(t)=\sum_{k=2}^{L_Z}\exp\left(-U^{(k)}(t)/k_BT\right),$$

$$U^{(n)}(t)=\sum_{k=-l_C}^{l_C}\rho^{(n+k)}(t)f^{(n+k)}, f^{(n+k)}\equiv\int_0^{\left(r_C^2-k^2\right)^{1/2}}2\pi r g^{(n+k)}(r)F(r)dr. \tag{A4.2}$$

Then, by using notations in eq.(A4.2), $U^{(n)}(t+\Delta t)$ is written as:

$$U^{(n)}(t+\Delta t)=U^{(n)}(t)+\sum_{k=-l_C}^{l_C}\Delta\overline{\rho^{(n+k)}}^{A}(t)f^{(n+k)}. \tag{A4.3}$$

We can simplify $H_T^{(A)}(t+\Delta t)$ by employing a linearized distribution of $\rho^{(n+k)}(t)$ around $\rho^{(n)}(t)$ $\rho^{(n+k)}(t) \approx \rho^{(n)}(t) + k\varepsilon(t)$, where $\varepsilon(t)$ denotes the discrete form of the slope of the particle concentration along the primary axis, assuming that the cut-off distance is sufficiently short to make the value of l_C relatively small (i.e., $l_C = 3$ when the molecular interaction among particles is described by the Lennard-Jones potential). Therefore, $U^{(n+k)}(t)$ is simplified as

$$U^{(n+k)}(t) \approx U^{(n)}(t) + k\varepsilon(t)\Phi_n,\ \Phi_n = \sum_{p=-l_C}^{l_C} f^{(n+p)}.$$

Without loss of generality we can employ an exponential decay model for the external potential from the attractive bottom wall $G^{(ext)}(n) \sim a\exp(-bn)$. Then, by using the simplified form of $U^{(n+k)}(t)$, $\Delta\overline{\rho^{(n+k)}}^{A}(t)$ in eq.(A4.3) is expressed as:

$$\begin{aligned}
\Delta\overline{\rho^{(n+k)}}^{A}(t) &= \Delta\overline{\rho^{(n)}}^{A}(t)\exp\left(-\frac{\left(U^{(n+k)}(t) - U^{(n)}(t)\right)}{k_B T}\right)\exp\left(-\frac{\left(G^{(ext)}(n+k) - G^{(ext)}(n)\right)}{k_B T}\right) \\
&\simeq \Delta\overline{\rho^{(n)}}^{A}(t)\exp\left(-\frac{k\varepsilon(t)\Phi_n}{k_B T}\right)\exp\left(\frac{abk\exp(-bn)}{k_B T}\right) \\
&\simeq \Delta\overline{\rho^{(n)}}^{A}(t)\left(1 - \frac{k\varepsilon(t)\Phi_n}{k_B T} + \frac{abk\exp(-bn)}{k_B T}\right).
\end{aligned} \tag{A4.4}$$

In eq.(A4.4), the second-order difference term is ignored. Using eq.(A4.4), eq.(A4.3) can be further simplified as follows

$$U^{(n)}(t+\Delta t) \simeq U^{(n)}(t) + \Delta\overline{\rho^{(n)}}^{A}(t)\sum_{k=-l_C}^{l_C}\left(1 - \frac{k\varepsilon(t)\Phi_n}{k_B T} + \frac{abk\exp(-bn)}{k_B T}\right)f^{(n+k)} = U^{(n)}(t) + \Delta\overline{\rho^{(n)}}^{A}(t)\Phi_n, \tag{A4.5}$$

where we used symmetric properties of the system along the primary axis $f^{(n+k)} = f^{(n-k)}$. Using eqs.(A4.3)-(A4.5), eq.(A4.2) can be further simplified as:

$$\begin{aligned}
H_T^{(A)}(t+\Delta t) &= \sum_{n=2}^{L_Z}\left(\rho^{(n)}(t) + \Delta\overline{\rho^{(n)}}^{A}(t)\right)\left(\frac{U^{(n)}(t) + \Delta\overline{\rho^{(n)}}^{A}(t)\Phi_n}{2} + G^{(ext)}(n)\right) + \left(\frac{U^{(1)}(t)}{2} + G^{(ext)}(1)\right) \\
&\simeq H_T^{(A)}(t) + \sum_{n=2}^{L_Z}\Delta\overline{\rho^{(n)}}^{A}(t)\left(\frac{\rho^{(n)}(t)\Phi_n + U^{(n)}(t)}{2} + G^{(ext)}(n)\right),
\end{aligned} \tag{A4.6}$$

in which the term involving second-order difference is ignored.

Similarly, we can find the total free energy of the system in scenario B at time $t+\Delta t$, $H_T^{(B)}(t+\Delta t)$. From eq.(A4.2),

$$H_T^{(B)}(t+\Delta t)=\sum_{n=1}^{L_Z}\left(\rho^{(n)}(t)+\Delta\overline{\rho^{(n)}}^{B}(t)\right)\left(\frac{U^{(n)}(t+\Delta t)}{2}+G^{(ext)}(n)\right)$$
$$=\sum_{n=1}^{L_Z}\left(\rho^{(n)}(t)+\Delta\overline{\rho^{(n)}}^{B}(t)\right)\left(\frac{U^{(n)}(t)+\Delta\overline{\rho^{(n)}}^{B}(t)}{2}+G^{(ext)}(n)\right), \qquad (A4.7)$$

With an expression for $\Delta\overline{\rho^{(n)}}^{B}(t)$,

$$\Delta\overline{\rho^{(n)}}^{B}(t)\equiv\Delta\rho\Delta tP_B^{(n)}(t)\simeq\Delta\overline{\rho^{(n)}}^{A}(t)+\Delta\rho_C P_A^{(n)}(t)-\Delta\rho\Delta tP^{(1)}(t),$$
$$P_B^{(n)}(t)=\exp\left(-\frac{\left(U^{(n)}(t)+G^{(ext)}(n)\right)}{k_BT}\right)/Z_B(t),\ Z_B(t)=\sum_{k=1}^{L_Z}\exp\left(-\frac{U^{(k)}(t)}{k_BT}\right),$$

eq.(A4.7) is further simplified into

$$H_T^{(B)}(t+\Delta t)=H_T^{(A)}(t+\Delta t)+\sum_{n=1}^{L_Z}\left(\Delta\rho_C P_A^{(n)}(t)-\Delta\rho\Delta tP^{(1)}(t)\right)\left(\frac{U^{(n)}(t)+\rho^{(n)}(t)\Phi_n}{2}+G^{(ext)}(n)\right)$$
$$\geq H_T^{(A)}(t+\Delta t)+(\Delta\rho_C-\Delta\rho\Delta t)\sum_{n=1}^{L_Z}P_A^{(n)}(t)\left(\frac{U^{(n)}(t)+\rho^{(n)}(t)\Phi_n}{2}+G^{(ext)}(n)\right), \qquad (A4.8)$$

where we used the fact that $P_A^{(n)}(t)\leq P^{(1)}(t)$; the lower the free energy the sooner the discrete layer is saturated with particles. As eq.(A4.8) indicates, increasing $\Delta\rho_C$ gives rise to an increase in the difference between $H_T^{(B)}(t+\Delta t)$ and $H_T^{(A)}(t+\Delta t)$; therefore, the system in scenario B tries to minimize $\Delta\rho_C$ so as to minimize the total free energy. When $\Delta\rho_C$ approaches zero, $H_T^{(B)}(t+\Delta t)$ converges to $H_T^{(A)}(t+\Delta t)$ because $P^{(1)}(t)$ also approaches zero. Therefore, scenario A is always energetically preferred to scenario B. This indicates that once a discrete layer is saturated with particles, there is no fluctuation in the particle concentrations in that saturated layer.

This scheme can easily be extended to other types of system including multi-component particles and confinements with the different functional forms of $G^{(ext)}(n)$. For example, we can safely exclude saturated discrete layers from the concentration update for a colloidal suspension of A and B NPs whether they are chemically favored to each other or not. First, if they are compatible, a similar logic can show

that the particles flux from the saturated layers (i.e., exchange of differential amount of A-particle concentration with B-particle concentraiton or vice versa) is energetically less probable. Second, if A- and B-particles are incompatible, it takes an additional energetic cost to make the flux of particles by exchanging differential amounts of A- or B-particles in the saturated layers. This results in lower probability of the particles flux from the saturated layers relative to the event without the particles flux. Similarly, the exclusion principle of the saturated layers during the concentration update using the SCMF algorithm in Chapther 4 can be applied to three or more different types of component mixture of CNPs in a liquid dispersion medium. Therefore, we can verify that the saturated discrete layers can be excluded from the calculation process to update the spatial distribution of particle concentrations along the primary axis.

Chapter 5

Fabrication of Functional Thin Films Comprised by Gradually Concentrated Colloidal Nanoparticles Driven by Magnetic Field*

Abstract

The preparation of CNPs in the form of thin films is a desirable method for applications that use CNPs as functional materials. Further, it is more interesting when the film contains a heterogeneous mixture of two or more different constituent CNPs to tailor concentration-dependent physical properties. To demonstrate experimentally the computational and theoretical research described in the previous chapters, we provide proof-of-concept experimental results on the control of the concentration distribution of a binary CNP mixture in thin films. For the CNPs, we employed Fe_3O_4 superparamagnetic NPs and non-magnetic SiO_2 NPs dispersed in UV-curable thin films such as acrylate monomers. To quantitatively measure the concentration distribution along the thickness direction of a thin film, we used spectroscopic methods such as microspectrophotometry, and compared the experimentally measured concentration profile to the results of simulations based on the self-consistent mean field (SCMF) model. The profile is also verified by spectroscopic analysis along different measurement directions. We observed good agreements between the simulation results and the experimental measurements in terms of the verified data from a comparison of two different spectroscopic measurement directions. We suggest that this research would be applicable to the preparation of optically functional materials such as gradient (refractive) index (GRIN) lenses for biomedical applications to replace the aging crystal lens in the eyes. The experimental ideas and approaches in this chapter are easily extended to more complicated cases involving a ternary mixture of CNPs in either a liquid or polymeric thin film, as demonstrated by calculations of the desired properties based on the SCMF simulations.

---

*Parts of Chapter 5 will be submitted to a peer-reviewed journal (Authored by S. Joon Kwon & T. Alan Hatton).

5.1. Introduction

In recent decades, research on nanoparticles (NPs), including both fundamental studies and practical applications [1-3], has been extended to various fields. In particular, metallic or inorganic NPs have attracted interests owing to their optical properties, such as relatively low refractive indices for transition metal NPs (i.e., Au, Ag, Pt, etc.) and relatively high refractive indices for metal-oxide NPs (i.e., ITO, silica, iron oxide, etc.) [4-13]. Regarding industrial applications, then, it is natural how to control and process the NP-related optical properties. One answer to this question has two parts: 1) dispersion of the NPs in desirable media and 2) processing the NP-dispersions in the form of thin films. These approaches consider the processability associated with reliable controllability of the NP-dispersion-related physical properties. In preparing well-dispersed NPs, one can use the NP concentration as one of the main control parameters. Further, after preparing an NP-dispersed thin film, one can expect to apply the material in a variety of useful cases such as micro-scale devices or parts for assembled structures. As we have explored in the previous chapters, colloidal NPs (CNPs) are a promising form of dispersion meeting the processability and controllability requirements for using NPs. In addition, they would show more potential when we can control the assembly structure and dynamics of CNPs in thin films for further applications.

Superparamagnetic magnetite iron oxide Fe_3O_4 NPs are a type of inorganic CNPs [4-7,9,12-15]. Experimental reports have shown that control measures involving field-assisted methods [4,5,7,12,14-15] and a micro-fluidic-assisted approach [9] are plausible and facile for manipulating the assembly structure and dynamics of magnetic CNPs. Owing to their magnetic susceptibility, a variety of external magnetic fields have been more aggressively considered as a reliable tool for controlling the assembly structure and dynamics of magnetic CNPs [4,5,7,12,14,15]. However, most of the experimental realizations of the controlled assembly and phase separation of Fe_3O_4 NPs focused on a homogeneous mixture of CNPs: -a binary mixture of NPs and a solvent. By introducing additional CNPs that are not miscible with Fe_3O_4 CNPs, one can expect wider applications exploiting the controlled physical properties produced by controlled assembly of heterogeneous CNPs. Therefore, it is highly desirable to discover whether the external-stimuli-assisted assembly of a binary mixture of CNPs in a thin film is feasible by experimental realization and quantitative analysis of of the assembly structure. For the realization, in particular, it would be necessary to measure the concentrations distribution of the binary mixture of CNPs in the thin film. This is because the concentration determines most of the physical properties of fluidic phase mixtures.

Kim *et al.* [8] recently reported the experimental realization of a controlled distribution of metallic CNPs in a polymeric thin film by introducing the concept of tailoring the thin film into different layers in which the spatial distribution of the CNPs is manipulated to be heterogeneous. They then extended the work to controlling the refractive index of the thin film using a controlled spatial distribution of the NP concentration. In a similar but more resourceful way, we propose experimental methods of realizing controlled spatial distributions of the concentrations of a binary mixture of CNPs in thin films in Chapter 5. Additionally, we propose that desirable physical properties based on the spatial distribution of the NP concentrations, such as the refractive index of the thin film, can be predicted using the self-consistent mean field (SCMF) algorithm suggested in Chapter 4. By combining experimental and computational work, we present a possible and plausible application of the prepared thin films as optically functional materials. We expect that this research in Chapter 5 would enable the use of a variety of combinations of CNPs in thin films for other functional materials, such as materials with a mechanical strength gradient or those composed of a set of layers with different conductivities.

5.2. Experimental Details

5.2.1. Preparation of NPs

To prepare two different NPs that will be separated asymmetrically by an external field, we employed Fe_3O_4 and SiO_2 NPs. To synthesize Fe_3O_4 CNPs, we first mixed 56 mmol $FeCl_2{\cdot}4H_2O$ (Sigma Aldrich) in 25 ml of deionized water (1.8 mS/m, Milipore) [6]. The aqueous solution was then heated to 80°C under a N_2 gas (99.99%, Air Gas) purge for 1-2 h. After heating, the solution was cooled to room temperature, and the cooled solution was sonicated for 10 min to disperse the as-synthesized NPs. After sonication, 30 ml of 0.33 M of tetramethylamonium hydroxide (TMAOH, Sigma Aldrich) was added and the solution was re-sonicated for 1 min. Second, to synthesize SiO_2 NPs, we employed the well-known Stöber method [16,17]. Specifically, 2 ml of 28 wt% NH_4OH (Sigma Aldrich) combined with 50 ml of ethanol (99.9%, VWR) was dispersed in 6.76 g of deionized water (1.8 mS/m, Milipore) at room temperature. Using a magnetic stirrer, the mixture was mixed for 2 hs at room temperature; 0.28 M of tetraethyl orthosilicate (TEOS, Sigma Aldrich) was then added to the mixture, followed by magnetic stirring for 2 hs. Figures 5.1 and 5.2 show bright-field transmission electron microscopy (TEM, JEOL 200CX accelerated at 200 kV) images of the as-prepared Fe_3O_4 and SiO_2 NPs.

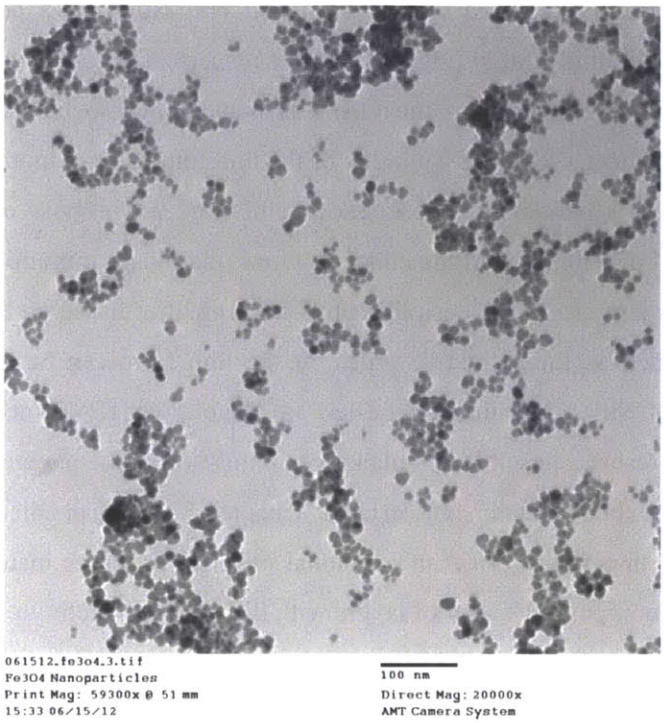

Figure 5.1. A TEM image of the synthesized Fe_3O_4 NPs

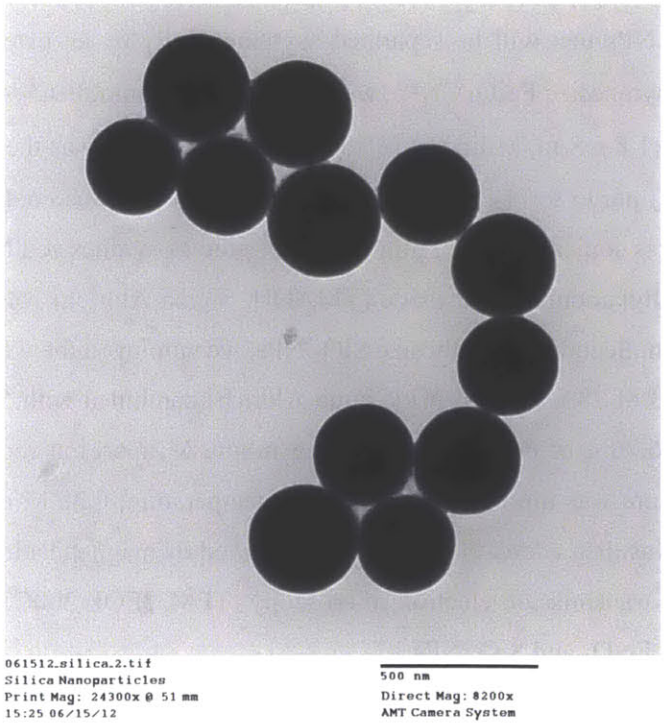

Figure 5.2. A TEM image of the synthesized SiO_2 NPs

Their average sizes are 19.8 ± 1.3 nm and 248.9 ± 18.1 nm for the Fe_3O_4 and SiO_2 NPs, respectively. The size was measured using an image analysis software (imaging software ImageJ®).

5.2.2. Preparation of a UV-Curable Thin Film

To prepare a thin film that can be cured by UV irradiation, we employed a monomer solution of (Poly(ethylene glycol) diacrylate (PEGDA), Sigma Aldrich) and a curing agent (2-Hydroxy-2-methylpropiophenone (2,2-HMPP), Sigma Aldrich) [11,14,15,18]. Figure 5.3. shows the molecular structures of PEGDA and 2,2-HMPP.

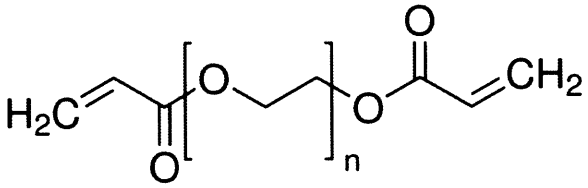

Poly(ethylene glycol) diacrylate (PEGDA)

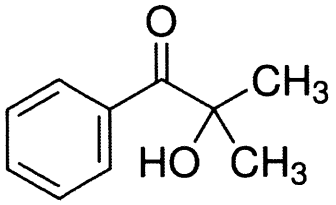

2-Hydroxy-2-methylpropiophenone (2,2-HMPP)

Figure 5.3. Molecular structures of the dispersion media (Poly(ethylene glycol) diacrylate (PEGDA)) and curing agent (2-Hydroxy-2-methylpropiophenone (2,2-HMPP))

The polymerization mechanism of PEGDA is essentially radical polymerization in which the curing agent works as a photoinitiator to induce initiation, which is followed by propagation and termination. To induce polymerization, we irradiated the solution with UV light at a wavelength of $\lambda = 280 - 310$ nm for 0.5-5 hs. Figure 5.4 shows the curing dynamics of PEGDA-2,2-HMPP aqueous solutions at room

temperature with different initial PEGDA concentrations and curing agent concentrations. As expected from radical polymerization kinetics [14,15,18,19], increases in the acrylic monomer concentration and curing agent ratio give rise to fast curing dynamics of the film (or a decrease in the curing time). Although it is not reported here, we also found that above a certain threshold concentration of the acrylic oligomer (i.e., 16 wt% of PEGDA monomer), the films showed wrinkles or other morphological deformations such as rupturing. Therefore, we employed an aqueous solution of 12 wt% PEGDA monomer combined with 2 wt% of 2,2-HMPP to obtain fast curing dynamics of the dispersion medium. We also observed volumetric shrinkage in the cured PEGDA thin films after UV-curing, with a 25-30 vol% reduction. For example, there was 27.8 volumetric% reduction when we used the 12 wt% PEGDA monomer combined with 2 wt% of 2,2-HMPP aqueous solution at $\lambda = 280 - 310$ nm for 1 hs. Notably, the volumetric reduction after UV-irradiation was isotropic (i.e., 10.19 vol%, 10.35 vol%, and 10.28 vol% reductions in the x -, y -, and, z -direction respectively). The thickness of the cured thin film was measured by an optical microscope.

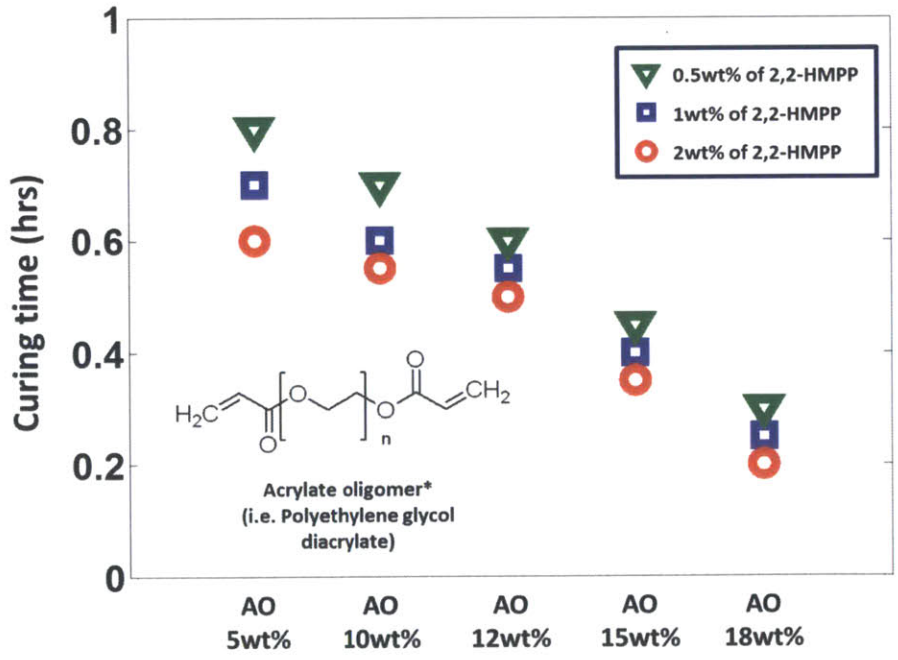

Figure 5.4. Curing dynamics of dispersion media (PEGDA) with different concentrations of the curing agent (2,2-HMPP)

5.2.3. Preparation of Thin Films CNPs Forms Concentration Gradient Inside

To form a concentration gradient of CNPs, we applied an external magnetic field of $0.018\ T$. A commercially available lab-scale bar-type magnet (VWR) was employed to generate a gradient magnetic field along the film thickness direction (i.e., the z-direction). To control the strength of the magnetic field, we used a transparent slide cover glass $130\ \mu m$ in thickness, under which the bar magnet is placed. A specific number of glasses was vertically accumulated to increase the thickness of the substrate, L_S, and we examined the effect of the external magnetic field strength on the formation of the NP concentration gradient in the film by controlling the screening effects of the substrate (i.e., done by varying the L_S, $L_S = 130\ \mu m$ and $L_S = 1.40\ mm$). Before the UV-curing, we mixed Fe_3O_4 CNPs and SiO_2 CNPs prepared as a dispersion in an aqueous solution with a desirable initial concentration typically smaller than 5 wt%. The mixture of the CNPs and the dispersion medium in the aqueous solution was well dispersed in an ultrasonicator for 20 min. The mixed aqueous solution was then poured into a polydimethylsiloxane (PDMS) well. The well was cylindrical with a diameter of 5 mm and a depth of 3-5 mm. To prepare the PDMS well, we mixed PDMS (Sylgard 184, Dow Chemical) monomers with a curing agent, and the PDMS was cured on a Si substrate with a cylindrical protrusion for 24 h [20,21]. Before providing UV irradiation, we allowed the CNPs and UV-curable dispersion medium to undergo phase separation induced by an external magnetic field in the PDMS well by placing the bar magnet under the substrate for 0.5-1 h. Next, we supplied UV irradiation and obtained a cured thin film 1-2 mm thick. Figure 5.5 shows a schematic of the experimental setup.

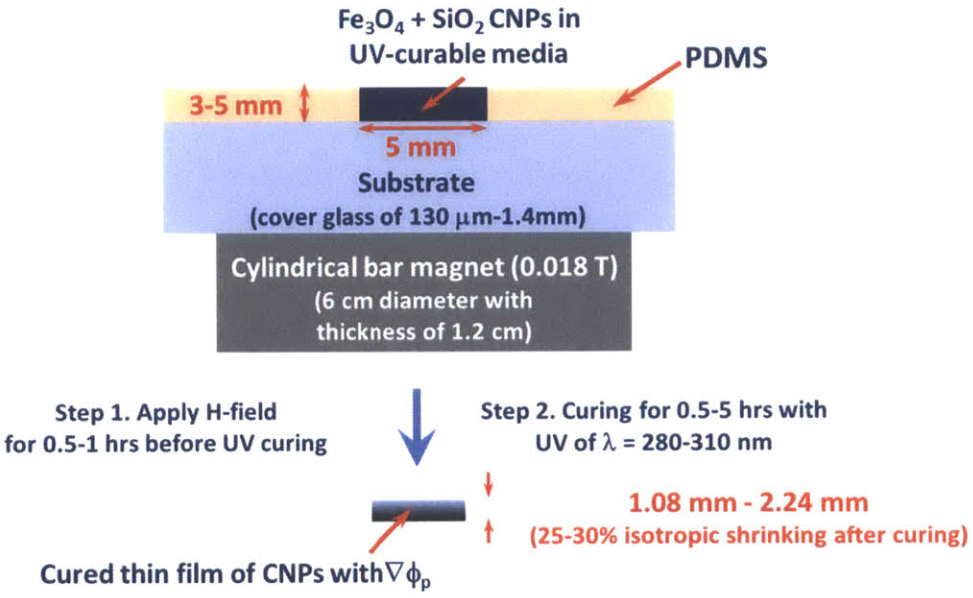

Figure 5.5. A schematic diagram for the experimental setting for the fabrication of a thin film inside which the concentration distribution of Fe_3O_4 and SiO_2 CNPs is controlled

5.2.4. Analysis of NP Concentration Profile

To quantitatively measure the NP concentration profiles inside the cured thin films, several techniques can be applied, such as dynamic secondary ion mass spectroscopy (D-SIMS), Auger electron spectroscopy (AES), and ellipsometry [8]. The most significant problem with using these methods is that they are typically limited to measuring the concentration over a spatial domain of at most 100 nm in a batch analysis. The measurement domain scale can be extended to 10 μm when ellipsometry is used. However, it is experimentally and practically nearly impossible to separate a thin film into unit thin films with thicknesses of 100 nm to 10 μm; therefore, these techniques are not suitable for films with thickness of a few millimeters in terms of practical application. In this study, instead, we employed a microspectrophotometer (μUV-Vis, CRAIC 20VM), which combines an optical microscope and UV-Vis spectrometer. By employing this device, it is possible to examine a local area with a maximum spatial resolution of up to 10×10 μm^2. In the actual examination, we employed a spatial resolution of 20×20 μm^2 on the basis of the suggested optimized device set-up to maximize the signal-to-noise ratio of the UV-Vis absorbance signal. The spatial resolution is determined by the resolution of the optical microscope and condenser lens. Figure 5.6 shows a schematic and a picture of the μUV-Vis spectrometer used in this study.

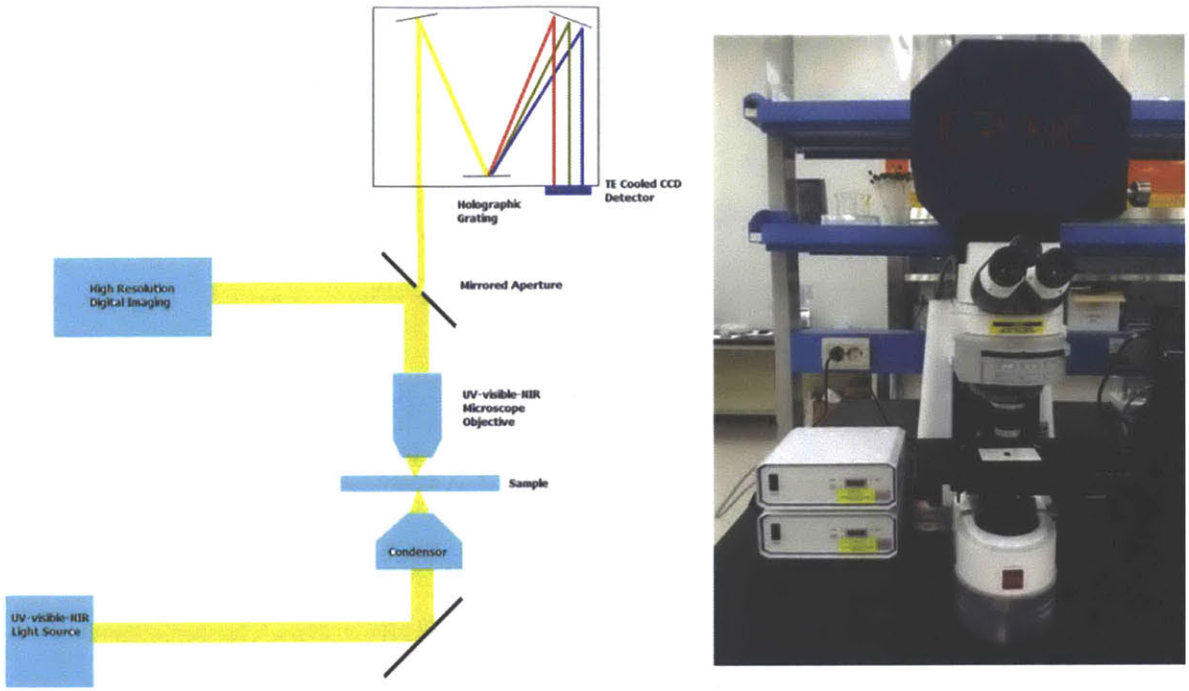

Figure 5.6. A schematic diagram of a microspectrophotometer (μUV-Vis) combined with an optical microscope (left) and a picture of the employed model of a μUV-Vis (model: CRAIC 20VM) (right). The original images are from http://www.microspectra.com/.

The other parts of the μUV-Vis spectrophotometer are similar to those of a typical UV-Vis spectrometer such as the double-beam UV-Vis spectroscope, in which incident light at a specific wavelength is divided into two sources, one for the sample and the other for the reference solvent (i.e., deionized water). The transmitted light from the sample and the reference solvent is gathered and integrated to calculate the calibrated transmittance and absorbance signals. In this UV-Vis spectroscopy scheme, the signal-to-noise ratio is increased by canceling out the unknown or hidden systematic and experimental erroneous signals or noise from the background. The absorbance of CNPs measured by UV-Vis spectroscopy at a specific incident wavelength λ, $A(\lambda)$, is defined as

$$A(\lambda) \equiv \log\left(\frac{I_0}{I}\right) = d\sum_{i=1}^{N_C} \varepsilon_i(\lambda) C_i^{\beta_i} = d\sum_{i=1}^{N_C} \overline{\varepsilon_i}(\lambda) \phi_i^{\beta_i},\ \overline{\varepsilon_i}(\lambda) \equiv \varepsilon_i(\lambda) / \upsilon_i^{\beta_i}, \tag{5.1}$$

where I is the intensity of the light with an initial intensity of I_0, d is the path length of the light, N_C is the number of components in the dispersion, ε is the molecular absorptivity, β is the nonlinear

attenuation exponent, υ is the molecular volume, and ϕ is the volumetric fraction. Further, ε and $\bar{\varepsilon}$ are proportional to the extinction cross-sectional area, $\sigma(\lambda)$ (i.e., $\sigma(\lambda)=\varepsilon(\lambda)\log 10$), which can be expressed using the Mie scattering coefficients for scattering of an electromagnetic wave by a hard-sphere-like particle as a function of the radius R and refractive index n of the particle [22,23]:

$$\begin{aligned}
&\sigma(\lambda)\simeq\frac{6\pi}{|k|^2}\mathrm{Re}(a_L+b_L),\ k\equiv\frac{2\pi\kappa_D{}^{1/2}}{\lambda},\\
&a_L\equiv\frac{\bar{n}\psi_L(\bar{n}kR)\psi_L'(kR)-\psi_L'(\bar{n}kR)\psi_L(kR)}{\bar{n}\psi_L(\bar{n}kR)\chi_L'(kR)-\psi_L'(\bar{n}kR)\chi_L(kR)},\\
&b_L\equiv\frac{\psi_L(\bar{n}kR)\psi_L'(kR)-\bar{n}\psi_L'(\bar{n}kR)\psi_L(kR)}{\psi_L(\bar{n}kR)\chi_L'(kR)-\bar{n}\psi_L'(\bar{n}kR)\chi_L(kR)},
\end{aligned}\tag{5.2}$$

where $\bar{n}=n/n_D$, and ψ_L and χ_L are the spherical Riccati-Bessel functions [24]. In addition, κ_D and n_D are the dielectric function and refractive index, respectively, of the dispersion medium. For eq.(5.2), we used the first electric dipole term approximation ($L=1$) considering $R<<\lambda$ for typical NPs. For a dilute solution, β is nearly unity (also known as the Beer-Lambert law), whereas it diverges from unity as the solute concentration increases [25]. Because β depends on the particle aggregation and dispersion properties, we can safely assume that it is constant with respect to λ. For eq.(5.1), the absorbance is assumed to be the collective (or additive) property consisting of contributions from the absorbance of each component. This principle can be applied to double-beam UV-Vis spectroscopy as follows:

$$\begin{aligned}
&A_M(\lambda)\equiv\log\left(\frac{I_0}{I_M}\right)=d\left[\varepsilon_S(\lambda)\phi_S{}^{\beta_S}+\varepsilon_P(\lambda)\phi_P{}^{\beta_S}\right],\\
&A_R(\lambda)\equiv\log\left(\frac{I_0}{I_R}\right)=d\varepsilon_S(\lambda),\\
&\rightarrow I_M=I_R\exp\left(-d\left(\varepsilon_S(\lambda)\left(\phi_S{}^{\beta_S}-1\right)+\varepsilon_P(\lambda)\phi_P{}^{\beta_S}\right)\right)\simeq I_R\exp\left(-d\varepsilon_P(\lambda)\phi_P{}^{\beta_S}\right),
\end{aligned}\tag{5.3}$$

where the subscripts M, P, and S indicate the mixture, particles, and reference solvent, respectively. In eq.(5.3), we assumed that the sample is composed of homogeneous particles and a solvent for the construction of the calibration curve. We also assumed that $\varepsilon_S(\lambda)$ is negligible compared to $\varepsilon_P(\lambda)$. Figure 5.7 shows a schematic of double-beam UV-Vis spectroscopy.

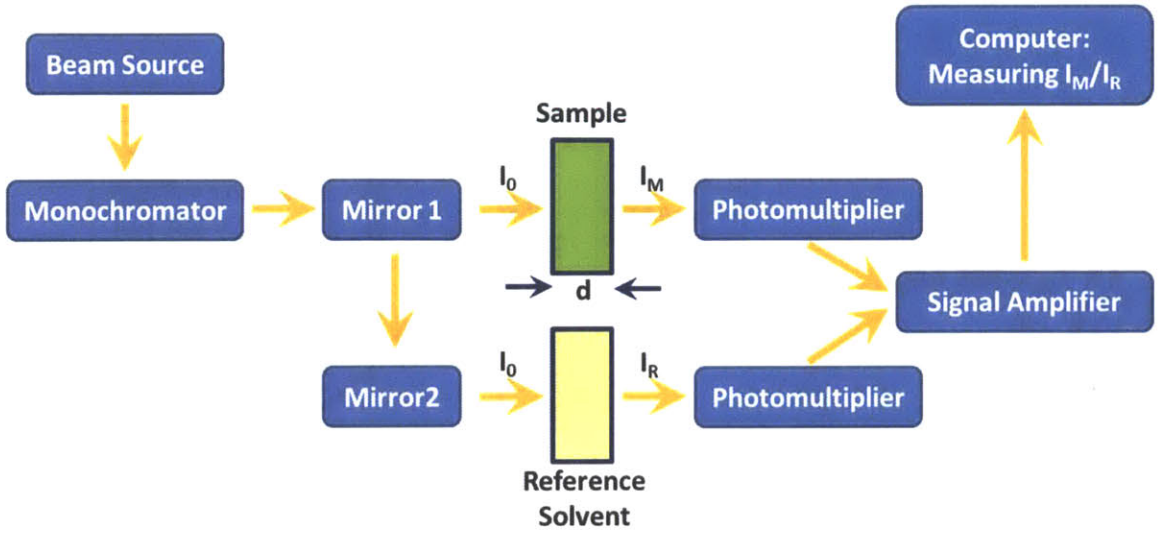

Figure 5.7. A schematic diagram for the double-beam UV-Vis spectroscopy

Eq.(5.3) indicates that the transmittance $T_r(\lambda)$ can be described by an exponential function with two fitting parameters. We applied eq.(5.3) to the measurement of ε and β for NPs dispersed in aqueous solutions with different volume fractions. Figure 5.8(a) shows the results of UV-Vis spectroscopy of Fe_3O_4 CNPs with volume fractions of NPs of $\phi_p = 6.20\times10^{-3}$ to 5.11×10^{-2} for a scanning incident wavelength range of $\lambda = 300-800$ nm. A shoulder peak appears around $\lambda = 386$ nm, which can serve as the standard wavelength λ_m at which ε and β for the Fe_3O_4 NPs can be calculated. We converted the absorbance data at $\lambda_m = 386$ nm into transmittance data, as shown in Figure 5.8(b), and then calculated the least-square fitting curve based on the exponential dependence of T_r to determine the two fitting parameters that correspond to ε and β. We found that $T_r = \exp\left(-27.54\phi_p^{\,0.84}\right)$, which yields the following relationship between A and ϕ_p for Fe_3O_4 NPs dispersed in the aqueous solution at $\lambda_m = 386$ nm

$$A(\lambda_m = 386\text{ nm}) = 27.54\left(\frac{L_Z}{d}\right)\phi_p^{\,0.84} \text{ for } Fe_3O_4 \text{ NPs,} \qquad (5.4)$$

where L_Z denotes the thickness of the film. As expected, eq.(5.4) shows that β deviates from unity, which leads to the nonlinear form of the Beer-Lambert law.

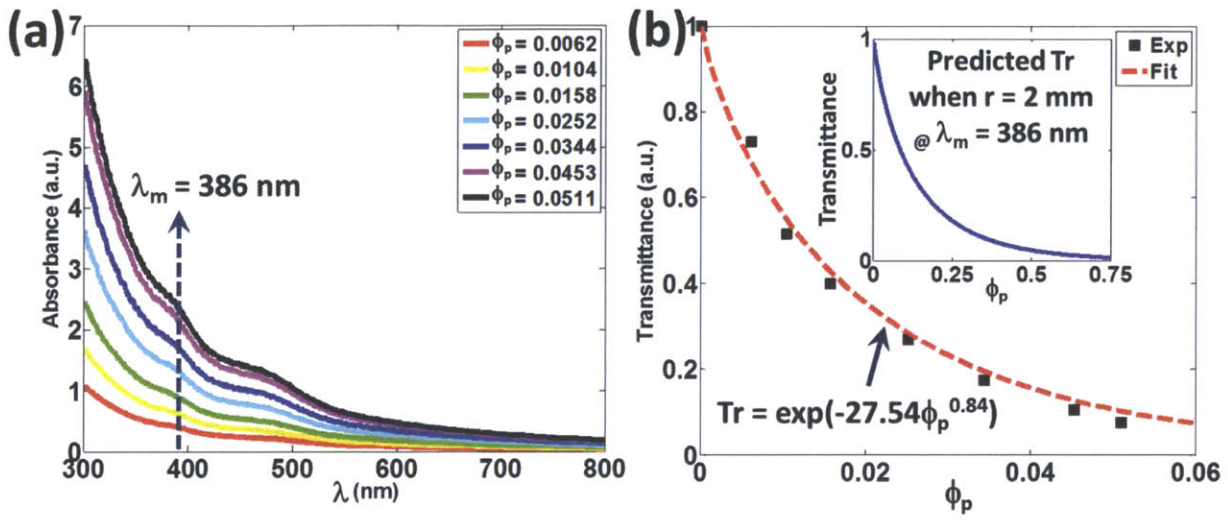

Figure 5.8. UV-Vis Absorbance (a) and the calibrated Tr spectra at $\lambda_m = 386$ nm (b) of Fe_3O_4 NPs-dispersed aqueous solution with different concentration of Fe_3O_4 NPs. Given in the inset of (b) is a predicted relationship between Tr and ϕ_p when the light path (r) is 2 mm.

Similarly, we measured A and T_r for SiO_2 CNPs with different ϕ_p (see Figure 5.9) and found the following relationship between A and ϕ_p for SiO_2 NPs dispersed in the aqueous solution at $\lambda_m = 507$ nm:

$$A(\lambda_m = 507 \text{ nm}) = 1.164\left(\frac{L_z}{d}\right)\phi_p^{0.97} \text{ for } SiO_2 \text{ NPs.} \tag{5.5}$$

Notably, the overall absorbance of SiO_2 NPs is smaller than that of Fe_3O_4 NPs, whereas the nonlinearity of SiO_2 NPs is weaker. Comparable experimentally measured values of A for Fe_3O_4 and SiO_2 NPs can be found in the literature [17,26]. Finally, we performed UV-Vis spectroscopy of PEGDA with 2,2-HMPP after UV-curing, as shown in Figure 5.10.

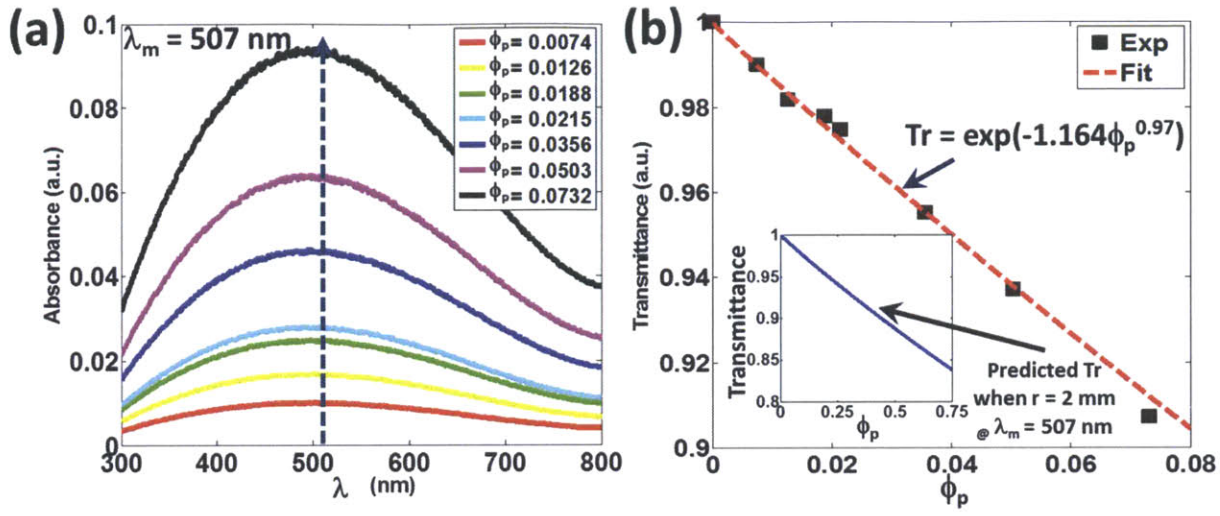

Figure 5.9. UV-Vis Absorbance (a) and the calibrated Tr spectra at $\lambda_m = 507$ nm (b) of SiO_2 NPs-dispersed aqueous solution with different concentration of SiO_2 NPs. Given in the inset of (b) is a predicted relationship between Tr and ϕ_p when the light path (r) is 2 mm.

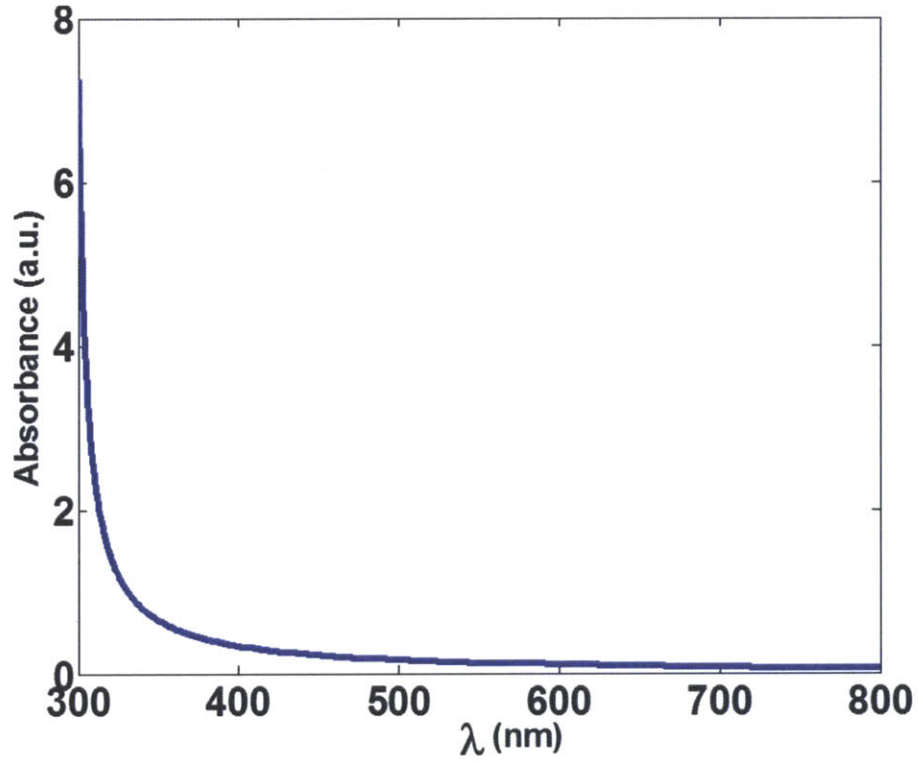

Figure 5.10. UV-Vis absorbance spectra of the UV-cross linked PEGDA with designated concentration of 2,2-HMPP

The spectra exhibit no distinctive peak, mainly because the PEGDA or 2,2-HMPP will absorb the incident light under $\lambda = 300$ nm, which excitates the C-C double bonds. In fact, we can observe a the steeply increasing slope as λ decreases.

We can quantitatively measure the concentration as expressed by the volume fraction of NPs in the local area of the thin film that was examined, on the basis of the UV-Vis measurement and calibration relationships in eqs.(5.4) and (5.5). It is also known that UV-Vis spectroscopy can be applied for quantitative measurement of the size, as well as the concentration, of NPs in a liquid medium [27]. In particular, by measuring the total absorbance of the NP-dispersed UV-cured thin film at two specific wavelengths (i.e., $\lambda_m = \lambda_{m1} = 386$ nm and $\lambda_m = \lambda_{m2} = 507$ nm), we can obtain the following relationships with two unknown variables, ϕ_{P1} and ϕ_{P2}, where the subscripts $P1$ and $P2$ indicate the two different NP [25]

$$\begin{aligned}
&\text{At } \lambda = \lambda_{m1},\\
&\quad A(\lambda_{m1}) = r\left(\varepsilon_{P1}(\lambda_{m1})\phi_{P1}{}^{\beta_A} + \varepsilon_{P2}(\lambda_{m1})\phi_{P2}{}^{\beta_{P2}} + \varepsilon_S(\lambda_{m1})(1-\phi_{P1}-\phi_{P2})\right)/d,\\
&\text{At } \lambda = \lambda_{m2},\\
&\quad A(\lambda_{m2}) = r\left(\varepsilon_{P1}(\lambda_{m2})\phi_{P1}{}^{\beta_{P1}} + \varepsilon_{P2}(\lambda_{m2})\phi_{P2}{}^{\beta_{P2}} + \varepsilon_S(\lambda_{m2})(1-\phi_{P1}-\phi_{P2})\right)/d.
\end{aligned} \tag{5.6}$$

The solutions of eq.(5.6) are ϕ_{P1} and ϕ_{P2} given $A(\lambda_{m1})$ and $A(\lambda_{m2})$. To solve eq.(5.6), we assumed that the nonlinear attenuation coefficient of the NPs, β, is constant irrespective of λ and of the UV-cured media, the A value of which is also assumed to not deviate from a linear relationship, $A \propto \phi$. As illustrated in Figure 5.11, μUV-Vis spectroscopy can be used to measure (1) $A(\lambda_{m1})\big|_{Z_i}$ and $A(\lambda_{m2})\big|_{Z_i}$ of the film at specific location, which is denoted by the ith resolution area at z_i of the film along the direction parallel to the film thickness (the z-direction defined as direction 1 (i.e., Dir 1)), and (2) $A_I(\lambda_{m1})$ and $A_I(\lambda_{m2})$ along the direction perpendicular to the thickness (the x-direction defined as direction 2 (i.e., Dir 2)), where the subscript I indicates the integrated absorbance signal. In particular, the experimentally measured data for $A_I(\lambda)$ can be compared to the calculated value from eqs.(5.4) and (5.5) as follows:

$$A_I(\lambda) = \int_0^{L_Z} dz \left(\frac{\sum_{i=A,B,D} \phi_i^{\beta_i}(z)\varepsilon_i(\lambda)}{d} \right) \simeq \frac{\Delta z}{d} \sum_{j=1}^{N_R} \sum_{i=A,B,D} \phi_i^{\beta_i}(j)\varepsilon_i(\lambda),\ N_R = \frac{L_Z}{\Delta z}, \tag{5.7}$$

where Δz denotes the spatial resolution of the μUV-Vis spectroscopy, and N_R is the total sampling number used to measure the UV-Vis spectra along direction 1. From eqs.(5.6) and (5.7), we can quantitatively determine the concentration gradient and distribution of NPs in the thin film.

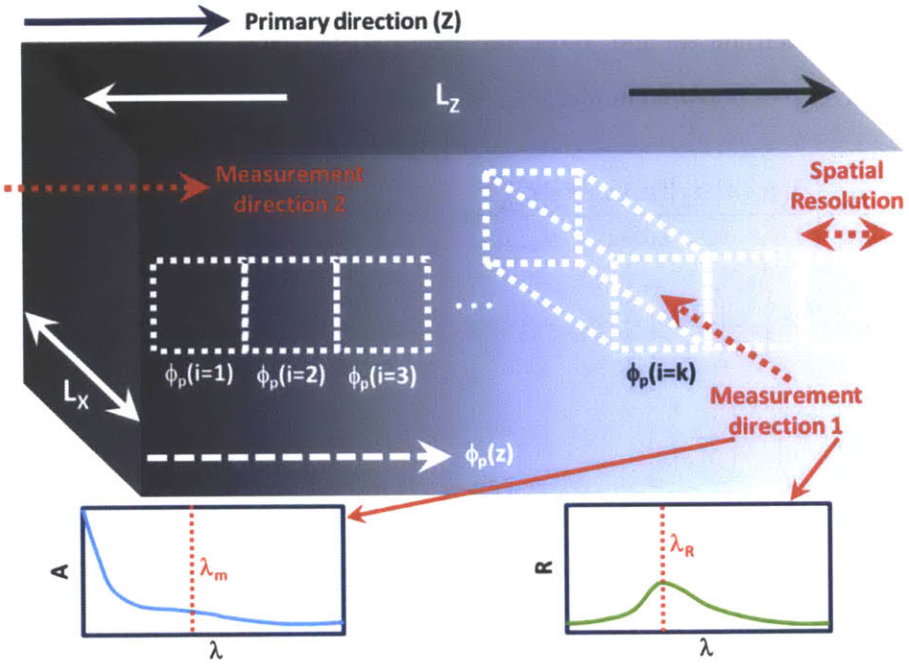

Figure 5.11. A schematic diagram of a thin film inside which a gradient of NPs concentration (ϕ_p) formed. Two different directions (i.e., directions 1 and 2) to measure UV-Vis spectra using the μUV-Vis are provided. In lower panels provided are schematic plots for the absorbance (A) and reflectance (R) spectra expected from the area under measurement.

5.3. Theoretical Framework

5.3.1. Self-Consistent Mean Field (SCMF) Algorithm for Binary CNPs

As analyzed and suggested in Chapter 4, a self-consistent mean field (SCMF) algorithm can be an effective and efficient method of calculating the concentration distribution of discrete-sized hard-sphere-like NPs in a thin film at equilibrium. In particular, it has also been suggested that the SCMF algorithm can be extended to the calculation of the concentration distribution of multiple CNP-components, such as

a binary or ternary mixture of NPs. In this chapter, we assume that one type of particles interacts via the van der Waals and magnetic dipolar potentials (superparamagnetic Fe_3O_4 NPs, denoted by A), and the other type interacts via the Lennard-Jones potential (nonmagnetic SiO_2 NPs, denoted by B). Further, the system is assumed to be confined in a thin film under an external magnetic field parallel to the z-axis. As one of the models describing the molecular interaction potential denoted by $F_{ij}(r)$ which is the inter-particle interaction between the ith and j th component particles, and includes dipolar interactions, we employed a Stockmayer pair potential model [28,29]:

$$
\begin{aligned}
F_{AA}(r_{ij}) &= -\frac{\mu_0}{4\pi r_{ij}^3}\left(\frac{3(\boldsymbol{\mu}_{\mathbf{i}}(n)\cdot\mathbf{r}_{\mathbf{ij}})(\boldsymbol{\mu}_{\mathbf{j}}(n+k)\cdot\mathbf{r}_{\mathbf{ij}})}{r_{ij}^3} - (\boldsymbol{\mu}_{\mathbf{i}}(n)\cdot\boldsymbol{\mu}_{\mathbf{j}}(n+k))\right) + 4\varepsilon_{AA}\left[\left(\frac{\sigma_A}{r_{ij}}\right)^{12} - \left(\frac{\sigma_A}{r_{ij}}\right)^{6}\right], \\
F_{AB}(r_{ij}) &= 4\varepsilon_{AB}\left[\left(\frac{\sigma_{AB}}{r_{ij}}\right)^{12} - \left(\frac{\sigma_{AB}}{r_{ij}}\right)^{6}\right],\ \varepsilon_{AB} = \delta_\varepsilon(\varepsilon_A\varepsilon_B)^{1/2},\ \sigma_{AB} = \frac{\delta_\sigma(\sigma_A+\sigma_B)}{2}, \\
F_{BB}(r_{ij}) &= 4\varepsilon_{BB}\left[\left(\frac{\sigma_B}{r_{ij}}\right)^{12} - \left(\frac{\sigma_B}{r_{ij}}\right)^{6}\right],
\end{aligned}
\tag{5.8}
$$

where μ_0 is the vacuum permeability ($\mu_0 = 4\pi\times10^{-7}$ NA^{-2}). The other notation in eq.(5.8) was taken from eqs.(4.1)-(4.5) in Chapter 4. The contribution from the external magnetic field is given as [5,22,23,28-30]:

$$
G_A^{(ext)}(n) = -\boldsymbol{\mu}_{\mathbf{i}}(n)\cdot\mathbf{B}(n),\ G_B^{(ext)}(n) = 0, \tag{5.9}
$$

where $\mathbf{B}(n)$ is the external magnetic field felt by a single A particle in the n th discrete layer. The magnetic dipole moment of the ith superparamagnetic A particle in the n th discrete layer, $\boldsymbol{\mu}_{\mathbf{i}}(n)$, is written as

$$
\boldsymbol{\mu}_{\mathbf{i}}(n) = \mathbf{M}_{\mathbf{S,i}}V_{p,i}L(\eta_i(n)),\ L(x) = \coth(x) - x^{-1},\ \eta_i(n) \equiv \frac{\mathbf{M}_{\mathbf{S,i}}\cdot\mathbf{B}(n)V_{p,i}}{k_BT}, \tag{5.10}
$$

where $\mathbf{M}_{\mathbf{S,i}}$ and $V_{p,i}$ are the saturation magnetization and volume of the magnetic domain of the ith superparamagnetic particle, respectively. The Langevin functional dependence based on the mean field approximation of magnetization by the external magnetic field, $L(\eta(n))$, is a function of the dimensionless parameter $\eta(n)$. To consider an external field with field strength gradient, we assumed

that the external magnetic field is generated by a bar-magnet directly beneath the film. Then, $\mathbf{B}(n)$ can be expressed as [31]:

$$\mathbf{B}(n)=\frac{\mu_0\mathbf{H}}{2\pi\sigma_B{}^3\left(l_M+l_S+n-0.5\right)^3}, \tag{5.11}$$

where $\mathbf{H}$ indicates the magnetic moment generated by the magnetic field. Further, l_M and l_S are the normalized thicknesses of the bar magnet and bottom substrate with respect to the NP size (if two NPs have different sizes, employ the smaller one), respectively. In eq.(5.8), $F_{AA}\left(r_{ij}\right)$ and $G_A^{(ext)}(n)$ can be further simplified into the following dimensionless form by assuming that the A particles are mono-disperse in size and saturation magnetization (i.e., $\mathbf{M}_{\mathbf{S,i}}=\mathbf{M}_{\mathbf{S}}$, $V_{p,i}=V_p=\pi\sigma_A{}^3/6$) and are aligned along the primary axis (i.e., the z-direction parallel to the orientational direction of $\mathbf{B}(n)$):

$$\begin{aligned}
&\frac{F_{AA}\left(r_{ij}\right)}{k_BT}=-\frac{\overline{\mu}L\left(\eta(n)\right)L\left(\eta(n+k)\right)\left(3\cos^2\theta_{ij}-1\right)}{r_{ij}{}^3}+4\frac{\varepsilon_{AA}}{k_BT}\left[\left(\frac{1}{r_{ij}}\right)^{12}-\left(\frac{1}{r_{ij}}\right)^{6}\right],\\
&\frac{G_A^{(ext)}(n)}{k_BT}=-\frac{\overline{H}L\left(\eta(n)\right)}{\left(l_M+l_S+n-0.5\right)^3},\\
&\overline{\mu}\equiv\frac{\pi\mu_0\sigma_A{}^3M_S{}^2}{144k_BT},\ \eta(n)=\frac{\overline{H}}{\left(l_M+l_S+n-0.5\right)^3},\ \overline{H}\equiv\frac{\mu_0\sigma_A{}^3M_SH}{12\sigma_B{}^3k_BT},
\end{aligned} \tag{5.12}$$

where θ_{ij} is the angle between $\mathbf{r_{ij}}$ and $\mathbf{B}(n)$, and r_{ij} is normalized relative to σ_A. In this calculation, we considered that the single magnet is a laboratory-scale cylindrical bar magnet 1 cm-thick with a field strength of 10^{-2} $NA^{-1}m^{-1}$, which indicates that $H\sim6\times10^{-3}$ Am^2.

For the molecular interaction parameters of the LJ potentials, we used the non-retarded Hamaker constants [32] for Fe_3O_4 ($A_1\sim2.1\times10^{-19}$ J) [33], SiO_2 ($A_2\sim6.7\times10^{-20}$ J) [34], PEG ($A_3\sim7.2\times10^{-20}$ J) [35], Fe_3O_4-PEG-Fe_3O_4 ($A_{131}\approx\left(A_1^{1/2}-A_3^{1/2}\right)^2\sim3.6\times10^{-20}$ J) [32], and SiO_2-PEG-SiO_2 ($A_{232}\approx\left(A_2^{1/2}-A_3^{1/2}\right)^2\sim8.3\times10^{-20}$ J) [32]. For the deviation factors of the effective interparticle-distance (δ_σ) and short-range interaction (δ_ε) among Fe_3O_4 and SiO_2 NPs, we started with the simulated data from Monte Carlo (MC) simulations, $\delta_\sigma=1.50$ and $\delta_\varepsilon=0.749$ [36]. From the experimentally measured concentration distribution profiles of the two CNPs, we fitted the SCMF simulation results

using δ_σ and δ_ε as the fitting parameters and found that $\delta_\sigma = 1.57$ and $\delta_\varepsilon = 0.83$, which are similar to the starting values predicted by the MC simulation of the two-demixed (or phase separating) particles. For superparamagnetic NPs, we assumed that the Fe_3O_4 CNPs have a single magnetic domain, whereby $M_S \sim 5\times10^5$ Am^{-1} when the NPs are dispersed in aqueous solution with a relatively dilute concentration [5,37]. By using eq.(5.12), we calculated the concentration profiles of Fe_3O_4 and SiO_2 CNPs given the thicknesses of the film and the bottom substrate.

5.4. Results and Discussion

5.4.1. Measurement of CNP Concentration Distribution in the Thin Film

By using eqs.(5.1)-(5.7), we translated the UV-Vis absorbance taken in direction 1 to the volume fractions of NPs at selected local positions along the z-direction. Given a μUV-Vis spatial resolution of 20×20 μm^2, data were obtained from 52-109 spatial points depending on the film thickness.

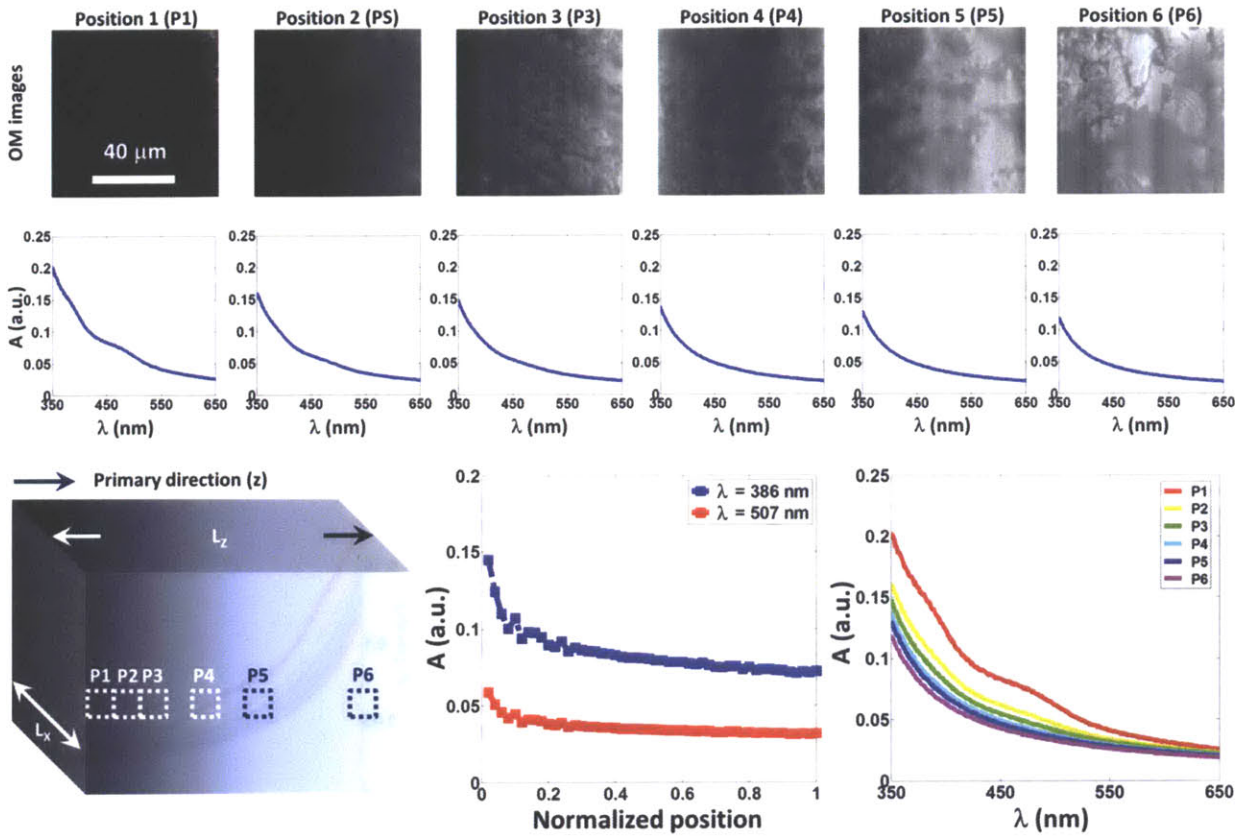

Figure 5.12. Experimental results of concentration-gradient-derived UV-Vis (middle row) absorbance (A) spectra taken at different positions (denoted by P1-P6) of the thin film along the primary direction (Z) accompanied by optical microscope images (top row with a 40 μm-scale bar is given in the first microscope image) for the case of a thin film composed of Fe_3O_4, SiO_2 NPs dispersed in UV-cured PEGDA media with $L_Z = 1.08$ mm and $L_m = 130$ μm under the normalized external magnetic field $H = 2.41$. Given in the bottom row are a schematic diagram of the film structure (cf. the color gradient is given for eye-guide) (left), UV-Vis absorbance of the film taken at two different wavelengths ($\lambda = 386$ nm for blue and $\lambda = 507$ nm for red) as a function of the position normalized with respect to the film thickness L_Z (middle), and UV-Vis absorbance of the film taken at the 6 different positions as a function of λ which denotes the wavelength of incident light (right).

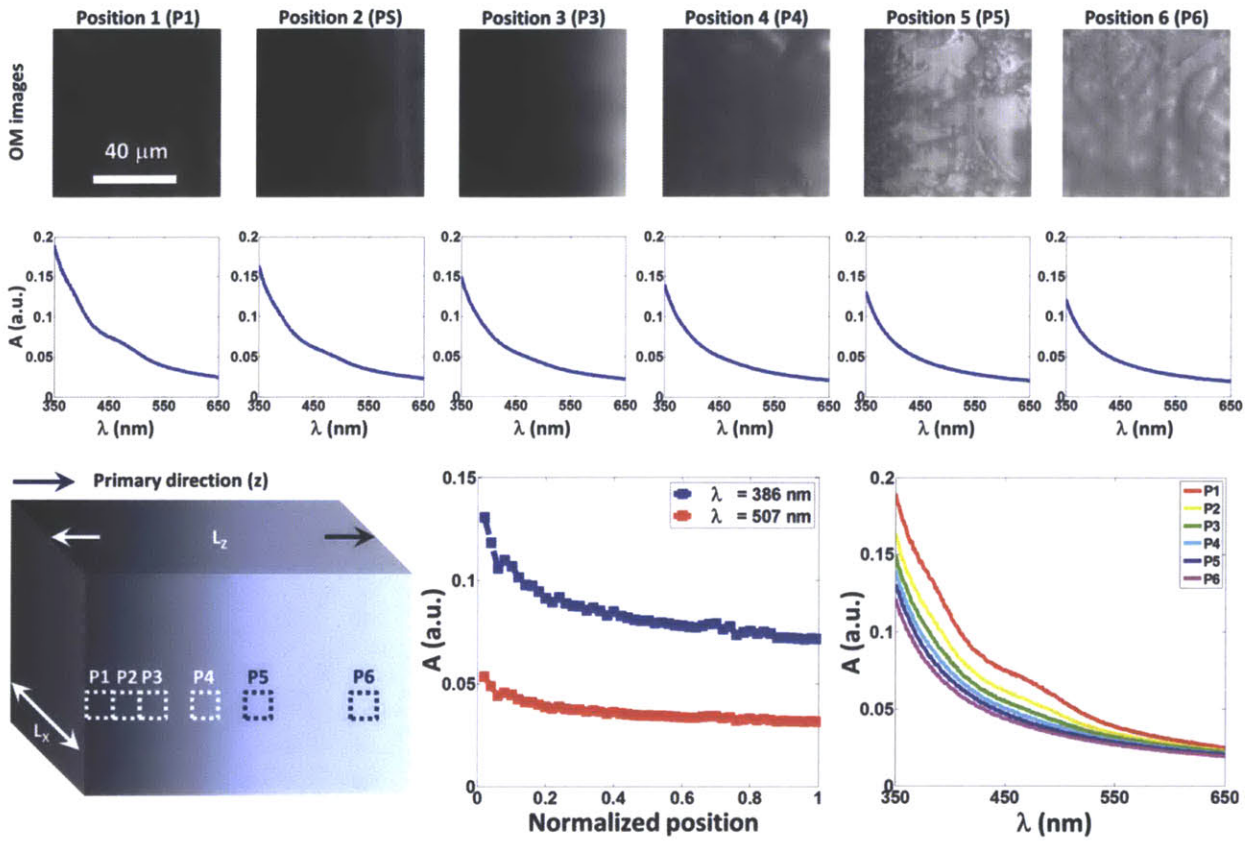

Figure 5.13. Experimental results of concentration-gradient-derived UV-Vis (middle row) absorbance (A) spectra taken at different positions (denoted by P1-P6) of the thin film along the primary direction (Z) accompanied by optical microscope images (top row with a 40 μm -scale bar is given in the first microscope image) for the case of a thin film composed of Fe_3O_4, SiO_2 NPs dispersed in UV-cured PEGDA media with $L_Z = 1.08$ mm and $L_m = 1.40$ mm under the normalized external magnetic field $H = 2.41$. Given in the bottom row are a schematic diagram of the film structure (cf. the color gradient is given for eye-guide) (left), UV-Vis absorbance of the film taken at two different wavelengths ($\lambda = 386$ nm for blue and $\lambda = 507$ nm for red) as a function of the position normalized with respect to the film thickness L_Z (middle), and UV-Vis absorbance of the film taken at the 6 different positions as a function of λ which denotes the wavelength of incident light (right).

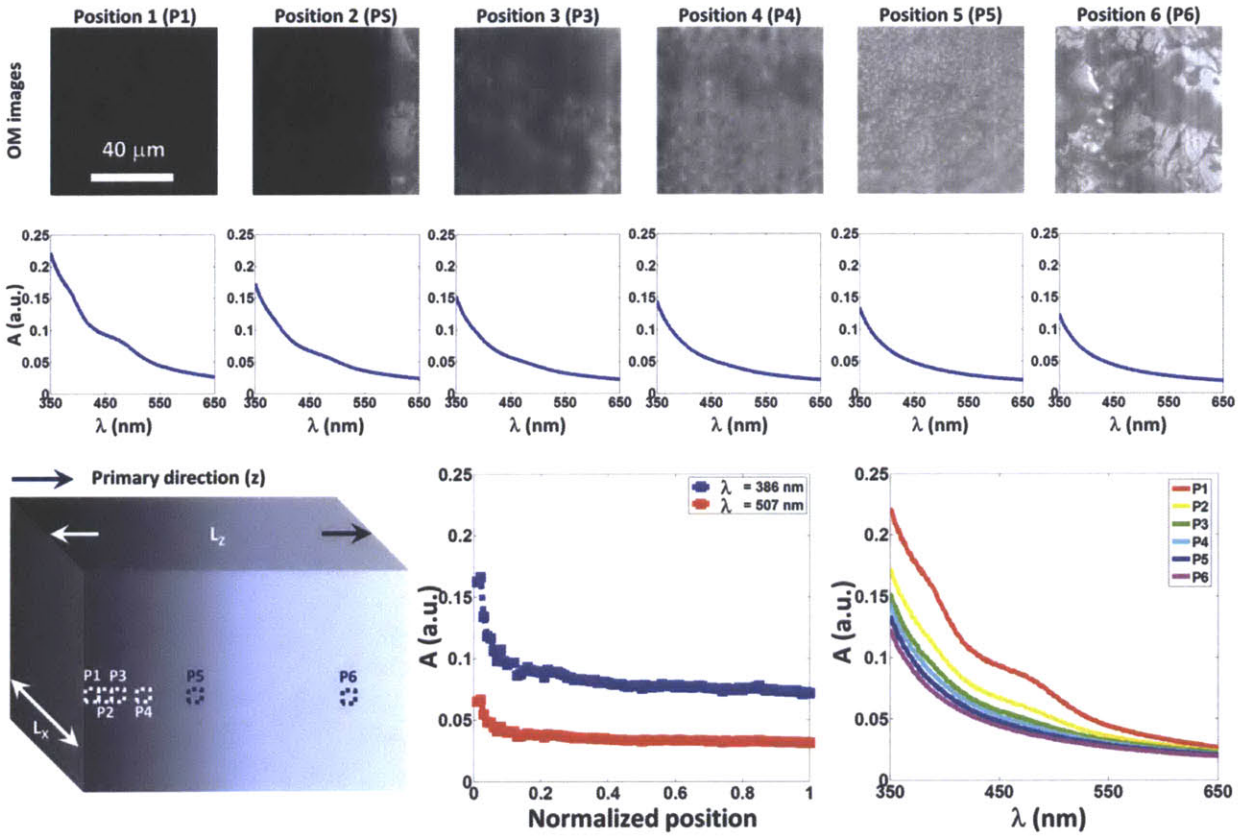

Figure 5.14. Experimental results of concentration-gradient-derived UV-Vis (middle row) absorbance (A) spectra taken at different positions (denoted by P1-P6) of the thin film along the primary direction (Z) accompanied by optical microscope images (top row with a 40 μm -scale bar is given in the first microscope image) for the case of a thin film composed of Fe_3O_4, SiO_2 NPs dispersed in UV-cured PEGDA media with $L_Z = 2.24$ mm and $L_m = 130$ μm under the normalized external magnetic field $H = 2.41$. Given in the bottom row are a schematic diagram of the film structure (cf. the color gradient is given for eye-guide) (left), UV-Vis absorbance of the film taken at two different wavelengths ($\lambda = 386$ nm for blue and $\lambda = 507$ nm for red) as a function of the position normalized with respect to the film thickness L_Z (middle), and UV-Vis absorbance of the film taken at the 6 different positions as a function of λ which denotes the wavelength of incident light (right).

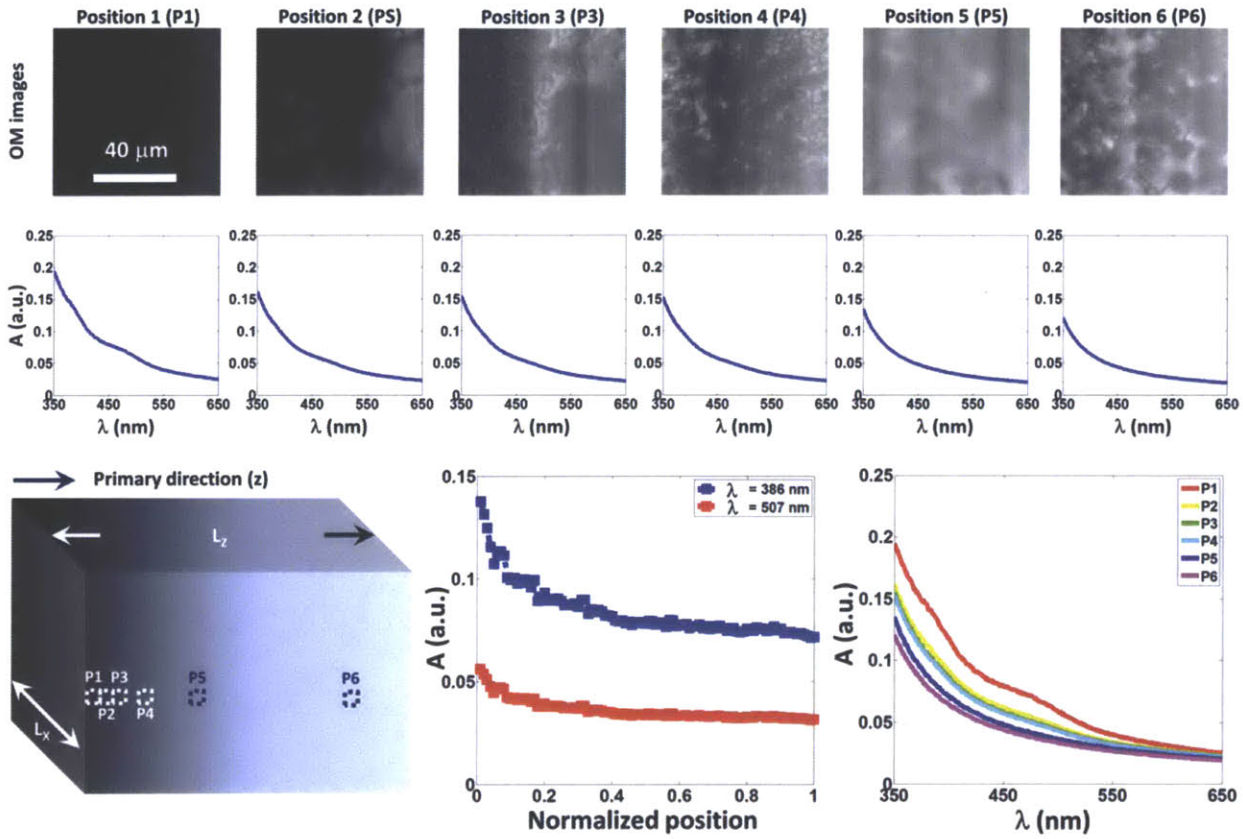

Figure 5.15. Experimental results of concentration-gradient-derived UV-Vis (middle row) absorbance (A) spectra taken at different positions (denoted by P1-P6) of the thin film along the primary direction (Z) accompanied by optical microscope images (top row with a 40 μm -scale bar is given in the first microscope image) for the case of a thin film composed of Fe_3O_4, SiO_2 NPs dispersed in UV-cured PEGDA media with $L_Z = 2.24$ mm and $L_m = 1.40$ mm under the normalized external magnetic field $H = 2.41$. Given in the bottom row are a schematic diagram of the film structure (cf. the color gradient is given for eye-guide) (left), UV-Vis absorbance of the film taken at two different wavelengths ($\lambda = 386$ nm for blue and $\lambda = 507$ nm for red) as a function of the position normalized with respect to the film thickness L_Z (middle), and UV-Vis absorbance of the film taken at the 6 different positions as a function of λ which denotes the wavelength of incident light (right).

Figures 5.12-15 summarize the experimentally obtained UV-Vis spectra and present optical microscope images for the cases with different film thicknesses L_Z and substrate thicknesses L_S (i.e., $[L_Z\ L_S] = [1.08\text{ mm}\ \ 130\ \mu\text{m}]$, $[1.08\text{ mm}\ \ 1.40\text{ mm}]$, $[2.24\text{ mm}\ \ 130\ \mu\text{m}]$, and $[2.24\text{ mm}\ \ 1.40\text{ mm}]$ in

order). The UV-Vis absorbance peak at $\lambda = 386$ nm diminishes as the measurement point moves away from the bottom (i.e., from P1 to P6 shown in the upper panel). This is easily explained by the fact that Fe_3O_4 CNPs will be more concentrated near the bottom substrate, where the magnetic field strength is strongest. As the distance from the bottom substrate increases, fewer Fe_3O_4 CNPs are concentrated, whereas more SiO_2 appears. This explanation is supported by the observation that the UV-Vis absorbance at $\lambda = 507$ nm varies less than that at $\lambda = 386$ nm with increasing distance from the bottom substrate (see the middle plot in the bottom panel). Optical microscope images also indicate that the concentration distribution behaviors of Fe_3O_4 and SiO_2 CNPs will be opposite. This is also supported by visual observation of the colors of each of the CNPs; Fe_3O_4 CNPs are dark-brown, whereas SiO_2 CNPs appear white.

5.4.2. Comparison between Experimental Data and SCMF Calculations

We calculated the volume fractions of CNPs and compared the data with the calculation results from the SCMF algorithm, on the basis of the experimental data. For the comparison, we employed three fitting parameters, two of which, δ_ε and δ_σ can be obtained from the molecular interaction parameters in eq.(5.8). The other fitting parameter was the conversion factor from the number density to the volume fraction δ_V. For example, for a hard-sphere-like particle with a diameter of σ_p, the conversion relationship between the volume fraction ϕ_p and the number density ρ_p is given as $\delta_V \rho_p \sigma_p^{\,3} = \phi_p$. By using the least-square fitting, we found that $[\delta_\varepsilon \ \delta_\sigma \ \delta_V] = [0.831 \ 1.574 \ 0.718]$ and used the obtained fitting parameter combination for other settings with different film thicknesses and substrate thicknesses. For computational efficiency, we limited one of the fitting parameters to a physically meaningful range, $0.65 \le \delta_V \le 0.73$ [38], where the maximum limit originated in the maximum volume fraction of hard spheres in the hexagonal close-packed (HCP) structure. From the calculated fitting parameter combination, interestingly, we found that δ_V is nearly equivalent to the ideal HCP conversion factor, 0.73 [38]. Other parameters responsible for deviations in the molecular interaction between two different particles are also in the range of physically meaningful values [32-36].

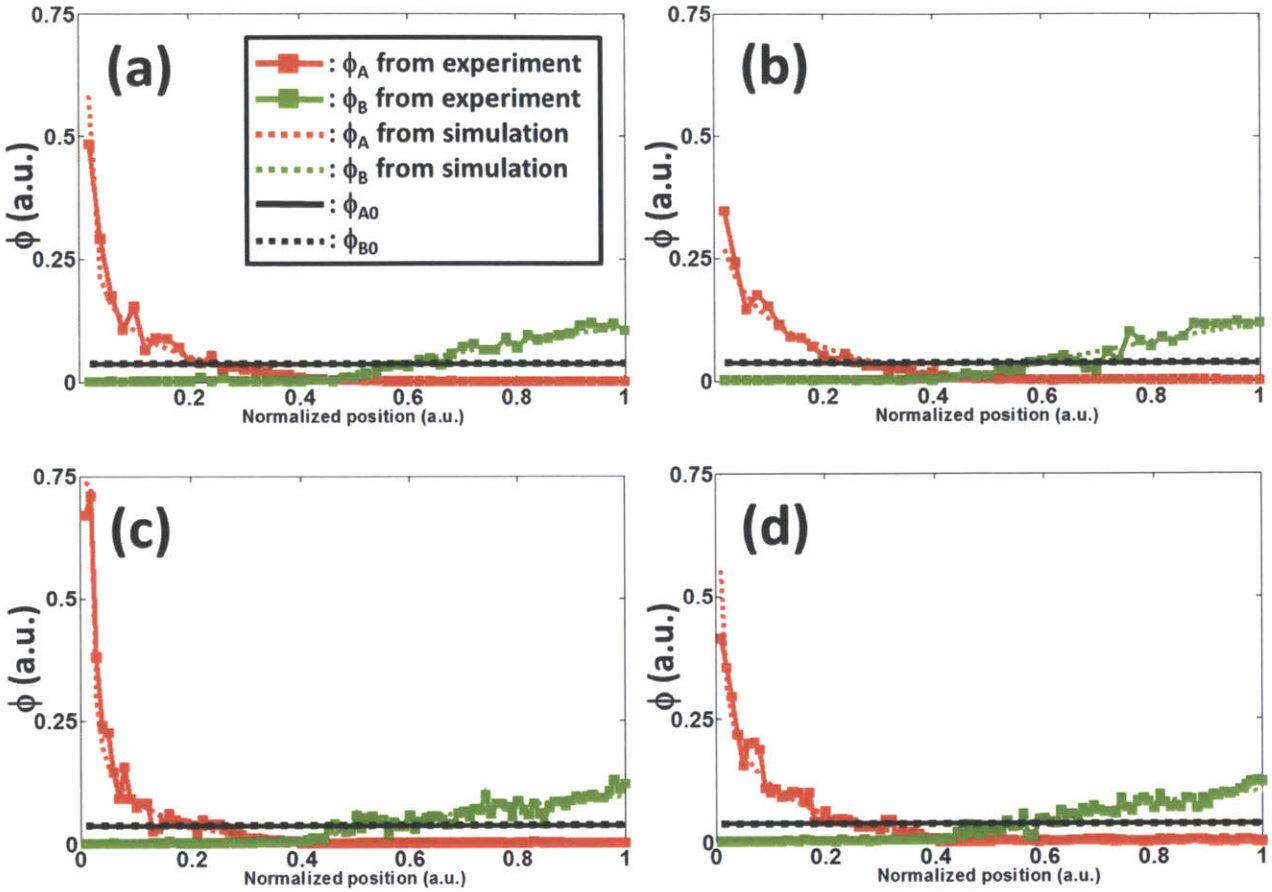

Figure 5.16. Comparison between the calculated from experimental data (solid symbols with solid lines) and simulated from the SCMF algorithm (dot lines) concentration profiles of CNPs in a thin film as a function of the position in the film normalized with respect to the film thickness with different film and substrate thicknesses (a) $L_Z = 1.08$ mm and $L_S = 130\ \mu$m, (b) $L_Z = 1.08$ mm and $L_S = 1.40$ mm, (c) $L_Z = 2.24$ mm and $L_S = 130\ \mu$m, and (d) $L_Z = 2.24$ mm and $L_S = 1.40$ mm under the normalized external magnetic field $H = 2.41$. Red and green colors denote Fe_3O_4 and SiO_2 CNPs, respectively.

However, considering that the potential model used in this chapter has one of the simplest forms, the obtained molecular interaction parameters are not necessarily the most appropriate for real-world cases. Figure 5.16 compares the experimental data for different film thicknesses and substrate thicknesses with the results of simulations using the SCMF algorithm with the obtained combination of the fitting parameters. The predictions of the SCMF calculation agree well with the experimental data irrespective of the combination of film thickness and substrate thickness. This indicates that the SCMF algorithm can be

progressively and proactively employed to design the desired concentration distribution profiles of CNPs in a thin film with a given film thickness and external magnetic field strength. One of the interesting points here is that we can control the CNP concentration gradient by controlling the film thickness and substrate thickness. For example, in Figure 5.16(c), where the film is relatively thick and the external magnetic field is relatively strong, we see that the Fe_3O_4 NPs are concentrated, forming nearly HCP structure near the bottom substrate. In contrast, as shown in Figure 5.16(b), whiere the film is relatively thin and the external magnetic field is relatively weak, the concentration of Fe_3O_4 NPs near the bottom substrate is about half of the value observed in Figure 5.16(c). Observations from other cases, shown in Figures 5.16(a) and (d), also indicate that the concentration gradient of NPs that are attracted by the external field can be controlled by varying the external field strength and film thickness. This finding implies future applications of this experimental study in terms of reliable and experimentally controllable factors that can be employed to design the desired concentration distribution. Interestingly, it appears that the concentration profile of SiO_2 NPs does not vary as much as that of Fe_3O_4 NPs with the film thickness and substrate thickness. This can be understood by considering that SiO_2 NPs are pushed away from the bottom substrate, forming a region where Fe_3O_4 NPs do not appear. In this region, the SiO_2 NPs feel nearly no interaction potential from the Fe_3O_4 NPs; therefore, only the molecular interactions among the SiO_2 NPs will determine the concentration distribution of SiO_2 NPs. Thus, controlling the magnetic field strength and film thickness will have no critical effect on the concentration distribution of SiO_2 NPs.

To verify the methodologies for converting the UV-Vis absorbance signal to the volume fraction shown in eqs.(5.1)-(5.6) and the SCMF calculation for quantitative measurement of the NP concentration, we compared the total UV-Vis absorbance signal measured along direction 2 with (1) the re-constructed UV-Vis absorbance signal obtained from the measurement along direction 1 based on eq.(5-7) and (2) the simulated UV-Vis absorbance signal obtained by reverse calculating the UV-Vis absorbance using eqs.(5.1)-(5.6) in the SCMF calculation (using the fitting parameters). As Figure 5.17 shows, the agreement among the three UV-Vis absorbance signals is good overall considering the different conditions. However, the absorbance value from the measurement along direction 2 is smaller than that from the signals along direction 1 and the simulated signals from the SCMF calculation irrespective of the incident wavelength. One possible reason for this discrepancy is scattering from the concentrated NPs.

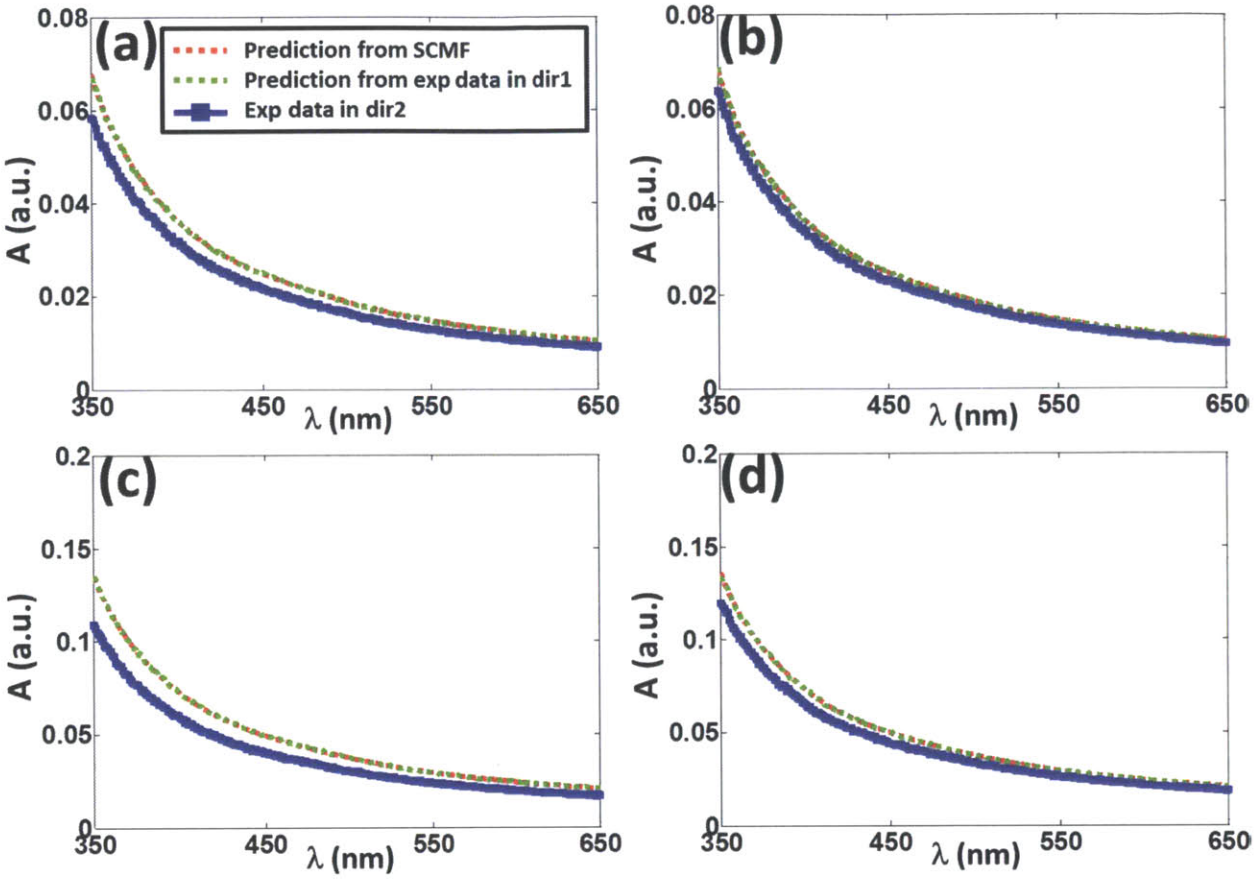

Figure 5.17. Comparison among the experimentally measured UV-Vis absorbance (A) along the direction 2 (see Figure 5.11) (blue symbol-line), re-constructed UV-Vis A spectra from experimental data obtained from the scanning along direction 1 (red dot line), and simulated UV-Vis A spectra from the SCMF algorithm (red dot line) with different film and substrate thicknesses (a) $L_Z = 1.08$ mm and $L_S = 130\ \mu$m, (b) $L_Z = 1.08$ mm and $L_S = 1.40$ mm, (c) $L_Z = 2.24$ mm and $L_S = 130\ \mu$m, and (d) $L_Z = 2.24$ mm and $L_S = 1.40$ mm under the normalized external magnetic field $H = 2.41$.

This conjecture is supported by a comparison of the cases with relatively strong magnetic fields (see Figures 5.17(a) and (c)) and relatively weak magnetic field (see Figures 5.17(b) and (d)). Indeed, the cases with a stronger field show a more distinctive discrepancy in the UV-Vis absorbance signal, whereas the others show a relatively small discrepancy. However, the overall behavior supports the calculation and conversion methods for quantitative measurement of the CNP concentration distribution in the film. Table 5.1 summarizes the observed, re-constructed, and simulated absorbance observed at the two specific

wavelengths. The data show overall agreement in the absorbance among the experimental measurements along the two measuring directions and the theoretical prediction.

Table 5.1. Comparison of the UV-Vis absorbance (A) value at the two different wavelengths of the incident light ($\lambda = 386$ nm and $\lambda = 507$ nm) obtained from the SCMF simulation, re-constructed from the experimental data along direction 1 (Dir 1), and experimentally measured along direction 2 (Dir 2) for different cases with different film thickness and substrate thickness

	$L_Z = 1.08$ mm and $L_S = 130$ μm			$L_Z = 1.08$ mm and $L_S = 1.40$ mm			$L_Z = 2.24$ mm and $L_S = 130$ μm			$L_Z = 2.24$ mm and $L_S = 1.40$ mm		
λ (nm)	SCMF	Dir 1	Dir 2	SCMF	Dir 1	Dir 2	SCMF	Dir 1	Dir 2	SCMF	Dir 1	Dir 2
386	0.042	0.042	0.037	0.042	0.042	0.038	0.084	0.085	0.068	0.084	0.084	0.075
507	0.018	0.018	0.016	0.018	0.018	0.017	0.036	0.036	0.029	0.036	0.036	0.032

5.4.3. Possible Applications of the Fabricated Thin Films as Functional Materials

The good agreement between the experimentally observed and calculated CNP concentration distributions also allows us to extend this study to the exploration of future applications. As an example, the expected distribution of the effective refractive index, $n_{eff}(z)$, was calculated along direction 1 in the film using the relationship [38]

$$n_{eff}(z) = \left(n_A^2 \phi_A(z) + n_B^2 \phi_B(z) + n_D^2 \left(1 - \phi_A(z) - \phi_B(z)\right)\right)^{1/2}, \qquad (5.13)$$

where $\phi_A(z)$ and $\phi_B(z)$ are obtained from the experimental data. Using the known values of the refractive indices of the composite materials, $n_A = 2.42$, $n_B = 1.54$, and $n_D = 1.31$ in the visible wavelength range, eq.(5.13) provides a continuous profile of $n_{eff}(z)$, as shown in Figure 5.18. Interestingly, the calculated profile of $n_{eff}(z)$ varies between 1.42 and 1.73, which suggests that the fabricated thin film might be employed to design optically functional materials such as a gradient

(refractive) index (GRIN) lens [39,40]. In particular, one of the most famous GRIN lenses is the human eye [41-43], in which the refractive index varies from 1.37 to 1.42 (see Figure 5.19). Aging or diabetes causes the refractive index distribution to deviate from the ideal distribution profile [41,43], reducing the eye's power by causiung failure to maintain the appropriate focal length. Thus, the fabricated thin film shown in this chapter can be actively employed to assist in modifying the refractive index distribution when the dispersion media are transparent. Another promising possibility for the fabricated functional thin film is that the dynamic controllability of the concentration distribution profiles of the CNPs can also be strategically enhanced, provided that we do not apply UV-curing to the dispersion medium. For example, by switching the external field on and off, the concentration distribution of CNPs can be dynamically controlled in the desired manner. Considering the expanding market for optically functional materials with biomedical applications [41-43], we can expect that the fabrication method, in conjunction with theoretical/computational analysis of thin films in which the CNP concentration gradient can be manipulated, will provide a substantial benefit for future application research.

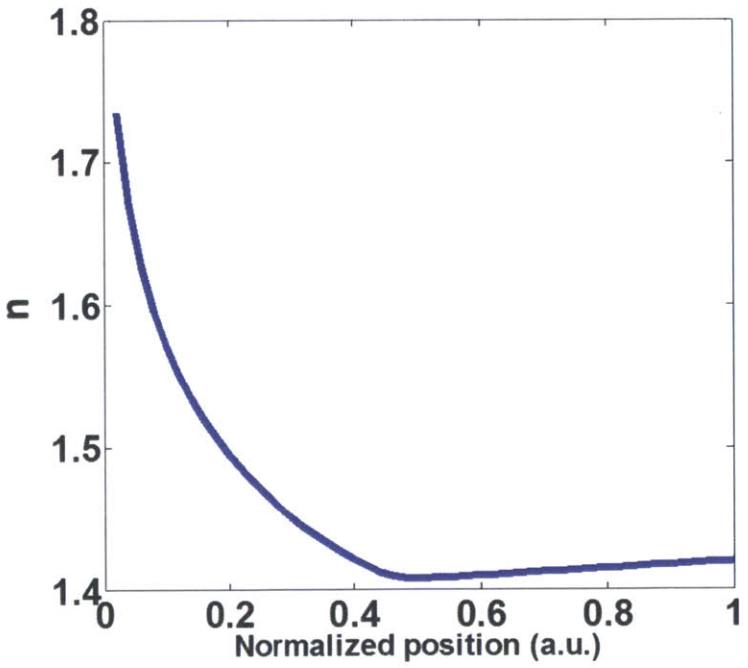

Figure 5.18. Calculated effective refractive index, $n_{eff}(z)$, as a function of the normalized position from the experimental data of the concentration gradient in the UV-cured thin film inside Fe_3O_4 and SiO_2 CNPs are dispersed. Film condition: $L_Z = 1.08$ mm and $L_S = 1.40$ mm under the normalized external magnetic field $H = 2.41$.

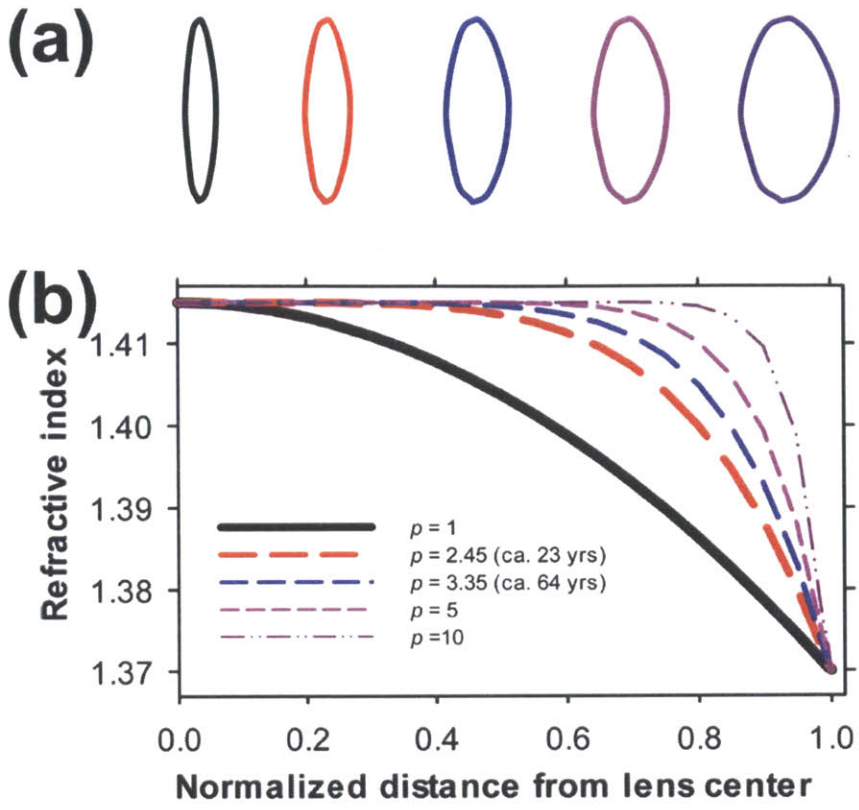

Figure 5.19. (a) Shape changes of crystalline lens with age. (b) Relationship between the refractive index of eye lens and the normalized distance from the lens center with different aging-related power law exponents p. The original data in (b) are from Charman *et al.* [43].

5.5. Conclusions

In Chapter 5, we presented experimental results on the fabrication of a film in which binary CNPs form a controlled concentration distribution. This experiment was intended to provide the proof-of-concept data that is the goal of this thesis. Additionally, it was intended to show the application potential of the suggested self-consistent mean-field (SCMF) computational algorithm and possible future applications in areas using the optical properties and other physical-properties. For the dispersion medium, we employed UV-curable monomers that can be cured within 1 h, and this curing dynamics also yields promising properties when it is important to control the CNPs separation dynamics at the desired moment to obtain the desired concentration distribution profile. By varying the film thickness and substrate thickness, which can be considered as a method of controlling the external magnetic field strength, we examined the variation in the concentration distribution of two different CNPs (i.e., Fe_3O_4 and SiO_2 CNPs) in the thin

film. For quantitative measurement of the concentration distribution, we used microspectrophotometery, which allowed us to convert the UV-Vis absorbance signal to the volume fraction of NPs at a specific point in the film. By using the SCMF algorithm, we compared the calculated concentration distribution with experimental data using fitting parameters from the molecular interaction parameters and the volume fraction-to-number density conversion factor. We found that the SCMF calculation can effectively and successfully predict the CNP concentration profile. We also checked the possibility of controlling the concentration distribution profiles by manipulating the film thickness and substrate thickness. We extended the study to determine whether the formed thin film with a controlled gradient of the CNP concentration can be used as a functional material such as a gradient refractive index (GRIN) lens. We found that it is feasible to prepare an optically functional material using the controlled refractive index distribution, which can be achieved by controlling the concentration distribution of multiple-CNP components.

5.6. References

[1]. B.L. Cushing, V.L. Kolesnichenko, and C.J. O'Connor, *Chem. Rev.*, **104**, 3893 (2001).

[2]. G. Schmid (*Ed.*), *'Nanoparticles: From Theory to Application'*, *2nd ed.* (John Wiley & Sons, New York, 2004).

[3]. M. Hosokawa, K. Nogi, M. Naito, and T. Yokoyama (*Ed.*), *'Nanoparticle Technology Handbook'*, (Elsevier, Oxford, 2007).

[4]. H. Singh, P.E. Laibnis, and T.A. Hatton, *Nano Lett.*, **5**, 2149 (2005); H. Singh, P.E. Laibinis, and T.A. Hatton, *Langmuir*, **21**, 11500 (2005).

[5]. J. Dzubiella, G.P. Hoffmann, and H. Lowen, *Phys. Rev. E*, **65**, 021402 (2002).

[6]. H. Iida, K. Takayanagi, T. Nakanishi, and T. Osaka, *J. Coll. Inter. Sci.*, **314**, 274 (2007).

[7]. K.H. Li and B.B. Yellen, *Appl. Phys. Lett.*, **97**, 083105 (2010).

[8]. J. Kim, H. Yang, and P.F. Green, *Langmuir*, **28**, 9735 (2012).

[9]. J. Zeng, C. Chen, P. Vedantam, V. Brown, T.J. Tzeng, and X. Xuan, *J. Micromech. Microeng.*, **22**, 105018 (2012).

[10]. A.R. Bijanzadeh, M.R. Vakili, and R. Khordad, *Inter. J. Phys. Sci.*, **7**, 1943 (2012).

[11]. K.M. Gattas-Asfura, Y. Zheng, M. Micic, M.J. Snedaker, X. Ji, G. Sui, J. Orbulescu, F.M. Andreopouos, S.M. Pham, C. Wang, and R.M. Leblanc, *J. Phys. Chem. B*, **107**, 10464 (2003).

[12]. H.E. Horng, C. Hong, S.Y. Yang, and H.C. Yang, *Appl. Phys. Lett.*, **82**, 2434 (2003).

[13]. R.E. Rosensweig, *'Ferrohydrodynamics'*, (Cambridge Univ. Press, New York, 1985).

[14]. D. Dendukuri, D.C. Pregibon, J. Collins, T.A. Hatton, and P.S. Doyle, *Nat. Mater.*, **5**, 365 (2006).

[15]. K.P. Yuet, D.K. Hwang, R. Haghgooie, and P.S. Doyle, *Langmuir*, **26**, 4281 (2009).

[16]. W. Stober, A. Fink, and E. Bohn, *J. Coll. Inter. Sci.*, **26**, 62 (1968).

[17]. R. Vacassy, R.J. Flatt, H. Hofmann, K.S. Choi, and R.K. Sing, *J. Coll. Inter. Sci.*, **227**, 302 (2000).

[18]. A. Priola, G. Gozzelino, F. Ferrero, and G. Maulcelli, *Polymer*, **34**, 3653 (1993).

[19]. K. Matyjaszewski and T.S. Davis (*Ed.*), *'Handbook of Radical Polymerization'*, (Wiley & Sons Inc., New York, 2003).

[20]. N. Bowden *et al.*, *Nature (London)*, **393**, 146 (1998); K.Y. Suh, Y.S. Kim, and H.H. Lee, *Adv. Mater. (Weinheim)*, **13**, 1386 (2001).

[21]. S.J. Kwon, J.H. Park, and J.G. Park, *Appl. Phys. Lett.*, **87**,133112 (2005).

[22]. C. Kittel, *'Introduction to Solid State Physics'*, *8th ed.*, (John Wiley & Sons Inc., New York, 2005).

[23]. N.W. Ashcroft and N.D. Mermin,*'Introduction to Solid State Physics'*, (Harcout College Publishers, New York, 1987).

[24]. H. Du, *Appl. Opt.*, **43**, 1951 (2004).

[25]. R.M. Erb, D.S. Sebba, A.A. Lazarides, and B.B. Yellen, *J. Appl. Phys.*, **103**, 063916 (2008).

[26]. A. Schlegel, S.F. Alvarado, and P. Wachter, *J. Phys. C*, **12**, 1157 (1979).

[27]. W. Haiss, N.T.K. Thanh, J. Aveyard, and D.G. Femig, *Anal. Chem.*, **79**, 4215 (2007).

[28]. J. Richardi, M.P. Pileni, and J.J. Weis, *Phys. Rev. E*, **77**, 061510 (2008).

[29]. T. Kruse, A. Spanoudaki, and R. Pelster, *Phys. Rev. B*, **68**, 054208 (2003).

[30]. Z. Di, D. Zhang, and X. Chen, *J. Appl. Phys.*, **104**, 093109 (2008).

[31]. J.D. Jackson, *'Classical Electrodynamics', 3rd ed.,* (Wiley, New York, 1999).

[32]. J.N. Israellachivili, *'Intermolecular and Surface Forces', 2nd ed.* (Academic Press, New York, 1992).

[33]. W.A. Steele, *J. Coll. Inter. Sci.*, **75**, 13 (1980).

[34]. J. Chan, J.J. Popov, S. Kolisnek-Kehl, and D.G. Leaist, *J. Soln. Chem.*, **32**, 197 (2003).

[35]. L. Shen, A. Stachowiak, S.K. Fateen, P.E. Laibinis, and T.A. Hatton, *Langmuir*, **17**, 288 (2000).

[36]. J.N. Canongia Lopes, *Phys. Chem. Chem. Phys.*, **4**, 949 (2002).

[37]. S.K. Suh, *Ph.D. Thesis, M.I.T.* (2011).

[38]. T.S. Shim *et al.*, *Adv. Mater. (Weinheim)*, **22**, 4494 (2010).

[39]. E.W. Marchand, '*Gradient Index Optics*', (Academic Press, New York, 1978).

[40]. E. Hecht, '*Optics*', *4th ed.* (Addison-Wesley Longman Inc., New York, 2002).

[41]. R.P. Hemegner, L.F. Garner, and C.S. Ooi, *Invest. Ophth. & Vis. Sci.*, **36**, 703 (1995).

[42]. M. Bahrami and A.V. Goncharov, *J. Biomed. Opt.*, **17**, 055001 (2012).

[43]. W.N. Charman, Adnan, and D.A. Atchison, *Biomed. Opt. Exp.*, **3**, 3033 (2012).

Chapter 6

A Phase Field Model and Numerical Simulations for Spinodal Decomposition of Binary Colloidal Nanoparticles*

Abstract

The phase field model (PFM) is an important theoretical model, that describes the phase equilibrium and separation dynamics of mixtures. A PFM-based approach is suitable for studies of the assembly structure and dynamics of colloidal dispersions of nanoparticles (CNPs) in spatially and temporally large-scale systems. In the continuum framework for the NPs, a PFM-based simulation was applied to investigate the assembly structure and dynamics governed by spinodal decomposition. In particular, we focused on a ternary mixture in which a heterogeneous mixture of NPs was dispersed in a single liquid medium. For effective and efficient computer simulations, we employed several advanced numerical algorithms, including the spectral transform and semi-implicit-explicit separation (semi-IMEX) methods. We also examined a ternary mixture of CNPs confined in a thin film with selective wall interactions to study the surface-directed phase separation of the CNPs. A numerical simulation successfully described the large-scale phase separation dynamics of the ternary mixture. The dynamics of the scaling behavior of the characteristic length scale was slower than the conventional prediction. When the diffusivities and initial concentrations of the two NPs differed, the temporal evolution of the phase separation exhibited three stages. The confinement effect provided by the walls also resulted in three-stage temporal evolution of spinodal decomposition in which each stage was distinguished by its scaling exponent. A decrease in the scaling exponent in the later stage was caused by a geometric limit arising from the thickness of the thin film. The numerical studies of the phase-equilibrium and separation dynamics of ternary mixture of CNPs suggest a way to control the assembly structure and dynamics by controlling the film thickness and surface-interaction strength.

---

*Parts of Chapter 6 will be submitted to a peer-reviewed journal (Authored by S. Joon Kwon & T. Alan Hatton).

6.1. Introduction

An assembly of CNPs consisting of a homogeneous mixture of NPs in a single liquid dispersion medium is a representative case of a binary mixture under phase instability. In terms of industrial applications, however, it would be more desirable to employ heterogeneous CNPs in a single liquid dispersion medium; one of the simplest cases of heterogeneous CNPs is a ternary mixture composed of A- and B-type NPs dispersed in a liquid medium. We have already presented the results of calculations based on the self-consistent mean field (SCMF) method for surface-selectivity-induced separation of ternary CNPs in Chapters 4 and 5 and the external-field-directed separation of quaternary CNPs in Chapter 4. However, even with the SCMF method, it would be a computationally expensive calculation for continuous phase separation governed by spinodal decomposition of a ternary mixture over a wide range of spatial dimensions. Additionally, as mentioned in Chapters 4 and 5, the SCMF method can be used only to describe the equilibrium morphology of a CNP. Considering that the dynamic properties of the phase separation would be important information for controlling the assembly of CNPs, a kinetic Monte Carlo (KMC) algorithm or Brownian dynamics (BD) simulation would be considered to analyze the non-equilibrium properties of phase separation of ternary CNPs. However, these methods are also computationally expensive for the description of realistic spatio-temporal dimensions for larger system sizes as mentioned in Chapter 1.

Therefore, we need a more computationally efficient method of solving the time-dependent phase separation dynamics of a ternary mixture of CNPs. Moreover, without considering the discreteness of the NPs, computational efficiency should require that the system dimensions are much larger than the feature size of the NPs. For example, if one type of NPs is 100 nm in diameter, we need to consider a system with x - y dimensions of at least $100 \times 100\ \mu m^2$. Provide we can neglect the effects of the discreteness of the NPs, we can employ a continuum-based model such as the phase field model (PFM), in which the concentrations of the NPs and the dispersion media are considered as continuum variables [1,2]. By using advanced numerical algorithms to solve the continuum-based differential equation that describes the temporal evolution of the concentration fields, we can efficiently and effectively analyze the problem of assembly driven by spinodal decomposition of ternary mixture of CNPs in terms of both the equilibrium and non-equilibrium properties.

In Chapter 6, we present computational studies using the PFM and the diffuse interface model of spinodal decomposition of ternary mixture of CNPs assuming that the CNPs are confined in thin films. We also apply the numerical method to extend the study to cover spinodal decomposition of ternary mixture of CNPs when the CNPs are confined in a thin film with surfaces that are selective to specific

NPs. On the basis of the studies, we calculate the time-dependence of the characteristic length scale such as the spinodal wavelength and the concentration variance of each component as a function of time. The dynamic properties of the assembled morphologies of ternary mixture of CNPs will provide a substantial advantage in understanding and controlling CNP mixtures at the desired moments.

6.2. Theoretical Framework

6.2.1. Phase Field Model for CNPs

The phase is defined as a physical entity that represents a specific microstructure in which specific thermodynamic properties are distinguished from others in other entities. Typically, the thermodynamic state function, such as the free energy in combinbation with the seleceted ensemble, is used to define the phase. The phase field model (PFM) was developed to describe the dynamics and equilibrium properties of a system composed of two or more phases that normally contain two or more components. In addition, it has been widely used in a continuum framework to analyze dynamic processes such as nucleation, crystallization, and other diffusion-driven processes, as well as spinodal decomposition [1,2]. In particular, it employs the diffuse interface model, which assumes a continuous variation in the order parameter at the interface between two different microstructures considered as two phases. For a multi-component mixture, the order parameter is typically set to the difference between the concentrations of the components, and the PFM considers the local fluctuation in the order parameter in response to the spontaneous phase separation of the mixture into multiple-phases at equilibrium. Before discussing complicated cases such as a ternary mixture, it would be instructive to recap how the PFM addresses the interface energy and thickness of a multi-phases system. For simplicity, we discuss a representative PFM of homogeneous CNPs (i.e., a binary mixture of NPs and the dispersion medium) in this section. Using the regular solution model [3-5], the free energy of the mixture at a temperature T with fixed number-temperature-volume ensemble (i.e., canonical ensemble) and no spatial fluctuation in the concentration field, Δf_0, can be written as

$$\frac{\Delta f_0}{k_B T} = \frac{\chi \phi_p \left(1-\phi_p\right)}{h} + \frac{1}{h^3}\left(\left(1-\phi_p\right)\ln\left(1-\phi_p\right) + \phi_p \ln \phi_p\right), \tag{6.1}$$

where k_B is the Boltzmann constant, ϕ_p is the volume fraction of NPs, and χ is the Flory-Huggins interaction parameter [5]. In eq.(6.1), the size difference between NPs and the unit molecule of the

dispersion medium is also considered by introducing the size ratio h. As shown by Cahn and Hilliard [1,2], the interfacial free energy between two phases originates in the non-uniformity of the thermodynamic intensive variables such as the concentration. This non-uniformity causes a phase transition in a mixture. The local fluctuation in the concentration field, $\phi_p(\mathbf{r})$, can be expanded using a Taylor series around the initial concentration $\phi_p^{(0)}$

$$\phi_p(\mathbf{r}) \approx \phi_p^{(0)} + \frac{1}{2}\sum_{i=1}^{3}\left(x_i^2 \frac{\partial^2 \phi_p}{\partial x_i^2} \right) = \phi_p^{(0)} + \frac{1}{2}\frac{\partial^2 \phi_p}{\partial x^2}\sum_{i=1}^{3} x_i^2, \; x = x_1.$$

Considering the local concentration fluctuation, the Helmholtz free energy for the non-uniform mixture, Δf_N, is given by

$$\frac{\Delta f_N}{k_B T} = \frac{\Delta f_0}{k_B T} - \kappa \phi_p \frac{\partial^2 \phi_p}{\partial X^2}, \; \kappa = \frac{h\chi}{2}, \tag{6.2}$$

where κ denotes the phenomenological gradient energy coefficient in the PFM based on the diffuse interface model [1,2] and can be approximated as a quantity proportional to χ when the molecular interaction among the components is effective only at short-range. In eq.(6.2), we transformed the spatial unit by normalization with respect to the size of the NP (i.e., $x \to X$). According to the original definition in the Cahn-Hilliard equation [1,2], the specific interfacial free energy per unit, Γ, is expressed by considering $\Delta f_N - \Delta f^{(eq)}$, which is the Helmholtz mixing free energy per unit volume for CNPs with a uniform and continuous concentration distribution, as follows:

$$\begin{aligned}
&\frac{\Gamma}{k_B T} = \int_{-\infty}^{\infty} \left(\frac{\Delta f_N - \Delta f^{(eq)}}{k_B T} \right) dX, \\
&\Delta f^{(eq)}\left(\phi_p\right) = \phi_p \mu_p\left(\phi_p^{(eq)}\right) + \left(1-\phi_p\right)\mu_1\left(\phi_p^{(eq)}\right), \\
&\mu_p = \Delta f_0 + \left(1-\phi_p\right)\left(\frac{\partial \Delta f_0}{\partial \phi_p}\right)_T, \; \mu_1 = \Delta f_0 - \phi_p\left(\frac{\partial \Delta f_0}{\partial \phi_p}\right)_T,
\end{aligned} \tag{6.3}$$

where μ_j is the chemical potential (i.e., $j=1$ for solvent and $j=p$ for the NPs) and $\phi_p^{(eq)}$ is the equilibrium volume fraction of NPs such that $\phi_p^{(eq)} = \phi_p^{(\alpha)}$, satisfying the bimodal phase boundary. The superscript α denotes the separated phase in which the NP-concentration is dilute. The bimodal boundary is given as

$$1 = h^2 \chi \left(2\phi_p{}^{(\alpha)} - 1\right) / \ln\left(\frac{\phi_p{}^{(\alpha)}}{1-\phi_p{}^{(\alpha)}}\right).$$

From eq.(6.3), we can obtain the following relationship:

$$\begin{aligned}
\frac{\Gamma}{k_B T} &= \int_{-\infty}^{\infty} \left(-\frac{\chi\left(\phi_p - \phi_p{}^{(\alpha)}\right)^2}{h} + \frac{1}{h^3}\left(\phi_p \ln\frac{\phi_p}{\phi_p{}^{(\alpha)}} + \left(1-\phi_p\right)\ln\frac{1-\phi_p}{1-\phi_p{}^{(\alpha)}} \right) - \kappa\phi_p \frac{\partial^2 \phi_p}{\partial X^2} \right) dX, \\
&= 2^{1/2}\chi \int_{\phi_p{}^{(\alpha)}}^{1-\phi_p{}^{(\alpha)}} \left(\phi_p - \phi_p{}^2 - \left(1-\phi_p{}^{(\alpha)}\right)^2 + \frac{\left(2\phi_p{}^{(\alpha)} - 1\right)\left(P\left(\phi_p\right) - \ln\phi_p{}^{(\alpha)}\right)}{\ln\left(\phi_p{}^{(\alpha)} / \left(1-\phi_p{}^{(\alpha)}\right)\right)} \right)^{1/2} d\phi_p, \\
P\left(\phi_p\right) &\equiv \phi_p \log\phi_p + \left(1-\phi_p\right)\log\left(1-\phi_p\right),
\end{aligned} \tag{6.4}$$

where we used the Euler equation to transform the integrand in the first row with a boundary condition such that the infinitesimal variance in Γ with respect to ϕ_p is zero. This boundary condition is equivalent to the condition that is used to obtain the stationary (minimum) value of Γ in the context of the least action principle derived from the Euler-Lagrange equation. From eq.(6.4), we can find an asymptotic value of Γ near the zero-temperature:

$$\frac{\Gamma_{(0)}}{k_B T} \equiv \lim_{\substack{T\to 0 \\ (or\ \phi_p{}^{(\alpha)}\to 0)}} \frac{\Gamma}{k_B T} = 2^{1/2}\chi \int_0^1 \left(\phi_p\left(1-\phi_p\right)\right)^{1/2} d\phi_p = 2^{-3/2}\pi\chi, \tag{6.5}$$

Notably, $\Gamma_{(0)}$ shows no dependence on the NP size and increases with χ. To analyze the behavior of Γ near the critical point (or spinodal point), $\Gamma_{(C)}$, at $\phi_p = 1/2$ when $T = T_C$, where T_C is the upper critical solution temperature (or the consolute temperature), $\Delta f_N - \Delta f_0^{(\alpha+\beta)}$ (where β denotes the separated phase in which NPs concentration is rich) can be expanded as follows:

$$\begin{aligned}
\frac{\Delta f_N - \Delta f_0^{(\alpha+\beta)}}{k_B T} &= \frac{3\left(t_C - 1\right)^2}{4h^3 t_C} + \frac{2\left(t_C - 1\right)\left(\phi_p - \frac{1}{2}\right)^2}{h^3} + \frac{4t_C\left(\phi_p - \frac{1}{2}\right)^4}{3h^3} + \cdots \\
&\approx \frac{3}{h^3 t_C}\left(\left(\frac{t_C - t}{2}\right) + \frac{2t_C}{3}\left(\phi_p - \frac{1}{2}\right)^2 \right)^2, \quad t_C = \frac{h^2 \chi\big|_{T=T_C}}{2}.
\end{aligned} \tag{6.6}$$

From eqs.(6.5) and (6.6), $\Gamma_{(C)}$ can be calculated as

$$\frac{\Gamma_{(C)}}{k_B T} = \frac{\chi}{h}\left(\frac{3}{2t_C}\right)^{1/2} \int_{\phi_p^{(\alpha)}}^{1-\phi_p^{(\alpha)}} \left(\frac{t_C - 1}{2} + \frac{2t_C\left(\phi_p - \frac{1}{2}\right)^2}{3} \right) d\phi_p \approx \frac{2^{1/2}\chi}{h}\frac{(t_C - 1)^{3/2}}{t_C}, \tag{6.7}$$

where we used the relationship $1-2\phi_p^{(\alpha)} \approx \left(3(t_C-1)/t_C\right)^{1/2}$ to calculate $1-2\phi_p^{(\alpha)}$ near the critical point. Eq.(6.7) indicates that $\Gamma_{(C)}$ is inversely proportional to the NP size. The temperature dependence of $\Gamma_{(C)}$ exhibits scaling behavior predicted by the mean-field approximation for a phase transforms in conjunction with a conserved order-parameter [1,2], as shown in Figure 6.1. In the figure, we show the relationship between Γ and the temperature for different χ ; Γ increases with increasing χ . To analyze the systematic temperature-dependence of Γ, we collapsed all the data by normalization $\Gamma/\Gamma_{(0)}$ and T/T_C. From the normalized plot, we can identify a single functional relationship between $\Gamma/\Gamma_{(0)}$ and T/T_C. Not surprisingly, this single dependence is due to a functional form of T/T_C , $T/T_C = 2\left(2\phi_p - 1\right)/\ln\left(\phi_p/\left(1-\phi_p\right)\right)$, which does not contain information on the physical properties of the NP represented by χ .

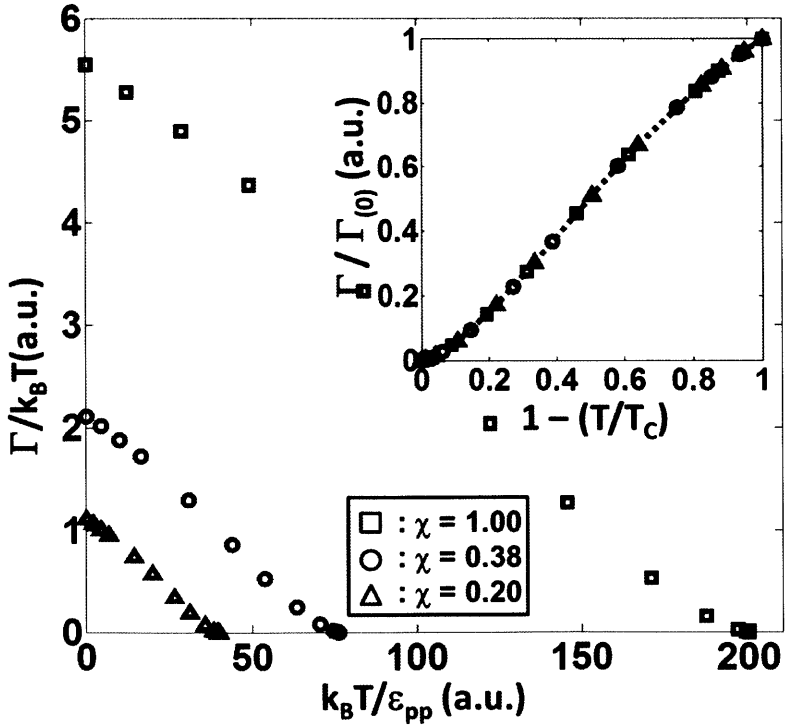

Figure 6.1. Relationship the specific interfacial energy, Γ, and the normalized temperature, $k_B T / \varepsilon_{pp}$, where ε_{pp} denotes the molecular interaction among the NPs with different Flory-Huggins interaction parameters (χ). Inset is for the normalized Γ with respect to the zero-temperature interfacial energy, $\Gamma / \Gamma_{(0)}$, as a function of the normalized deviation from the critical temperature (T_C).

In addition, the NP size and long-range interactions have no effect on the temperature dependence of $\Gamma / \Gamma_{(0)}$. The temperature dependence of $\Gamma / \Gamma_{(0)}$ can be fitted with a power function proposed by van der Waals (called the vdW function), which is given by

$$\frac{\Gamma}{\Gamma_{(0)}} = \left(1 - \frac{T}{T_C}\right)^n .$$

According to the Cahn-Hilliard theoretical analysis based on the lattice model and Guggenheim's research on liquid phase Ne, Ar, N_2, and O_2, the best-fit scaling exponent for the vdW function is $n = 1.21 \sim 1.22$ [6,7]. We applied the vdW fitting for $\Gamma / \Gamma_{(0)}$ and found an optimal fitting exponent of $n = 1.108 \pm 0.056$, which is in good agreement with the prediciton; but is slightly smaller.

The interface profile of CNPs is continuous from the NP-dilute to the NP-rich phase at equilibrium. This is mainly because the composition is a conserved order-parameter in the PFM. As illustrated in Figure 6.2(a), the concentration variation over the interface is continuous; therefore, it is possible to describe the interface thickness as a functional of $\phi_p(\mathbf{r})$. To perform a systematic analysis, we can adapt a definition of the interface thickness L_I using the diffuse interface method as suggested by Cahn and Hilliard [1,2]:

$$L_I \equiv \frac{\Delta\phi_p^{(eq)}}{\max\left(\frac{\partial \phi_p}{\partial X}\right)} = \Delta\phi_p^{(eq)} \left(\frac{h\chi}{2\max\left(\Delta f_N - \Delta f_0^{(\alpha+\beta)}\right)} \right)^{1/2}, \tag{6.8}$$

where the volume fraction difference between the NP-rich and NP-dilute phases at equilibrium, $\Delta\phi_p^{(eq)}$, is equal to $1 - 2\Delta\phi_p^{(\alpha)}$.

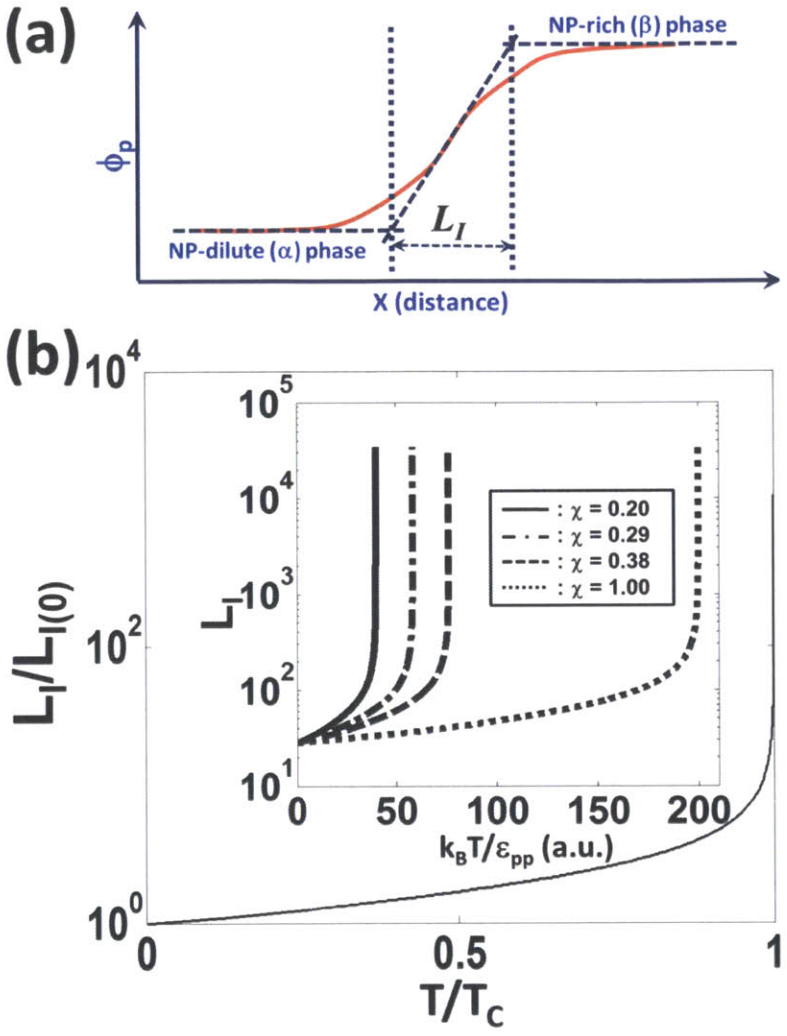

Figure 6.2. (a) A schematic diagram showing the concentration (ϕ_p) profile (red solid line) in the interface area with depicted interface thickness (L_I) based on the diffuse interface model. (b) A relationship between the normalized interface thickness form by the phase separation of CNPs with size factor $h = 20$, $L_I / L_{I(0)}$, where $L_{I(0)}$ is for the interface thickness at zero temperature, and the normalized temperature, T / T_C. Given in the inset are the relationship between L_I and the normalized temperature with different values of χ. As $T \to T_C$, L_I shows a diverging behavior which indicates that the two phases become homogeneous to form one phase.

In eq.(6.8), $\max\left(\partial\phi_p / \partial X\right)$ is obtained at $\phi_p = 1/2$; therefore, it is straightforward to find L_I as follows:

$$L_I = \frac{\left(1-2\phi_p^{(\alpha)}\right)h}{\left(\frac{\left(1-4\left(1-\phi_p^{(\alpha)}\right)^2\right)}{2} - \frac{2\ln\left(2\phi_p^{(\alpha)}\right)}{\chi h^2}\right)^{1/2}}. \tag{6.9}$$

Further, from eqs.(6.8) and (6.9), we can also find the interface thickness near zero temperature, $L_{I(0)}$, and the critical points $L_{I(C)}$ as follows:

$$L_{I(0)} = 2^{1/2}h,\ L_{I(C)} = 2^{1/2}h^2\left(\frac{\chi}{(T_C/T)-1}\right)^{1/2}, \tag{6.10}$$

From eq.(6.10), we can observe that $L_{I(0)}$ is linearly proportional to the NP size, whereas $L_{I(C)}$ has a quadratic proportionality to the NP size. From these size dependences at two extreme temperatures, we can conjecture that the NP size dependence of the interface thickness would be $L_I \propto h^{\upsilon}$, where $1 \le \upsilon \le 2$. As eq.(6.10) shows, L_I diverges as $T \to T_C$, as predicted by van der Waals and Cahn-Hilliard [1,2,7]. In Figure 6.2(b), we see the divergent behavior of the normalized interface thickness $L_I / L_{I(0)}$ as $T \to T_C$ irrespective of the values of χ.

6.2.2. Model of Spinodal Decomposition of a Ternary Mixture

To develop a computational framework for the ternary mixture, let us model the system as non-uniform in terms of the spatial distribution of the concentrations of the species. For the model mixture of the materials, we consider a ternary mixture of A- and B-NPs dispersed in a medium denoted by S. Therefore, we need to employ two independent variables describing the free energy of the system at constant temperature, ϕ_A and ϕ_B, where ϕ_i denotes the volume fraction of the ith species. For this model, we assumed that voids in the system can be included in S. When two or more different chemical species are mixed and are energetically favorable to each other, the distribution of the materials is completely random, and the system has free energy per unit volume, $f_0\left(\phi_A, \phi_B\right)$. In the spirit of the regular solution model based on the discrete lattice-type system [3,4], $f_0\left(\phi_A, \phi_B\right)$ is written as:

$$\frac{f_0(\phi_A,\phi_B)}{k_BT}=\frac{\chi_{AB}\phi_A\phi_B}{h^2}+\frac{\chi_{AS}\phi_A\phi_S}{h}+\frac{\chi_{BS}\phi_B\phi_S}{h}+\left(\frac{\phi_A\ln\phi_A}{h^3}+\frac{\phi_B\ln\phi_B}{h^3}+\phi_S\ln\phi_S\right), \tag{6.11}$$

where χ_{ij} represents the Flory-Huggins interaction parameters for the molecular interaction between the ith and j th species. The therrmodynamic stability criteria for the temperature T and pressure P at which a ternary mixture is unstable should be given by [4]

$$\prod_i\left(\left.\frac{\partial^2 f_0}{\partial\phi_i^{\,2}}\right|_{\phi_{j\neq S},T,P}\right)>\left(\left.\frac{\partial^2 f_0}{\partial\phi_i\partial\phi_j}\right|_{T,P}\right)^2. \tag{6.12}$$

The condition in eq.(6.12) is associated with unrestricted instability of the phase, which leads to spinodal decomposition of a ternary mixture.

When the ternary mixture exhibits a non-uniform distribution of the components (only two compositions of the ternary mixtures are independent), we should consider the variance in the free energy produced by the gradient effects of the distributions. In the spirit of Cahn and Hilliard's original concept [1,2], we can identify the driving force for phase separation as the difference in the chemical potential in two coexisting phases. For a homogeneous system with a spatially non-uniform distribution of NPs deviating from their initial conditions, $\phi_{A,0}$ and $\phi_{B,0}$, we can express the Helmholtz free energies per unit lattice as a functional of $\phi_A(\mathbf{r})$ and $\phi_B(\mathbf{r})$, $f_N\left[\phi_A(\mathbf{r}),\phi_B(\mathbf{r})\right]=f_N\left(\phi_A,\phi_B,\nabla\phi_A,\nabla\phi_B,\nabla^2\phi_A,\nabla^2\phi_B,\cdots\right)$, where the subscript N denotes the non-uniform case. The spatial non-uniformity of the composition across the system is derived mainly from local fluctuations in ϕ_A and ϕ_B, which can be expressed as a function of the distance vector $\mathbf{r}$,

$$\phi_j(\mathbf{r})=\phi_j^{(0)}+(\mathbf{r}\cdot\nabla)\phi_j+\frac{(\mathbf{r}\cdot\nabla)^2\phi_j}{2}+\cdots,\ j=A\text{ or }B,$$

where the superscript (0) denotes the initial volume fraction. Considering the inversion operation for symmetry and neglecting the fourth- and higher-order derivative terms, $\phi_A(\mathbf{r})$ and $\phi_B(\mathbf{r})$ are approximated as

$$\phi_j(\mathbf{r})\approx\phi_j^{(0)}+\frac{1}{2}\frac{\partial^2\phi_j}{\partial x^2}\sum_{i=1}^{3}x_i^{\,2},\ j=A\text{ or }B,$$

assuming an isotropic lattice system. Therefore, f_N on the continuum basis can be written as an expanded function around f_0 as

$$\frac{f_N}{k_BT} \approx \frac{f_0}{k_BT} + \frac{1}{2}\sum_{i,j}^{A,B} \kappa_{ij}\left(\nabla\phi_i \cdot \nabla\phi_j\right),\ \kappa_{ij} = \left.\frac{\partial^2\left(f_0/k_BT\right)}{\partial\left(\nabla\phi_i\right)\partial\left(\nabla\phi_j\right)}\right|_{\nabla\phi_i=\nabla\phi_j=0},$$
$$F_N = \int_V f_N dV, \tag{6.13}$$

where V is the total volume of the system and F_N is the total free energy of the system. In eq.(6.13), the second-order terms κ_{ij} are defined as the phenomenological gradient energy coefficients, which determine the energy cost to form the diffuse interface among phases [1,2].

To find the phase separation kinetics, we can express the fluxes of A- and B-NPs in a closed system, $\mathbf{J_A}$ and $\mathbf{J_B}$, as [8]:

$$\mathbf{J_A} = \mathbf{j_A} - c_A\left(\upsilon_A\mathbf{j_A} + \upsilon_B\mathbf{j_B} + \upsilon_S\mathbf{j_S}\right),\ \mathbf{J}_B = \mathbf{j_B} - c_B\left(\upsilon_A\mathbf{j_A} + \upsilon_B\mathbf{j_B} + \upsilon_S\mathbf{j_S}\right),$$
$$\mathbf{j_A} = -c_AL_Ah^3\nabla\mu_A,\ \mathbf{j_B} = -c_BL_Bh^3\nabla\mu_B,\ \mathbf{j_S} = -c_SL_S\nabla\mu_S,$$
$$L_A = \frac{1}{h^3}\left(\frac{L_{AA}}{c_A} - \frac{L_{AS}}{c_S} - \frac{L_{AB}}{c_B}\right), L_B = \frac{1}{h^3}\left(\frac{L_{BB}}{c_2} - \frac{L_{BS}}{c_S} - \frac{L_{BA}}{c_A}\right),\ L_S = \left(\frac{L_{SS}}{c_S} - \frac{L_{SA}}{c_A} - \frac{L_{SB}}{c_B}\right),$$
$$c_A = \frac{\phi_A}{h^3l^3},\ c_B = \frac{\phi_B}{h^3l^3},\ c_S = \frac{\phi_S}{l^3},\ \upsilon_A = \upsilon_B = h^3l^3,\ \upsilon_S = l^3, \tag{6.14}$$

where c_A, c_B, and c_S are the number densities of A- and B-NPs and the solvent, respectively, and L_{ij} is the Onsager coefficient for ternary mixture inter-diffusion [2]. Further, l^3 denotes the unit molecular volume of the solvent molecules. According to Manning [9], we can ignore the cross Onsager coefficients such as $L_{SA}(=L_{AS})$, $L_{BA}(=L_{AB})$, and $L_{SB}(=L_{BS})$ for isotropic transport with a negligible vacancy fraction. From the Gibbs-Duhem relationship, $\sum_i^{A,B,S}\phi_i\nabla\mu_i = 0$ [2], and a zero-lattice flux condition, $\phi_AL_Ah^3\nabla\mu_A + \phi_BL_Bh^3\nabla\mu_B + \phi_SL_S\nabla\mu_S = 0$, we can also find that $h^3L_A = h^3L_B = L_S$. From this fact and by using eq.(6.14), we can simplify $\mathbf{J_A}$ as follows:

$$\mathbf{J}_A = -\frac{D_A\phi_A}{k_BTh^3l^3}\left[\left(1-\phi_A\right)\nabla\left(\left.\frac{\partial f_0}{\partial\phi_A}\right|_{T,P,\phi_B} - \kappa_{AA}\nabla^2\phi_A - \bar{\kappa}\nabla^2\phi_B\right) - \phi_B\nabla\left(\left.\frac{\partial f_0}{\partial\phi_B}\right|_{T,P,\phi_A} - \kappa_{BB}\nabla^2\phi_B - \bar{\kappa}\nabla^2\phi_A\right)\right],\ \bar{\kappa} \equiv \frac{\left(\kappa_{BA}+\kappa_{AB}\right)}{2}, \tag{6.15}$$

and $\mathbf{J_B}$ can be found in a similar form. By inserting eq.(6.15) into the continuity equation for mass conservation, we can obtain the governing partial differential equation describing the phase separation dynamics of a ternary mixture by spinodal decomposition

$$\frac{\partial \phi_A}{\partial t} = \nabla\left[M_{AA}\nabla\left(\left.\frac{\partial f_0}{\partial \phi_A}\right|_{T,P,\phi_B} - \kappa_{AA}\nabla^2\phi_A - \bar{\kappa}\nabla^2\phi_B \right) - M_{AB}\nabla\left(\left.\frac{\partial f_0}{\partial \phi_B}\right|_{T,P,\phi_A} - \kappa_{BB}\nabla^2\phi_B - \bar{\kappa}\nabla^2\phi_A \right)\right],$$

$$M_{ii} \equiv \frac{D_i\phi_i(1-\phi_i)}{k_BT}, M_{ij} \equiv \frac{D_i\phi_i\phi_j}{k_BT},$$

$$\kappa_{AA} = l^2\chi_{AS},\ \kappa_{BB} = l^2\chi_{BS},\ \kappa_{AB} = \kappa_{BA} = \frac{\bar{\kappa}}{2} = h^2l^2\frac{(\chi_{AS} + \chi_{BS} - \chi_{AB})}{2}, \qquad (6.16)$$

where the spatial dimension was normalized with respect to the NP size. In addition, the relationships between κ_{ij} and χ_{lk} are obtained using a regular solution model considering only nearest-neighbor interactions with constant χ_{lk} [4]. To analyze the characteristic length scale, we first calculate the critical wave vector $\mathbf{q_C}$, which dominates the growth of the decomposed domain in the earlier stage of phase separation. For this analysis, eq.(6.16) is further simplified around the initial condition $\phi_i = \phi_{i,0}$ as follows:

$$\frac{\partial \phi_i}{\partial t} \approx M_{ii,0}\left[\left(\left.\frac{\partial^2 f_0}{\partial \phi_i^2}\right|_{T,P,\phi_j,\phi_i=\phi_{i,0}}\right)\nabla^2\phi_i - \kappa_{ii}\nabla^4\phi_i - \bar{\kappa}\nabla^4\phi_j\right] - M_{ij,0}\left[\left(\left.\frac{\partial^2 f_0}{\partial \phi_j^2}\right|_{T,P,\phi_i,\phi_j=\phi_{j,0}}\right)\nabla^2\phi_j - \kappa_{jj}\nabla^4\phi_j - \bar{\kappa}\nabla^4\phi_i\right], \qquad (6.17)$$

From the Fourier-transformed form of eq.(6.17), $\mathbf{q_C}$ is found as

$$\left.\frac{\partial \hat{\phi}_i}{\partial t}\right|_{\mathbf{q}=\mathbf{q_C}} \approx -\mathbf{q_C}^2\left[\hat{\phi}_i\left(M_{ii,0}f_{0,i}'' + \mathbf{q_C}^2M_{ii,0}\kappa_{ii} - \mathbf{q_C}^2M_{ij,0}\bar{\kappa}\right) - \hat{\phi}_j\left(M_{ij,0}f_{0,j}'' + \mathbf{q_C}^2M_{ij,0}\kappa_{jj} - \mathbf{q_C}^2M_{ii,0}\bar{\kappa}\right)\right] = 0,$$

$$f_{0,i}'' \equiv \left(\left.\frac{\partial^2 f_0}{\partial \phi_i^2}\right|_{T,P,\phi_j,\phi_i=\phi_{i,0}}\right). \qquad (6.18)$$

From eq.(6.18), the fastest growing mode $\mathbf{q_m}$ governing fluctuations of both ϕ_A and ϕ_B can be obtained by calculating $\left.\frac{\partial\left(\partial\hat{\phi}_i/\partial t\right)}{\partial \mathbf{q}^2}\right|_{\mathbf{q}^2=\mathbf{q_m}^2} = 0$.

6.3. Numerical Methods

6.3.1. Transformation by Spectral Methods

Depending on the boundary condition, a spectral method such as the fast Fourier transform (FFT) can be employed for the periodic boundary condition or the discrete cosine transform (DCT) for the non-flux boundary condition (or Neumann condition) [10-12]. For example, the DCT for the concentration variable for spinodal decomposition in three spatial dimensions can be expressed as:

$$\phi_A\left(\frac{L_x(i-1)}{N_x},\frac{L_y(j-1)}{N_y},\frac{L_z(k-1)}{N_z},\tau_n\right)\equiv\phi_{A(i,j,k,n)},$$

$$\phi_{A(i,j,k,n)}=\sum_{r=0}^{N_x-1}\sum_{s=0}^{N_y-1}\sum_{p=0}^{N_z-1}\alpha_r\alpha_s\alpha_p\widetilde{\phi}_{A(r,s,p,n)}\cos\left(\frac{\pi r(2i+1)}{2N_x}\right)\cos\left(\frac{\pi s(2j+1)}{2N_y}\right)\cos\left(\frac{\pi p(2k+1)}{2N_z}\right),$$

$$\text{where } \alpha_r=\frac{1}{N_x^{1/2}},\ \alpha_s=\frac{1}{N_y^{1/2}},\ \alpha_p=\frac{1}{N_z^{1/2}} \text{ for } r=s=p=0,$$

$$\alpha_r=\frac{2}{N_x^{1/2}},\ \alpha_s=\frac{2}{N_y^{1/2}},\ \alpha_p=\frac{2}{N_z^{1/2}} \text{ for } 1\le r\le N_x-1,\ 1\le s\le N_y-1,\ 1\le p\le N_z-1, \tag{6.19}$$

where N_x, N_y, and N_z are the numbers of finite difference points on each axis in 3D, and L_x, L_y, and L_z, are the lengths of the 3D system. In eq.(6.19), $\widetilde{\phi_A}$ denotes the transformed concentration of ϕ_A in the reciprocal space. On the basis of the eigenvalues for each of the points, $\lambda_{(r,s,p)}$,

$$\lambda_{(r,s,p)}=\left[2\left(\cos\left(\frac{2\pi r}{N_x}\right)+\cos\left(\frac{2\pi s}{N_y}\right)+\cos\left(\frac{2\pi p}{N_z}\right)\right)-6\right]/(\Delta X)^2,\ \Delta X=\frac{L_x}{N_x-1},$$

$$\nabla^2\phi_{p(i,j,k,n)}=\frac{\left(\phi_{p(i+1,j,k,n)}+\phi_{p(i,j+1,k,n)}+\phi_{p(i,j,k+1,n)}-6\phi_{p(i,j,k,n)}+\phi_{p(i-1,j,k,n)}+\phi_{p(i,j-1,k,n)}+\phi_{p(i,j,k-1,n)}\right)}{(\Delta X)}. \tag{6.20}$$

Then, we can express the transformed governing partial differential equation as:

$$\frac{\widetilde{\phi}_A(t_{n+1})-\widetilde{\phi}_A(t_n)}{\Delta t}\approx M_{AA}\left[\lambda\widetilde{\partial_{AB}f_0}(t_n)-2\kappa_{AA}\lambda^2\widetilde{\phi}_A(t_{n+1})-(\kappa_{AB}+\kappa_{BA})\lambda^2\widetilde{\phi}_B(t_{n+1})\right]$$
$$-M_{AB}\left[\lambda\widetilde{\partial_{BA}f_0}(t_n)-2\kappa_{BB}\lambda^2\widetilde{\phi}_B(t_{n+1})-(\kappa_{AB}+\kappa_{BA})\lambda^2\widetilde{\phi}_A(t_{n+1})\right], \tag{6.21}$$

where $\widetilde{\partial_{AB} f_0}(t_n)$ denotes the transformed functional of $\left(\left. \frac{\partial^2 f_0}{\partial \phi_A^{\,2}} \right|_{T,P,\phi_B} \right)$ at time t_n. Similarly, the transformed relationship for $\left(\widetilde{\phi_A}(t_{n+1}) - \widetilde{\phi_A}(t_n) \right) / \Delta t$ can be found. In eq.(6.21), we employed the forward Euler scheme to describe the temporal evolution. The meaning of eq.(6.21) is that we can transform the original partial differential equation into an ordinary differential equation only with respect to the temporal dimension. Therefore, the computational cost should decrease significantly if we numerically simulate a dynamic process governed by spinodal decomposition using a spectral transform. Similarly, the FFT, which describes the problem using a periodic boundary condition, will also greatly enhance the computational efficiency; however, it takes about twice the computational time of a DCT-based calculation, because the FFT considers both the sine and cosine terms for the transformation step, whereas the DCT considers only the cosine terms.

6.3.2. Separation of the Implicit and Explicit Parts

To enhance the numerical simulation efficiency and stability without divergence, we can employ advanced numerical techniques such as the semi-Implicit-Explicit parts separation (semi-IMEX) method. Considering the log-function in the expression of the free energy, we can apply the IMEX method as follows [8,10]:

$$\ln \phi_{l(i,j,k)}(\tau_{n+1}) \simeq \ln \phi_{l(i,j,k)}(\tau_n) + \frac{\phi_{l(i,j,k)}(\tau_{n+1})}{\phi_{l(i,j,k)}(\tau_n)} - 1, \; l = A \text{ and } B. \tag{6.22}$$

Furhter, eq.(6.22) can be inserted into eq.(6.21). From a calculation, we found that the IMEX method, combined with a spectral transform, allows us to increase the computational efficiency while maintaining numerical stability by increasing the integration time from $\delta t = 2 \sim 3 \times 10^{-6} s$ to $\delta t \sim 2 \times 10^{-5} s$, assuming a diffusivity of A- and B-NPs of $D_A = D_B = 10^{-12}$ $m^2 s^{-1}$. Although it is not shown in this chapter, we also found that a stable differential integration time should be set considering the relationship $\delta t D \sim 10^{-17}$ m^2. For further computational enhancement in solving the differential equation in eq.(6.21) with the semi-IMEX method, one can also adopt an advanced numerical technique such as the adaptive time-step spectral transform [8,10].

6.4. Results and Discussion

6.4.1. Spinodal Decomposition of Binary Mixture of CNPs

As the simplest case of phase separation of A-B binary CNPs, an unstable mixture was investigated with the initial condition $[\phi_{A0}\ \phi_{B0}\ \phi_{S0}]=[0.25\ 0.25\ 0.50]$ and the molecular interaction parameter $[\chi_{AB}\ \chi_{AS}\ \chi_{BS}]=[6\ 3\ 3]$. To initiate the decomposition, we applied a random fluctuation concentration field at the initial stage and numerically iterated the governing equation with a periodic boundary condition, assuming that $h=20$ and the diffusivities of A- and B-NPs are both 10^{-12} m^2s^{-1}. For numerical stability, a differential time of 10^{-5}s was employed. Considering that the typical unit molecular size of the solvent molecule is about 0.5 nm, the condition $h=20$ indicates that the size of NPs studied in the present simulation is about 10 nm. For the simulation box, we applied a 2D plane, which can be considered as a model for a thin film when the film thickness is comparable to the size of an NP or at most a few NPs. As Figure 6.3 shows, the phase separation is a continuous process initiated by a wavy concentration fluctuation followed by growth of the characteristic length scale of the system. For example, relatively small droplet-like concentrated regions of CNPs appear at earlier times (i.e., t = 10 s), and these concentrated regions merge to form larger concentrated areas. This process is similar to the well-known Ostwald ripening; however, spinodal decomposition is a continuous phase separation process, whereas the Ostwald ripening includes discontinuities in the concentration gradient near the boundaries of the concentrated droplets [13].

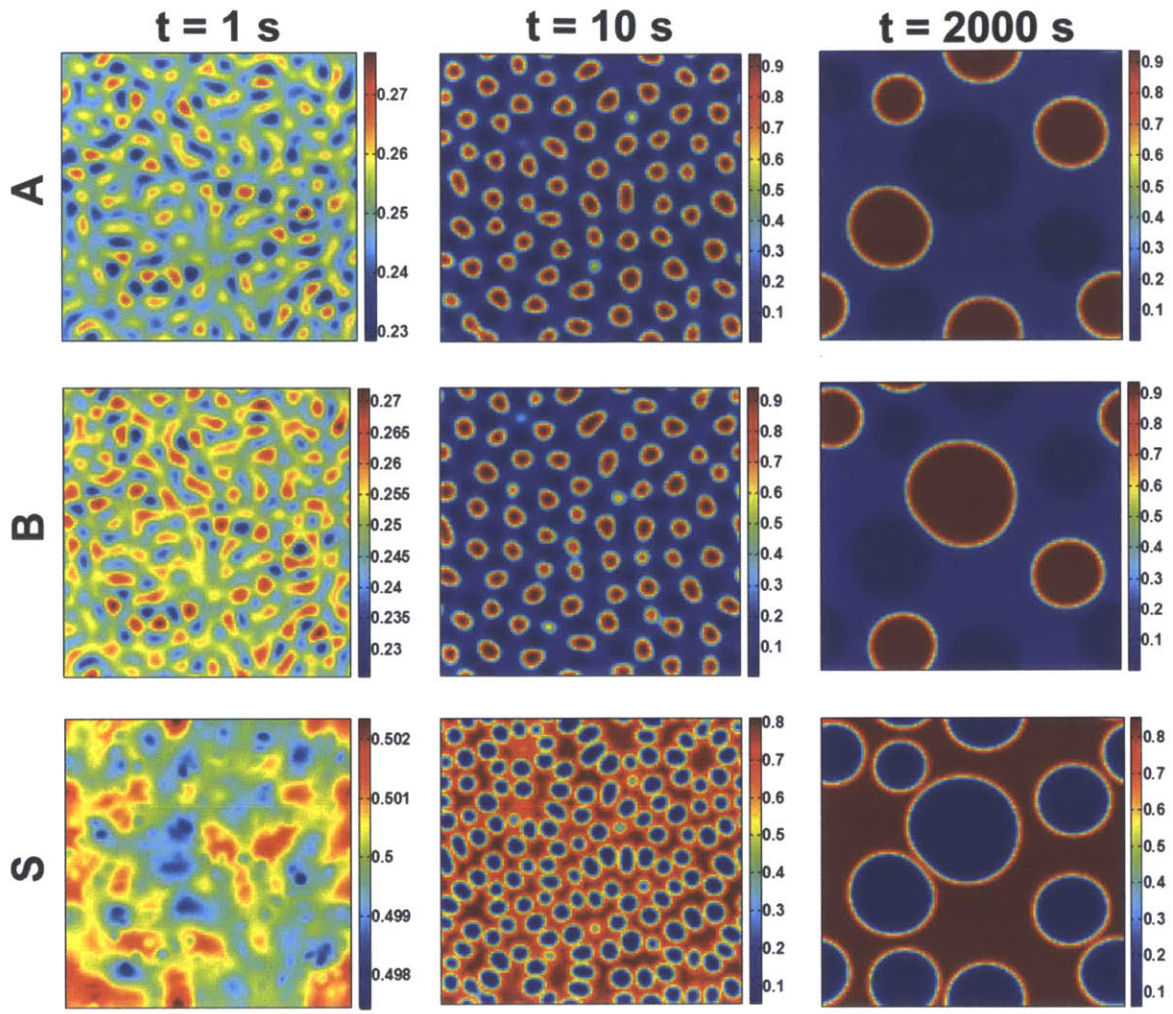

Figure 6.3. Time dependent concentration distributions of A- and B-NPs and the solvent S by spinodal decomposition when $[\phi_{A0}\ \phi_{B0}\ \phi_{S0}]=[0.25\ 0.25\ 0.50]$ and $[\chi_{AB}\ \chi_{AS}\ \chi_{BS}]=[6\ 3\ 3]$ with $D_A = D_B = 10^{-12}\ \mathrm{m^2 s^{-1}}$. The dimensions for the 2D simulation box is $24\times 24\ \mu\mathrm{m}^2$ incorporated with finite points of 120×120 with 10 nm-diameter both for A- and B-NPs.

To facilitate comprehension, we visualized the concentrated regions observed in Figure 6.3 using different colors to indicate the governing species in Figure 6.4. For example, in the red region in Figure 6.4, $\phi_A(\mathbf{r}) \geq \phi_{A0}$, whereas $\phi_B(\mathbf{r}) < \phi_{B0}$ and $\phi_S(\mathbf{r}) < \phi_{S0}$. In the accompanying phase diagram, we also see that the concentration distribution will approach the spinodal and bimodal boundaries in the ternary phase diagram with time.

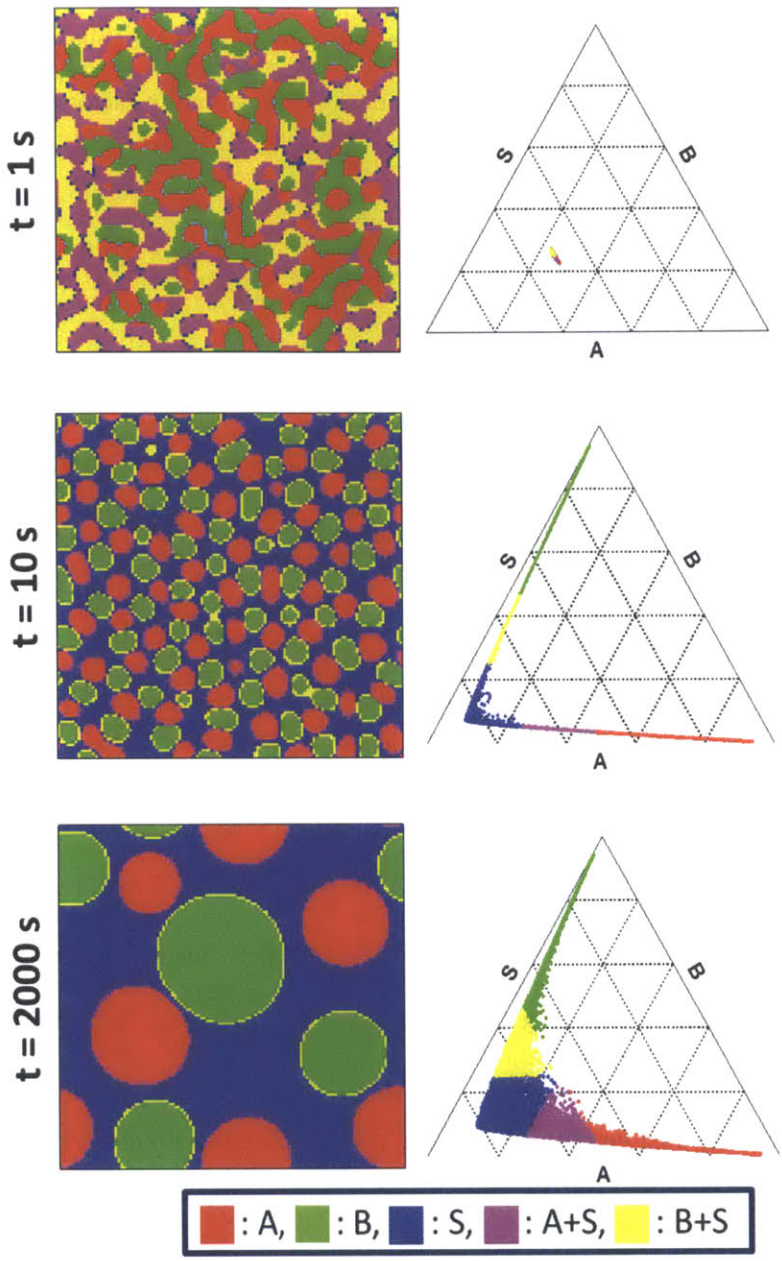

Figure 6.4. Visualized concentration distributions taken at different times of A- and B-NPs and the solvent S by spinodal decomposition with the identical condition in Figure 6.3 (left). Corresponding ternary phase diagrams showing the concentration distributions of the different species are shown on right side. In the images, different colors denote regions occupied by different governing species with identical color information in the visualized concentration distributions.

To analyze the characteristic wavelength λ_m, we applied a structure factor followed by the characteristic length scale of the decomposed patterns. In two dimension, the structure factor for the reciprocal space, $S_{(r,s,n)}$, is defined as [12,13,16]:

$$S_{(r,s,n)} = \frac{1}{N_x N_y}\left[\sum_{i=0}^{N_x-1}\sum_{j=0}^{N_y-1}\left(\phi_{p(i,j,n)} - \phi_{p,0}\right)\exp\left(-2\pi\left(\frac{ri}{N_x}+\frac{sj}{N_x}\right)\right)\right]^2. \tag{6.23}$$

Considering two independent concentration variables in the ternary mixture, we should calculate $S_{(r,s,n)}$ on the basis of both ϕ_A and ϕ_B, i.e., $S^{(A)}_{(r,s,n)}$ and $S^{(B)}_{(r,s,n)}$. From the structure factor, we can calculate the autocorrelation functions for the real space on the basis of both ϕ_A and ϕ_B, $G_{(i,j,n)}$, as [12,13,16]:

$$G^{(l)}_{(i,j,n)} = \frac{1}{N_x N_y}\left[\sum_{r=-N_x/2}^{(N_x-2)/2}\sum_{s=-N_y/2}^{(N_y-2)/2} S^{l}_{(r,s,n)}\exp\left(2\pi\hat{i}\left(\frac{rL_x(i-1)}{(N_x-1)^2}+\frac{sL_y(j-1)}{(N_y-1)^2}\right)\right)\right],\ l = A \text{ and } B, \tag{6.24}$$

where $\hat{i}$ is an imaginary constant. The 2D characteristic wavelength λ_m given by the pair-correlations of the order parameters is defined as the shortest length at which $G_{(i,j,n)} = 0$. As Figure 6.5 shows, λ_m from the pair-correlation function based on either ϕ_A or ϕ_B indicates linearity at the later stages of phase separation. This implies a power-law dependence, $\lambda_m \sim (t - t_d)^{\alpha}$, after the induction time t_d. This scaling behavior of λ has been observed in both theoretical and experimental studies under a variety of experimental and computational conditions [17-26]. The conventional prediction for the scaling exponent of the growth rate of λ_m is $\alpha \sim 1/3$ [1,14,15,17,19,22-26]; interestingly, the numerical simulation results shows that α is smaller than expected (i.e., $\alpha \sim 0.26$). We have already observed a similar discrepancy in Chapter 3 for a binary mixture of homogeneous CNPs. In Chapter 3, we explained the discrepancy by considering the composition-dependent mobility [26], which would interfere with the interface-diffusion-driven phase separation. The discrepancy observed in the simulation of the ternary mixture of CNPs by the PFM modeling in this study suggests another explanation. For example, the scaling exponent would decrease owing to the size difference between the NPs and the solvent. The conventional prediction does not consider the size differences among the components, which results in the ideal behavior of the Onsager coefficient [2,9] and the physically relevant assumption that the concentration field can replace the activity as the order parameter. In contrast, when the components differ considerably in size such that $h = 20$, there is a deviation in the Onsager coefficient and non-unity activity coefficients for each

component. Another possible reason for the decrease in the scaling exponent would be the screening effect between a specific type of NP and the solvent by the other type of NP.

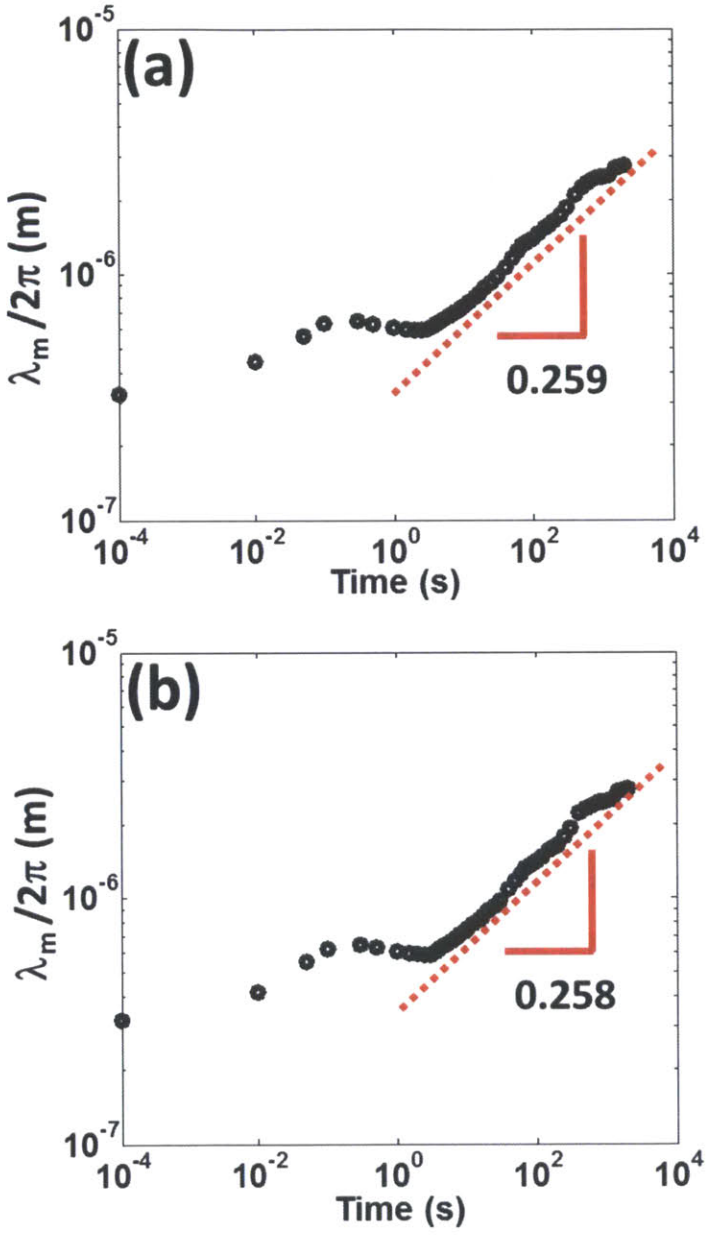

Figure 6.5. Characteristic wavelength, λ_m, measured by pair correlation function based on ϕ_A (a) and on ϕ_B (b). for the ternary mixture analyzed in Figures 6.3 and 6.4. In the plots, the slopes for the linear fitting curves (only for the later stage) are provided.

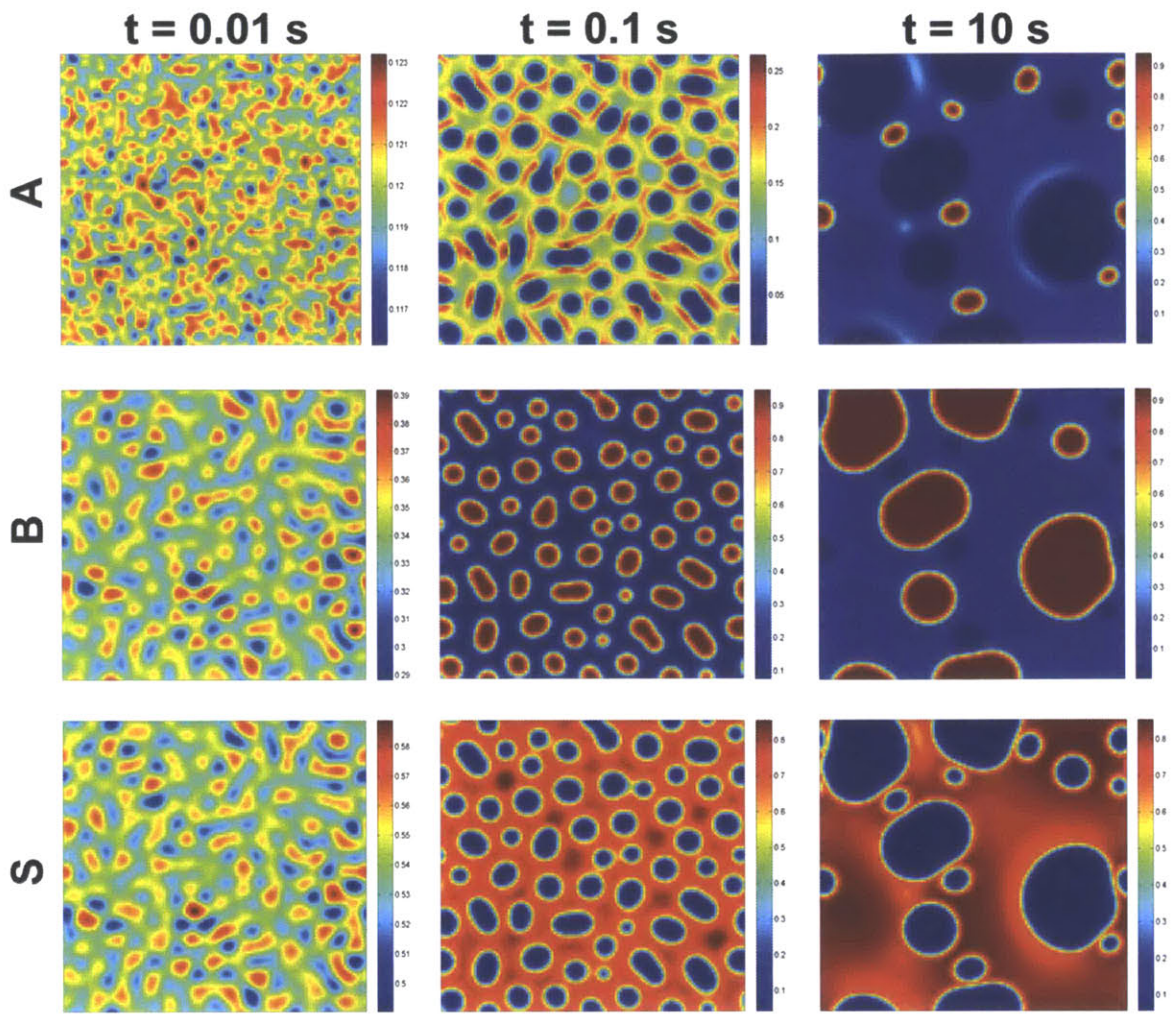

Figure 6.6. Time dependent concentration distribution of A- and B-NPs and the solvent S by spinodal decomposition when $[\phi_{A0}\ \phi_{B0}\ \phi_{S0}]=[0.12\ 0.34\ 0.54]$ and $[\chi_{AB}\ \chi_{AS}\ \chi_{BS}]=[6\ 3\ 3]$ with $D_B=5\times10^{-11}$ m^{2}s^{-1} while $D_A=10^{-12}$ m^{2}s^{-1}. The dimension for the 2D simulation box is 24×24 μm^2 incorporated with finite points of 120×120 with 10 nm-diameter both for A- and B-NPs.

To examine the effects of the asymmetric diffusivity and initial concentrations among the NPs on phase separation, we also simulated spinodal decomposition of ternary mixture of CNPs under the condition that $[\phi_{A0}\ \phi_{B0}\ \phi_{S0}]=[0.12\ 0.34\ 0.54]$ and $[\chi_{AB}\ \chi_{AS}\ \chi_{BS}]=[6\ 3\ 3]$ with $D_B=5\times10^{-11}$ m^{2}s^{-1} and $D_A=10^{-12}$ m^{2}s^{-1}. As shown in Figures 6.6 and 6.7, droplet-like concentrated regions of CNPs appear, as observed in Figures 6.3 and 6.4; however, the main difference is that the shape of the droplets is less

isotropic. This difference is attributed to the considerably large difference in the diffusivities of the two NPs.

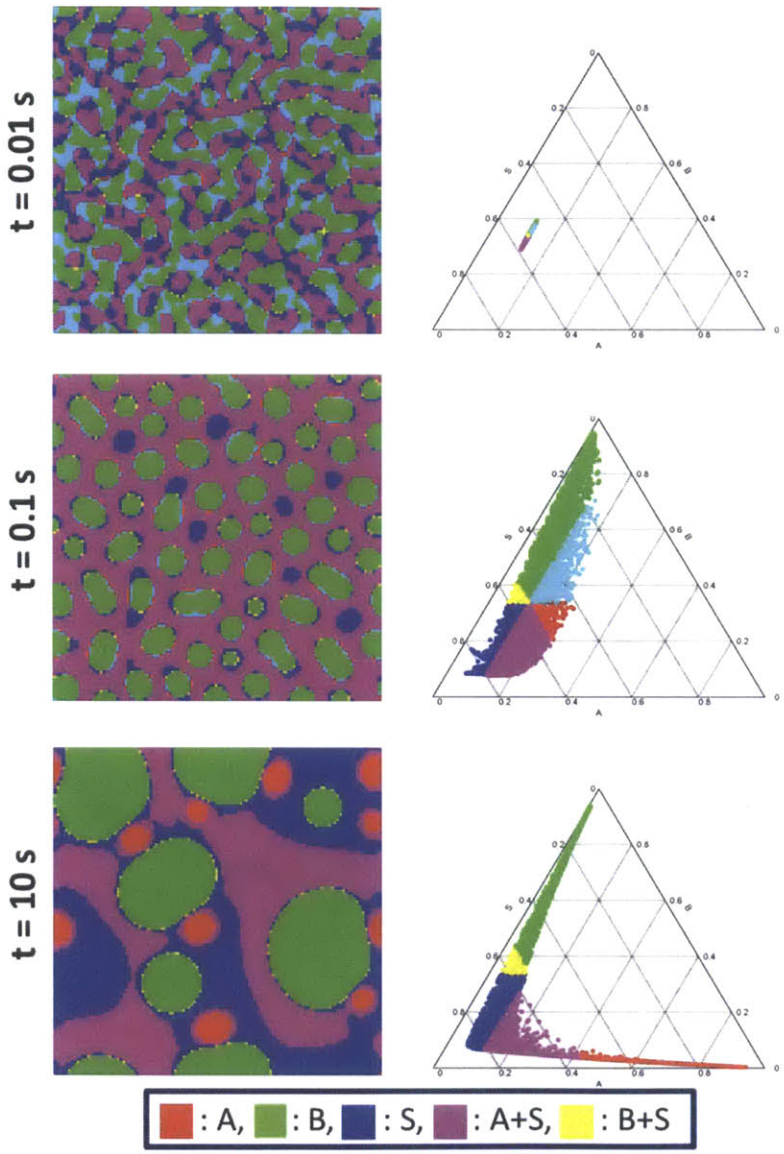

Figure 6.7. Visualized concentration distribution as a function of time of A- and B-NPs and the solvent S by spinodal decomposition with the identical condition in Figure 6.6 (left). Corresponding ternary phase diagram showing the distribution of concentration combination of the different species are shown in right side. In the images, different colors denote regions occupied by different governing species with identical color information in the visualized concentration distribution.

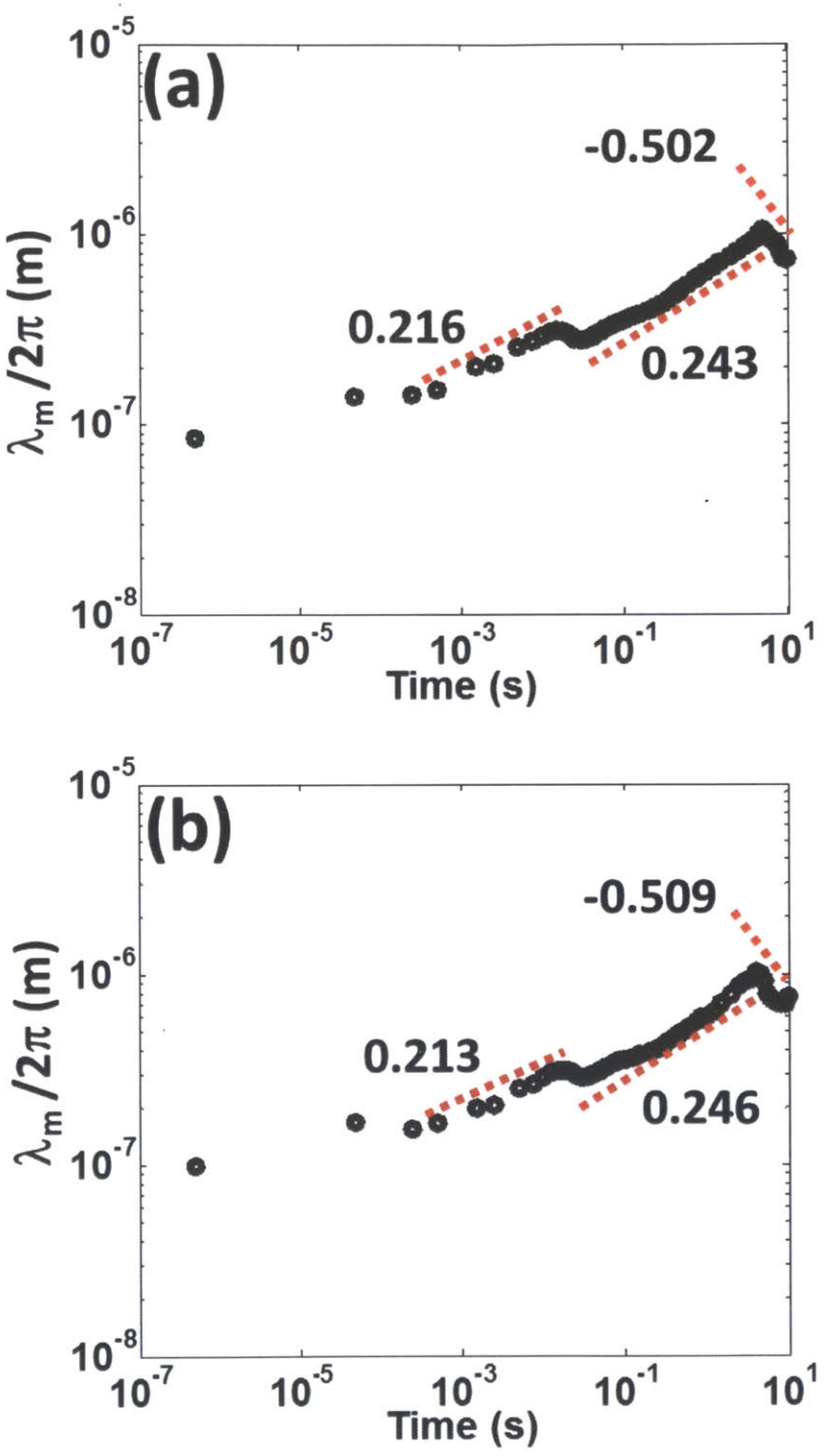

Figure 6.8. Characteristic wavelength, λ_m, measured by pair correlation function based on ϕ_A (a) and on ϕ_B (b) for the ternary mixture analyzed in Figures 6.6 and 6.7. In the plots, the slopes for the linear fitting curves (for 1) the earlier, 2) intermediate, and 3) later stages) are provided.

Another interesting observation from Figure 6.7 is the appearance of a wide range of areas in which A-NPs form nearly homogeneous CNPs (i.e., pink-colored region) that surround the droplet-like concentrated regions of B-CNPs. In particular, compared to Figure 6.5, the area occupied by A-NPs and the solvent is much larger. This finding implies that phase separation by spinodal decomposition of ternary mixture of CNPs with different diffusivities of NPs will produce a more complicated micro-phase mixture after a sufficiently long time.

Figure 6.8 shows are the temporal evolution of λ_m measured from the pair-correlation functions based on either ϕ_A (a) or ϕ_B (b). Notably, spinodal decomposition occurs in at least three stages, earlier, intermediate, and later stages, which can be distinguished by their scaling exponents. For example, the earlier stage has a slightly smaller scaling exponent than the intermediate stage, and both exponents are smaller than the conventional prediction of 1/3. In the later stage, λ_m decreases, and the absolute value of the scaling exponent is much larger than the conventional prediction, like those in the earlier and intermediate stages. The observed decrease in λ_m in the later stage does not necessarily indicate a canceling-out mechanism for spinodal decomposition; rather, it originates from the considerably large difference in the diffusivities of A- and B-NPs, which results in a local drag effect for the formation of large droplet-like areas occupied by B-CNPs. Indeed, we can observe a number of smaller droplet-like areas in Figure 6.6; these areas will contribute to the decrease in λ_m in the later stage. From the numerical simulations of spinodal decomposition of the mixture of A- and B-CNPs, we can observe that the scaling behavior and phase separation morphologies are strongly affected by the given conditions; this findings suggests the possibility of future applications of control of the phase separation behaviors, represented by the characteristic length scale and separation time scale. In the next section, we discuss a method of controlling the assembly of a ternary mixture of CNPs by surface-directed spinodal decomposition in thin films.

6.4.2. Surface-Directed Spinodal Decomposition of Ternary Mixture of CNPs.

Considering a ternary mixture of CNPs confined in a thin film, it is natural to try incorporate chemical selectivity in the confining substrate (either top or bottom substrate) that will direct the overall phase separation governed by spinodal decomposition. This idea is called the surface-directed spinodal decomposition and has been a subject of intensive research interest [27-36] for more than two decades in both experimental and computational studies. The chemical selectivity of the confining walls can be

realized by surface treatment of the substrate using specific functional groups such as polar groups, amine groups, or hydrogen-bonding groups [27,29]. To add the chemical selectivity effect, we can modify eq.(6.16) by adding the surface interaction terms governed by the interface energy between A- and B-NPs against the confining surfaces, as follows:

For bottom layer :

$$\left.\frac{\partial f_0}{\partial \phi_A}\right|_{T,P,\phi_B} = \left.\frac{\partial f_0}{\partial \phi_A}\right|_{T,P,\phi_B,original} + \left(\gamma_A^{(bot)} - \gamma_S^{(bot)}\right), \quad \left.\frac{\partial f_0}{\partial \phi_B}\right|_{T,P,\phi_A} = \left.\frac{\partial f_0}{\partial \phi_B}\right|_{T,P,\phi_A,original} + \left(\gamma_B^{(bot)} - \gamma_S^{(bot)}\right),$$

For top layer :

$$\left.\frac{\partial f_0}{\partial \phi_A}\right|_{T,P,\phi_B} = \left.\frac{\partial f_0}{\partial \phi_A}\right|_{T,P,\phi_B,original} + \left(\gamma_A^{(top)} - \gamma_S^{(top)}\right), \quad \left.\frac{\partial f_0}{\partial \phi_B}\right|_{T,P,\phi_A} = \left.\frac{\partial f_0}{\partial \phi_B}\right|_{T,P,\phi_A,original} + \left(\gamma_B^{(top)} - \gamma_S^{(top)}\right),$$

where $\gamma_i^{(k)}$ denotes the interface energy between the i th species and the k th confining wall. We examined the surface-directed spinodal decomposition of a ternary mixture of CNPs with $[\phi_{A0}\ \phi_{B0}\ \phi_{S0}] = [0.25\ 0.25\ 0.50]$, $[\chi_{AB}\ \chi_{AS}\ \chi_{BS}] = [6\ 3\ 3]$, $\left[\gamma_A^{(bot)}\ \gamma_B^{(bot)}\ \gamma_S^{(bot)}\right] = k_B T[0.1\ 0.5\ 0.3]$, $\left[\gamma_A^{(top)}\ \gamma_B^{(top)}\ \gamma_S^{(top)}\right] = k_B T[0.5\ 0.1\ 0.3]$, and $D_A = D_B = 10^{-12}$ $\mathrm{m^2 s^{-1}}$. In particular, the surface-interaction parameters were designed to provide a symmetrical contrast bewteen A- and B-NPs against the bottom and top confining walls. As Figure 6.9 shows, concentrated regions of A- and B-NPs appear near the top and bottom confining walls, respectively, at later stages of spinodal decomposition. This is easily predicted from the thermodynamics, which drives the system to minimize the total free energy, providing attraction and repulsion for specific components. Although the confining walls produce neither an actual attractive potential nor an actual repulsive potential, it is interesting that the relative surface interaction strength can draw particular NPs toward the corresponding surface. As Figure 6.10 shows, an undulation in the concentration appears along the direction normal to the confining walls (i.e., the z -direction). We can conjecture from the simulation results that the undulation will be damped out with time, nearly flatteninig the distribution of the concentrated regions of A- and B-CNPs parallel to the confining walls after a long time. Note also that the overall phase diagram at later times is nearly identical to that observed in spinodal decomposition without directing effects provided by the confining surfaces (i.e., Figure 6.4).

Figure 6.11 shows an additional analysis in terms of the correlation length. In surface-directed spinodal decomposition, it is important to analyze the characteristic length along the thickness direction (i.e., thye z -direction); therefore, we need to employ ϕ_S as the driving variable to calculate the pair-

correlation function instead of ϕ_A or ϕ_B. The main reason is that the concentration distribution over the thickness direction is biased (i.e., asymmetric surface interaction from the bottom and top confining walls) for A- and B-NPs, whereas the solvent feels a relatively neutral interaction against both the top and bottom confining walls. As shown in the figure, the phase separation exhibits three distinctive stages in terms of the scaling exponent of λ_m, earlier, intermediate, and later stages. Notably, the scaling exponents for the first two stages are similar to the conventionally predicted value of 1/3 and are nearly identical to each other. However, in the later stage, the exponent decreases significantly. Interestingly, a significant decrease in the scaling exponent was also observed in a computational study of surface-directed nucleation [30]. This can be understood by considering whether the characteristic length scale is comparable to the thickness of the film. For example, the film thickness exceeds the characteristic length scale for the separate domains of the concentrated regions by one or two orders of magnitude. In contrast, in the later stage, the length scale is comparable to the film thickness, indicating that the growth of λ_m along the film thickness direction will be geometrically limited, which results in slower growth of λ_m in the later stage of phase separation.

The possibility of controlling the phase separation morphology and dynamic properties using surface-directed spinodal decomposition of a binary mixture of CNPs in a thin film suggests the use of a designated confining substrate designed to have desirable chemical selectivity and a filme of the desired film thickness. In terms of applications, we can consider the controlled morphology as a functional thin film in which the distribution of the CNP concentration exhibits interesting periodicity and geometry when patterned substrates are used.

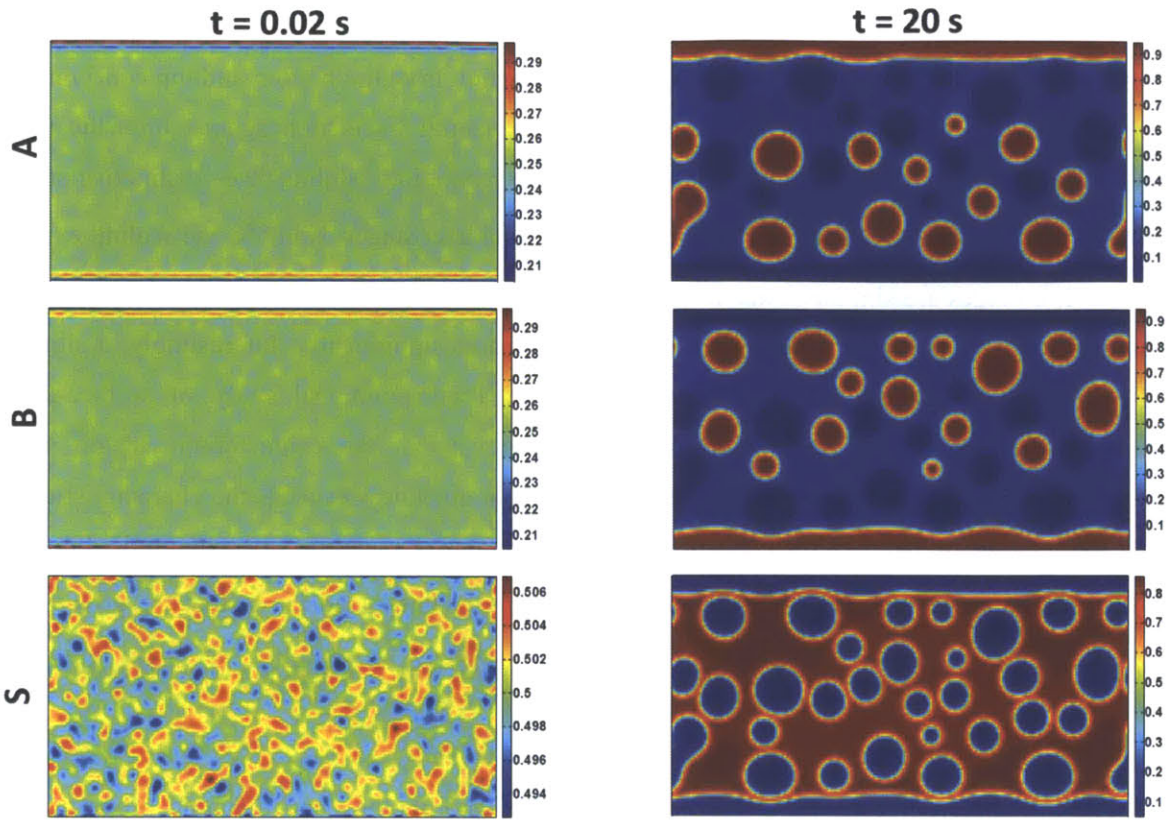

Figure 6.9. Time dependence concentration distribution of A- and B-NPs and the solvent S by the surface-directed spinodal decomposition (i.e., top wall: A-selective, bottom-wall: B-selective) when $[\phi_{A0}\ \phi_{B0}\ \phi_{S0}]=[0.25\ 0.25\ 0.50]$ and $[\chi_{AB}\ \chi_{AS}\ \chi_{BS}]=[6\ 3\ 3]$ with $D_A=D_B=10^{-12}$ m^2s^{-1}. The surface interaction condition for A- and B-NPs and the solvent molecule was assumed to $\left[\gamma_A^{(bot)}\ \gamma_B^{(bot)}\ \gamma_S^{(bot)}\right]=k_BT[0.1\ 0.5\ 0.3]$ and $\left[\gamma_A^{(top)}\ \gamma_B^{(top)}\ \gamma_S^{(top)}\right]=k_BT[0.5\ 0.1\ 0.3]$. The dimension for the 2D simulation box is 20×10 μm^2 incorporated with finite points of 200×100 with 10 nm-diameter both for A- and B-NPs.

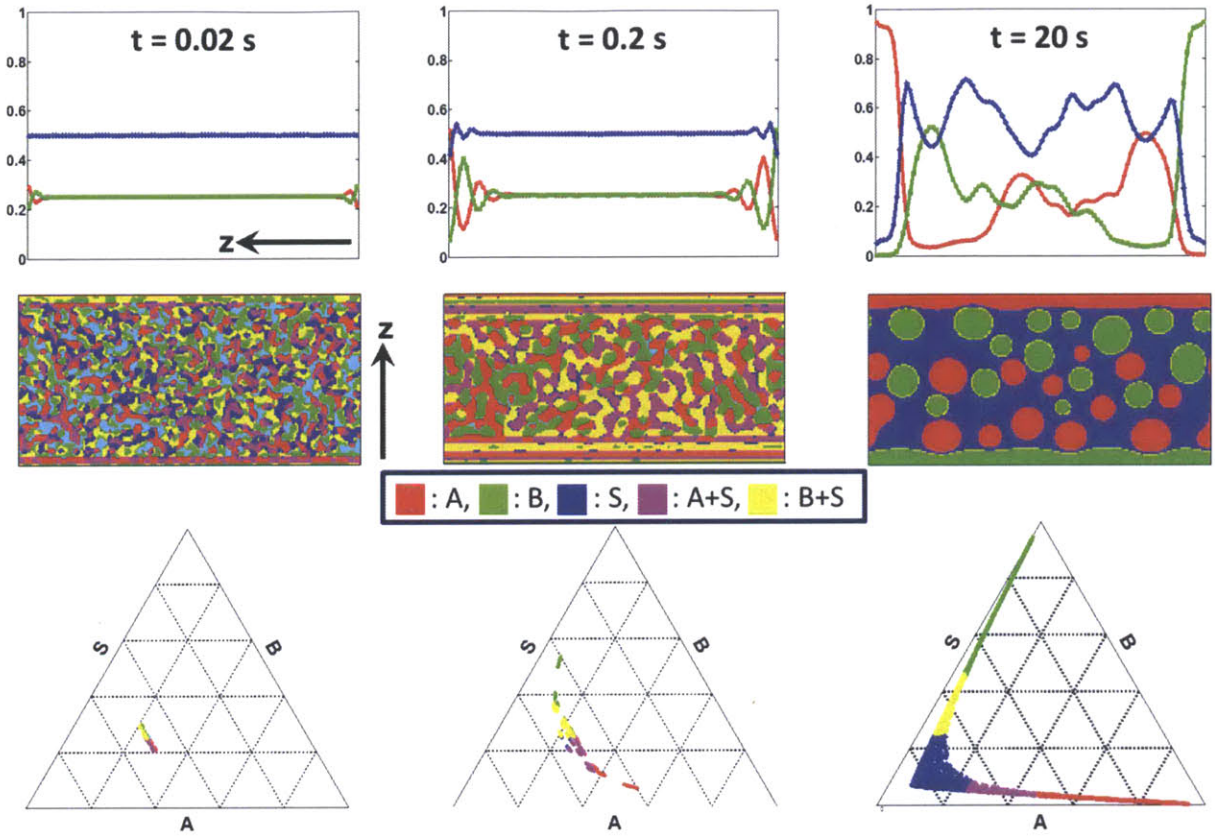

Figure 6.10. (Top row) Concentration profile of A- and B-NPs, and solvent (red, green, and blue solid lines, respectively) along the direction normal to the confining substrate (i.e., the z -direction) measured at different moments of the surface-directed spinodal decomposition of the binary mixture of CNPs. (Middle row) Visualized concentration distribution as a function of time of A- and B-NPs and the solvent S by the surface directed spinodal decomposition with the identical condition in Figure 6.9. In the images, different colors denote regions occupied by different governing species. (Bottom row) Corresponding ternary phase diagram showing the distribution of concentration combination of the different governing species with identical color information in the visualized concentration distribution.

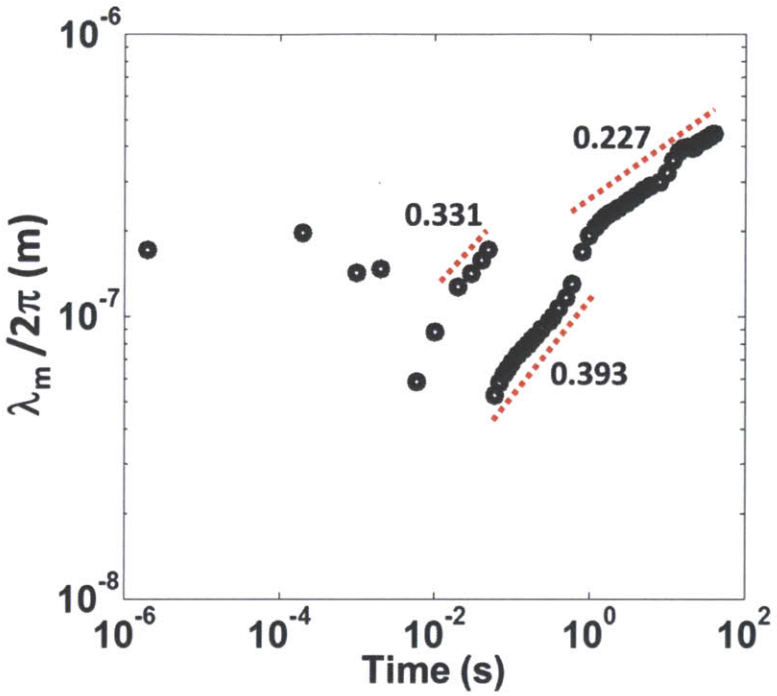

Figure 6.11. Characteristic wavelength, λ_m, along the direction normal to the confining walls measured by a pair correlation function based on ϕ_S for the ternary mixture analyzed in Figures 6.9 and 6.10. In the plots, the slopes for the linear fitting curves (for 1) the earlier, 2) intermediate, and 3) later stages) are provided.

6.5. Conclusions

In Chapter 6, we constructed a theoretical framework for a continuum-based numerical simulation of a ternary mixutre of CNPs in a thin film. Because of the computational cost, the use of previous methogologies and algorithms to describe phase-separation-driven assembly of multi-component CNPs would be a time-limited approach. Instead, we used the phase field model (PFM), which assumes that the system size is much larger than the NP size, in conjunction with the diffuse interface model. Considering a continuous phase separation mechanism such as spinodal decomposition, we explored several different phase separation scenarios with different concentration and molecular interaction conditions. For the study, an advanced numerical algorithm was used to solve the master partial differential equation by employing the spectral method such as fast Fourier transform or discrete cosine transform. By employing the spectral method in conjunction with an additional numerical technique, the semi-IMEX method, we could simulate the phase separation of a ternary mixture of CNPs governed by spinodal decomposition in

a large-scale system for considerably a long time while maintaining computational efficiency and numerical stability. We observed that the dynamics of the scaling behavior of the characteristic length scale, which represents the size of the areas occupied by specific CNPs, is slower than the conventional prediction; this confirms the effect of the size difference between the NPs and the solvent molecules. We examined asymmetric diffusivities and initial concentrations of the two NPs and identified three stages of spinodal decomposition. We extended the study to cover the more interesting situation of surface-directed spinodal decomposition of a ternary mixture of CNPs confined between upper and lower walls when the mixture is confined in thin films. We incorporated the effects of the surface by considering asymmetric surface interaction strengths between specific NPs against the confining walls. A numerical simulation showed that the confinement effect gives rise to three different phase separation stages distinguished by different scaling exponents. We also found a decrease in the scaling exponent in the later stage, which was attributed to a geometric limit imposed by the thickness of the thin film. We confirmed that when the characteristic size of the concentrated domain of the CNPs is comparable to the thickness, the growth rate of the characteristic length scale decreases. On the basis of the simulation results and discussion, we suggest that spinodal-decomposition-driven assembly of multi-component CNPs dispersed in a liquid medium, followed by thin film formation, will provide a useful route to controlling the assembly morphology and dynamic properties by controlling the film thickness and surface-interaction strength.

6.6. References

[1]. J.W. Chan and J.E. Hilliard, *J. Chem. Phys.* **28**, 258 (1958); J.W. Cahn, *Acta Metall.* **9**, 795 (1961); J.W. Chan, *J. Chem. Phys.* **42**, 93 (1965).

[2]. R.W. Balluffi, S.M. Allen, and W.C. Carter, *'Kinetics of Materials'*, (Wiley-Interscience, Cambridge, MA, 2005).

[3]. J.H. Hildebrand, J.M. Prausnitz, and R.L. Scott, *'Regular and Related Solutions'*, (Van Nostrand Reinhold Com., New York, 1970).

[4]. H.T. Davis, *'Statistical Mechanics of Phases, Interfaces, and Thin Films'*, (VCH Publishers Inc., New York, 1996).

[5]. P.J. Flory, *'Principles of Polymer Chemistry'*, (Cornell Univ. Press, Ithaca, NY, 1953).

[6]. E.A. Guggenheim, *J. Chem. Phys.*, **13**, 253 (1945).

[7]. J.D. van der Waals, *J. Stat. Phys.*, **20**, 200, (1979).

[8]. D.A. Cogswell, *Ph.D. Thesis, M.I.T.* (2010);
D.A. Cogswell and W.C. Carter, *Phys. Rev.E*, **83**, 061601 (2011);
D.A. Cogswell and M. Bazant, *Nano Lett.*, ASAP (2013).

[9]. J.R. Manning, *Phys. Rev. B*, **4**, 1111 (1971).

[10]. D.J. Eyre, *SIAM J. Appl. Math.*, **53**, 1086 (1993).

[11]. M.I.M. Copetti and C.M. Elliott, *Mater. Sci. and Tech.* **6**, 273 (1990).

[12]. R. Mauri, R. Shinnar, and G. Triantafyllou, *Phys. Rev. E*, **53**, 2613 (1996).

[13]. J.H. Yao, K.R. Elder, H. Guo, and M. Grant, *Phys. Rev. B*, **47**, 14110 (1993).

[14]. J.S. Langer and C.W.J. Beenakker, *'Fundamental Problems in Statistical Mechanics: Part 6'* (*Ed.* E.G.D. Cohen, Elsevier Science Publishers B.V., New York, 1985).

[15]. I.M. Lifshitz and V.V. Slylosov, J. Phys. Chem. Solids, **19**, 35 (1961);
C. Wagner, Z. Elektrochem., **65**, 581 (1961).

[16]. D. Frenkel and B Smit, *'Understanding Molecular Simulation: From Algorithms to Applications'*, (Academic Press, New York, 2002).

[17]. F. Shi, Y. Shim, and J.G. Amar, *Phys. Rev. E*, **76**, 031607 (2007).

[18]. B. Sauerwine, M. Widom, *Phys. Rev. E*, **84**, 061912 (2011).

[19]. E.D. Siggia, *Phys. Rev. A*, **20**, 595 (1979).

[20]. Y. Oono and S. Suri, *Phys. Rev. Lett.*, **58**, 836 (1987).

[21]. A.M. Lacast, A.H.Machado, and J.M. Sancho, *Phys. Rev. B*, **45**, 5276 (1992).

[22]. X. Shan and H. Chen, *Phys. Rev. E*, **47**, 1815 (1993).

[23]. S.C. Glotzer, D. Stauffer, and N. Jan, *Phys. Rev. Lett.*, **72**, 4109 (1994).

[24]. S. Toxvaerd, *Phys. Rev. E*, **53**, 3710 (1996).

[25]. E. Sander and T. Wanner, *J. Stat. Phys.*, **95**, 925 (1999).

[26]. J. Zhu *et al.*, *Phys. Rev. E*, **60**, 3564 (1999).

[27]. R.A.L. Jones, F.S. Bates, and P. Wiltzius, *Phys. Rev. Lett.*, **66**, 1326 (1992);
R.A.L. Jones, *Phys. Rev. E*, **47**, 1437 (1993).

[28]. G. Brown and A. Chakrabarti, *Phys. Rev. A*, **46**, 4829 (1992).

[29]. J.F. Marko, *Phys. Rev. E*, **48**, 2861 (1993);
G. Krausch, C. Dai, E.J. Kramer, J.F. Marko, and F.S. Bates, *Macromolecules*, **26**, 5566 (1993);
E. Kim, G. Krausch, E.J. Kramer, and J.O. Osby, *Macromolecules*, **27**, 5927 (1994);

[30]. G. Brown, A. Chakrabarti, and J.F. Marko, *Phys. Rev. E*, **50**, 1674 (1994).

[31]. S.K. Das, S. Puri, J. Horbach, and K. Binder, *Phys. Rev. E*, **73**, 031604 (2006).

[32]. S. Namilae, D.M. Nicholson, P.K.V.V. Nukala, C.Y. Gao, Y.N. Osetsky, and D.J. Keffer, *Phys. Rev. B*, **76**, 144111 (2007).

[33]. K. Binder, S. Puri, S.K. Das, and J. Horbach, *J. Stat. Phys.*, **138**, 51 (2010).

[34]. P.K. Jaiswal, K. Binder, and S. Puri, *Phys. Rev. E*, **85**, 041602 (2012).

[35]. M. Tang and A. Karma, *Phys. Rev. Lett.*, **108**, 265701 (2012).

[36]. D.A. Cogswell and M. Bazant, *Nano Lett.*, ASAP (2013).

(This page is intentionally left blank.)

Chapter 7

Conclusion

In this thesis, we explored a variety of computational methodologies and theoretical models for analyzing and understanding phase-equilibrium behavior and phase-separation-driven assembly of colloidal dispersion of nanoparticles (CNPs). The main reason to use these computational and theoretical approaches is the need to cover the wide range of spatial and temporal dimensions of systems in which NPs are applied and to consider them as either a continuum variable, a coarse-grained field, or discrete particles. The wider we extrend the range of our understanding, the more we can elucidate the unknown equilibrium and non-equilibrium properties of CNPs; consequently, more fruitful application possibilities and deeper insights can be identified. The preliminary study described in the Introduction revealed that the phase equilibrium of CNPs can be considerably complicated compared to that of a conventional mixture because of the high-surface energy of NPs, size difference between NPs and solvent molecule, the stochasticity for the motion of NPs, and the possibility of longer-range interaction among NPs.

To examine the smallest spatio-temporal dimension for the system in which NPs are dispersed, in Chapter 2 we studied the formation of NP clusters as a method of phase separation of CNPs. To take advantage of the colloidal environments of the NPs, we employed a mechanism based on NP motion driven by configuration-dependent diffusion, considering a single NP as a discrete particle. To describe the dynamics, a kinetic Monte Carlo (KMC) simulation based on an advanced stochastic algorithm was employed. Further, the simulation results were compared to a theoretical analysis based on rate theory (RT). From the KMC simulation and RT calculation, we identified the scaling behaviors of the cluster, namely, the power-law dependence of the average cluster size/weight and its distribution. Because of the good agreement between the KMC simulation and the RT calculation, we concluded that the cluster formation dynamics is scale-invariant irrespective of the NP materials and dispersion medium, although the kinetics is slower than that of conventional diffusion-limited aggregation dynamics. Our observation and analysis of cluster formation in CNPs are expected to provide several important implications and

guidance for both for fundamental materials science focusing on understanding the dynamic properties of CNPs and industrial applications concentrating on the control of CNP clustering to prepare functional materials.

In Chapter 3, we described a comprehensive study of spinodal decomposition of CNPs by introducing a computational method based on a KMC simulation. For the KMC simulation, we developed an advanced stochastic algorithm, such as a free-energy next reaction method (FENRM), that considers the interface energy variance, such as the phase field model (PFM). Unlike conventional computational studies based on the PFM employed in the continuum framework, we suggest that the FENRM algorithm can address discreteness of the NPs while maintaining computational efficiency for relatively large spatio-temporal dimensions. This gives the FENRM several advantages: 1) it combines the hard-sphere-like characteristics of NPs with the continuum field of the medimum in which they are disperse, 2) it describes the dynamics in considerably larger system dimensions than conventional Monte Carlo (MC) or molecular dynamics (MD) simulations, and 3) it provides greater computational exactness by addressing the composition-dependent mobility of NPs. In this study, we observed that the scaling exponent of the characteristic wavelength for each domain size is smaller than the conventional prediction, which reveals the importance of the interface-driven diffusion of NPs during spinodal decomposition. The computational results were also compared to a continuum-based numerical simulation, which also confirmed the validity of the stochastic algorithm we developed. The FENRM algorithm can easily be extended to more complicated cases involving multi-component, multi-phase phase transitions where several different types of NPs are dispersed in solvent mixtures. Another promising point from the study is that the method can be made more efficient by incorporating a parallelizable computation approach such as a GUGPU-based parallel-data-distribution method.

In Chapter 4, we introduced another efficient computational algorithm based on the self-consistent mean-field (SCMF) model to describe the phase equilibrium properties in mesoscopic/macroscopic dimensions, particularly in the spatial dimension. In practical terms, it is possible to extend the system's spatial dimensions up to even the millimeter scale. Focusing on the application of CNPs as functional materials, we studied a distribution of A- and B-NPs in a thin film at equilibrium. To analyze the separation morphology, we also introduced asymmetric selectivity effects provided by the confining walls. From the simulation results, we could observe and identify the effects of different combinations of the initial NP concentration, film thickness, chemical selectivity strength of the confining walls, and molecular interaction among the NPs. To validate the SCMF-based algorithm, we compared the simulation results with 3D Monte Carlo (MC) simulations and found good agreement between the calculated distribution profiles of A- and B-NPs over the entire film and 3D MC simulations

under different conditions. Additionally, we also found that the computational efficiency is greatly enhanced. The simulations revealed that the NPs attracted to the bottom substrate are concentrated and even form built-up layers near the substrate, whereas those repelled from the substrate form a gradual concentration distribution profile along the thickness direction. By using the SCMF algorithm, we found that it can be extensively applied to the design of CNP-based functional thin films with desirable physical properties by computationally predicting a suitable combination of controllable parameters. As a proof-of-concept demonstration, we illustrated the feasibility of fabricating functional optical materials composed of three types of NPs in a liquid medium, such as a gradient (refractive) index (GRIN) lens with micrometer-scale focal length resolution. This algorithm could easily be extended to more complicated suspensions of multiple NP of various sizes and systems with different geometries, as well as thin films.

In Chapter 5, we provided a proof-of-concept experimental demonstration of a functional thin film composed of CNPs. As the model materials, we employed Fe_3O_4 and SiO_2 NPs dispersed in UV-curable monomers. In particular, we found that it is experimentally possible to control the phase separation of the two NPs by driving the superparamagnetic Fe_3O_4 CNPs toward the bottom substrate, under which we applied a relatively weak external magnetic field. For the colloidal dispersion, dispersions of the two NPs in aqueous solution were mixed with an acrylate-oligomer followed by curing in a well with a designed geometry. To quantitatively measure the concentration distribution of the CNPs, we used a microspectrophotometer, which combines an optical microscope with a UV-Vis spectrometer. The measured concentration distribution profiles of the two NPs were compared to the calculation results of the SCMF algorithm provided in Chapter 4. The comparison revealed that the experimental data agree with the calculation results when several fitting parameters are introduced for different combinations of film thickness and magnetic field strength. The possibility of controlling the concentration distribution profiles of multi-component CNPs in a thin film, as we observed, suggests further applications such as the preparation of a GRIN lens in which the concentration gradient of CNPs will generate a gradient in the refractive index along the direction normal to the film. We suggested that this scheme and the controllability of the concentration distribution of a ternary mixture of CNPs in a thin film can be progressively extended to design a GRIN lens for biomedical applications; for example, to replace the lens in the eye, which loses focusing performance with aging.

Finally, in Chapter 6, we presented theoretical and numerical studies of phase separation governed by spinodal decomposition of a ternary mixture of CNPs, assuming that the system's dimensions are sufficiently large to be treated as a continuum framework. The analysis was based on the phase field model (PFM), which employs a continuum order parameter and a diffuse interface between

phases. Essentially, the mixture of CNPs is a ternary mixture (A- and B-NPs dispersed in solvent S), and it is computationally challenging to describe the phase separation dynamics governed by two order parameters on a large scale in both the spatial and temporal domains by employing discrete-particle-based methods such as MD, MC, or KMC. Instead, we suggested the of a PFM-based numerical simulation that employs two advanced numerical techniques: the spectral transform and the semi-IMEX methods. The continuum-based partial differential equation set governing the spatio-temporal evolution of the two order parameters during spinodal decomposition was effectively described by the numerical simulation. The results of simulations under different condition, demonstrated the evolution of the phase-separation morphology as a function of time; in particular, we measured the time-dependent behavior of the characteristic length scale, which corresponds to the separate domains. The characteristic length scale analysis revealed several interesting features: 1) smaller scaling exponents than those found in conventional spinodal decomposition studies and 2) three-stage phase separation dynamics for the scaling behavior when the two NPs have very different diffusivities. We also extended the study to surface-directed spinodal decomposition of a ternary mixture of CNPs in which the CNPs are confined in a thin film with upper and lower surfaces having asymmetric chemical selectivity for specific NPs. The simulation results also exhibited three-stage phase separation dynamics even with equivalent diffusivities and initial concentrations: in addition, they revealed the time-dependent evolution of an undulation in the concentration field along the direction normal to the film. On the basis of the simulation results and discussion, we suggest that spinodal-decomposition-driven assembly of multi-component CNPs dispersed in a liquid medium, followed by thin film formation, will provide a useful route to controlling the assembly morphology and dynamic properties of thin films by controlling the film thickness and surface-interaction strength.

In conclusion, this thesis tried to address problems regarding the equilibrium and non-equilibrium properties of an assembly of CNPs by employing several types of computational approaches to cover a wide range of spatio-temporal dimensions. Additionally, it provided several novel and efficient computational algorithms to solve complicated problems concerning the phase equilibrium and separation dynamics of CNPs. The computational studies and developed algorithm were compared to mathematical proofs and theoretical analysis as well as other types of computational approaches to check their validity. Further, this thesis presented proof-of-concept experimental data regarding the application of CNPs to the fabrication of functional thin films in which the concentration distribution of CNPs can be controlled with proven agreement between the experimental observations and computational or theoretical predictions. The original works presented in this thesis can be progressively applied to both industrial applications, such as the preparation of functional materials or devices composed of CNPs with a desiged shape, scale,

and geometry, and fundamental understanding of the dynamics of the assembly and structural andstatistical properties of CNPs under various conditions.

(This page is intentionally left blank.)

Chapter 8

Future Works

8.1. Cluster Formation of Colloidal Dispersion of Janus NPs

8.1.1. Introduction

As development of experimental techniques to synthesize colloidal NPs progresses, there have been notable advances in preparation of NPs that have anisotropic features [1-4]. The "anisotropicity" of the particle would originate from a variety of physico-chemical properties, such as anisotropic geometry or shape, multi-facet crystalline particle with different surface energies, asymmetric interaction strength or range, asymmetric elastic properties of the coating ligand molecules, asymmetric patchy molecule distribution over the surface [5]. One notable example of the anisotropic NP is a Janus NP which has the binary properties in terms of the molecular interaction with neighboring particle [1,5]. As its nickname indicates, the asymmetry in the molecular interaction is provided by two chemically different functional groups (compared to the 'two faces' of Janus) on the particle surfaces. For example, let us imagine a Janus NP partially covered by hydrophobic functional group including oligomers and by hydrophilic groups including hydroxyl groups. The asymmetry in the molecular interaction mainly concerns the rotation of the particles. In other words, the alignment of the orientation between the neighboring particles governs the particle assembly; therefore, phase separation morphologies such as cluster formation, spinodal decomposition, and nucleation at equilibrium are determined accordingly. The cluster formation of Janus NPs would be distinguishable from other conventional cases of molecular self-assembly, such as assembled structure of micelles in that micelles are chain-like molecules in which functional group distribution is aligned along the direction parallel to the chain. In Janus NPs, the particle's shape is considered as spherical (3D) or circular (2D) which does not reflect on the shape anisotropy. This difference between micelles and Janus NPs is expected to produce the different assembly morphologies. In particular, we can expect that Janus NPs will produce dendrite-like self-assembled structures while

micelles will produce sphere-like assembled structures to minimize the interfacial free energy between the two different chemical groups. In this section, we provide some results under on-going research of the cluster formation of colloidal dispersion of Janus NPs using two different interaction models to explorer the dynamics on cluster formation focusing on the scaling behavior of cluster size and weight as well as anlaysis of fractal dimension. For the study, we extended and modified the kinetic Monte Carlo (KMC) algorithm used in Chapters 2 and 3.

8.1.2. Models for Molecular Interaction in Janus NPs

To consider anisotropicity in the molecular interaction, we considered two models. First, as illustrated in Figure 8.1, we assumes that the interaction is a linear combination of the isotropic and anisotropic parts as:

$$\begin{aligned}
&\frac{U_{tot}}{A_{iso}} = \frac{U_{iso}}{A_{iso}} + f_{iso}\frac{U_{aniso}}{A_{iso}}, f_{iso} \equiv \frac{A_{iso}}{A_{aniso}}, \\
&\frac{U_{iso}}{A_{iso}} = 4\left(\left(\frac{1}{r}\right)^{12} - \left(\frac{1}{r}\right)^{6}\right), \\
&\frac{U_{aniso}}{A_{aniso}} = -\sum_{i=A,B}\left(r^2 + \frac{1}{4} \pm r\cos\left(\theta_i + \phi\right)\right)^{-3},
\end{aligned} \tag{8.1}$$

where the Lennard-Jones potential was employed for the isotropic part (U_{iso}) and van der Waals attractive interaction was used for the anisotropic part (U_{aniso}). In eq.(8.1), the spatial unit was normalized with respect to the particle size, σ. In particular, for U_{aniso}, we also considered the orientational angle of the particle with respect to the pre-determined primary system direction, θ, as well as the orientation angle of a certain particle relative to other particles, ϕ. The degree of the anisotropy is controlled quantitatively by the ratio between interaction energy density of A_{iso} and A_{aniso}, namely f_{iso}. Figure 8.2 shows some examples of the total interaction energy as a function of the orientational angles and the interdistance among NPs. From the figure, as expected, we can find that U_{tot} is minimized when the orientational axis is aligned and orientational angles are identical.

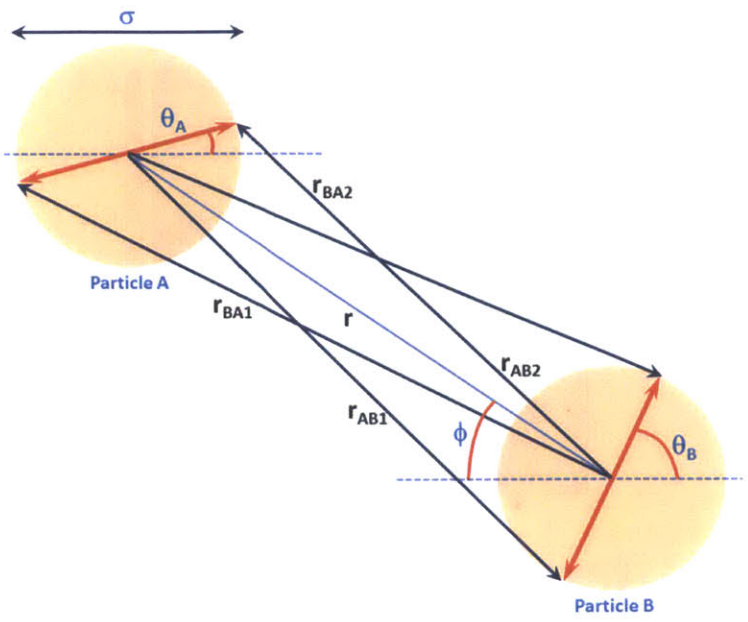

Figure 8.1. A schematic of the isotropic and anisotropic interaction between two Janus NPs

The second model was adapted from the original model suggested by Kern and Frenkel [6] recently. As illustrated in Figure 8.3, this model assumes that the molecular interaction is the Lennard-Jones type and acts like a switch whether the neighboring particles face to each to other (On) or not (Off). The anisotropicity can be controlled by the 'On' range of the alignment of the orientations of neighboring particles. For controlling the interaction range, the model introduces the polar angle δ that works as a parameter manipulating the potential as

$$\begin{aligned} &\text{If } \widehat{\mathbf{n}_1}\cdot\widehat{\mathbf{r}_{12}} \geq \cos\delta \;\;\&\;\; \widehat{\mathbf{n}_2}\cdot\widehat{\mathbf{r}_{12}} \geq -\cos\delta \\ &\quad U_{12}(r) = 4\varepsilon\left(r^{-12} - r^{-6}\right) \\ &\text{Else} \\ &\quad U_{12}(r) = 0, \end{aligned} \tag{8.2}$$

where $\widehat{\mathbf{r}_{12}}$ denotes the unit vector of particle 1 relative to particle 2 and $\widehat{\mathbf{n}_i}$ denotes the orientational vector of the ith particle.

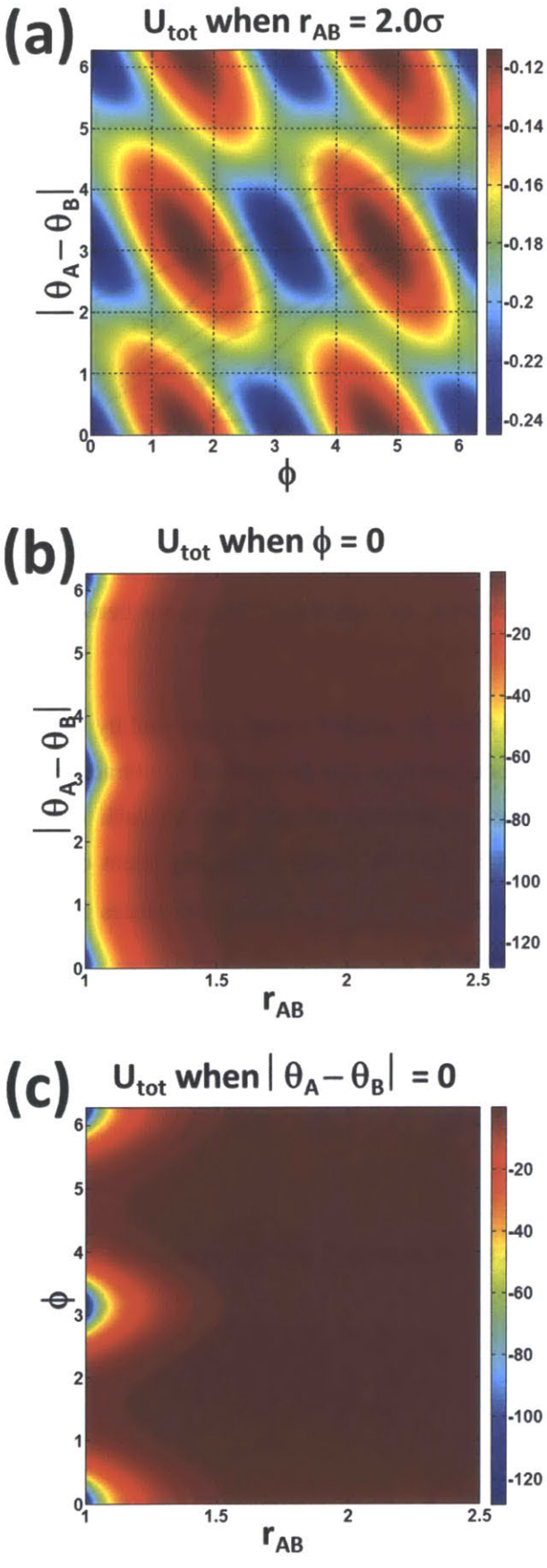
(a)
U_{tot} when $r_{AB} = 2.0\sigma$
$|\theta_A - \theta_B|$
ϕ
-0.12
-0.14
-0.16
-0.18
-0.2
-0.22
-0.24
(b)
U_{tot} when $\phi = 0$
$|\theta_A - \theta_B|$
r_{AB}
-20
-40
-60
-80
-100
-120
(c)
U_{tot} when $|\theta_A - \theta_B| = 0$
ϕ
r_{AB}
-20
-40
-60
-80
-100
-120

Figure 8.2. (a) A 2D map for the total interaction energy (U_{tot}) between two (A and B) Janus NPs as a function of the relative orientational angle (ϕ) and the difference between the orientational angle ($|\theta_A - \theta_B|$) when the inter-distance (r_{AB}) is 2σ. (b) A 2D map for U_{tot} as a function of r_{AB} and $|\theta_A - \theta_B|$ when $\phi = 0$. (c) A 2D map for U_{tot} as a function of r_{AB} and ϕ when $|\theta_A - \theta_B| = 0$.

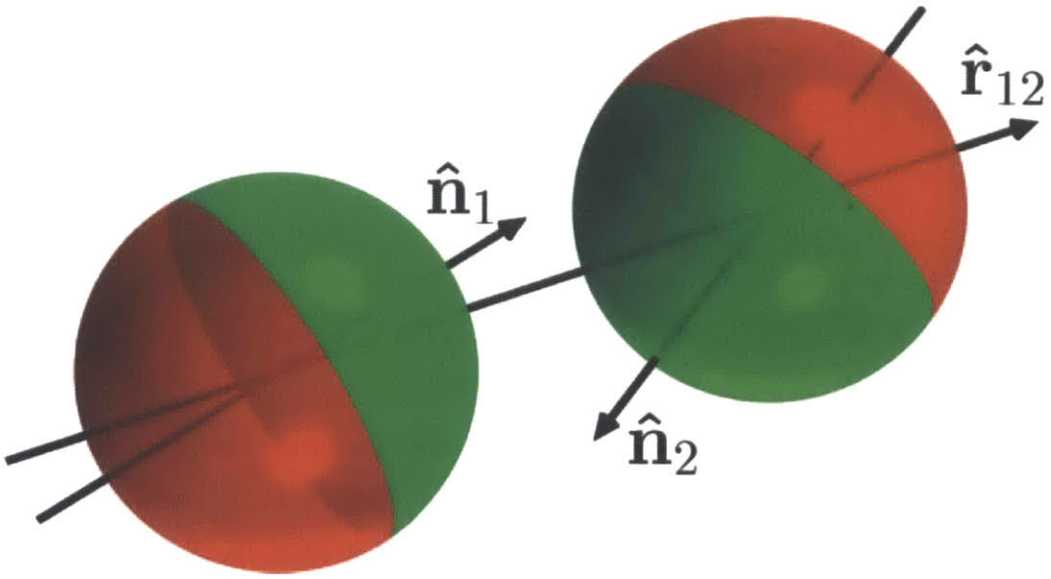

Figure 8.3. A schematic of the model for Janus NPs suggested by Kern-Frenkel model [6] (The original image was taken from [7]). Different colors indicate different surface properties which generate anisotropic interaction potential between the two Janus NPs.

The particles illustrated in Figure 8.3 are for a specific case where $\delta = \pi / 2$, that indicates that the 'face' of a particle is a half and half mixture like the two heads of Janus. Compared to the first model, the Kern-Frenkel model produce less close-packed assembly structures due to its discrete nature in the interaction potential. This difference is due mainly to the fact that the first model allows the particles to have more attempts to match the alignments, whereas the second model attempts is limited to more robustly restricted manner. This is similar to the difference in observed morphology of the assembled structures of particles governed by either diffusion-limited aggregation (DLA) or reaction-limited aggregation (RLA), whereby RLA drives the particle to form more compact morphology, whereas DLA is less robust to form the close-packed structures.

8.1.3. Results and Discussion

By employing the KMC algorithm, we simulated how the cluster formation is affected by the introduction of the anisotropic part in the molecular interaction. For the simulations, we examined a 2D case. In terms of the computational cost, it takes normally double amount of computational time compared to isotropic NPs, since the simulation of Janus NPs requires updating the heapsort data structure of the waiting times of NPs' rotational diffusions as well as translation diffusions. In a 3D case, further increase in the computational cost is expected when addressing two independent angles for the rotational degrees of freedom. We examined the models 1 and 2, respectively. For the simulation, the NVT ensemble with $n_0\sigma^2 = 0.174$, $f_{iso} = 10^{-2}$ was assumed when the diffusivity of a NP as $D = 10^{-12}$ m^2s^{-1} at $k_BT/\varepsilon = 0.5$. Quantitative measurements of the average cluster size and weight were performed by using the ACCA as used in Chapter 2. Figure 8.4 shows clusters of Janus NPs according to model 1. The clusters appear to be close-packed structures with increasing. This is more clearly demonstrated by the temporal evolution of the radial distribution function, $g(r)$. However, note that the formed cluster shapes are asymmetric rather isotropic as was observed in the case of isotropic CNPs in Chapter 2. For example, the average aspect ratio (not shown in this chapter), which can be defined as the longest to shortest interdistance ratio between particles on the perimeter of the cluster, of clusters was measured to 1.97 , and this is considerably larger than the observed value 1.14 in the case of isotropic CNPs. Therefore, we can find that the anisotropic nature in the molecular interaction affects the shape of the clusters. Additionally, we can also observe that the distribution of the orientation angle (θ) becomes a binary distribution; in particular, the distance between the peaks in the binary distribution of θ becomes π with increasing time. This result is easily expected from the eq.(8.1), which indicates the total system free energy is minimized at $\langle|\theta_i - \theta_j|\rangle = 0$ or π.

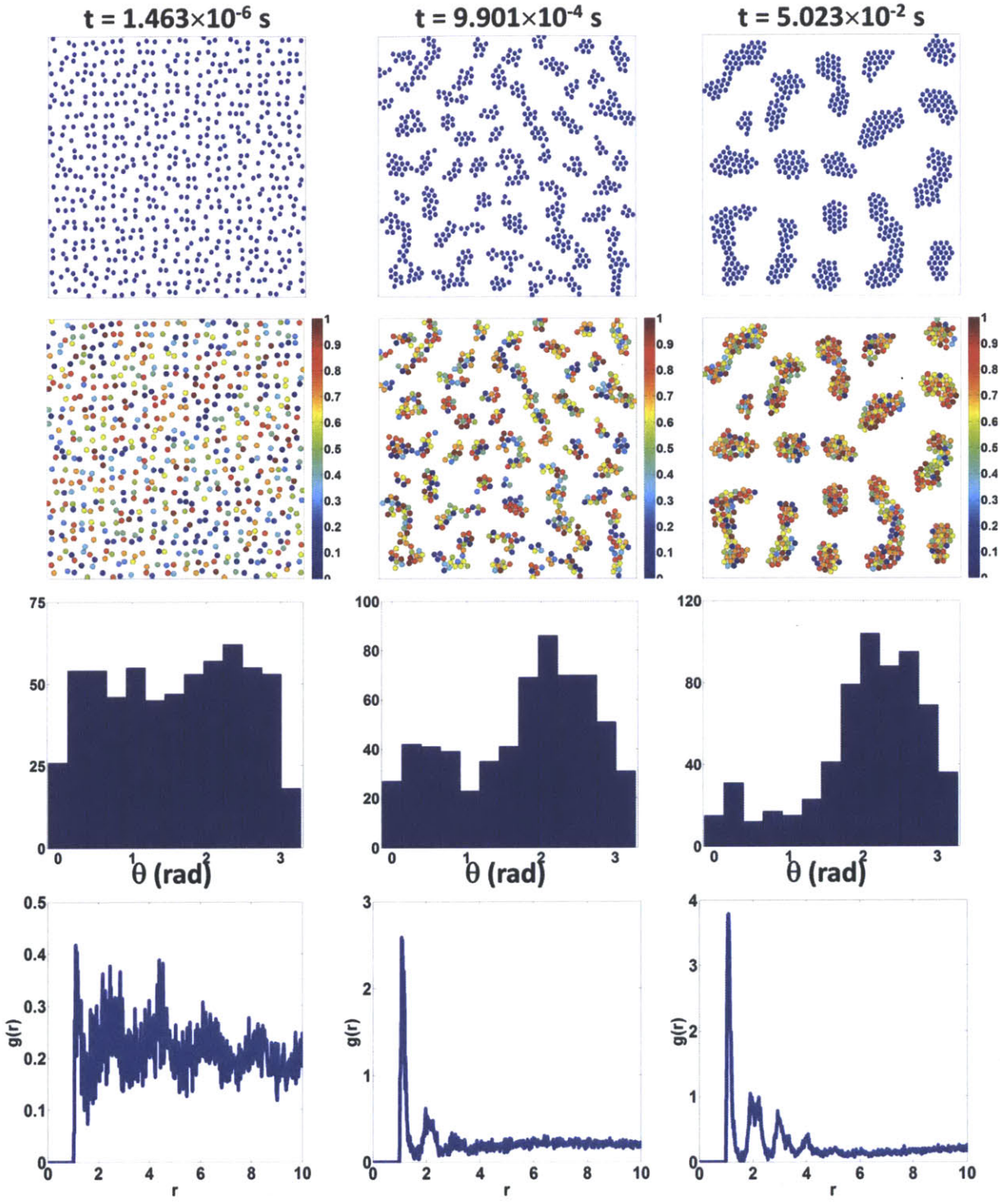

Figure 8.4. Temporal evolution of cluster morphology of Janus CNPs according to model 1. The first row denotes cluster morphology accompanied by illustration with the orientation angle ($\theta/2\pi$) with different colors (in second row). On the third row, distribution of θ is given, and on the fourth row, radial distribution function ($g(r)$) is provided.

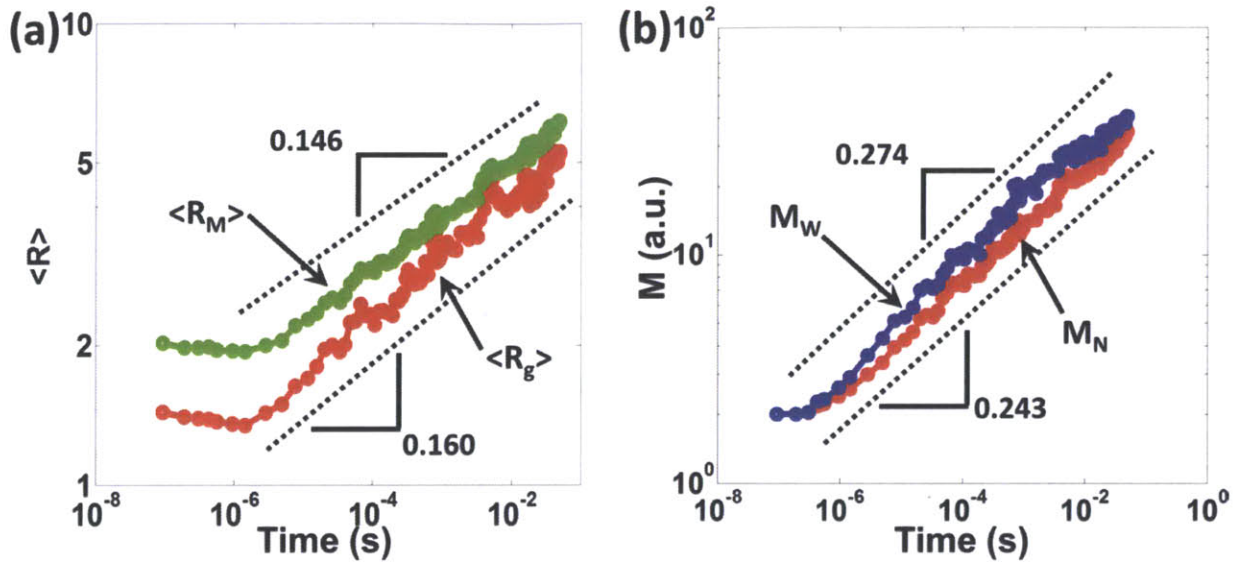

Figure 8.5. (a) Scaling behavior of the average size of the clusters of Janus NPs according to model 1 (green and red lines are for $\langle R_M \rangle$ and $\langle R_g \rangle$ with linear fitting slopes). (b) Scaling behavior of the average weight of clusters (blue and red lines are for M_W and M_N with linear fitting slopes).

Figure 8.5 shows scaling behaviors of clusters represented by power-law dependences of the average cluster size (measured by R_M or R_g) and weight (measured by M_N or M_W). Interestingly and qualitatively, it is notable that the growth rates of the size and weight are not much different from those from the case of isotropic CNPs clusters in Chapter 2. However, it is also notable that the growth rate of size measured by R_g is greater than the one by R_M. Note that there is a considerably large difference in the growth rates of weight between M_W and M_N. This indicates that the anisotropic nature of the molecular interaction gives rise to the greater polydispersity of the clusters, which results in more non-universal distribution of the weight and size. For future works, quantitative analysis of the size/weight distribution with appropriate physical model based on rate theory is required. From the least-square fitting, we can also calculate the fractal dimension of clusters d_f; $d_f \sim 1.67-1.88$ based on R_M and $d_f \sim 1.52-1.71$ based on R_g. This is a striking in that d_f is considerably smaller than the one observed from isotropic CNP clusters. The less the value of d_f, the more the shape of cluster appeared dendrite- or chain-like. From the simulation results based on the first model, we can conclude that the anisotropic

feature in the molecular interaction leads to a decrease in the fractal dimension, non-universal distribution of weight/size, and high aspect ratio of the cluster shape.

From the simulation results based on the second model, we can observe more interesting properties of Janus CPN clusters. First, as Figure 8.6 shows, as expected, they form less-compact clusters. This is distinctively represented in the analysis of $g(r)$, whereby intensities of peaks corresponding to the nearest neighboring shells are weak as well as low signal-to-noise ratios. Further, the orientation-orientation correlation among Janus NPs represented by the distribution of $\hat{\mathbf{n}}_i \bullet \hat{\mathbf{n}}_j$ indicates that there are two major orientational configurations of the nearest pair of the Janus NPs such that (1) the parallel orientational directions which are normal to the inter-distance vector corresponding to the relationship of $\hat{\mathbf{n}}_i \bullet \hat{\mathbf{n}}_j = 1$ and (2) the opposite orientational directions which are parallel to the inter-distance vector corresponding to the relationship of $\hat{\mathbf{n}}_i \bullet \hat{\mathbf{n}}_j = -1$ at later times [7]. Considering that the intensities of the two peaks found from the distribution of $\hat{\mathbf{n}}_i \bullet \hat{\mathbf{n}}_j$ are considerably greater than those measured at other positions, it can be conjectured that the cluster formation of the Janus NPs under the second interaction model is mainly driven by interaction between nearest neighboring NP pair. This will result in the less compact cluster structure, and may give rise to non-fractal relationship for the cluster formation. This finding also implies that the power-law dependences of the growth of cluster size and weight would be deviating either from the typical behavior or observation from model 1 and the case of isotropic CNPs. Indeed, more interestingly, the cluster growth appears to be relatively slow and even stalled after certain time as shown in Figure 8.7. In particular, the growth rate of the average cluster size measured either by $\langle R_M \rangle$ or $\langle R_g \rangle$ shows the scaling exponents which are about half the values observed from model 1 or from isotropic CNP clusters, whereas the exponents for the growth of the average weight of clusters are similar to the previous analysis. This results in unphysical measurement of the fractal dimension $d_f \sim 2.67-3.39$ on the basis of R_M and $d_f \sim 2.27-2.88$ on the basis of R_g. Considering the simulation is done in a 2D system, this observation of fractal dimensions indicates the morphology of the cluster might not be a fractal entity. Notably, increasing fluctuations in the size and weight are observable with increasing time. It appears that the cluster virtually stops growing after a certain time (i.e., around 4×10^{-4} s). This stalling in the growth is also observed in Figure 8.6, where the cluster morphology of Janus CNPs does not change much between $t = 3.381\times10^{-4}$ s and $t = 1.238\times10^{-2}$ s. Moreover, the functional forms of $g(r)$ between the two times are also considerably identical.

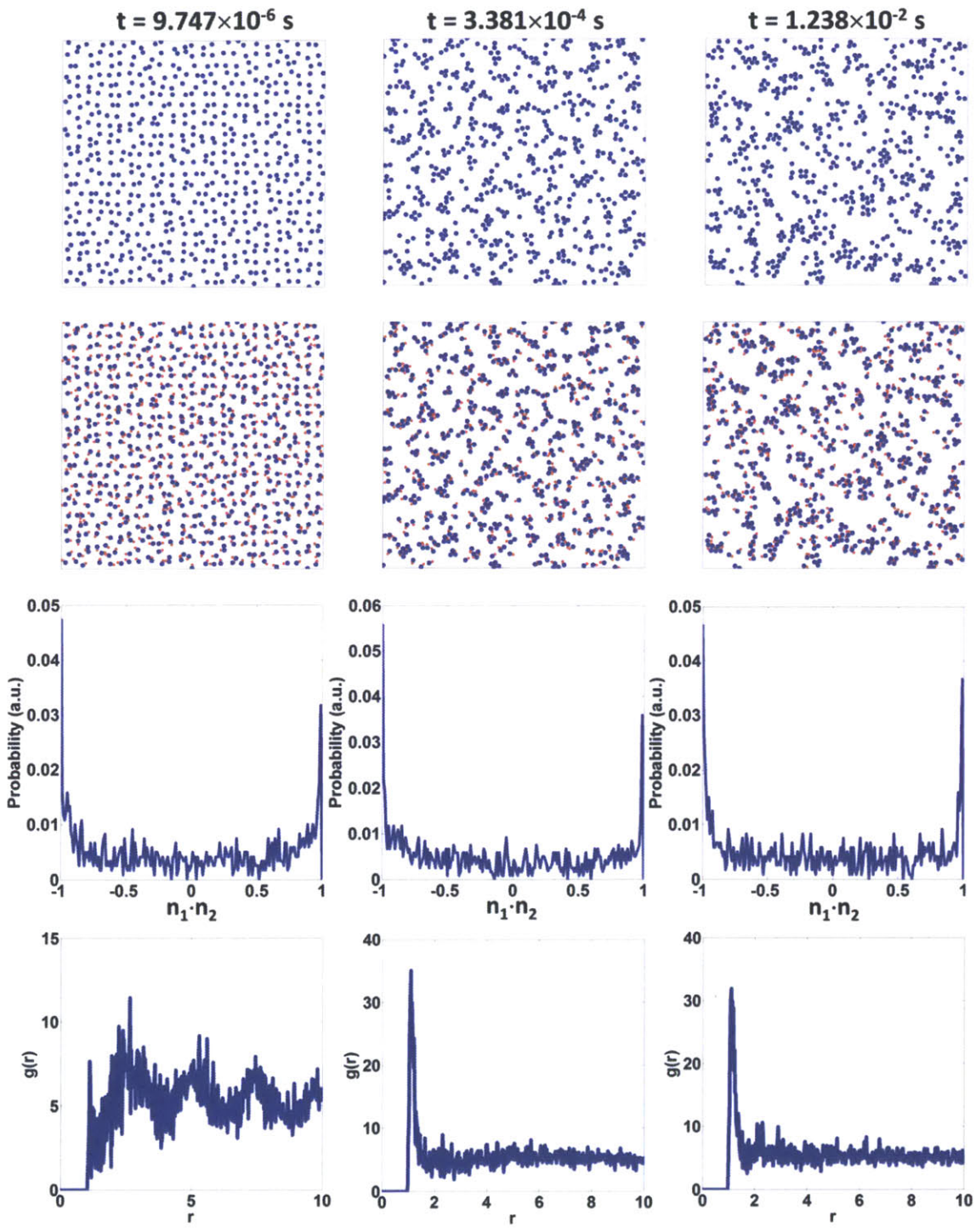

Figure 8.6. Temporal evolution of the cluster of Janus CNPs according to model 2. The first row denotes the cluster morphology with decpited orientational vector with red arrows (in second row). On the third row, a distribution of the inner product of the orientational vectors of the nearest neighbors $\mathbf{n}_1 \bullet \mathbf{n}_2$ is given, and on the fourth row, $g(r)$ is provided.

This finding indicates that Janus NPs according to model 2 would not form the 'real' cluster in terms of fractal properties measurement. For future work, detailed and more fundamental studies on the basis of equation of state for the phase diagram and transition [7-9] for more realistically-modeled Janus NPs would be necessary.

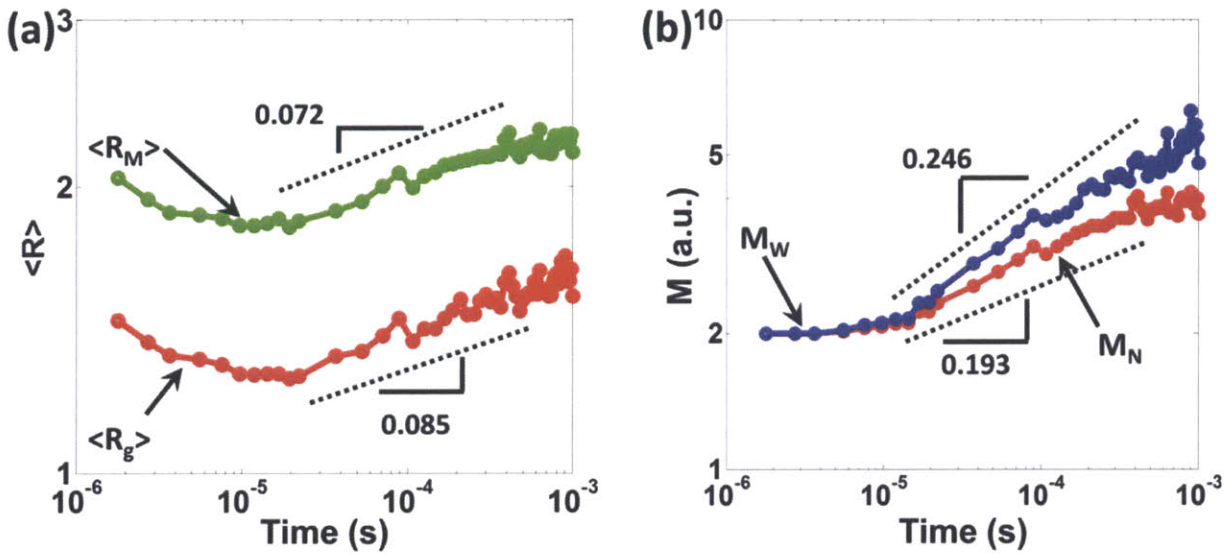

Figure 8.7. (a) Scaling behavior of the average size of the clusters composed of the Janus NPs according to model 2 (green and red lines are for $\langle R_M \rangle$ and $\langle R_g \rangle$ with linear fitting slopes). (b) Scaling behavior of the average weight of the clusters (blue and red lines are for M_W and M_N with linear fitting slopes).

8.2. Cluster Formation of CNPs in Polymer Gel Mesh

8.2.1. Introduction

We have provided theoretical, computational, and experimental results on the use of an external field for controlling the phase-equilibrium-mediated assembly of CNPs in this thesis. Another method of controlling the phase separation of CNPs without using of external fields or stimuli, phase stabilizers or surfactants can be employed. Further, preparation of additional components in more functionally organized forms would be more useful for this purpose. Recently, controlled nucleation of precursor pharmaceutical molecules using a polymer gel mesh, whereby the pore size distribution is uniform around

few nanometer-scale [10]. What we can observe from the reported experimental results is that the gel mesh can work as a frame in which the cluster formation is physically controlled. In this section, the concept of employing the polymer gel mesh is applied for the simulation on the basis of the KMC algorithm with preliminary simulation results for the controlled cluster formation of CNPs. With different gel mesh sizes and initial concentrations, cluster formation can be controlled in terms of the average cluster size/weight as well as scaling behaviors.

8.2.2. Model for Polymer Gel Mesh

To model the effects of the polymer gel mesh, NPs are assumed to interact with the gel mesh via the attractive van der Waals potential, $U_{GP}(r)$, as [11,12]

$$U_{GP}(r) = -\frac{16A_{GP}\left(r^2+3r+6\right)}{9r(r+2)^3(r+4)}, \tag{8.3.}$$

where A_{GP} denotes the interaction parameter. Eq.(8.3) is based on the van der Waals interaction between a hard-sphere and an infinite cylinder as illustrated in Figure 8.8. The mesh structure of the gel is also described as a 2D square lattice-type structure accompanied by the periodicity of ξ, which is comparable to NP size. More realistic description of the mesh structure, such as a model based on the percolation theory, would be more appropriate for future work,. In this section, it would be sufficient to assume that the mesh has the network structure with a characteristic periodicity.

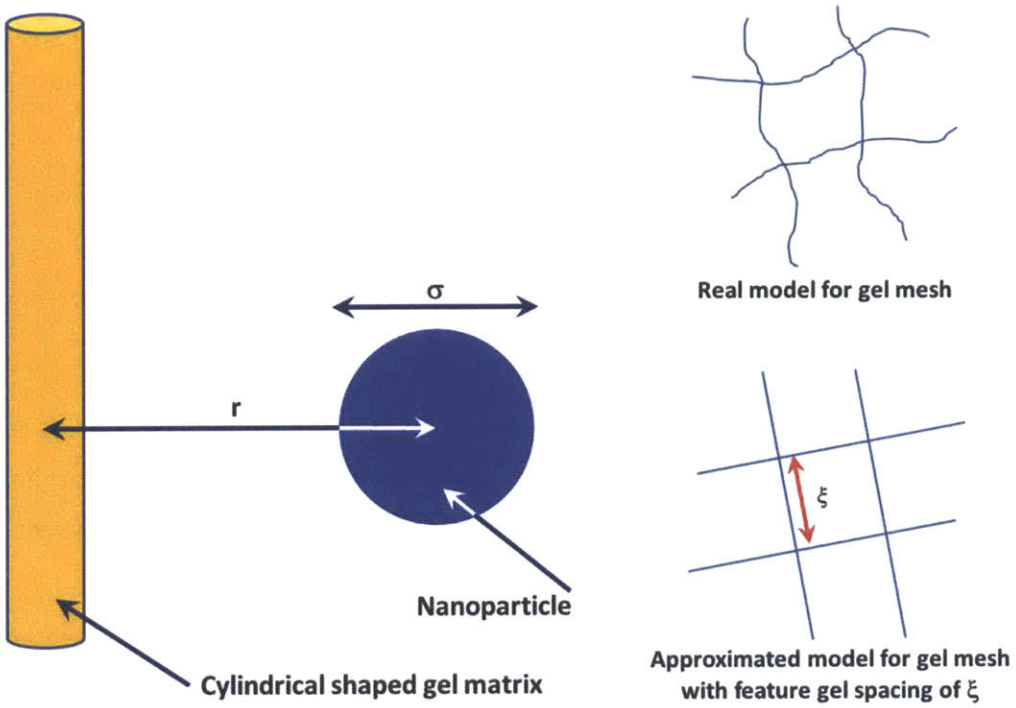

Figure 8.8. A schematic for the interaction between a single NP and the polymer gel mesh (left). The gel mesh modele as network structure with a 2D square lattice periodicity of ξ (right).

8.2.3. Results and Discussion

Using the model shown in the above section and the KMC algorithm, we simulated cluster formation of CNPs when they are dispersed in a thin film in which the polymer gel mesh is implanted. To examine the effects given by the periodicity of the polymer gel mesh, we introduced five different periodicities such that $\xi/\sigma = 2,\ 5,\ 10,\ 20,$ and 40. Figure 8.9 shows the cluster morphologies of CNPs at long times with different values of ξ and different initial concentrations ϕ_{p0}. As the figure shows, we can observe an increasing behavior of cluster size with increasing ξ and ϕ_p. However, a close look reveals more interesting dependence of the cluster size and weight on ξ. For example, there is the optimized gel spacing for achieving the maximum cluster size when the initial concentration is high (see Figure 8.10). In particular, $\xi \sim 20\sigma$ is observed to be the optimal gel spacing when $\phi_{p0} > 0.09$. Interestingly, this finding is also observable from the experimental results on the controlled nucleation of precursor particles in the polymer gel mesh [10] reported by Ying *et al.*, who suggested that it would be critical to control the nuclei size by balancing the solute-solute (i.e., Aspirin precursor particles) interaction relative to solute-

polymer interaction, and the balance is mainly governed by the mesh spacing [10]. As apparent from the results in this ssection, we also suggest that the interaction among NPs will be screened by the discrete but periodic field of the gel mesh; therefore, the effective gel mesh size optimized by balancing the distance between NPs will be the critical factor in controlling the cluster size and weight (or to maximize the average cluster size). Although it is not shown here, it is also notable from the simulations that the polydispersity given by M_W / M_N, which represents the uniformity of the cluster morphology, reaches the maximum at a certain gel spacing; and this spacing decreases with increasing ϕ_{p0}. However, this spacing is not equivalent to the spacing for determination of the optimal cluster formation reported in Figure 8.10. This finding implies that the control of the cluster size and morphology by controlling the gel mesh spacing should also consider the variation in the cluster polydispersity as well as the change in the maximum nuclei size and compactness. For future work, a 3D simulation considering more realistic decription of the gel mesh structure with a balancing factor among the NPs with respect to the polymer gel mesh would be necessary. The on-going research in this section is expected to provide a substantial advantage for controlling phase-equilibrium/separation-mediated-assembly of colloidal quantum dots and atomic-level solutes as well as NPs.

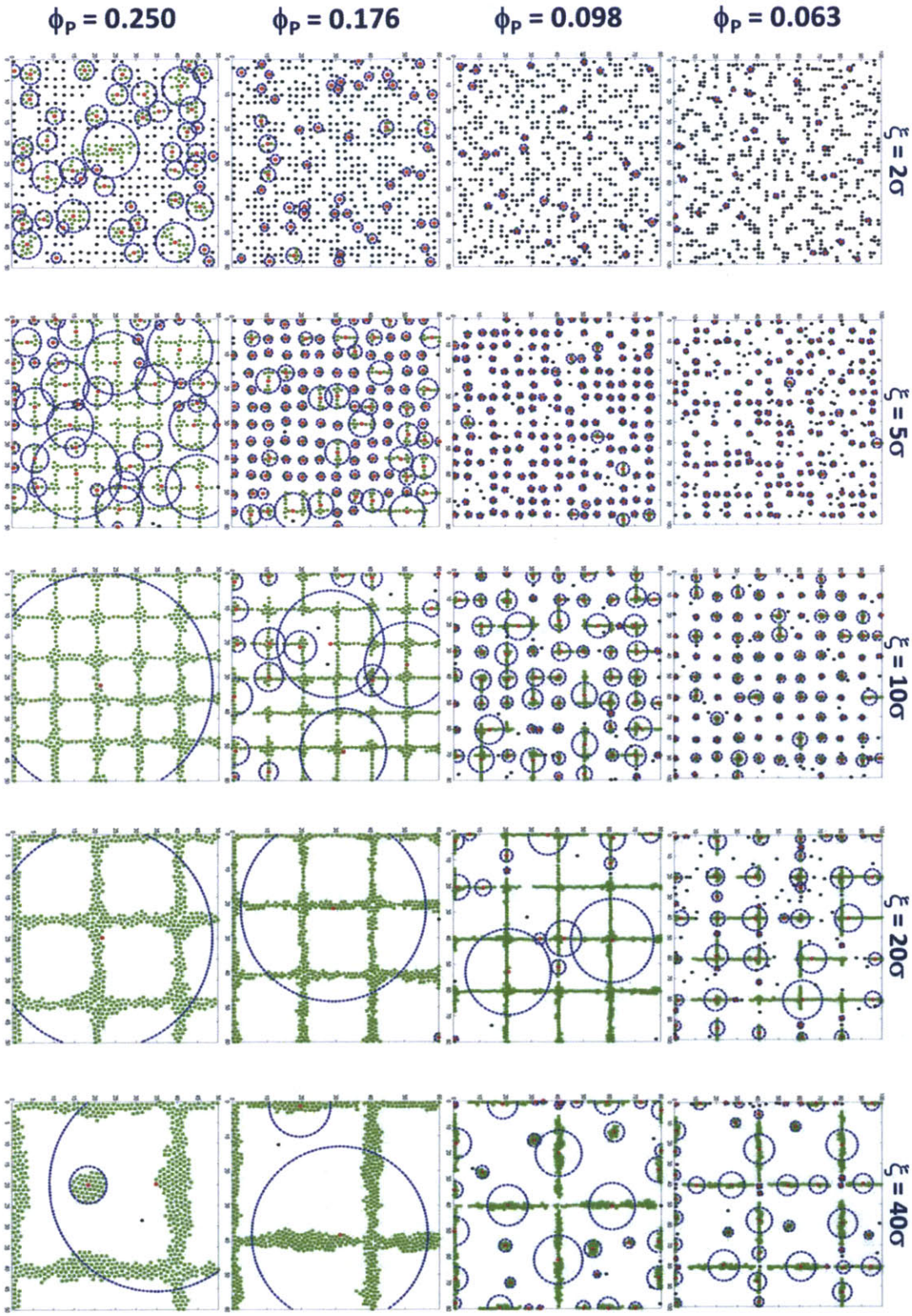

Figure 8.9. Cluster of CNPs with different initial concentration of NPs (ϕ_{p0}) and gel spacing periodicities ξ . Blue dot-lined circles with red-dot at the center are for the cluster size measured by R_g .

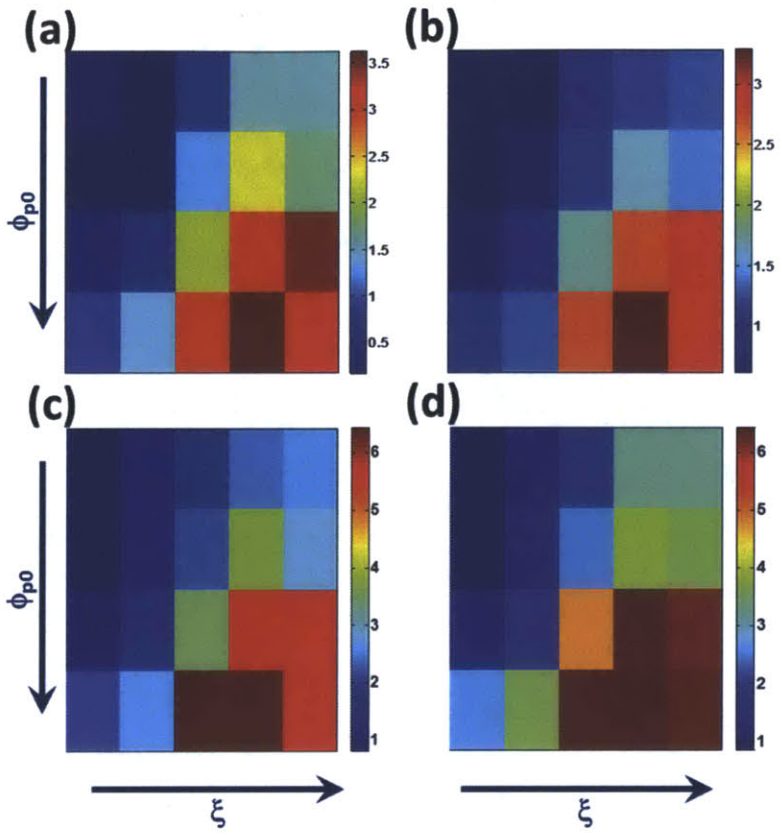

Figure 8.10. A 2D maps for the dependences of $\langle R_M \rangle$ (a), $\langle R_g \rangle$ (b), M_N (c), and M_W (d), on ξ and ϕ_{p0}. The examined combinations of ξ and ϕ_{p0} are taken from Figure 8.9. The values of the average cluster size and weights denoted by different colors indicate log-scale values.

8.3. Physical Assembly of CNPs by Controlled Spinodal Decomposition

8.3.1. Introduction

As presented in Chapters 4, 5, and 6, it is strategically possible to employ the external stimulation, such as an external field to drive and control the assembly structure of CNPs by controlled phase-separation and -equilibrium. However, this approach would be limited to practical applications owing to additional process costs, unknown correlations in the phase equilibrium arising from long-range interaction between NPs and the external stimuli, and designing preferable structure of the assembly with desirable patterns and periodicity. Here, we present some results obtained from another strategy of controlling the phase separation of CNPs: physically controlled spinodal decomposition. By the physical control, we mean the

technique on the basis of control of fluctuations in the initial concentration. This technique is distinguishable from the chemical control, i.e., functional-group treatment of the confining substrate surfaces. Rather, as mentioned in Chapters 3 and 6, the technique aims manipuatling the spontaneous phase separation by controlling spinodal decomposition. This fluctuation is actively initiated by thermal or background white noise. If we ever can control this initial noise by certain methods, it would be interesting because we can control the initial instability to give designated morphologies or patterned assembly structures. This approach is also expected to enable easier but more complicated patterning of 3D sturctures. In this section, we present numerical simulation results for the physically controlled spinodal decomposition of CNPs in which homogeneous NPs are dispersed and under phase. For the computational method, we used similar approaches provided in Chapter 6 on the basis of the continuum framework assuming that the dimensions of the system under consideration is sufficiently greater than the NP size. From the simulation results, we found that it is possible to control the phase separation morphology of CNPs and the characteristic wavelength in both periodicity and domain size, at least theoretically and computationally.

8.3.2. Theoretical and Experimentally Applicable Model

One possible method of controlling the initial concentration fluctuation is to employ laser interferometry, whereby either NP or dispersion medium is sensitive to a wavelength in specific range of incident light. As Figure 8.11 shows, it is advantageous to control the interference intensity and time-drag to produce various interference patterns by using a beam splitter and reflection mirror sets. Among the representative interference patterns are the Hermite-Gaussian (HG) and Laguerre-Gaussian (LG) patterns [13-15]. Detailed information on the formation of these patterns is beyond this thesis; however, note that these patterns are on the basis of the controlled transverse modes of electromagnetic wave in either Cartesian (for the HG patterns) or cylindrical coordinates (for the LG patterns). By controlling the interference path and diffraction angle, as shown in Figure 8.12, various patterns are obtained. If these interference patterns are directly mapped onto the surface of a thin film of the CNPs and can be translated into the information on the initial concentration fluctuation by the proportional relationship between the concentration fluctuation and intensity of the interference pattern felt by either by NP or dispersion medium, it can be conjectured that the initial random noise would be under control to be transformed into the non-random one. The obstacles among the theory and practical applications, such as a relationship between the concentration fluctuation and light intensity are still under question for realistic implementation; however, the idea would be the first step.

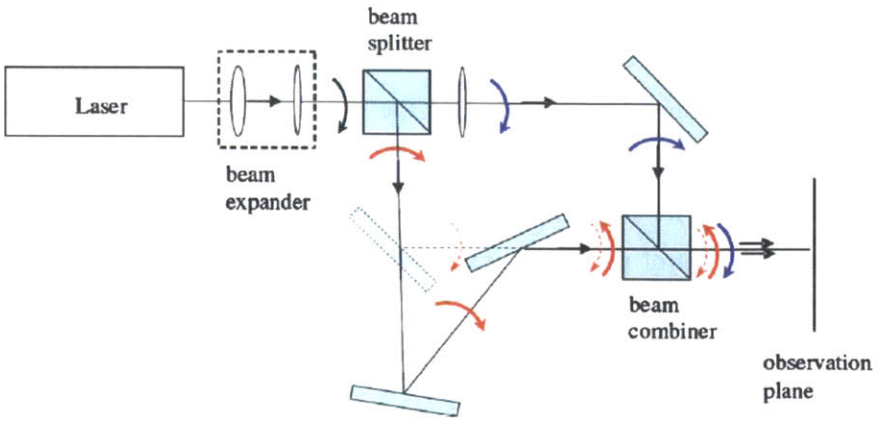

Figure 8.11. A schematic illustration of the laser interferometry. The original image was taken from [14].

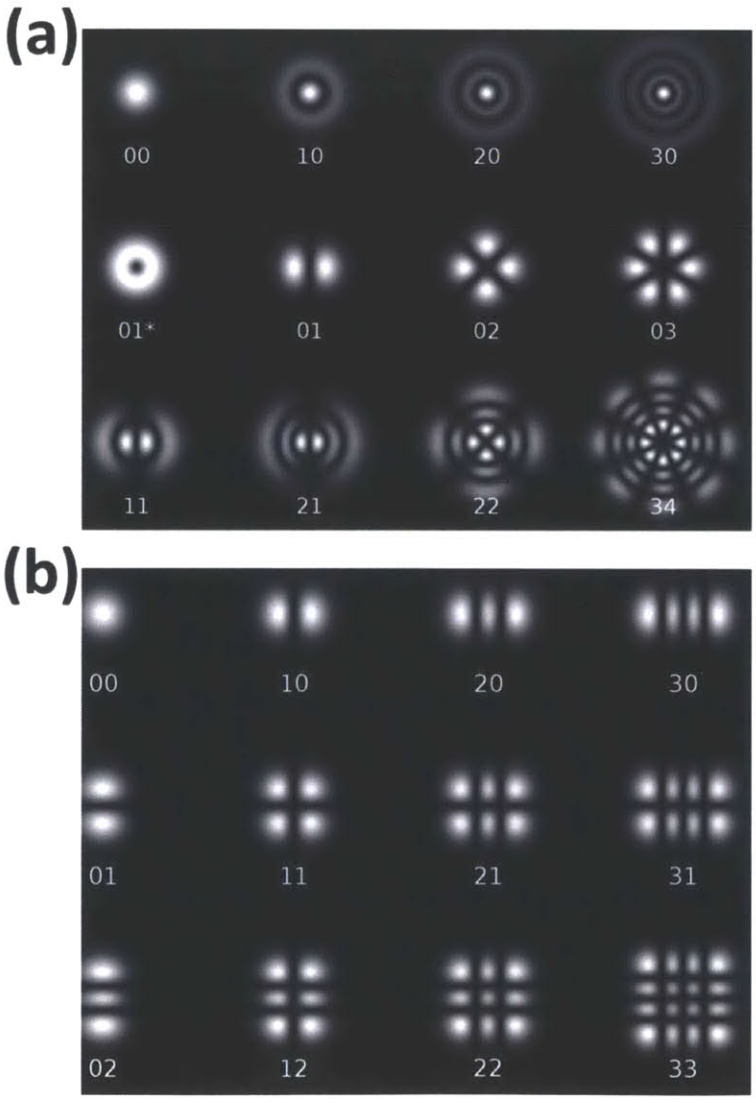

Figure 8.12. Interference patterns which can be produced by the laser interferometry and diffraction. (a) The Laguerre-Gaussian (LG) and (b) Hermite-Gaussian (HG) patterns. In the pattern images, two-digit numbers are for the radial-angular group number for the symmetry nodes (for (a)) and horizontal-vertical group number for the symmetry nodes (for (b)). The original images were taken from [14].

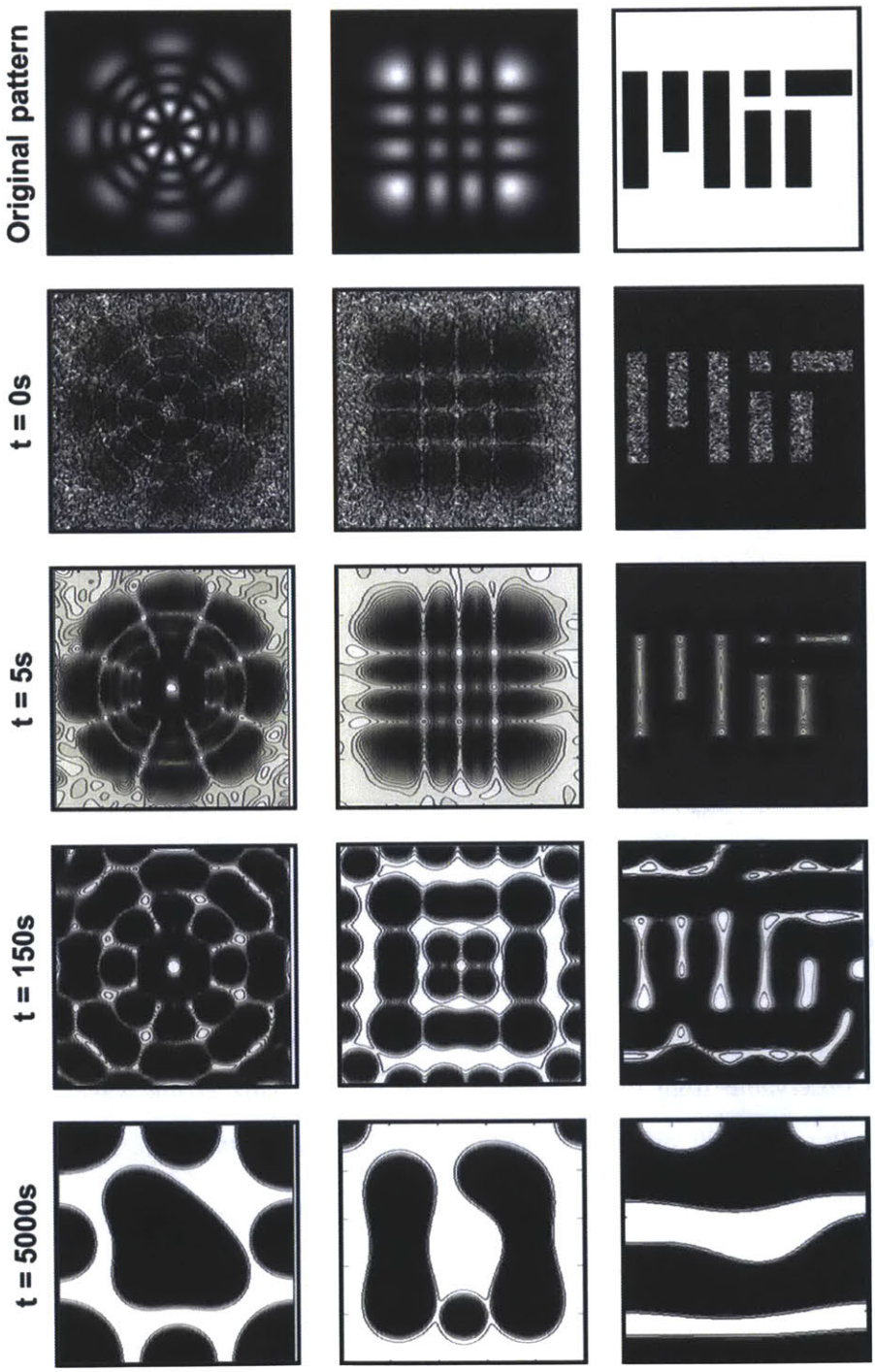

Figure 8.13. Temporal evolution of the physically-controlled spinodal decomposition of CNPs initiated with different controlled patterns; the first column for the case with the LG [3 4] pattern, the second column for the case with the HG [3 3] pattern, and the third column for the case with the designated theoretical pattern with the MIT logo. Initial condition was commonly examined at $\phi_{p0} = 0.5$ with $\chi = 0.29$, $h = 20$, $D = 10^{-11}$ m^2s^{-1}, and non-flux boundary condition.

Shown in Figure 8.13 are the images obtained from the 2D numerical simulations of the exemplary temporal evolution of the assembly structure of the CNPs by the physically controlled spinodal decomposition with different initial patterns. As apparent from the simulation results, we can observe that the initial control of the fluctuation in the concentration field would result in symmetric and anisotropic separation domains of CNPs directed by the initial patterns throughout the phase separation. However, the direction effects would be diminished as time goes by, which shall give rise to the separation domain morphology similar to the one predicted and observed in the case of intrinsic spinodal decomposition.

We extended the idea to examine the effects given by the different periodicities (λ_E) of the initially controlled concentration fluctuation as provided in Figure 8.14. As the model initially controlled concentration fluctuation, we tried a sinusoidal profile of $\phi_p(\mathbf{r})\big|_{t=0}$ such that

$$\phi_p(X,Y,Z)\big|_{t=0} = \prod_{j=X,Y,Z} \left(\phi_{p0} + a_j \phi_{p0} \cos\left(q_{ext,j} j\right)\right), \tag{8.4}$$

where $q_{ext,j}$ is the wave vector for the periodicity (i.e., $q_{ext,j} = 2\pi / \lambda_{E,j}$) and a_j is the amplitude of the initial fluctuation in j th dimension. From the simulation results in 2D where $\lambda_{E,X} = \lambda_{E,Y}$, we could also observe that the initial periodicity will direct the spinodal decomposition morphology with directed periodicities and symmetries; however there is a converging behavior of the phase separation which is similar to the one observed in the case of intrinsic spinodal decomposition at long times. This converging behavior is also observable from the time-dependence of the characteristic wavelength of the phase separation of CNPs, λ_C, with different periodicities at the initial stage (see Figure 8.15). From the temporal evolution of λ_C, we can find that will converge into the one predicted by the intrinsic spinodal decomposition. This finding is interesting in that one can utilize the possibility of controlling the symmetry of the separated domain with predictable domain size.

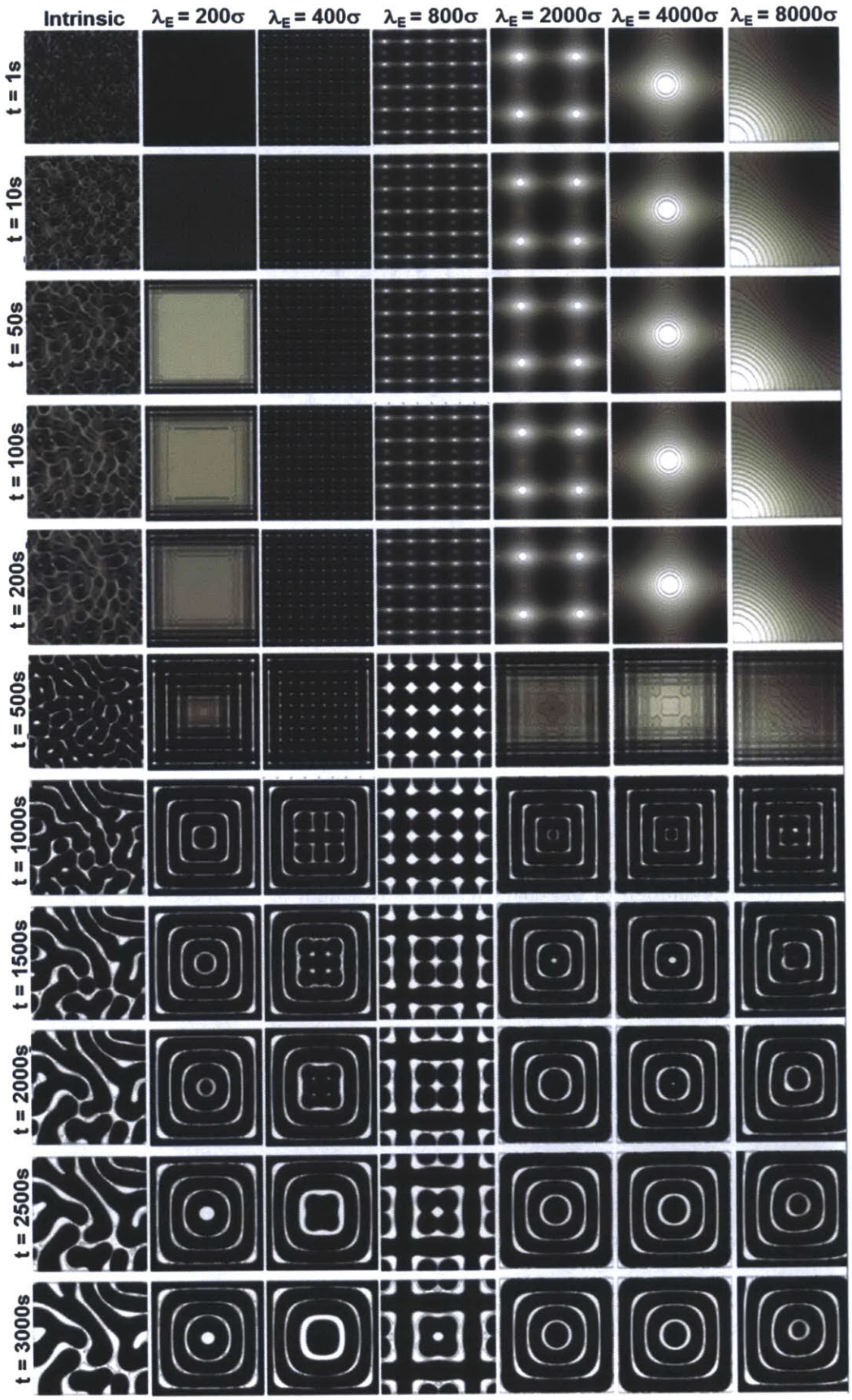
Intrinsic
λE = 200σ
λE = 400σ
λE = 800σ
λE = 2000σ
λE = 4000σ
λE = 8000σ
t = 1s
t = 10s
t = 50s
t = 100s
t = 200s
t = 500s
t = 1000s
t = 1500s
t = 2000s
t = 2500s
t = 3000s

Figure 8.14. Temporal evolution of the phase separation in 2D governed by the physically controlled spinodal decomposition with different periodicities of the initial pattern for the fluctuation control (λ_E). Initial condition was commonly examined at $\phi_{p0} = 0.5$ with $\chi = 0.29$, $h = 20$, $D = 10^{-11}$ m^2s^{-1}, and non-flux boundary condition.

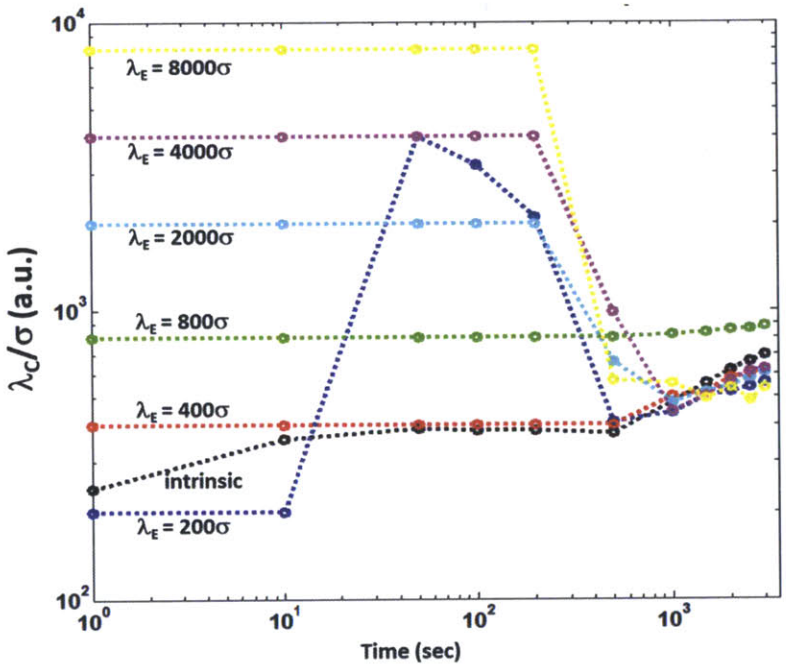

Figure 8.15. Temporal evolution of the characteristic wavelength of the phase-separated domains (λ_C) from the physically controlled spinodal decomposition with different λ_E. λ_C was analyzed from the images in Figure 8.14.

The other way for the physical controlling is to employ photo-sensitive dispersion materials such as photoresist monomers. These materials react under the specific range of the incident light to produce polymerized or cross-linked structure. Interestingly this approach will result in change in the chemical properties of the materials as well as in the initial concentration fluctuation. We applied the same numerical methods to examine this way of physical control in 3D case as shown in Figure 8.16. From the simulation results, we can find that the controlling strategy will be sustained at the long time of the spinodal decomposition both in periodicity and symmetry of the separated domain. For the future work,

more practical ideas and procedures are required to implement the present strategy for the physical control for the spinodal decomposition.

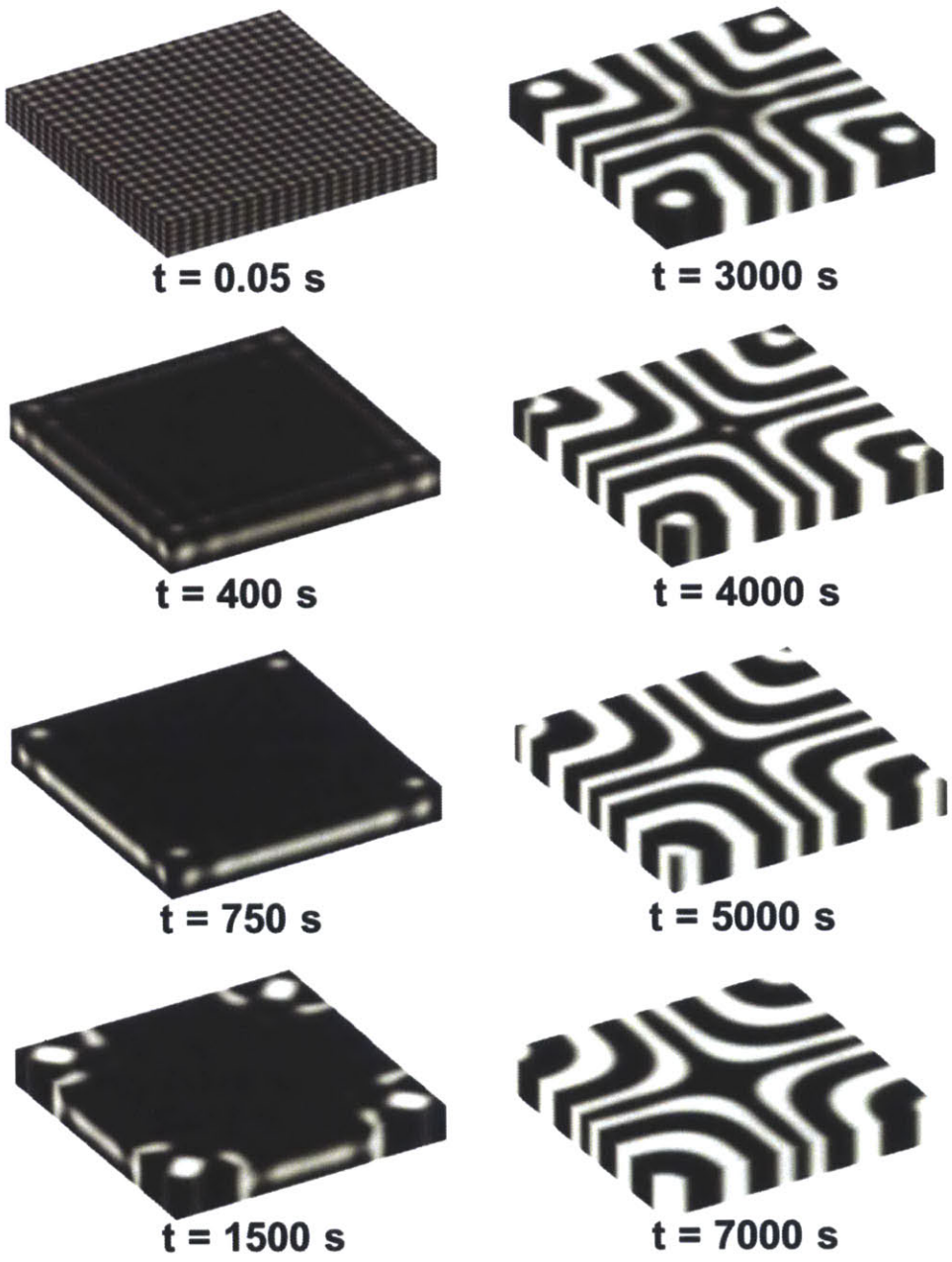

Figure 8.16. Temporal evolution of the phase separation in 3D governed by physically controlled spinodal decomposition. Initial condition was commonly examined at $\phi_{p0} = 0.5$ with $\chi = 0.29$, $h = 20$, $D = 10^{-11}$ m^2s^{-1}, and periodic boundary condition.

8.4. References

[1]. P.G. deGennes, *Angew. Chem. Int. Ed. (Weinheim),* **31**, 842 (1992);
P.G. deGennes, *Rev. Mod. Phys.*, **64**, 645 (1992).

[2]. H.M. Lindsay, R. Klein, D.A. Weitz, M.Y. Lin, and P. Meakin, *Phys. Rev. A*, **39**, 3112 (1989).

[3]. Z. Nie, W. Li, M. Seo, S. Xu, and E. Kumacheva, *J. Am. Chem. Soc.*, **128**, 9408 (2006).

[4]. M. Lattuada and T.A. Hatton, *J. Am. Chem. Soc.*, **129**, 12878 (2007);
M. Lattuada and T.A. Hatton, *Nano Today*, **6**, 286 (2011).

[5]. F. Baletto, '*Metal Clusters and Nanoalloys: From Modeling to Applications, Nanostructure Science and Technology*', (*Ed.* M.M. Mariscal *et al.*)
(Springer Science and Business Media, New York, 2013).

[6]. N. Kern and D. Frenkel, *J. Chem. Phys.*, **118**, 9882 (2003).

[7]. F. Sciortino, A. Giacometti, and G. Pastore, *Phys. Rev. Lett.*, **103**, 237801 (2009);
C. Gogelein, F. Romano, F. Sciortino, and A. Giaometti, *J. Chem. Phys.*, **136**, 094512 (2012).

[8]. R. Fantoni, A. Giacometti, F. Sciortino, and G. Pastore, *Soft Matt.*, **7**, 2419 (2011).

[9]. A. Giacometti, F. Lado, J. Largo, G. Pastore, and F. Sciortino, *J. Chem. Phys.*, **132**, 174110 (2010).

[10]. Y. Diao, M.E. Helgeson, A.S. Myerson, T.A. Hatton, P.S. Doyle, and B.L. Trout, *J. Am. Chem. Soc.*, **133**, 3756 (2011); Y. Diao, M.E. Helgesson, Z.A. Siam, P.S. Doyle, A.S. Myerson, and T.A. Hatton, *Crystal Growth & Design*, **12**, 508 (2012).

[11]. J.N. Israellachivili, '*Intermolecular and Surface Forces*', *2nd ed.* (Academic Press, New York, 1992).

[12]. R. Everaers and M.R. Ejtehadi, *Phys. Rev. E*, **67**, 014710 (2003).

[13]. E. Hecht, '*Optics*', *4th ed.* (Addison-Wesley Longman Inc., New York, 2002).

[14]. J. Henningsen, *Am. J. Phys.*, **79**, 85 (2011).

[15]. S.R. Seshadri, *Opt. Lett.*, **28**, 595 (2003).

Appendices

Appendix A. Kinetic Monte Carlo Algorithm on the Basis of Next Reaction Method

A.A.1. A Kinetic Monte Carlo Algorithm on the Basis of First Reaction Method

The fundamental idea about the stochastic simulation algorithm (SSA) suggested by Gillespie [1] was to find the minimum waiting time among all the reaction propensities followed by to update the reaction configuration. This method is also called the first reaction method (FRM) because it finds the first reaction which is on the top of the list for the fastest reaction. Although this method is stochastically exact and relatively easy to implement, it is computationally expensive; from the generation of random numbers at every iteration step. This gives rise to computational cost proportional to the number of reactions ($\mathrm{O}\left(N_{rxn}\right)$). Additionally it is inefficient for diffusion-related problems including spinodal decomposition.

A.A.2. A Kinetic Monte Carlo Algorithm on the Basis of Next Reaction Method

Instead of the FRM, Gibson and Bruck [2] suggested much more computationally efficient algorithm based on the reusing of the random numbers and maintaining the data structure on the order of the waiting time of the reactions. A detailed mathematical proof and the principle showing how it can enhance the computational efficiency from $\mathrm{O}\left(N_{rxn}\right)$ to $\mathrm{O}\left(\log\left(N_{rxn}\right)\right)$ can be found in the original paper of Gibson and Bruck. In this part, we showed how it can work for the diffusion-related problem. The first step to solve the diffusion-related problem is to set the diffusivity as a quantity which is equivalent to the 'reaction kinetic constant' such that

$$d = \frac{D}{h^2},$$

where h denotes the size of compartment. The unit of d is equal to $(\text{Number of Events/Unit Time})$.

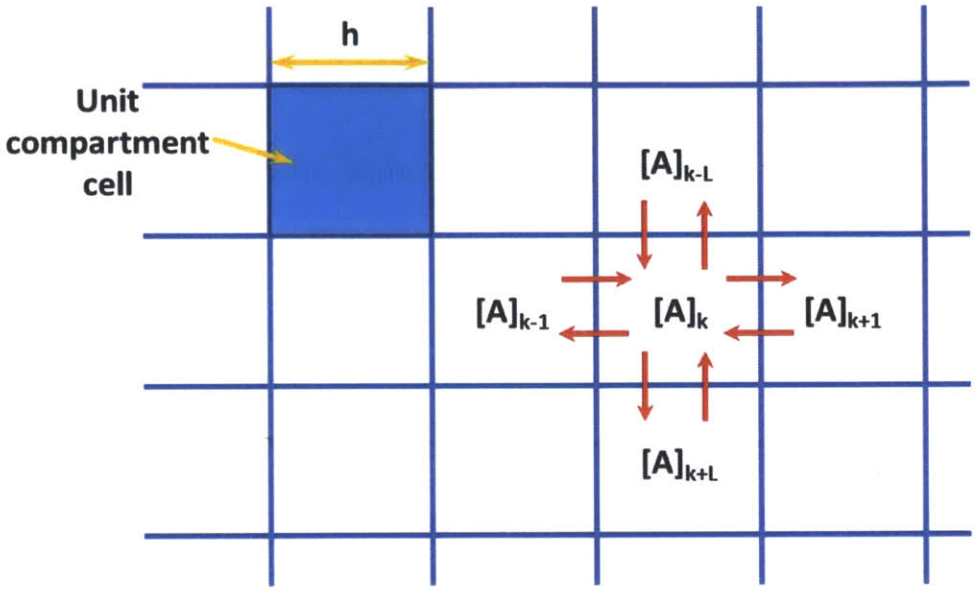

Figure A.A.1. A schematic diagram for the diffusion process of A-type particles among compartments in 2D.

As shown in Figure A.A.1, the diffusion of matter among the compartments can be described as the effective chemical reaction among neighboring cells such that

$$\text{At t, } [A]_{k-1}(t) \xrightarrow{d} [A]_k(t), \qquad (A.A.1)$$

where $[A]_k(t)$ is for the number of A-type particles in the k th compartment at time t. The mean waiting time for the diffusion of a single particle in eq.(A.A.1), τ_d, can be written as [1]

$$\tau_d = \frac{1}{d[A]_{k-1}(t)} \log\left(\frac{1}{rand}\right), \qquad (A.A.2)$$

where $rand$ is for the random number which is uniformly distributed from zero and unity. Then after τ_d, there will be change in the number of A-type particles such as

$$[A]_{k-1}(t+\tau_d) = [A]_{k-1}(t)\text{-}1,$$
$$[A]_k(t+\tau_d) = [A]_k(t) + 1. \qquad (A.3)$$

This can be applied in the 1D diffusion case with a periodic boundary condition for instruction as presented in Figure A.A.2.

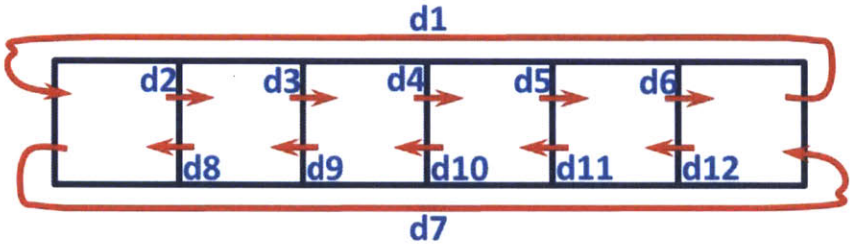

Figure A.A.2. A schematic diagram of the 1D diffusion with periodic boundary condition

In this diffusion case, we can start with an exemplary initial configuration with the number of particles (N_p) in each of the boxes such that

Box #	1	2	3	4	5	6
N_p	8	6	9	4	3	5

Next, we calculate the propensity, $\Pr_i$, and subsequent average waiting time, τ_i, $i = 1, 2, \cdots, 12$, of the diffusion of a particle in each of the boxes such that

Diff rxn #	1	2	3	4	5	6	7	8	9	10	11	12
τ	0.0395	0.0963	0.1844	0.4204	0.6905	0.0161	0.0473	0.1294	0.0371	0.1054	0.7250	0.0957

Based on the calculated τ_i, we can apply a sorting method such as the heapsort which utilizes the binary tree structure to find out which box has the shortest average diffusion waiting time. In this case, the heapsort makes following binary structure;

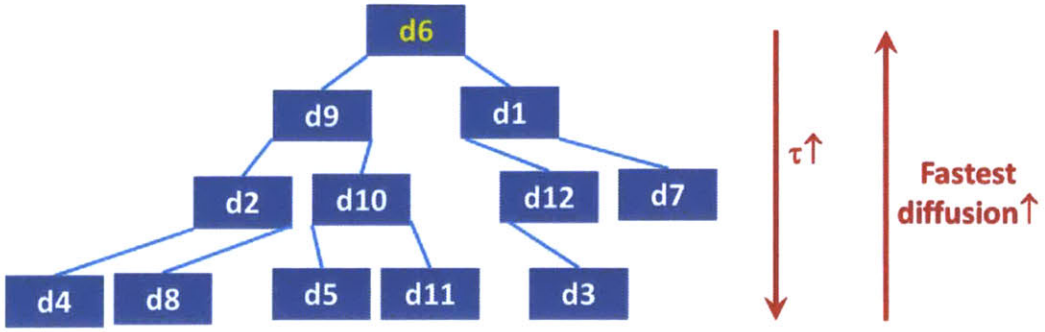

and on top of the tree structure, the diffusion process $d6$ is located because it has the shortest waiting time. By letting the diffusion process $d6$ occur, and update the system time as

$$t_{new} = t_{old} + \tau_6.$$

By the diffusion process $d6$, we can update the number of particles in each of the boxes as

Box #	1	2	3	4	5	6
N_p	8	6	9	4	2	6

And this gives rise to the updated diffusion propensities followed by update of the average waiting time for the diffusion as

Diff rxn #	1	2	3	4	5	6	7	8	9	10	11	12
τ	0.0356	0.0963	0.1844	0.4204	0.6905	0.2449	0.0473	0.1294	0.0371	0.1500	0.4069	0.0957

In this updated waiting time list, it should be noted that the update was done only for the diffusion processes which were affected by the diffusion process $d6$. (i.e., the diffusion processes $d1$, $d6$, $d10$, and $d11$). Then, we again apply the heapsort to construct the binary structure and find the fastest diffusion in the updated system configuration as follows:

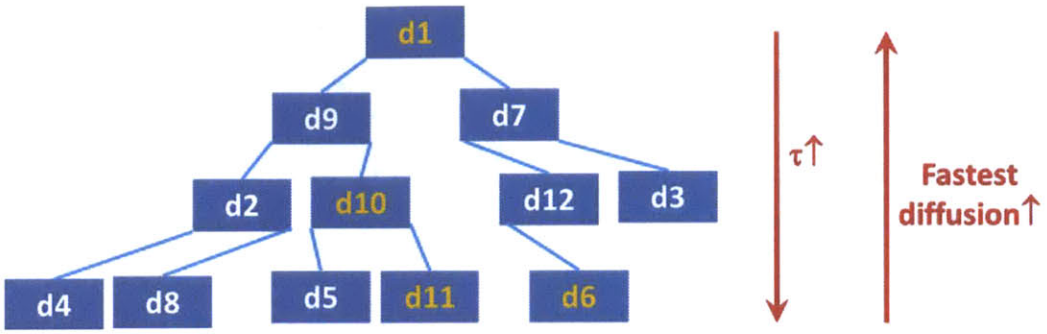

On top of the updated binary structure is located the diffusion process $d1$, and therefore, we can update the system time as

$$t_{new} = t_{old} + \tau_1.$$

The simple illustrated 1D diffusion tells us about the importance of maintaining the binary structure of the average waiting time of the diffusion propensities as well as finding diffusion propensities which affected by the fastest diffusion process. In order to effectively and efficiently find the affected processes, we need to construct an additional data structure such as dependency graph which how the different diffusion or reaction processes are dependent of each other. This is a necessary condition to reduce computational load for the generation of random numbers as well as finding the fastest diffusion which results in the reduction in the computational cost from $\mathrm{O}(N_{rxn})$ to $\mathrm{O}(\log(N_{rxn}))$. In Figure A.A.3, we presented a time-dependent 2D diffusion based on the NRM assuming non-flux boundary condition with diffusivity of 10^{-11} $\mathrm{m^2 s^{-1}}$. From the figure, we can find that the NRM can exactly describe the 2D diffusion process.

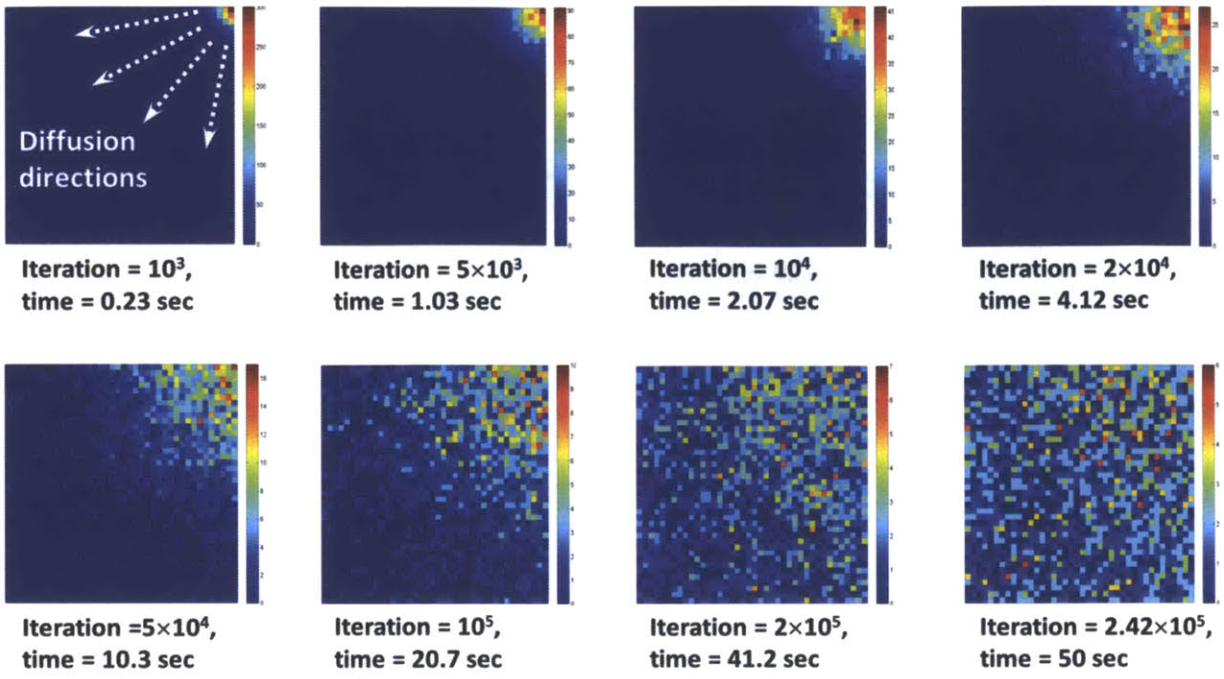

Figure A.A.3. A temporal evolution of concentration distribution over the 2D box by diffusion simulated by kinetic Monte Carlo method based on the NRM.

A.A.3. References

[1]. D.T. Gillespie, *J. Comp. Phys.*, **22**, 403 (1976).

[2]. M. Gibson and J. Bruck, *J. Phys. Chem. A*, **104**, 1876 (2000).

Appendix B. An Algorithm for Cluster Configuration Analysis

A.B.1. Structural Analysis of Clusters by the Radial Distribution Function

The first method to analyze the structure and geometry of the clusters composed of particles is radial distribution function (also known as pair-distribution function), $g(r)$. This function provides how much the cluster is similar to the ideal close-packed structure (i.e., hexagonal close-packed (HCP) structure in 2D) and how many neighboring shells a single particle in the cluster has in average. It also helps one to determine the boundary of the clusters based on the peak positions.

In Figure A.B.1, we provided an image of exemplary clusters accompanied by the resulting $g(r)$. From the figure, we can find that the clusters try to maintain the structures similar to the HCP structure; each of the peaks in $g(r)$ is matched with different numbers of neighboring shells. Another information obtained from $g(r)$ is the critical inter-distance among particles such that $r = 1.58\sigma \equiv r_s$, which is responsible for the distance at which $g(r)$ has the local minimum value between the first two peaks. r_s can be employed to determine an independent cluster from others. For example, we can assume that two particles with inter-distance over r_s are not in the same cluster.

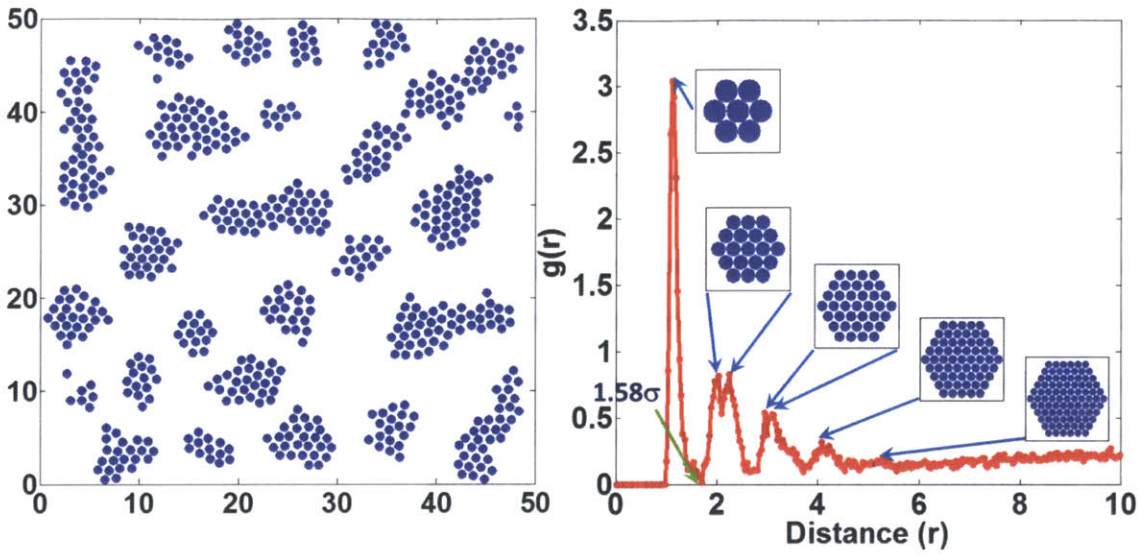

Figure A.B.1. An exemplary simulated image of clusters by KMC algorithm (left) and the resulting radial distribution function, $g(r)$ (right). For $g(r)$, the distance was normalized with respect to the particle diameter σ. Given in the insets of the right plot are illustrated hexagon-shaped clusters with increasing number of shells. Each of the peaks in $g(r)$ was matched with the expected cluster structures to demonstrate how the peak positions in correspond to the number of shells.

A.B.2. Configuration of Cluster: Size Measurement

Although the information from $g(r)$ is substantial to analyze the structure and crystallinity of clusters, it cannot provide information about the shape and size of clusters and volume occupied by clusters. To quantitatively analyze the nucleation/growth process, I also developed an algorithm which analyzes statistical, geometrical, and topological information of formed nuclei and its growth termed as algorithm for cluster configuration analysis (ACCA). The detailed procedure to run the ACCA is provided in Table A.B.1. By using the ACCA, we can quantitatively define the clusters as well as determine whether a certain particle is a monomer or not.

Provided coordinates information of particles in a certain cluster, we can also determine the size of clusters by employing following size definitions:

(1) The radius of gyration, R_g

$$R_g = \left(\sum_{\mathbf{r}} |\mathbf{r} - \mathbf{r_0}|^2 \right)^{1/2},$$

where $\mathbf{r_0}$ is the position of the particle which has the minimum total inter-distance among other particles at the position $\mathbf{r}$ in the cluster.

(2) Maximum distance from $\mathbf{r_0}$ to the farthest position of particle in the cluster, R_M

$$R_M = \max\left(|\mathbf{r} - \mathbf{r_0}|\right).$$

(3) Radius from the random walk model, R_R

This quantity is calculated as follows:

Find the shortest inter-distance of each of the particles from its neighboring particles in the cluster ($d_i = \min\left(\left|\mathbf{r_i} - \mathbf{r_i^{(n)}}\right|\right)$), and calculate root of the sum of d_i.

$$R_R = \left(\sum_i d_i \right)^{1/2}, \quad d_i = \min\left(\left|\mathbf{r_i} - \mathbf{r_i^{(n)}}\right|\right)$$

Table A.B.1. A summarized computational procedure to quantitatively measure the cluster size based on the algorithm for cluster configuration analysis (ACCA)

Algorithm for Cluster Configuration Analysis (ACCA) for Cluster Formation Simulation
Step 1. Set initial positions (considering self-exclusion effects) of NPs
Step 2. Find a list of nearest neighbors (nns) for each of the NPs within the cutoff distance $r_s = 1.58\sigma$
Step 3. Find monomers (particles with no nns)
Step 4. For the remaining particles (not monomers) accompanied by respective nns
Step 4.1. Find a list of nns of the 1st particle (≡ $\{NN_1\}$), and make a set for particles indices involved in the 1st cluster (≡ $\{CLUS_1\}$) including the 1st particle itself and its nns
Step 4.2. For the ith nn particle of the 1st particle (n_{1i}), find a list of nns of the 1th nn particles ($\{NN_{n1i}\}$) and update $\{CLUS_1\}$ such that $\{CLUS_{1\_new}\} = \{CLUS_{1\_old}\} \cup \{NN_{n1i}\}$
Step 4.3. Repeat Step 4.2 until $\{CLUS_{1\_new}\} = \{CLUS_{1\_old}\}$
Step 4.4. If $\{CLUS_{1\_new}\} = \{CLUS_{1\_old}\}$, set $\{CLUS_1\} = \{CLUS_{1\_new}\}$ and exclude particle indices

in {$CLUS_1$} from entire particles' indices and repeat Step 4 to construct {$CLUS_2$} by repeating Steps 4.1-4.3.

Step 4.5. Repeat Step 4 until there are no particles to be included in clusters.

End of Algorithm

The three quantities are not necessarily equivalent to each other, but are strongly correlated. Figure A.B.2 compares the size measurement of clusters by R_g, R_M, and R_R. From the figure, we can find the size measurement increases in order of R_g, R_M, and R_R. However, note that the order of size measured between R_M and R_R is not necessarily fixed, since it depends on the cluster anisotropy or symmetry of shape. For example, we compared the size measurement of clusters between R_M and R_R with different shapes, anisotropy, and configuration of particles as shown in Figure A.B.3.

From the figure, we can observe following properties;

(1) $R_M < R_R$ for an isotropic and symmetric clusters.

(2) $R_M > R_R$ for an anisotropic but symmetric clusters.

(3) $R_M \approx R_R$ for a randomly-shaped and asymmetric clusters, espeeially, they get closer to each other when the number of shells in a cluster increases

(4) An inner cavity in the cluster produces an error in the size measurement by R_R compared to the measurement by R_M.

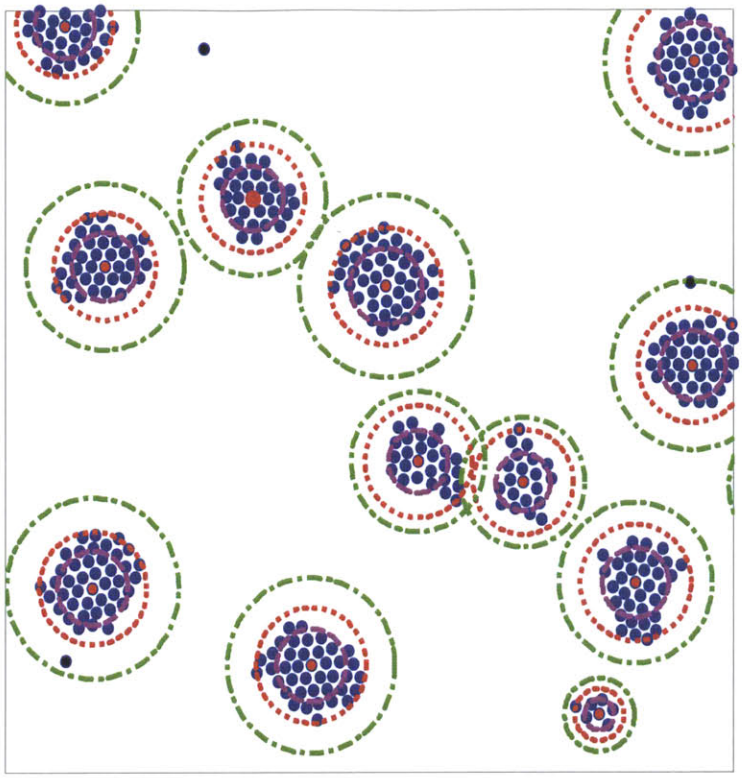

Figure A.B.2. Size measurements of clusters by R_g (maroon dash lined circle), R_M (red dot lined circle), and R_R (green dash-do lined circle). Red circular close symbols s denote the center of the clusters and black circular close symbols denote the monomers

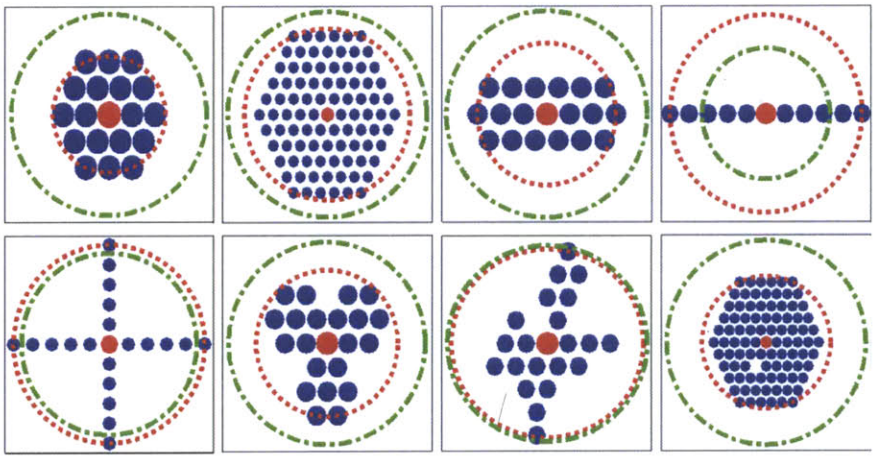

Figure A.B.3. Size measurements of clusters by R_M (red dot line) and R_R (green dash-do line) with different shape and configurations of the particles which compose clusters.

A.B.3. Configuration of Cluster: Topological Analysis

Although size measurement of the clusters provides useful information about the geometric properties of clusters, we may need additional information such as topological properties of clusters including shape, average inter-distance among clusters, average volume occupied by clusters, and so on. These properties can be quantitatively analyzed by employing the Voronoi tessellation, the deLaunay triangulation which gives reciprocal property of the Voronoi tessellation, and the convex hull measurement. In Figure A.B.4., we provided a comparison the three measurements for the topological property of the clusters. From the figure, we can find that the convex hull gives shape information, while the Voronoi tessellation and deLaunay triangulation give information on how the particles or clusters are topologically distributed. In particular, the Voronoi tessellation provides information on the free space independently occupied by particles or clusters, the deLaunay triangulation provides information on the topological space independently occupied by particles or clusters (i.e., information on the nearest neighbors), and the convex hull makes an envelope which defines the realistic shape of the clusters by calculating the minimal area occupied by the cluster. The envelope area can also be calculated by the coordinate of the vertices of the envelope.

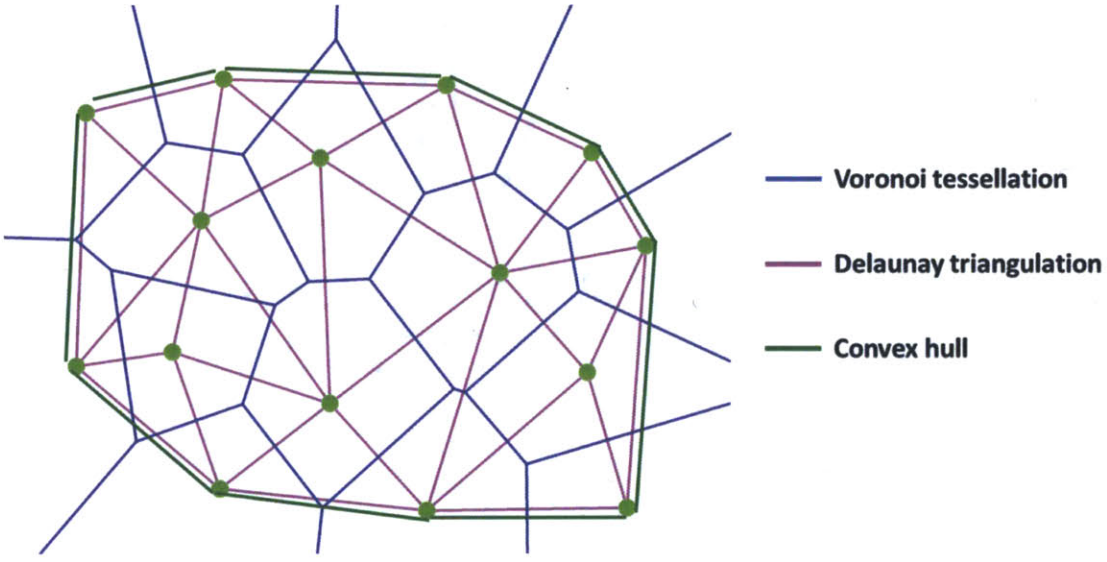

Figure A.B.4. Comparison of the topological measurements of a cluster by the Voronoi tessellation, deLaunay triangulation, and the application of the convex hull.

In Figures A.B.5, 6, and 7, we provided an image of exemplary clusters analyzed by the Voronoi tessellation, the deLaunay triangulation, and the convex hull construction, respectively. From figures, we can find that each of the methods of analysis provides distinct topological information about the clusters.

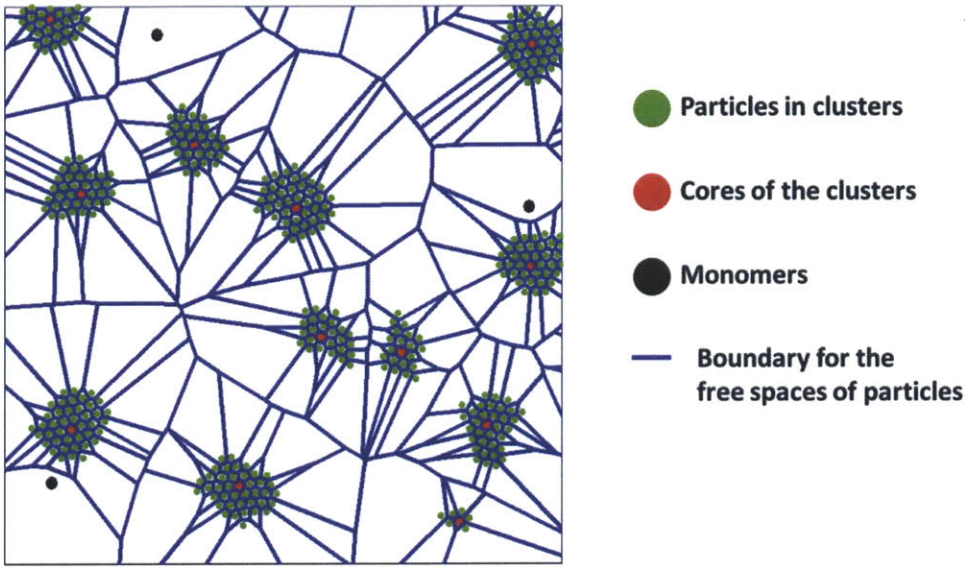

Figure A.B.5. Clusters analyzed by the Voronoi tessellation

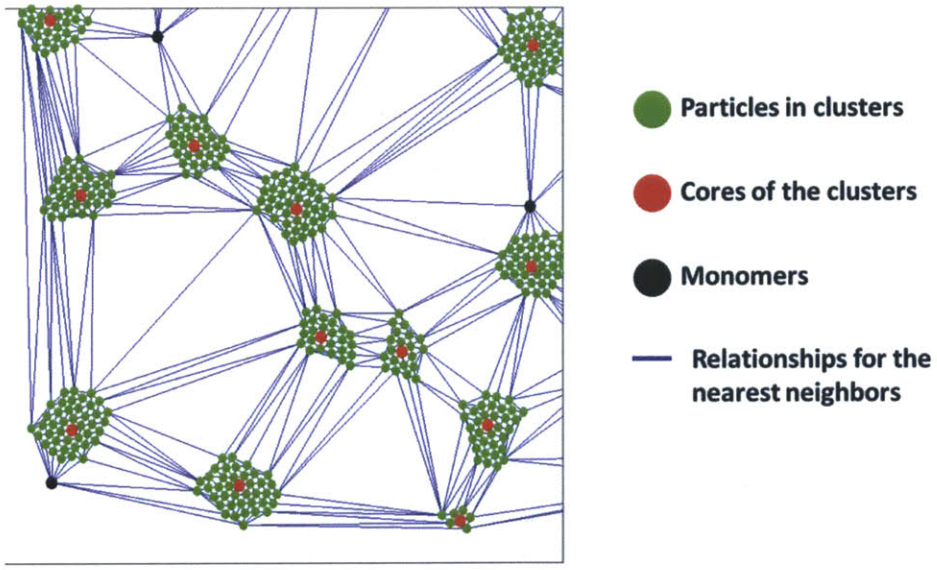

Figure A.B.6. Clusters analyzed by the deLaunay triangulation

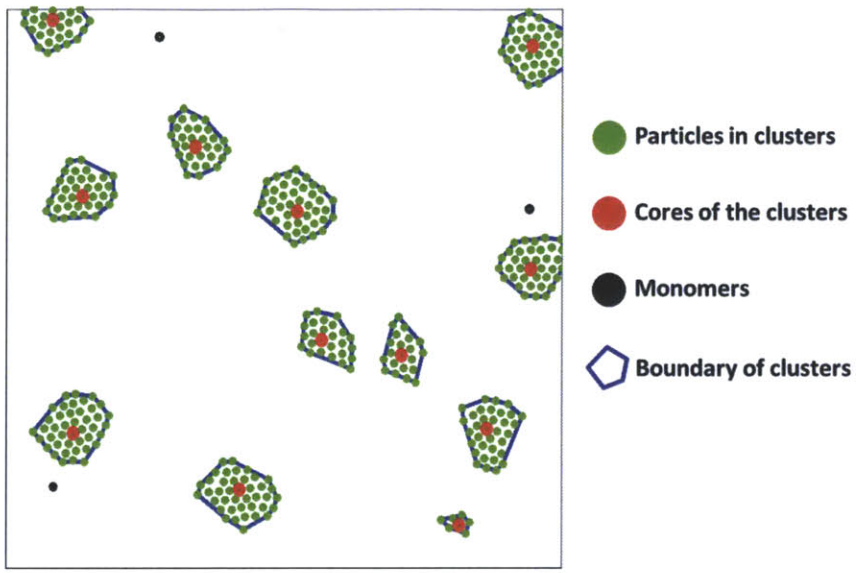

Figure A.B.7. Clusters analyzed by the construction of the convex hull

Appendix C. An Algorithm for Configuration Entropy Analysis of 2D Nanoparticles Superlattice

A.C.1. Configuration Entropy

The algorithm provided in Appendix C was not directly employed in the present thesis. This part is for the future work and further application for quantitative analysis of 2D structures composed of NPs. One of the direct ways of examining whether the phase transition is first- or second-order one is to calculate the entropy of the system, S. In a computer simulation, this can be done by tracing and calculating the variation of the total system free energy, E, as a function of a thermodynamic variable such as the system temperature T given as

$$S(T_1) - S(T_0) = \int_{T_0}^{T_1} \frac{1}{T} \frac{\partial E}{\partial T} dT. \qquad (A.C.1)$$

If S discontinuously changes around the transition point, then the phase transition is first-order while second order transition requires continuity in the profile of S.

At fixed finite temperature, a 2D system can suffer a disorder-induced phase transition. In a case in which the time-dependence trajectory of the system energy is not available, we can calculate the degree of randomness of the system, which can be translated into S. From the relationship between the disorder strength and S, one can determine whether the phase transition is first or second-order. In order to calculate S, we considered topological properties of the 2D NPSCs from which we extracted configuration entropy. As one of the methods to calculate the configuration entropy, one can count the frequency of different kinds of cells constructed by Voronoi tessellation. Given the maximum nearest neighbors (i.e., by threshold inter-distance), one can construct Voronoi tessellation for each of the particles, and count the frequency of tessellation cells with different nearest neighbors. In the crystal-like 2D NPs superlattice, most of the tessellation cells belong to 6-membered polygon, while melting decreases the 6-membered polygon cells frequency. Because every particle can be involved in different tessellation cells, the occurrence frequency of the tessellation cells is averaged over the participating particles. This scheme can be summarized as follows:

$$S = -k_B \sum_{i=1}^{N_t} p_i \log p_i, p_i = \frac{N_i}{N_T}, N_T = \sum_{i=1}^{N_t} N_i, \qquad (A.C.2)$$

where N_T is the total number of tessellation cells, N_i is the number of different kinds of tessellation cells, and N_i is the number of the i th kind of tessellation cells. Although this method can be easily implemented to calculate the configuration entropy, it is less exact than the method based on the graph isomorphism and Shannon's information theory. This is mainly because the latter takes more diverse and potential arrangement of 2D NPSC into account of both geometrical and topological analysis. The graph isomorphism considers two graphs are essentially equal if their topological structures are equivalent. This indicates that the shape or size of the graph composed of identical number of nearest neighbor particles does not affect the graph isomorphism as long as the bond connectivity among the particles in the graph does not vary. According to the Shannon's information theory, the configuration entropy is expresses as follows [1]:

$$S(m,n_S) = -k_B \sum_{i=1}^{N_g} p_i(m,n_S) \log_2 p_i(m,n_S), p_i(m,n_S) = \frac{f_i(n_S)}{m}, \qquad (A.C.3)$$

where $f_i(n_S)$ is the frequency of the i th graph isomorphism composed of n_S nearest neighbors involving oneself when m different random position coordinates of particles are chosen among entire system. In Figure A.C.1, we provided an exemplary coordinates of NPs in 2D NPSCs accompanied by the Voronoi tessellation when $n_S = 8$. In order to compensate dimensionality of the system, d, and crystallinity, Vink and Barkema [2] proposed a correction term for the entropy in eq.(A.C.3) such that

$$S_C(m,n_S) = S(m,n_S) - k_B(d-1)\log n_S. \qquad (A.C.4)$$

Given that the structure to be analyzed has a finite dimension (i.e. no periodic boundary condition), one can expect that $S_C(m,n_S)$ will converge into $S_C^*(n_S)$ as m increases, and there exists a threshold value of m, m^*, which makes $\lim_{m\to\infty} S_C(m,n_S) = S_C^*(n_S) \approx S_C(m^*,n_S)$.

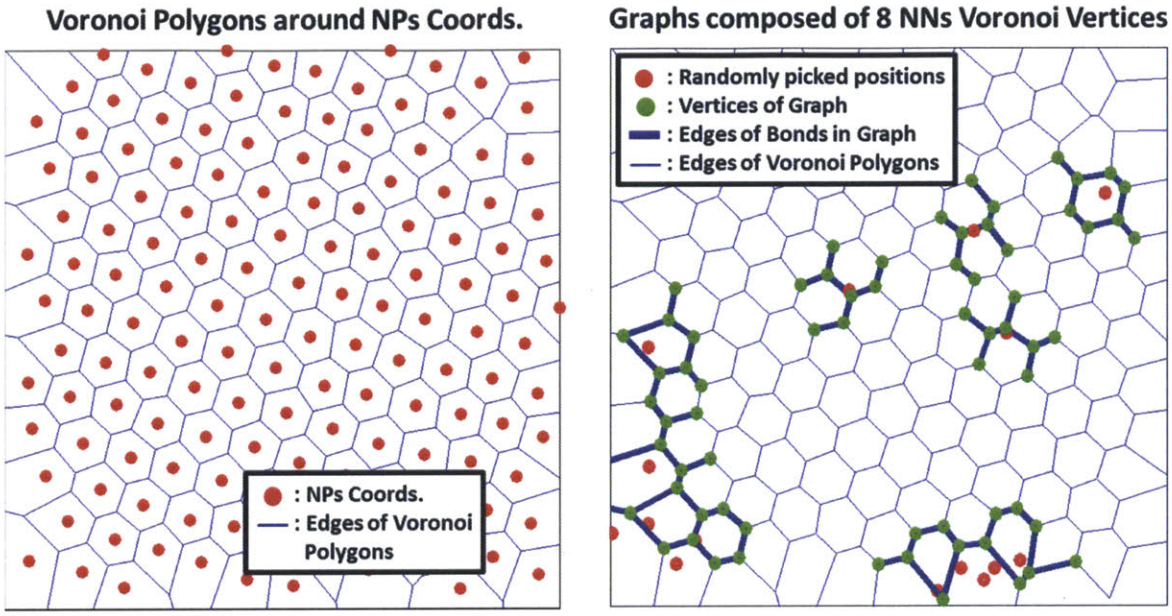

Figure A.C.1. A reconstructed coordinates of NPs (denoted by red circular close symbols) from TEM images (not shown due to copyright) with boundaries for the Voronoi tessellation (blue solid edges) (left) and several different graphs composed of 8 nearest neighbors (NNs denoted by green circular close symbols) found on the Voronoi tessellation of the NPs (right) given randomly picked positions (denoted by red points). The NNs are considered as vertices in the graphs and the edges in each of the graphs are represented by bold blue lines.

Given in Figure A.C.2 is the compilation of different graphs with respective occurrence frequency (probability) when $n_S = 8$. Information in Figure A.C.2 is translated into histogram as given in Figure A.C.3. Although not provided here, we found that $m^* \sim 8{,}000$ for network structures composed of Voronoi polygons encompassing 2D NPSCs of 7,800-8,100 NPs. In order to compare specific configuration entropy, $S_C(n_S)$ is normalized by introducing the configuration entropy per NP, s_C

$$s_c = \lim_{n_S \to \infty} \left[S_C(n_S) - S_C(n_S - 1) \right] \approx \left. \frac{\Delta S_C(n_S)}{\Delta n_S} \right|_{n_S^*}, \qquad (A.C.5)$$

where n_S^* denotes a threshold value of n over which a deviation from a linear proportion relationship between n_S and $S_C(n_S)$ increases. This deviation is mainly due to the finite number of NPs and dimension of the samples to be analyzed.

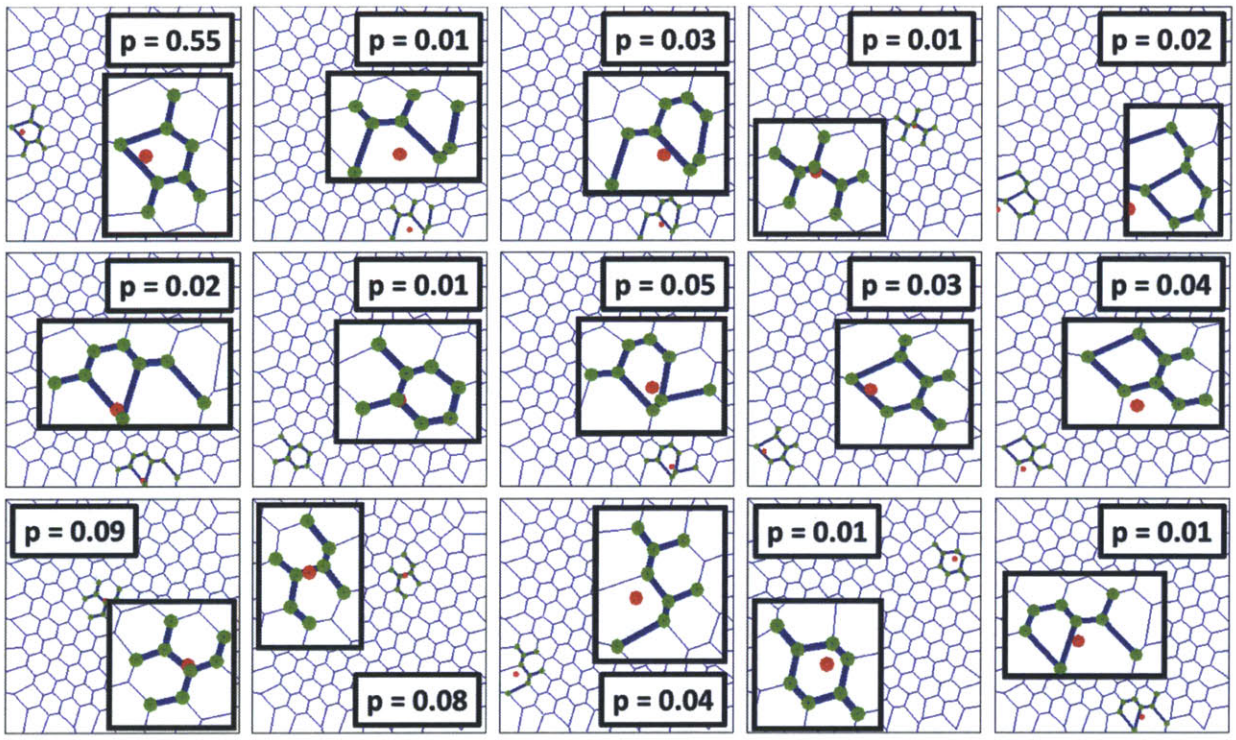

Figure A.C.2. Compilation of different graphs composed of 8 NNs (green vertices for NNs with bold blue lines for the edges with red points as the randomly picked point) with the normalized occurring frequency (or probability), p. In each of the panel, expanded pictures of the graph are provided.

A.C.2. A Graph Isomorphism Algorithm for Configuration Entropy

In the calculation process, we set a range of n_S according to n_S^* for each of the different samples while optimizing the linearity by maximizing the correlation coefficient. For the counting the occurrence frequency of different kinds of graph isomorphism, we can propose an algorithm as provided in Table A.C.1.

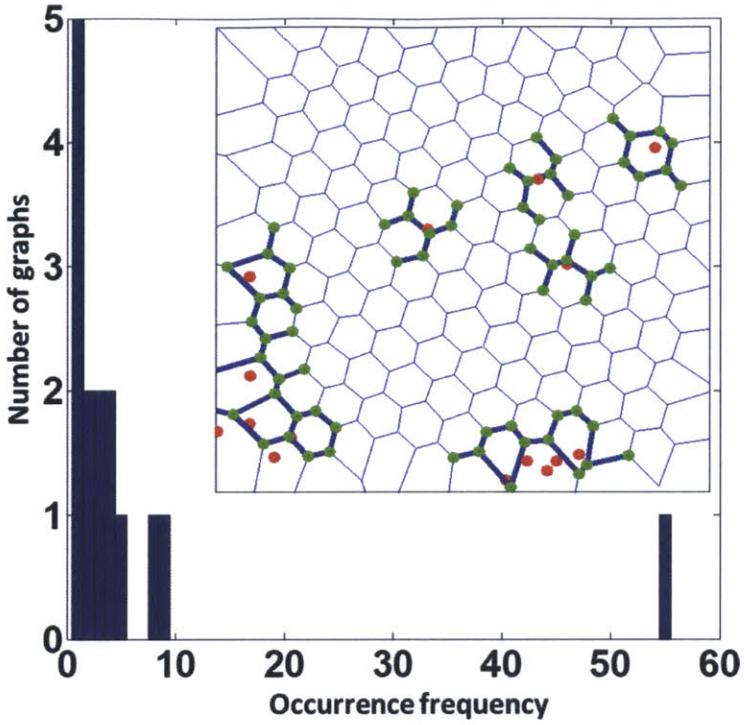

Figure A.C.3. A histogram for the occurrence frequency of the graphs composed of 8 NNs. Inset is for the exemplary graphs composed of 8 NNs.

Table A.C.1. A summarized algorithm to calculate the configuration entropy of 2D NPSCs

Algorithm to Calculate Configuration Entropy of 2D NPSCs
Step 1. Initialize coordinates of NPs
Step 2. Construct Voronoi tessellation around the NPs
Step 3. Construct an adjacency matrix for the vertices created in the Voronoi tessellation to find out nearest vertices to each other
Step 4. For given number of randomly picked positions (m), find out n nearest neighboring vertices.
Step 5. For the found vertices, construct a partial adjacency matrix to construct a graph which indicates whether each of the vertices are connected or not.
Step 6. Construct graphs composed of vertices for each of the random positions.
Step 7. Sort the graphs using graph isomorphism (topological point of view)
Step 8. Find out distribution of the topologically different graphs and make a group for identical graphs
Step 9. Calculate configuration entropy based on Shannon's information theory

Step 10. Correct the configuration entropy considering finite dimension and number of NPs in the 2D NPSC
Step 11. Repeat Steps 4-10 for different values of n, and linear fitting for the relationship between the configuration entropy and n (should be less than the threshold value of n)
Step 12. Calculate configuration entropy per an individual NP
End of Algorithm

As an exemplary and practical application, we analyzed the configuration entropy of 2D NPSC in which Au NPs are coated by dodecylthiol ($C_{16}H_{28}S$, DDT) ligand molecules. The 2D NPSCs were formed by the Langmuir-Blogett pressure device. Starting with the reconstructed NPs coordinates information from TEM image [3] (the original image was not presented due to copyright), we can construct the Voronoi tessellation as shown in Figure A.C.4(a) and from which, we can calculate S_C as a function of n as shown in Figure A.C.4(b) by applying the algorithm in Table A.C.1. From the plot, we can find the linearity between S_C and n, and from the slope of the fitting line, we can obtain $s_C = 0.1640 k_B$.

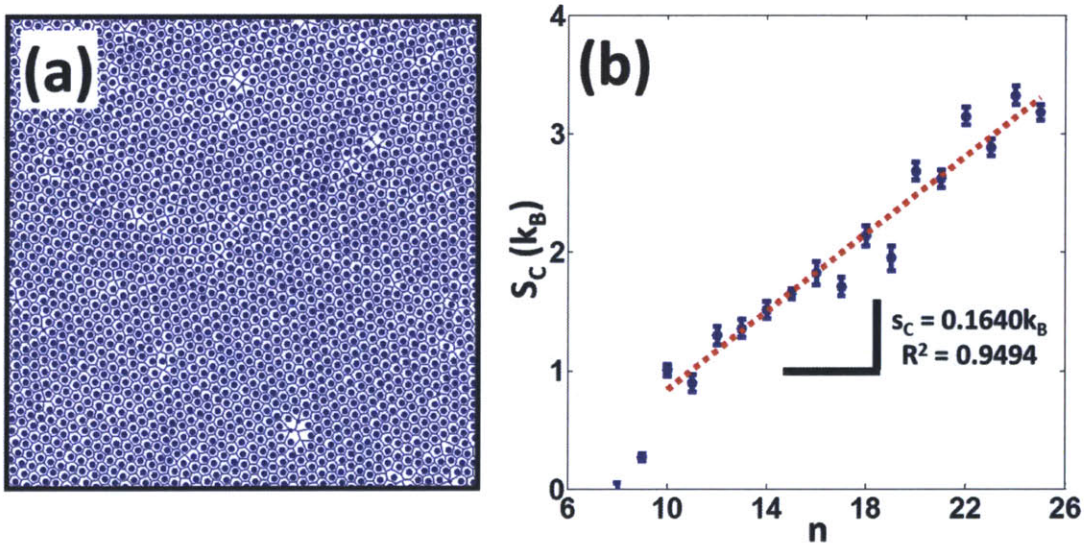

Figure A.C.4. (a) A Voronoi tessellated image from the coordinate information of Au NPs in 2D NPSCs [3] (c.f., constructed from an original TEM image, where the original image was not provided due to copyright.). Circular close symbols are for the NPs and blue edges are for the tessellated boundary. (b) A

relationship between S_C and n. The simulation to calculate S_C was repeated 160 times to obtain the statistically meaningful data.

A.C.3. References

[1]. C.E. Shannon, *Bell System Tech. J.*, **27**, 379 (1948).

[2]. R.L.C. Vink and G.T. Barkema, *Phys. Rev. Lett.*, **89**, 076405 (2002).

[3]. J.Y. Kim, S.J. Kwon, J.B. Jang, C.A. Ross, T.A. Hatton, and F. Stellacci, *to be submitted* (2013).